Strategies for improving the effectiveness of nanomedicine in triple negative breast cancer model

Guojun Xiong

A dissertation submitted in partial fulfilment

of the requirements for the degree of

Doctor of Philosophy

of

University College London

Department of Pharmaceutics

UCL School of Pharmacy

March 2023

Declaration

I, Guojun Xiong confirm that the work presented in my thesis is my own. Where information has been derived from other sources, I confirm that this has been indicated in the thesis.

Signature: _____

Date: _____

Abstract

Breast cancer is the most prevalent and the second leading cause of death among women worldwide. Metastatic triple negative breast cancer (mTNBC) is the most aggressive type of breast cancer, and an effective treatment for mTNBC patients remains a high unmet medical need. Nowadays, [nab-paclitaxel (Abraxane®)] based combination therapy is recommended by the National Comprehensive Cancer Network® (NCCN®) as the first-line treatment for mTNBC. However, Abraxane® exhibited limited survival benefit as a monotherapy in cancer patients when compared with the innovator PTX formulation, Taxol®. In this work, two feasible solutions have been proposed that may further enhance the chemotherapeutic effect of PTX in the treatment of mTNBC.

Firstly, by increasing the colloidal stability and payload of the nanocarrier, thereby improving the tumour deposition of PTX. The eligible nanocarrier (HSA-PLA nanoparticle) was created by the covalent binding of poly(L-lactide) to albumin cysteine residue. The PTX-loaded HSA-PLA nanomedicine has shown superior tumoricidal activity when compared to the Abraxane® in 4T1 tumour bearing mice at the same PTX dose. The final tumour weight of the mice treated with the HSA-PLA (PTX) was 239.8 ± 43.0 mg (n = 5) and was statistically smaller than the group (n = 5) treated with the Abraxane®, where the tumour weight was 340.6 ± 62.8 mg ($p < 0.5$).

Secondly, by further modifying the albumin, this nanocarrier is enabled to target

the CD44 and folate receptors of the TNBC tumours. Briefly, this tumour-tropism nanocarrier (Ac-HSA-PLA nanoparticle) was fabricated by acetylating the albumin (Ac-HSA) and subsequently conjugating of the polymer PLA to the acetylated albumin. In MDA-MB-231 tumour bearing mice, the TNBC tumours (n = 5) were completely eliminated after the treatment with the Ac-HSA-PLA (PTX), whereas the injected Abraxane® and HSA-PLA (PTX) at the same PTX dose could not achieve the same results. These promising *in vivo* results have encouraged us to further investigate these nanomedicines.

Impact Statement

Since the approval of the paclitaxel nanoformulation (nab-PTX), Abraxane®, as a chemotherapeutic agent for the treatment of various advanced cancers in 2005, nab-PTX-based combination therapies have been developed as the current first-line option for the treatment of advanced cancers. However, Abraxane® exhibited limited survival benefit as a monotherapy for metastatic breast cancer patients, when compared to the Taxol® (first generation of PTX injection). In response to the lack of effectiveness of the Abraxane® in patients, scientists have raised many assumptions. For example, after intravenous injection, Abraxane® nanoparticles become unstable when diluted by large amounts of blood and dissociate into albumin molecules, releasing PTX within a short period of time.

My research is focused on particle engineering to produce nanomedicines that are aimed at providing solutions for unmet clinical needs. In an elaboration of this aim, we have proposed two practicable strategies to increase the delivery of PTX to solid tumours in animal models. ***Chapter 2, 3 and 4*** comprehensively explain how the tumour deposition of PTX can be increased by improving the colloidal stability of nanomedicine, as demonstrated by comparing the HSA-PLA (PTX) with the Abraxane®. In ***Chapter 5 and 6***, by further acetylating the albumin L-lysine residues, the Ac-HSA-PLA nanocarriers were created. The tumour-tropism of the Ac-HSA-PLA nanocarriers to the TNBC cells largely improves the tumourcidal activity of the PTX in tumour-bearing mice.

In addition, in my PhD project, some interesting points are proposed that may explain the low effectiveness of the Abraxane® in patients. Firstly, the current understanding on the morphology of the Abraxane® (albumin-PTX bound spherical nanoparticle with a size of 130 nm) is potentially problematic. The morphology of the Abraxane® nanoparticles shown in my TEM images is that of spherical particles with a diameter of approximately 40 nm, rather than the stated 130 nm in size. Therefore, it is hypothesized that due to the low colloidal stability of the Abraxane® nanoparticles, they agglomerate into clusters with different shapes (approx. 130 nm in diameter) in aqueous medium. Details of this finding are provided in ***Chapter 3***. To the best of our knowledge, the description and interpretation for the inconsistency of the Abraxane® nanoparticle morphology in official concepts and the fact shown in the TEM/Cryo-EM images are not currently available. This work should be the first attempt to prove and explain the low colloidal stability of the Abraxane® in terms of DLVO theory and thermodynamics. Secondly, it is found that the pharmacokinetics profiles of the Abraxane® are not superior to the Taxol® in our preclinical studies, which is rarely mentioned in other publications. Meanwhile, according to the results of the Abraxane® in phase I clinical trial, a possible hypothesis was proposed on the cause of the rapid clearance of Abraxane® nanoparticles in patients. The albumin of the Abraxane® could be denatured during preparation, as native albumin should have a very long circulation time in the body ($t_{1/2}$ ~ 21 days). Details can be found in ***Chapter 2.***

Acknowledgements

In my PhD journey, I am filled with gratitude towards many people who have supported and guided me along the way.

First and foremost, I extend my sincere appreciation to my supervisors, Prof Ijeoma Uchegbu and Prof. Andreas Schätzlein. Their unwavering support, invaluable guidance, and positive decisions have been instrumental in shaping my academic path. Throughout the past four years, my academic capabilities have flourished under their nurturing mentorship. Their strategic direction and constant revisions to my research have kept me on the right track during my PhD.

I also want to express my gratitude to all those who have lent their helping hands. In particular, I extend my thanks to the members of our Nanomedicine Group. Their support during the initial stages of my PhD studies has been immensely valuable. Additionally, I would like to acknowledge the assistance provided by the staff at the UCL School of Pharmacy and the Biological Services Unit.

Lastly, I am deeply indebted to my parents, Mr. Xiong Yuzhi and Mrs. Sun Guilan, whose love and unwavering support have been the foundation of my journey. Without them, none of this would have been possible. I want to express my heartfelt gratitude to all of you!

Thank you, everyone, for being an integral part of my PhD life and for helping me become the person I am today.

Table of contents

List of Abbreviation

Ac-HSA-PLA – Acetylated human serum albumin-polylactic acid

ACN – Acetonitrile

ADC – Antibody drug conjugate

AIDS – Acquired immune deficiency syndrome

APC – Antigen-presenting cells

API – Active pharmaceutical ingredient

ASR – Age standardized rate

AUC – Area under curve

BRCA 1 – Breast cancer gene 1

BRCA 2 – Breast cancer gene 2

BSA – Bovine serum albumin

CAST Therapy – Cancer Stromal Targeting Therapy

CD – Circular dichroism

CHEK 2 – Checkpoint kinase 2

CLIC/GEEC – Clathrin-independent carrier/ glycosylphosphatidylinositol-anchored protein enriched early endocytic compartment endocytosis

CLSM – Confocal Laser Scanning Microscope

CMC – Critical micelle concentration

Cou-6 – Coumarin 6

Cryo-EM – Cryogenic electron microscopy

D_H – Hydrodynamic diameter

DLS – Dynamic light scattering

DLVO theory – Derjaguin–Landau–Verwey–Overbeek theory

DMSO – Dimethyl sulfoxide

DNA – Deoxyribonucleic acid

DSPE – Distearoyl phosphoethanolamine

DTNB – 5,5-dithio-bis-(2-nitrobenzoic acid)

EDTA – Ethylenediaminetetraacetic acid

EI – Electron impact

EMA – European Medicines Agency

EndoPDI – Endothelial protein-disulfide isomerase

EPR effect – Enhanced permeability and retention effect

ER – Estrogen receptor

ESI – Electrospray ionisation

NIR – Near Infrared

FA – Folic acid

FEME – Fast endophilin-mediated endocytosis

FSC – Forward scatter

FT-IR – Fourier-transform infrared spectroscopy

FITC – Fluorescein isothiocyanate

HER2 – Human epidermal growth factor receptor 2

HA – Hyaluronic acid

HSA – Human serum albumin

HSA-PLA – Human serum albumin-polylactic acid

MALDI-TOF – Matrix-Assisted Laser Desorption-Time of Flight

MAL-PLA – Maleimide-polylactic acid

MeOH – Methanol

MPS – Mononuclear phagocyte system

MRM – Multiple reaction monitoring

MTD – Maximum tolerated dose

mTNBC – metastatic triple negative breast cancer

MWCO – Molecular weight cut off

NCCN® – National Comprehensive Cancer Network®

NCI – National Cancer Institute

NIH – National Institutes of Health

nm – nanometre

NMSC – Non-melanoma skin cancer

NOD-SCID – Non-Obese Diabetic-Severe Combined Immunodeficiency

PAGE – Polyacrylamide gel electrophoresis

PALB2 – Partner and localizer of BRCA2

PCB – Polycarboxybetaine

PDI – Polydispersity index

PEG – Polyethylene glycol

PET/CT – Positron emission tomography/computed tomography

PFS – Progression free survival

PK – Pharmacokinetics

PMT – Photomultiplier tube

PR – Progesterone receptor

PTX – Paclitaxel

RNAi – Ribonucleic acid interference

RP-HPLC – Reverse phase high performance liquid chromatography

SD – Standard deviation

SD rat – Sprague-Dawley rat

SDS – Sodium dodecyl sulfate

SPION – Superparamagnetic iron oxide nanoparticle

SRM – Selected reaction monitoring

SSC – Side scatter

TCEP – Tris(2-carboxyethyl) phosphine

TEM – Transmission electron microscopy

TFA – Trifluoroacetic acid

TME – Tumour microenvironment

TNBC – Triple negative breast cancer

TRITC-dextran – Tetramethylrhodamine isothiocyanate–Dextran

US FDA – United States Food and Drug Administration

USDA – United States Department of Agriculture

UV – Ultraviolet

WHO – World Health Organization

w/w – weight to weight

XRD – X ray diffraction

µL – Microliter

µM – Micromolar

List of Figures

List of Tables

Chapter 1. Cancer and Nanomedicine

1.1 Introduction

The aim of this project is to design and create new chemical entity delivery systems to provide solutions for improving the chemotherapeutic effect of anticancer drugs. Before presenting the data and outcomes achieved in this project, a comprehensive review for the background of this project has been demonstrated in ***Chapter 1***. The introduction covers the general overview of cancer and provides a detailed classification of different cancer types to give an overall understanding of the disease and explain relevant terminologies used in this thesis.

Among all types of cancer, breast cancer has the highest incidence rate. Then breast cancer murine models were chosen as the *in vivo* test subjects to evaluate tumoricidal activity of our paclitaxel nanoformulations. Thus, the subdivisions of breast cancer, current treatment strategies for each subtype of breast cancer, and challenges for the treatment of triple-negative breast cancer are all clearly described in this part. Subsequently, the next generation therapeutic formulation – nanomedicine has been introduced in this chapter. Cancer nanotechnology is considered as the most promising approach to improve the overall survival of advanced cancer patients. Meanwhile, the major obstacles and future

expectations of nanomedicine have also been discussed. At last, the motivation and rationale of this project have been deeply expounded.

1.2 Overview of Cancer

Cancer is a general term for fatal diseases caused by abnormal differentiation, division and uncontrolled growth of cells with aberrant genomes: also known as malignant tumours and neoplasms, and cancer is also the major cause of death globally [1]. According to global statistical data [2] provided by the World Health Organization (WHO), approximately 16.7% of the deaths were due to cancer in 2020.

Cancers are generally divided into two major categories: malignant tumours and hematologic cancers. The carcinogenesis of normal cells is due to the malignant alteration of proto-oncogenes, tumour suppressor genes, or DNA repair genes of cells [3]. The cytogenetic errors may lead to the fundamental abnormality in any cell, theoretically allowing cancer to occur anywhere in the body. If the cancer originates in solid tissues, such as myoideum and organs, cancerous cells may develop into malignant tumours due to rapid and unlimited proliferation in situ. Hematologic cancer, also called blood cancer, is due to abnormalities of blood cells or immune cells derived from blood stem cells in the bone marrow. Normally hematologic cancers do not form solid tumours, such as leukaemia, multiple myelomas and Hodgkin lymphomas [4].

1.2.1 Introduction – Malignant tumours

Cancerous cells do not respond to signals and instructions for stopping proliferation or apoptosis, as normal cells do. Therefore, cancerous cells in solid tissues are able to multiply themselves infinitely and form primary solid tumours [5]. Owing to the continuous proliferation of cancerous cells, tumours require more nutrients and oxygen for supporting their rapid growth. Thus, cancer cells release angiogenic growth factors such as vascular endothelial growth factor and angiogenin to build the extra blood vessels from the existing vasculature to take nutrients and oxygen from the blood circulation. This process is called tumour angiogenesis [6]. Meanwhile, tumour cells also secrete the lymphangiogenic growth factors, such as vascular endothelial growth factor C and D, to induce the formation of lymphatic vessels. This process is known as tumour lymphangiogenesis [7].

A key function of the blood circulation [8] is to transport and deliver endogenous substances, xenobiotics and cells to and from organs and tissues. Conversely, lymphatics maintain homeostasis [9] by draining the interstitial fluid and cleaning extravascular substances. As the primary tumour can build both of blood vessels and lymphatic vessels, the free cancer cells divided from solid tumour can be probabilistically spread to other sites through the built vasculatures, such as hematogenous spread and lymphogenous spread, to develop secondary tumour

[10]. This process is called cancer metastasis (***Fig 1***). Metastatic cancer, also called advanced or stage IV cancer, is the leading cause of death in patients diagnosed with malignancy.

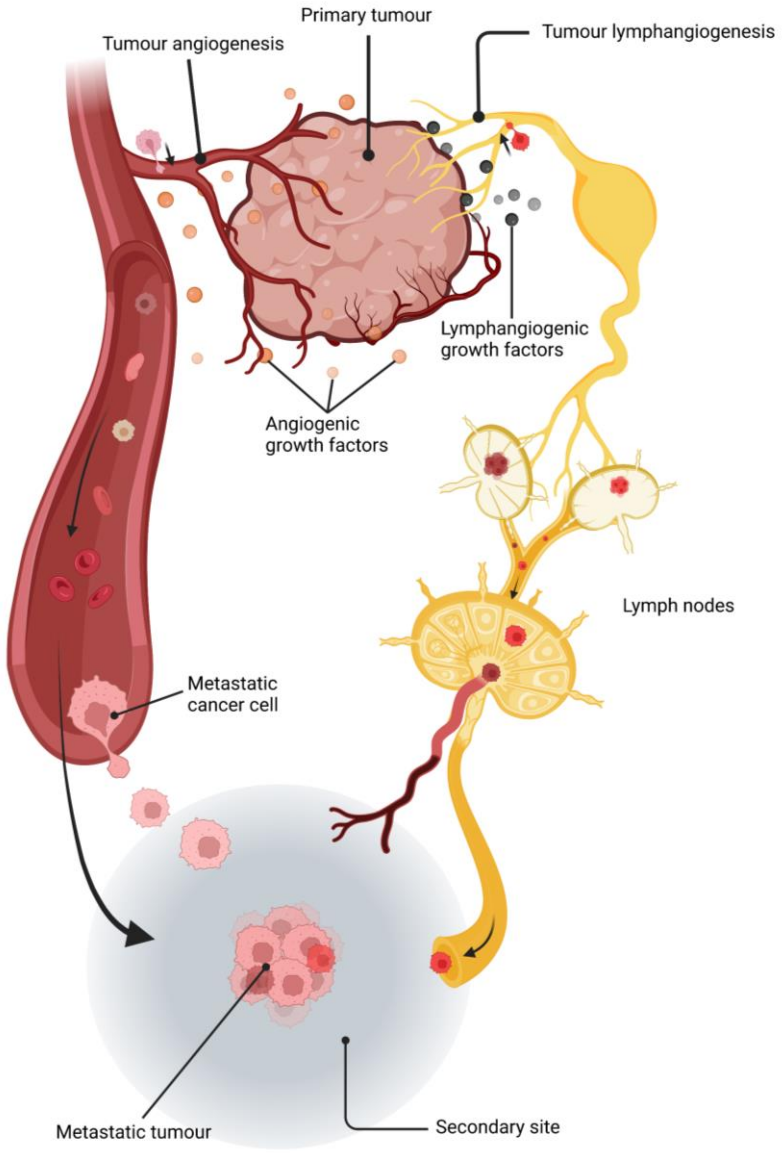

Fig 1. Schematic illustration of tumour angiogenesis, lymphangiogenesis and metastasis. Cancer cells of malignant tumour are able to secrete the angiogenic growth factors to build extra blood vessels from the existing blood vasculature - tumour angiogenesis. Meanwhile, lymphangiogenesis launched by tumour induces the generation of extra lymphatic vessels from the normal lymphatics. Free cancer cells metastasize to the secondary site through the circulatory system to form the metastatic tumours. Created with BioRender.com.

1.2.2 Introduction – Hematologic cancers

Hematologic cancers are normally different from solid malignant tumours [11], and they are caused by abnormalities in blood cells or immune cells derived from blood stem cells in bone marrow. Stem cells in the bone marrow can eventually differentiate into red blood cells, platelets and white blood cells [12], as shown in ***Fig 2***. Those blood cells have different functions in the circulatory system and immune system. For example, red blood cells carry oxygen from the lungs and return carbon dioxide to the lungs, platelets are involved in blood clotting and hemostasis, plasma cells produce different antibodies, and white blood cells play an important part in the immune system [13].

The formation of blood cancer cells is generally considered as genetic errors that occur during the differentiation or proliferation of different blood cells [14]. As a result, these abnormal blood cells lose their intrinsic immune functions, and the uncontrolled proliferation of cancerous blood cells reduces the production of normal blood cells, further weakening the immune system.

For instance, acute lymphocytic leukaemia arises from the cancerous changes of lymphoid progenitor cells and rapid proliferation of abnormal immature blood cells [15]. The uncontrolled growth of malignant lymphoblasts largely occupies the space of bone marrow that is used for the production of other normal blood cells [16]. Moreover, these malignantly immature blood cells are unable to develop into

normal lymphocytes and cannot contribute to the immune defence against infections. The job of plasma cells in the bone marrow is to produce antibodies for infected pathogens. Myeloma cells are abnormal plasma cells that produce useless proteins called paraproteins [17]. Continuous production of myeloma cells leads to bone destruction, immunologic deficiency, renal diseases and the spreading of this proliferative disease to multiple sites in the bone marrow, known as multiple myeloma.

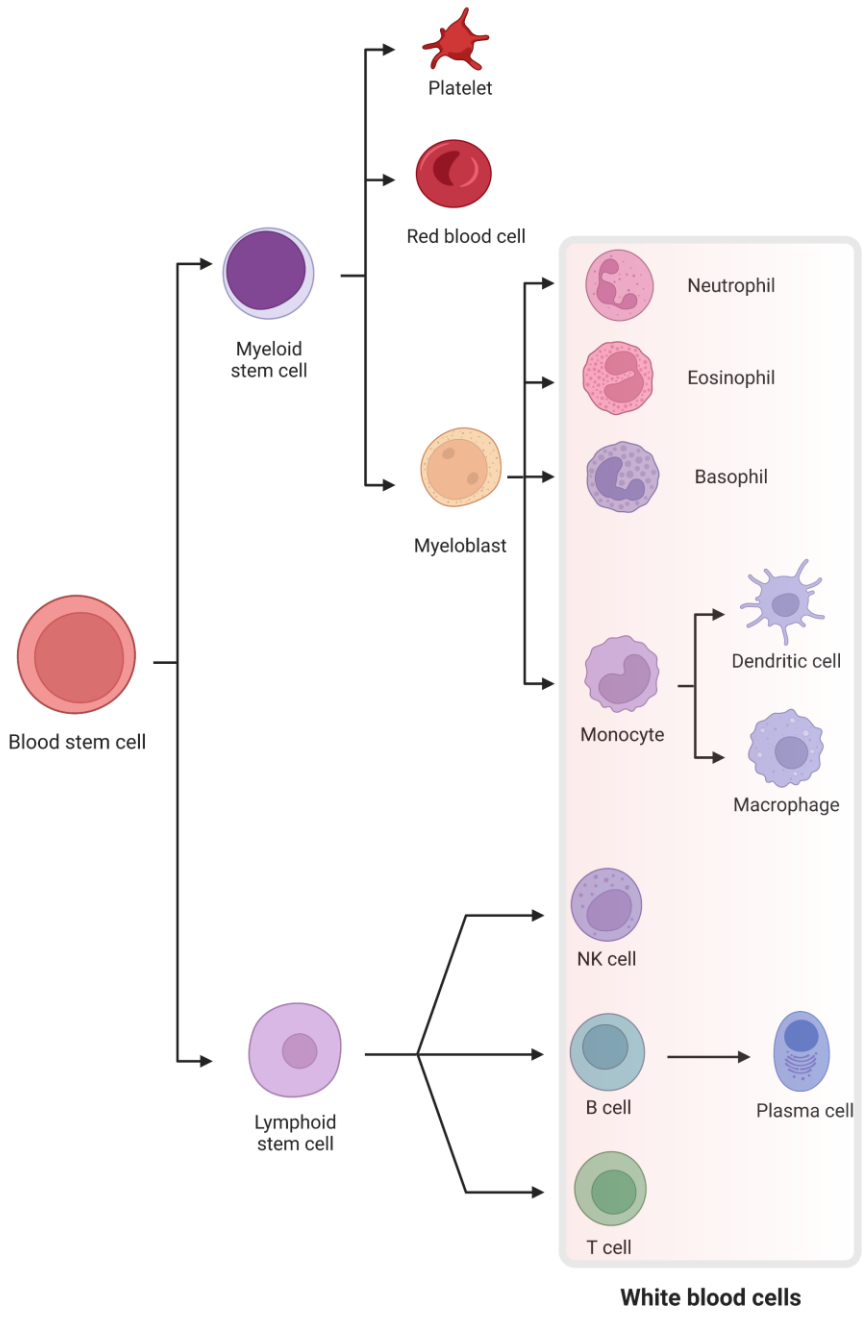

Fig 2. The tree of blood cells. Red blood cells, platelets and white blood cells are derived from blood stem cells in the bone marrow. Malignant transformation of blood cells will lead to blood cancers. For example, the cancerous plasma cells will develop into myeloma. Blood cancers arisen by abnormally proliferated white blood cells are broadly classified as leukaemia. Created with BioRender.com.

1.2.3 Introduction – Tumours

The concept of the word ‘tumour’ is not equal to ‘cancer’ [18]. A tumour refers to a solid mass of any abnormally proliferative cells. Thus, tumours are divided into benign tumours, premalignant tumours and malignant tumours.

Benign tumours [19] are not cancerous and are unable to metastasize to other sites and invade nearby tissue. The common benign tumours [20] include adenomas, lipomas, myomas, fibroids, nevi, haemangiomas, meningiomas, neuromas and osteomas.

Premalignant tumours refer to tumour cells that have the possibility to transform into malignant cells from a benign state. For example, human papillomaviruses infect squamous epithelia to induce the abnormal proliferation of cells, with the resulting cervical dysplasia being able to develop into cervical cancer [21] as time goes on.

The characteristics of uncontrollable growth, aggressiveness, metastasis and fatality are used to differentiate malignant tumours from benign tumours and premalignant tumours. Based on different types of cells, malignant tumours [22] are generally divided into carcinomas and sarcomas.

1.3 Classification of Malignant tumours

Cancer may be subdivided into more than one hundred types. Patients with malignant tumours account for approximately 90% of cancer cases [23]. According to the specific cellular type for the tumour composition, malignant tumours are mainly grouped into carcinomas and sarcomas.

1.3.1 Solid tumour – Carcinomas

The formation of carcinomas [24] is due to the malignantly abnormal proliferation of epithelia that are derived from ectoderm and endoderm germ layers during embryogenesis. Carcinomas start from the skin or the epithelial tissues lining or covering the organs and account for more than 80% of cancer cases. Based on the different phenotypes and sites of epithelial cells, carcinomas are generally divided into adenocarcinoma, transitional cell carcinoma, squamous cell carcinoma, basal cell carcinoma, etc.

Adenocarcinoma refers to the malignant tumours formed by cancerous glandular cells. The glandular epithelial cells are important parts of glands, which process and release secretory products and fluids. The adenocarcinomas caused by gland carcinogenesis (***Fig 3***) are the most common in many cancers, such as non-small cell lung cancer, prostate cancer, pancreatic cancer, oesophageal cancer, colorectal cancer, breast cancer, and stomach cancer [25].

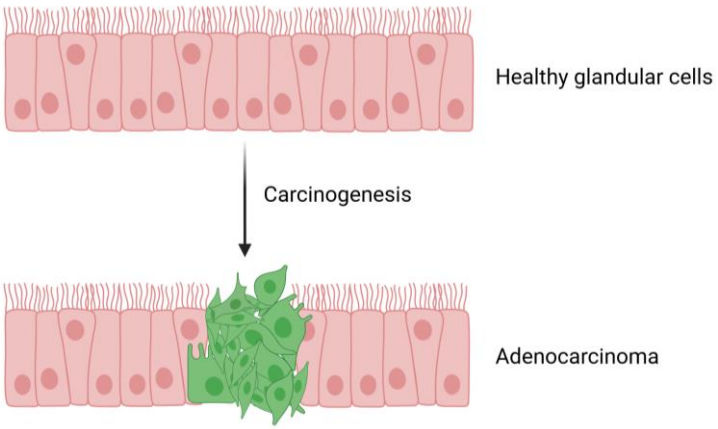

Fig 3. Adenocarcinoma originating from glandular cells. The glandular epithelial cells are the important parts of glands, which process and release secretory products and fluids. Adenocarcinoma is one subclassification of carcinomas. Created with BioRender.com.

Squamous cell carcinomas involve the carcinogenesis of squamous cells (***Fig 4***). Squamous epithelial cells have a flat cellular morphology and are located at the outermost layer of the skin, endothelium, mesothelium and the lining of the hollow organs [26]. The majority of non-melanoma skin cancer, head and neck cancer, oesophageal cancer, and non-small cell lung cancer are squamous cell carcinomas [27].

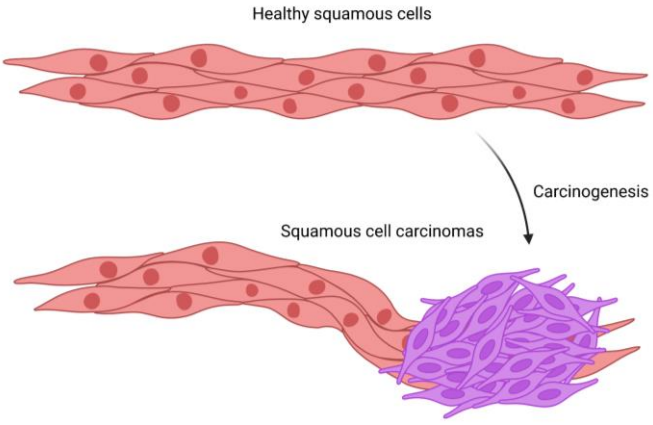

Fig 4. Squamous cell carcinoma starts from squamous cells. The majority of non-melanoma skin cancer, head and neck cancer, oesophageal cancer, and non-small cell lung cancer is squamous cell carcinoma. Created with BioRender.com.

Basal cell carcinoma is the most common skin cancer. The cuboid basal cells can be found at the bottom layer of the epidermis, and they constantly divide and differentiate into new skin cells to push and replace the old skin cells [28]. Radiation exposure to the skin can induce the carcinogenesis of basal cells. The resulting basal cell carcinomas rarely metastasize to other sites and can be cured by surgery in most cases [29].

Transitional cell carcinomas involve the carcinogenesis in transitional epithelium tissues that cover the bladder or line the hollow organs. Transitional cell carcinomas mainly occur in the urinary system [30].

1.3.2 Solid tumour – Sarcomas

Sarcomas refer to the diverse array of primary malignant tumours that grow in the supportive and connective tissues of the body, such as bones, cartilage, tendons, fat, muscle etc [31]. In contrast to the cancer cases of carcinoma, the incidence of sarcomas is much lower [32], approximately 1% of total malignant tumours. Normally, sarcomas can be divided into two major groups – primary bone sarcomas and soft tissue sarcomas [33].

Bone sarcomas represent a rare collection of sarcomas with heterogeneous behaviours affecting bones. The most common bone sarcomas [34] are osteosarcomas, Ewing sarcomas, chondrosarcomas and giant cell tumours.

Soft tissue sarcomas involve a series of uncommon malignantly mesenchymal tumours [35]. Soft tissue sarcomas can start from any part of the body that contains connective and supportive tissues, such as cartilage, muscle, fat, vasculature, nerves, tendons, ligaments and any joint tissues etc. The common soft tissue sarcomas [36] include leiomyosarcomas, liposarcomas, fibrosarcoma, rhabdomyosarcomas, synovial sarcomas, angiosarcoma, Kaposi's sarcoma, malignant peripheral nerve sheath tumours, gastrointestinal stromal tumours, and follicular dendritic cell sarcomas.

1.4 Breast cancer

Among all kinds of cancer, breast cancer has the highest incidence rate and the second highest mortality rate in the world, based on the cancer statistics of the WHO (***Fig 5***). Moreover, approximately 40% of breast cancer patients experienced the recurrence of breast cancer after the primary therapy and the metastasis of cancer cells is the leading cause of death in breast cancer patients [37].

In terms of the physiology of the breast, breast cancer represents a group of malignant tumours originating from different tissues in the breast, and breast cancer is generally divided into breast carcinomas and sarcomas [38]. The breast contains connective and supportive tissues, such as fat, muscle, vascular system,

skin, mammary glands and ducts. The diagrammatic sketch of the cross-section anatomy of the female breast is shown in ***Fig 6***.

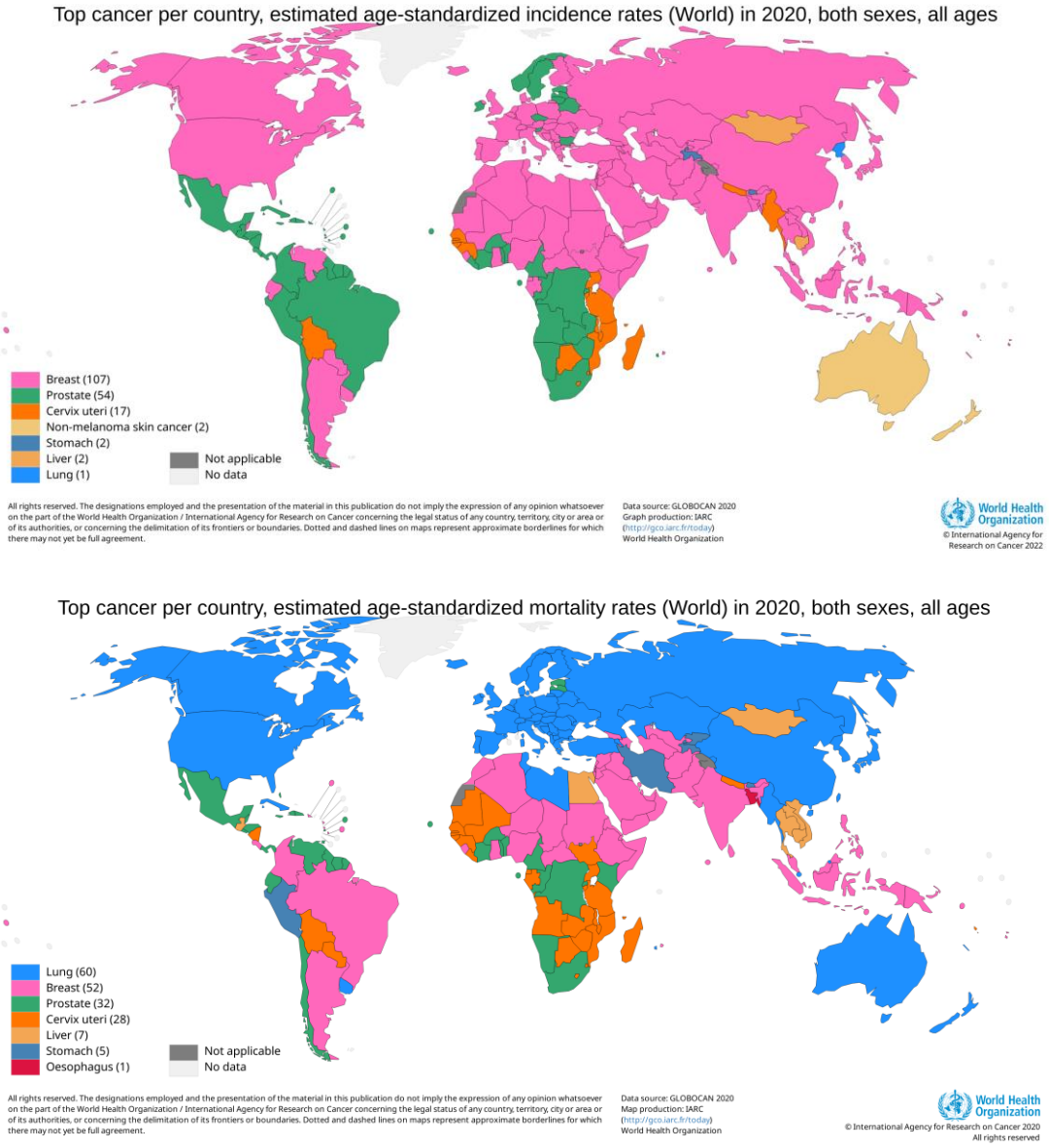

Fig 5. Cancer statistics obtained from World Health Organization (WHO). Breast cancer has the highest incidence rate and second mortality rate in the world. The numbers beside the legend indicate the age-standardized incidence or mortality rate of per 100,000 persons of each cancer. Source: World Health Organization.

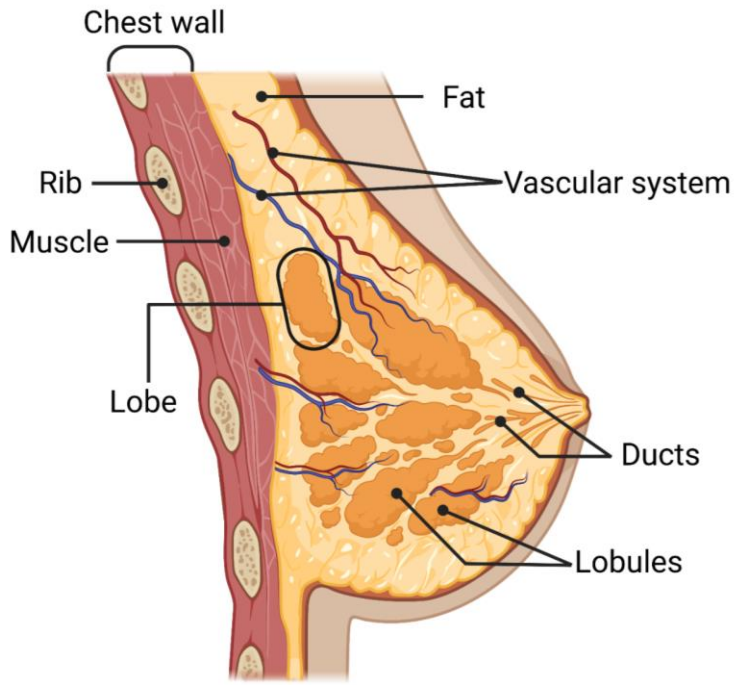

Fig 6. Anatomy of the female breast. Connective and supportive tissues in the breast include fat, muscle, skin and vascular system. The most commonly carcinogenic tissues are ducts and lobes. Created with BioRender.com.

The malignant genetic changes of different cells in the breast result in the carcinogenesis in different breast tissues. Therefore, there are some different kinds of breast cancers [39]. These include pre-malignant tumours in the breast, such as ductal carcinoma in situ and lobular carcinoma in situ. The breast malignant tumours consist of invasive ductal carcinomas, invasive lobular carcinomas, inflammatory breast cancer, Paget's disease of the breast, angiosarcoma, papillary carcinomas and phyllodes tumours [39].

Breast cancer surgery, such as a lumpectomy or mastectomy, is the main strategy

for the treatment of early-stage breast cancer. However, the high recurrence rate of breast cancer is a constant threat to the lives of patients. Therefore, apart from breast surgery, some adjuvant systemic treatments are also important for patients to reduce the recurrence rate of breast cancer, such as chemotherapy, hormone therapy, and immunotherapy, etc [40].

The combination of treatment strategies depends on the intrinsic nature of cancerous cells, such as the presence or absence of hormone receptors expressed by the cancer cells. Carcinogenesis of the breast is due to the genetic mutations of cells. For examples, the errors of tumour suppressor genes (BRCA1, BRCA2, CHEK2 or PALB2 gene) [41,42] lead to neoplasms. The heterogeneity of cancer is due to the diverse subtypes of cancerous cells that arise due to various genetic errors in cellular differentiation and proliferation. Based on the molecular subtypes of breast cancer cells, breast cancers can be subdivided into luminal A breast cancer, luminal B breast cancer, normal like breast cancer, HER2 enriched breast cancer and triple negative breast cancer [43]. The characteristics of these subtypes are summarized in ***Table 1***.

Table 1. Characteristics of five molecular subtypes of breast cancer.

Molecular subtypes	Cellular signatures	Prognosis
Luminal A breast cancer	HR+ (ER+ and/or PR+) HER2- Ki-67 low level	Good
Luminal B breast cancer	HR+ (ER+ and/or PR+) HER2- Ki-67 high level	Intermediate
Normal-like breast cancer	HR+ (ER+ and/or PR+) HER2- Ki-67 low level	Intermediate
HER2 enriched breast cancer	HR- (ER- and PR-) HER2+ Ki-67 any level	Poor
Triple negative breast cancer	HR- (ER- and PR-) HER2- Ki-67 any level	Worst

Abbreviations: HR - hormone receptor; ER – estrogen receptor; PR – progesterone receptor; HER2 – human epidermal growth factor receptor 2.

1.4.1 Luminal A breast cancer

The cancerous cells of luminal A breast tumour contain estrogen-receptor (ER) and/or progesterone-receptor (PR) and no human epidermal growth factor receptor 2 (HER2, -), and have a low Ki-67 index [43]. The Ki-67 index is positively correlated with the aggressiveness of cancer [44]. Thus, luminal A breast cancer has the best prognosis in comparison with other types of breast cancer. Therefore, utilizing hormone therapy before or after surgery is the best choice for luminal A breast cancer patients as well as those with metastatic luminal A breast cancer.

1.4.2 Luminal B breast cancer

In contrast to the luminal A breast cancer, luminal B cancerous cells have a higher Ki-67 index and may express the human epidermal growth factor receptor 2, resulting in a worse prognosis [43]. Luminal B breast cancer is more aggressive than the luminal A breast cancer.

1.4.3 HER2 enriched breast cancer

HER2 enriched breast cancer is characterized by the overexpression of the human epidermal growth factor receptor 2 and the absence of hormone receptors (ER-, PR-) on the cancerous cells. The prognosis of the HER2 enriched breast

cancer is worse than the luminal A and B breast cancer, and the prognosis biomarker (Ki-67 index) is unclear in this type breast cancer [45]. The overexpressed protein (HER2) can be effectively targeted in breast cancer treatment using drugs such as trastuzumab and pertuzumab [46].

1.4.4 Normal like breast cancer

For this cancer, the cancerous cells have similar immunohistochemistry markers with the luminal A type breast cancer, such as a low level of Ki-67 index, ER and/or PR positive expression and negative expression of the HER2 [47]. Therefore, the prognosis of normal like breast cancer is better than the luminal B breast cancer, but worse than the luminal A breast cancer [43].

1.4.5 Triple negative breast cancer (TNBC)

Unlike the other subtypes of breast cancers, the cancer cells of triple negative breast tumours do not develop estrogen or progesterone receptor as well as no human epidermal growth factor receptor 2 (HER2) [48]. As a result, the options for clinical treatment for TNBC patients are limited and insufficient, because of the lack of targeting receptors on TNBC cells [48]. Meanwhile, patients with the TNBC have a higher rate of distant recurrence and a worse five-year prognosis

compared to patients with other subtypes of breast cancer [49]. Statistically, triple negative breast cancer accounts for 10% to 20% of total breast cancers and frequently affects younger women [50], exhibiting an aggressive behaviour characterized by rapid proliferation and a high rate of metastasis.

In a study of 1601 invasive breast cancer patients [51], 11.2% patients (180) were diagnosed with triple negative breast cancer. 66% of TNBC cases were grade III tumours while 28% of other breast tumours were grade III. TNBC is a highly recurrent cancer, with 13% of TNBC patients experiencing local recurrence and 33.9% undergoing distant metastasis of breast cancer. In their study, the mortality rate of the TNBC patients after treatment was 42.2%, which was significantly higher than the 28% mortality rate of other breast cancer patients. Therefore, TNBC was considered as the most aggressive breast cancer among all molecular subtypes of breast cancer.

Due to this type of breast cancer lacking the estrogenic receptors and HER2, TNBC patients cannot benefit from hormone therapy and HER2-targeted drugs (trastuzumab-based therapies) in treatment. The current main treatment options for TNBC patients are surgery, radiotherapy and chemotherapy [52]. However, after the initial treatment, at least one-third of TNBC patients experienced the distant recurrence (metastasis) of breast cancer. Moreover, chemotherapy is recommended as the first-line treatment for metastatic triple negative breast cancer (mTNBC) patients [53]. Although scientists have made remarkable

achievements in the pathological research of the triple negative breast cancer and TNBC cells positively respond to diverse anticancer agents, such as docetaxel, paclitaxel, capecitabine, gemcitabine, methotrexate, and cisplatin, etc. The mortality rate of mTNBC patients is still extremely high.

According to an investigation on 608 mTNBC patients in 2020 [54], 505 of the 608 mTNBC patients were treated with systemic chemotherapy and the remaining patients had not received any systemic therapy, the five-year survival rate of treated and untreated mTNBC patients was 5.3% and 5.8%, respectively. The systemic chemotherapy for mTNBC patients in this investigation involved the use of single or combination of chemotherapeutic agents, including bevacizumab, capecitabine, carboplatin, gemcitabine, cisplatin, cyclophosphamide, docetaxel, eribulin, Taxol®, and Abraxane®. However, the five-year survival rate of patients receiving chemotherapy and those not receiving treatment was quite low and not significantly different. The longest survival for treated and untreated mTNBC patients was 7.5 years and 5.5 years, respectively.

1.5 Nanomedicine in Cancer therapy

The extremely high mortality rate and short overall survival of mTNBC patients imply that the current treatment regimens are insufficient and need to be improved. Although many chemotherapeutic drugs exhibit outstanding anticancer activity against TNBC cells *in vitro*, the real therapeutic effect of these drugs in mTNBC patients is not as great as suggested by the in vitro data. For example, Volk-Draper et al. [55] reported the IC50 of paclitaxel in MDA-MB-231 and HCC1806 (both cell lines are TNBC cells) was around 12 nM (10.25 μg/mL) and 0.78 nM (0.67 μg/mL), respectively. However, the clinical efficacy of these anticancer drugs in mTNBC patients is limited when used as monotherapy. Similarly, the clinically available targeted drugs, such as olaparib [56] and pembrolizumab [57], have shown limited survival benefits to mTNBC patients when used as monotherapy. Therefore, developing an effective chemotherapeutic agent to extend the life of mTNBC patients is an urgent topic.

1.5.1 Suboptimal conventional formulation limits efficacy

Limitations that affect the performance of anti-cancer drugs in the body include the poor solubility of most active ingredients [58], encountering various biological barriers [59], non-specific distribution of drugs in organs and tissues, rapid clearance of drugs from plasma [60] and the complexity of the tumour

microenvironment [61]. Unfortunately, many drugs with anticancer activity have low solubility in water, resulting in the suboptimal formulations of hydrophobic drugs or the addition of biologically toxic excipients to solubilize the anticancer drugs. For example, sorafenib [62] is an inhibitor of tyrosine protein kinases, it is used for the treatment of hepatocellular carcinoma, advanced renal cell carcinoma and thyroid cancer. However, sorafenib itself is insoluble in water. The commercially available sorafenib (Nexavar®) is the tosylate salt of sorafenib. Although salt formation is a common method to increase the solubility of drugs, sorafenib tosylate (Nexavar®) is hard to be dissolved in gastrointestinal tract after oral administration, resulting in a low and erratic bioavailability of sorafenib in patients and unnecessary toxicity to patients. Another example is the formulation of Taxol®, Taxol® is a commercial chemotherapeutic drug (micelle formulation of paclitaxel) for systematic treatment of numerous cancers, including metastatic breast cancer, by parenteral administration [63]. Paclitaxel (PTX) is a hydrophobic anticancer drug. In order to solubilize PTX, biologically toxic excipients, polyethoxylated castor oil and ethanol, are added in the formulation. The lack of an optimal preparation technique is one of the major reasons that the promising *in vitro* performance of these hydrophobic drugs is difficult to be achieved *in vivo*.

1.5.2 Nano-formulations developed for oncotherapy

To address the deficiencies of conventional chemotherapeutic drugs in cancer treatment, the emergence of nanoscale drug delivery systems has ushered in a new era of systemic chemotherapy. Nanoscale drug delivery systems are a crucial component of nanomedicine, a term proposed in the 1990s to describe nanoscale systems or materials designed for various medical purposes [64]. To date, several nanomedicines have reached the market for the treatment of metastatic breast cancer [65], such as Doxil®, Abraxane®, Onivyde® and Genexol-PM®, etc. Most nanomedicines have shown improved pharmacokinetics profiles, reduced systemic toxicity, and enhanced therapeutic efficacy compared to traditional chemotherapeutic drugs with the same active pharmaceutical ingredient (API). For example, in a phase III clinical trial [66], patients administrated Abraxane® at 260 mg/m^2 every 3 weeks showed significantly higher response rates (39%) compared to 175 mg/m^2 of Taxol® (19%).

The significant advantage of formulating hydrophobic drugs through nanotechnology is that lipophilic drugs can acquire high water-solubility through nanocarriers without the need for additional toxic excipients in the formulation. For example, the water solubility of paclitaxel is lower than 50 μg/mL, but when formulated as albumin bound paclitaxel nanoparticles (Abraxane®), the water solubility of PTX can be increased to at least 2,000 μg/mL by nanocarriers.

Furthermore, Abraxane® is composed of human serum albumin and paclitaxel, while Taxol® contains organic solvent ethanol and toxic Cremophor EL. As a result, Abraxane® is capable of providing a higher maximum tolerated dose of PTX and much lower systematic toxicity to patients when compared with Taxol®. According to statistics [67], approximately 75% of drug candidates have poor water solubility and only 0.02% to 0.04% of prospective anticancer drugs are ultimately approved by the United States Food and Drug Administration (US FDA). Suboptimal formulation of lipophilic drugs is a significant factor limiting the transition of prospective drugs from the laboratory to clinical applications [67].

Applying nanotechnology in pharmaceutics allows for the positive improvement of the properties of many conventional drugs [68]. Various nanoplatforms, including polymeric nanoparticles, polymer micelles, liposomal nanoparticles, dendrimers, solid lipid nanoparticles, polymer/antibody – drug conjugates, inorganic nanoparticles and carbon-based nanomaterials, have been developed and applied for diverse medical purposes. These include acting as nontoxic nanocarriers for peptides, genes, or hydrophobic drugs, as magnetic resonance imaging (MRI) contrast agents for tumor imaging and cancer diagnosis. A number of relevant commercial nanomedicines are listed in ***Table 2***.

In summary, incorporating nanotechnology in pharmaceutics offers a novel and reliable strategy to formulate biomolecules, easily degraded APIs, or poorly water-soluble APIs, thus presenting exciting possibilities for advancing cancer

treatment and beyond.

Table 2. Examples of clinically approved nanomedicines.

Trade name	Composition	Application	Approval (year)
Doxil®	Doxorubicin in pegylated liposome	Ovarian cancer, metastatic breast cancer, AIDS-related Kaposi's sarcoma	FDA (1995) EMA (1996)
Abraxane®	Albumin – paclitaxel nanoparticle	Non-small cell lung cancer, metastatic breast cancer and pancreatic cancer	FDA (2005) EMA (2008)
NanoTherm®	Iron oxide nanoparticle	Glioblastoma	EMA (2010)
Onpattro®	RNAi - Lipid nanoparticle	Transthyretin – mediated amyloidosis	FDA (2018) EMA (2018)
Feridex®	Dextran – coated SPION	Magnetic resonance imaging of liver	FDA (1996)

Abbreviations: AIDS – Acquired immune deficiency syndrome; FDA – Food and Drug Administration; EMA – European Medicines Agency; RANi – Ribonucleic acid interference; SPION – Superparamagnetic iron oxide nanoparticle.

1.5.3 Progress, challenges and perspectives of nanomedicines

The application of nanotechnology in oncotherapy has provided many feasible solutions for the treatment and diagnosis of patients. Although the currently available commercial nanomedicines may improve the overall survival of cancer patients limitedly [69], there is no doubt about the significant success and clinical benefits derived from these nanomedicines. Since the approval of the first FDA-approved nanomedicine (Doxil®) in 1995, nanomedicines have been used in various fields of medical care. For example, the estimated market value of Abraxane® is more than 10 billion USD [70] and the worldwide sales of the Pfizer-BioNTech COVID-19 vaccine (mRNA in lipid nanoparticles) [71] were around 20 billion USD. These examples underscore the significant impact of nanotechnology on the medical industry, particularly in cancer treatment and vaccine development. The ongoing research and development in the field of nanomedicine hold great promise for further improving cancer therapies and addressing the challenges associated with conventional chemotherapeutic agents. With the continuous advancements in nanotechnology, it is likely that more innovative and effective nanomedicines will emerge, providing hope for better outcomes for cancer patients in the future.

The famous concept of the enhanced permeability and retention effect (EPR effect, ***Fig 7***) of tumours was proposed in 1986 [72]. Matsumura and Maeda

observed that radiolabelled proteins and fluorescently labelled proteins gradually accumulated and remained in the tumours of tumour-bearing mice for an extended period. They hypothesized that macromolecules could exploit the hyper-vascularization and defective lymphatic drainage in tumour tissues to facilitate the diagnosis and treatment of tumours. While the EPR effect had been extensively demonstrated in tumour-bearing mouse models, its presence or absence in cancer patients was a subject of controversy at that time. In 2012, the Alliance for Nanotechnology in Cancer organized a meeting [73] at the National Institutes of Health (NIH) to gain a deeper understanding of the EPR effect in tumour-bearing animal models and cancer patients, as well as to explore the medical potential of combining the EPR effect with nanotechnology for the diagnosis and treatment of cancer. During this workshop, they concluded that the EPR effect in tumours may be heterogeneous among cancer patients. Consequently, the heterogeneity of the EPR effect has been proposed as a potential explanation for the different responses of patients to nanomedicines.

It is worth mentioning that the existence of the EPR effect in cancer patient has been validated in a recent clinical study [74]. In this study, radiolabelled (^{64}Cu-) liposomes were administered to metastatic breast cancer patients through intravenous infusion, and the distribution of these radiolabelled nanoparticles in patients was visualized using PET/CT. Three days after the injection, the signals of radiolabelled nanoparticles were notably stronger in metastatic liver tumours

compared to normal tissues and organs (***Fig 8***). This clinical evidence demonstrates the enhanced permeability and retention effect of tumour tissues, which enables the prolonged exposure of nanoparticles to tumour cells in patients. However, it is important to note that the EPR effect can still vary among patients with different or even identical types of cancer. The heterogeneity of the EPR effect emphasizes the need for personalized approaches in utilizing nanomedicines for cancer treatment. Understanding and characterizing the factors that influence the EPR effect in individual patients will be crucial for optimizing the efficacy of nanomedicine-based therapies and ensuring the best possible outcomes for cancer patients.

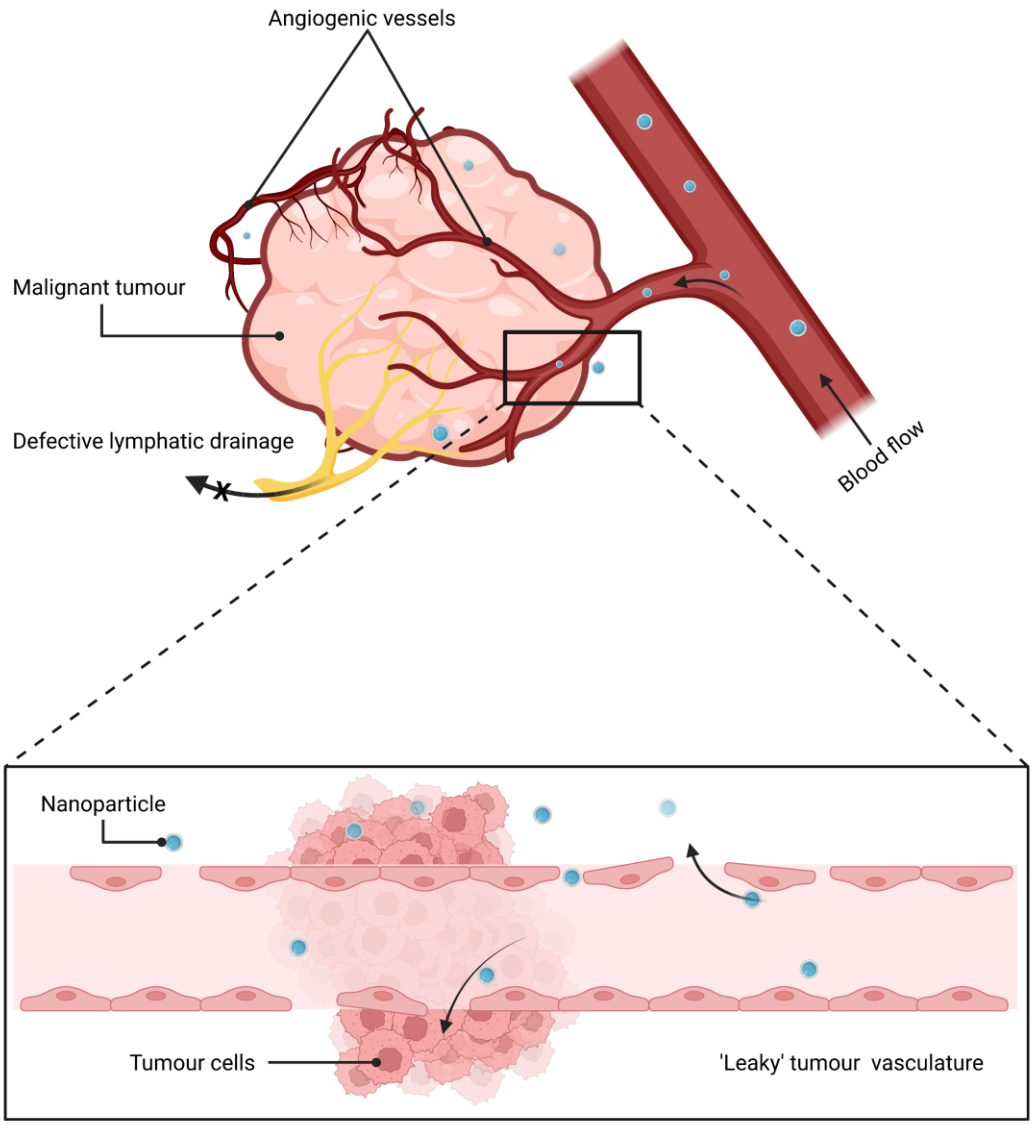

Fig 7. Schematic illustration of accumulation of nanoparticles for a long period of time in malignant tumour site via enhanced permeability and retention effect (EPR effect). Malignant tumour secretes the angiogenic growth factors to build abnormal blood vessels from the existing vasculature to achieve enough nutrition and oxygen for growing. The abnormally angiogenic vessels are permeable and leaky for the nanoscale substances, such as nanoparticles and macromolecules. In addition, malignant tumours can also induce the generation of extra lymphatic vessels from the normal lymphatics to remove the waste produced by cancer cells. Meanwhile, this tumour's lymphatics can only provide defective lymphatic drainage for macromolecules and nanoparticles. Therefore, the escaped nanoparticles around malignant tumour can be retained for a long time. Created with BioRender.com.

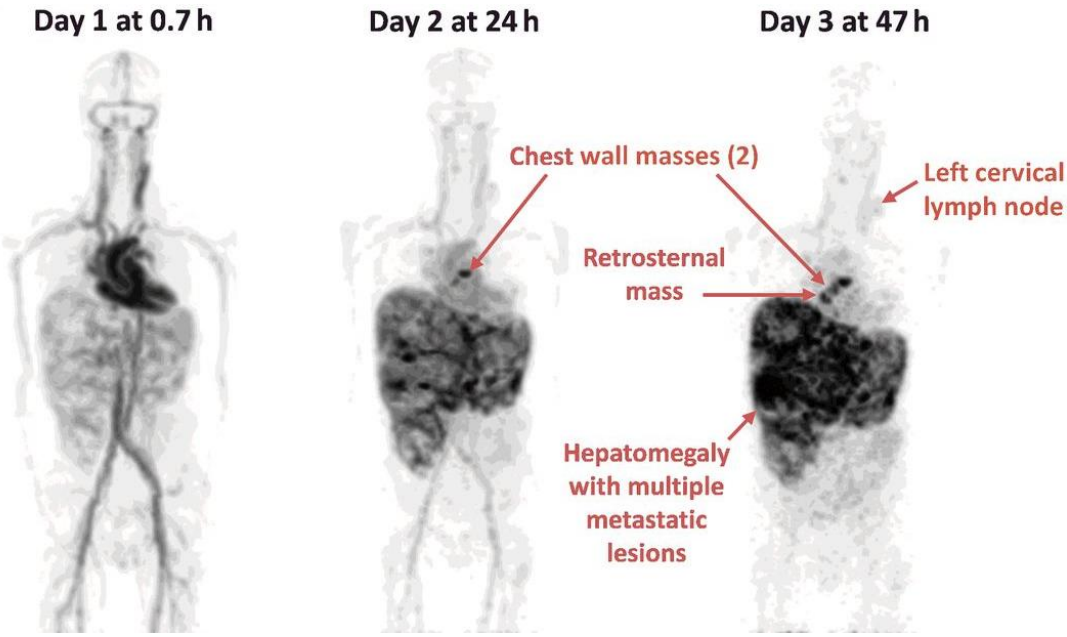

Fig 8. The presence of EPR effect in malignant tumour of patient. After intravenous administration of ^{64}Cu-labeled PEGylated liposomes to a metastatic breast cancer patient, the biodistribution of radiolabelled nanoparticles was visualized at 0.7 h, 24 h and 47 h post injection by Positron emission tomography/computed tomography (PET/CT). The ^{64}Cu-labeled nanoparticles gradually accumulated and retained in metastatic tumours (Liver site). "Adapted from Clinical Cancer Research, Copyright 2017, 23/15, 4190–4202, Lee, Helen et al. ^{64}Cu-MM-302 Positron Emission Tomography Quantifies Variability of Enhanced Permeability and Retention of Nanoparticles in Relation to Treatment Response in Patients with Metastatic Breast Cancer, with permission from AACR".

Indeed, nanomedicine has brought significant advancements to cancer treatment, but it also comes with formidable challenges. While nanotechnology has addressed the issue of suboptimal drug formulations, the effective utilization of drugs in the body still needs improvement. For instance, even though nanomedicines have shown promise, their actual impact on statistically prolonging the life of metastatic breast cancer patients compared to conventional

drug formulations in solution remains limited [66]. Therefore, increasing the safe and efficient accumulation of active pharmaceutical ingredients (APIs) in tumours is a major challenge for the development of nanomedicine [75]. Another significant challenge is achieving large-scale and cost-effective production of nanomedicine in an environmentally friendly manner [76]. Reproducibility and scalability are critical factors in the successful translation of nanomedicines from the laboratory to clinical applications.

Notably, a meta-analysis (232 data sets) of nanoparticle delivery to tumours launched by Wilhelm et al. concluded that the median efficiency of drug delivery to tumours by nanoparticles was only 0.7% of injected dose [77]. In other words, only less than 1% of injected nanoparticles were effectively utilized by tumours in tumour-bearing animal models. This low efficiency of drug tumour deposition in animal models highlights the need to improve the targeting and delivery mechanisms of nanocarriers..

To address these challenges, scientists have been working on various strategies to enhance the efficiency of nanocarriers. Some of these strategies include enhancing the EPR effect, prolonging the circulation time of nanocarriers, utilizing active targeting approaches, and exploring other methods to increase the effectiveness of nanocarriers. Some relevant achievements have been concretely discussed in the following sections.

Strategies - EPR effect enhancement

The preferential accumulation and long retention times of nanoparticles in mouse tumours have been explained since the theory of the EPR effect was proposed in 1986. The EPR effect (***Fig 7***) is attributed to the fact that the tumour induces the rapid angiogenesis, resulting in the tumour neovasculature with the aberrant vascular architecture [78]. The pores (200 nm to 1.2 μm in diameter) presented on the abnormal blood vessels allow nanoscale substances to extravasate into the interstitial space [79]. Meanwhile, the lymphatic drainage in tumour tissue is defective for macromolecules and nanoparticles. Therefore, researchers have endeavoured to enhance the EPR effect to deliver more drugs to the tumour. For example, by applying ultrasound to the tumour site, the injected ultrasound contrast agents, such as sulphur hexafluoride microbubbles (SonoVue®), can be excited by ultrasound energy to mechanically create pores ranging from several nanometres to several micrometres on the cell membrane and enlarge the gap between vascular endothelial cells through the stable and inertial cavitation, this process is also known as sonoporation [80]. In one clinical trial [81], pancreatic cancer patients (n = 63) were treated with chemotherapy using gemcitabine (Gemzar®) as the control group, while ten pancreatic cancer patients were treated with a combination of gemcitabine chemotherapy and sonoporation. The treatment cycles of the control group were 8.3 ± 6.0, while the ten patients who received chemotherapy and sonoporation underwent 13.8 ± 5.6 treatment cycles

(p = 0.008). The more treatment cycles represented a longer treatment period for patients and led to a better treatment effect. In addition, the median survival of the control group was 8.9 months, significantly shorter than the 17.6 months of sonoporation-treated patients (p = 0.011). As a summary, this clinical trial has proven that the chemotherapy combined with sonoporation can improve the efficiency of anticancer drug to enhance the chemotherapeutic effect in patients with highly stromal tumours (pancreatic cancer). In the work of Theek, B. et al., the delivery of passively targeting nanoparticles to low EPR tumours or highly stromal tumours was both increased twofold in combination with sonoporation when compared with the non-ultrasound treated group [82]. Combining the sonoporation therapy with nanomedicine is a promising solution to increase the efficacy of chemotherapy in patients with low or no EPR effect [83].

In addition to the use of sonoporation, the EPR effect in patients with solid tumours can also be enhanced by elevating the blood pressure. In 1986, Maeda and Matsumura discovered the EPR effect in a tumour bearing mouse model. The preferential and prolonged accumulation of polystyrene/maleic acid (SMA) - neocarzinostatin (NCS) conjugates in mouse solid tumours was thus explained [84]. They then believed that the EPR effect found in mice could also be extended to patients with solid tumours. In 1993, their SMANCS/Lipiodol system was approved for the treatment of hepatocellular carcinoma in Japan. However, due to the highly heterogenous EPR effect among different malignant tumours or even

the same type of tumours [85], the final therapeutic effect of the SMANCS/Lipiodol system in patients was not consistent. To overcome this issue caused by the heterogenous EPR effect, Maeda and his colleagues came up with a strategy [86] to enhance the EPR effect via the introduction of angiotensin II to transiently increase the blood pressure and thus promote the tumour deposition of SMANCS (***Fig 9***). This strategy of inducing systemic hypertension to enhance the EPR effect to deliver more macromolecules to tumours has been successfully applied into patients with different cancer types, including metastatic tumours. Detailed information can be found in their excellent report [86].

Furthermore, hyperthermia [87] can be used as an adjuvant treatment to enhance the EPR effect and aid in the delivery of nanoparticles. Given the heterogeneity of the EPR effect in patients, appropriate measures to enhance the EPR effect can be selected to improve the therapeutic effect of nanomedicines in a clinical setting.

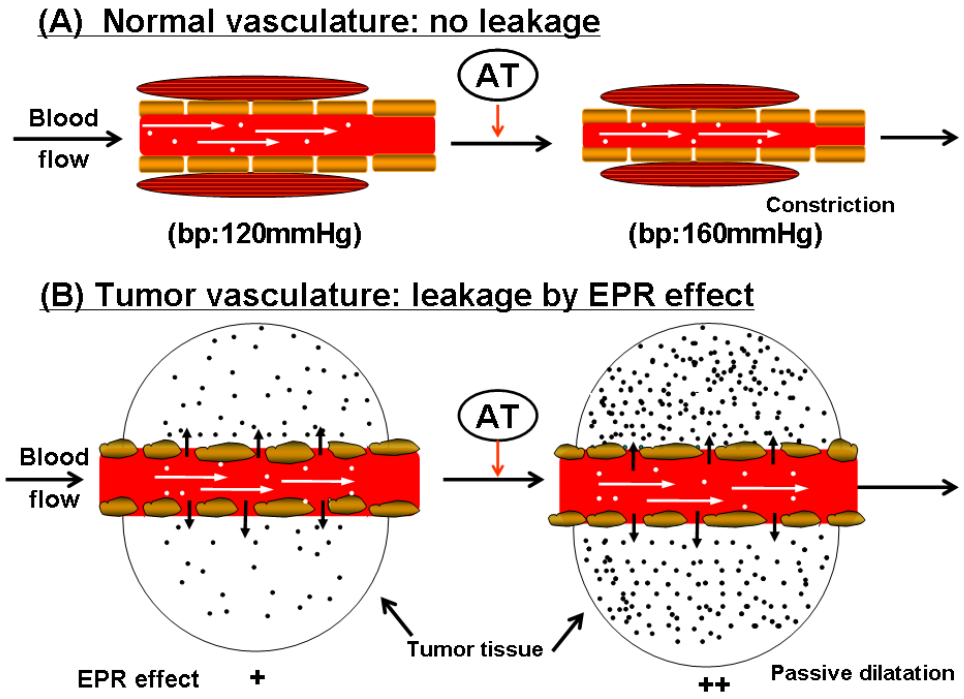

Fig 9. Diagram for demonstrating the principle of EPR effect enhancement by applying angiotensin II. After the administration of angiotensin II (AT II), the blood flow volume in **(A)** healthy tissues and organs is relatively homeostatic because AT induces the vasoconstriction to increase blood pressure to increase the velocity of blood flow. Contrarily, the leaky vasculatures **(B)** do not response the vasoconstriction, meanwhile the accelerated blood flow and increased blood pressure can promote the delivery of macromolecules to tumour site. 'Adapted from Akinori Nagamitsu, Khaled Greish, Hiroshi Maeda, Elevating Blood Pressure as a Strategy to Increase Tumor-targeted Delivery of Macromolecular Drug SMANCS: Cases of Advanced Solid Tumors, Japanese Journal of Clinical Oncology, 2009, Volume 39, Issue 11, Pages 756–766, by permission of Oxford University Press.'

Strategies - Extending the circulation time of nanocarriers

Apart from physically and chemically enhancing the EPR effect, extending the time of nanocarrier blood circulation is another approach to improve the therapeutic effect of nanomedicines. Based on the theory of the EPR effect, nanocarriers and macromolecules preferentially accumulate around the tumour site through the leaky tumour vasculatures. However, a meta-analysis [88] of 376 data sets of nanoparticle delivery to tumours from publications between 2005 and 2018 showed that the median tumour deposition of nanoparticles was only around 0.76% of the injected dose. This is because most of the injected nanoparticles were cleared from the blood circulation by the mononuclear phagocyte system (MPS) [89] in the blood, tissues and organs.

The mononuclear phagocyte system, also known as reticuloendothelial system, is generally composed of monocytes, macrophages and dendritic cells [90]. These MPS cells originate from myeloid progenitor cells in the bone marrow, as shown in ***Fig 2***. Myeloblasts can differentiate into monocytes, macrophages and dendritic cells, and they are released into the bloodstream. Most of these cells will leave the blood circulation and enter into tissues and organs. For example, alveolar macrophages can be found in the lung, Kupffer cells reside in the liver and monocytes transmigrate to the peripheral tissues and organs. Each mononuclear phagocytic cell is capable of mounting a defence against the invasion of foreign substances, including nanoparticles.

Therefore, in order to achieve a better utilization of the EPR effect for delivering nanoparticles to tumour sites, scientists have developed some methods to circumvent the immune system recognition of nanoparticles and prolong their blood circulation time.

The most frequently used strategy is to coat the surface of nanoparticles with antifouling materials to reduce the formation of the protein corona and escape the MPS clearance. PEGylation is a common approach to protect nanoparticles from the MPS clearance [91]. The clinical applications of PEGylation of nanoparticle include Doxil® (PEGylated liposomal doxorubicin) and Onivyde® (PEGylated liposomal irinotecan), which were approved by FDA in 1995 and 2015 [92], respectively. Although PEGylation of nanocarriers can provide a bio-inert surface to reduce the MPS clearance and prolong the circulation time of encapsulated drugs, over-PEGylation can impede the cellular uptake of nanocarriers [93]. Additionally, several publications [94–96] have reported some negative effects following the use of PEGylated nanocarriers. The injected PEGylated nanoparticles can induce the production of anti-PEG IgM in animal models [97], leading to faster clearance of the second dose of PEGylated nanoparticles by the immune system. This phenomenon is known as accelerated blood clearance. Moreover, severe adverse effects, such as hypersensitivity and anaphylactic shock [98], may occur after multiple doses of PEGylated nanomedicine. For instance, Doxil® has been associated with side effects such as hand–foot

syndrome, stomatitis, mucositis, and other hypersensitivity reactions [92].

In addition to the polyethylene glycol (PEG), several zwitterionic materials have been developed as coatings or shells for nanoparticles to reduce protein corona formation and the resulting immune-mediated rapid clearance. Inspired by the zwitterionic surfaces of viruses, these materials include chemistries such as polycarboxybetaine (PCB) and polypeptides (EK10) [99].

Li et al. exploited the zwitterionic material, distearoyl phosphoethanolamine – polycarboxybetaine (DSPE-PCB), to prepare the liposomal nanoparticles with a zwitterionic surface (a PCB surface) and compared it with DSPE-PEG for the preparation of PEGylated liposomal nanoparticles used in the control group [94]. In their work, pharmacokinetics profiles and the accelerated blood clearance phenomenon of topotecan in PCB-liposomes and PEG-liposomes were compared by the measurement of the topotecan concentration in rat plasma after the 1st, 2nd and 3rd repeated injections of each liposomal formulation, as shown in ***Fig 10***. The pharmacokinetics profiles of the topotecan in both liposomal formulations were significantly improved when compared with the free topotecan (***Fig 10***). However, the PEGylated topotecan liposomes induced the accelerated blood clearance after the intravenous injection in Sprague Dawley rats, as the 2nd injected topotecan loaded PEG-liposomes was cleared from the blood circulation more quickly than the 1st injection (***Fig 10. A***). On the other hand, the blood circulation of repeated injection of topotecan PCB-liposomes was not significantly

altered (***Fig 10. B***). This research demonstrated that PCB-coated liposomes could provide even better pharmacokinetics profiles of encapsulated drugs than PEGylated liposomes without inducing the accelerated blood clearance phenomenon.

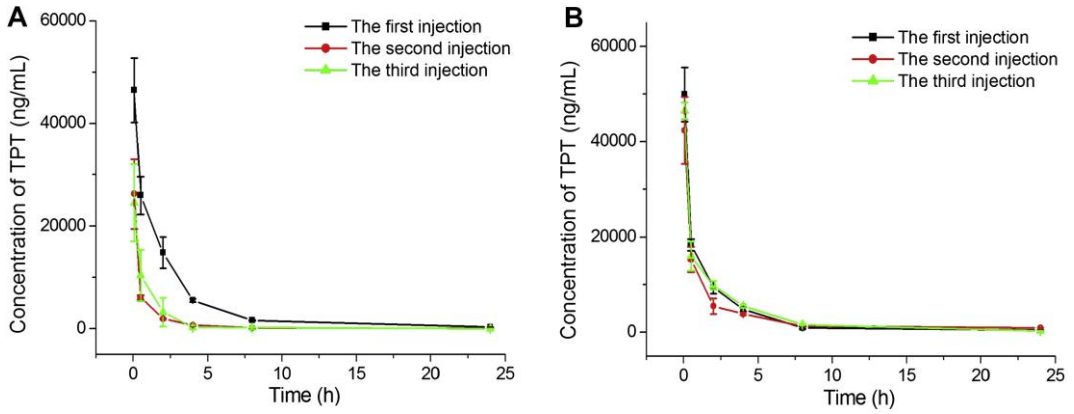

Fig 10. Pharmacokinetics profiles of PCB-liposomal and PEG-liposomal formulations. Plasma concentration of topotecan after 1st, 2nd and 3rd repeated injection of **A**) PEG-liposomal formulation and **B**) PCB-liposomal formulation. The intravenously injected topotecan concentration to Sprague Dawley rats (200-250 g, n = 3) was according to 7 mg/kg and the interval of each injection was 5 days. "Reprinted from Biomaterials, Vol 41, Yan Li, Ruiyuan Liu, Jun Yang, Yuanjie Shi, Guanghui Ma, Zhenzhong Zhang, Xin Zhang, Enhanced retention and anti-tumor efficacy of liposomes by changing their cellular uptake and pharmacokinetics behavior, Pages 1-14., Copyright (2015), with permission from Elsevier."

The DSPE-PCB can also be utilized as a scaffold for the preparation of zwitterionic micelles to facilitate the oral delivery of insulin[100]. The resulting PCB-DSPE micelles showed a 6.7 times higher diffusion rate for penetrating the mucus compared to the PEGylated nanoparticles and over 100-fold faster penetration than anionic and cationic particles. This research on insulin delivery indicated that the zwitterionic shell of nanoparticles could significantly reduce the

absorption of proteins in mucus and the formation of protein corona in plasma.

In addition to stealth coating, Anselmo et al. emphasized the importance of nanoparticle elasticity (bulk modulus) in designing nanoparticles, as it is associated with their in vivo behaviors [101]. They designed the soft (10 kPa) and hard (3000 kPa) nanoparticles with similar particle size, polydispersity index and zeta-potential to compare their *in vivo* fate. The elasticity of nanoparticles in their work was precisely adjusted by using different volume ratio of poly(ethylene glycol) diacrylate to water. The soft nanoparticles exhibited a significantly prolonged circulation time when compared with the hard nanoparticles.

Overall, as the understanding of the interaction between nanoparticles and the immune system continues to progress, it is expected that more satisfactory materials and formulations will be designed for clinical use.

Strategies - Active targeting drug delivery

In 1897, Paul Ehrlich [102] developed the ‘Side-Chain Theory’ to describe the specific binding phenomenon between a substance and the side chain on the cell surface. In 1900, Ehrlich updated this ‘Side-Chain Theory’ to the ‘Receptor-Ligand Theory’, which laid the foundation for targeted therapy. The concept of the ‘magic bullet’, a drug that could specifically bind to its target, was put forward by Paul Ehrlich in 1906. Since then, targeted cancer therapies have become well-known, such as the use of trastuzumab, an antibody that specifically binds to the

overexpressed HER2 receptor, in the treatment of HER2-enriched breast cancer patients.

However, due to the intra- and inter-tumour heterogeneity, it is not feasible to apply personalized cancer medicine to all patients in the clinic [103]. The current strategy for targeted therapy is primarily based on the Ehrlich's Receptor-Ligand Theory, leading scientists to develop various nanocarriers coated with different ligands to specifically bind to target cells. Over the past decade, more than forty thousand research papers on actively targeted delivery have been published [98]. Many passively targeted nanomedicines have been approved for various clinical purposes [104]. However, none of the actively targeted versions (excluding antibody-drug conjugates) have been successfully marketed. The clinical translation of actively targeted nanomedicines from animal studies to human trials is hindered by several factors, such as the more complex physiological barriers in the human body and the heterogeneity between patients [105].

Generally, the aim of active targeted drug delivery is to increase the delivery of therapeutics to the tumour site. Cancer cells arise from genetic mutations in normal cells, resulting in the overexpression of certain genes. These overexpressed genes lead to an excessive production of relevant proteins, which can cause the corresponding cell receptors to be overexpressed as well. For example, cancer cells with an overexpressed FOLR1 gene will have more folate

receptors compared to normal cells. This overexpression allows cancer cells to take up more folate, which is required for their aggressive biosynthetic reactions [106]. Consequently, the overexpressed folate receptors can serve as biomarkers for folate receptor-enriched tumours, including triple-negative breast cancer, non-small cell lung cancer, and epithelial ovarian cancer [107]. A recent phase III clinical trial [108] conducted on platinum-resistant ovarian cancer patients compared the treatment outcomes of mirvetuximab soravtansine (MIRV), an anti-FRα (folate receptor alpha) drug conjugate, with traditional chemotherapy (paclitaxel, pegylated liposomal doxorubicin, or topotecan). The trial revealed that high FRα-patients treated with MIRV had a significantly longer median progression-free survival (PFS) compared to those who received chemotherapy alone, with PFS of 4.8 months versus 3.3 months ($p = 0.049$). This indicates the potential effectiveness of using antibodies to improve treatment outcomes for specific cancer types characterized by overexpressed biomarkers.

Dr Yasuhiro Matsumura, one of the discoverers of the EPR effect, holds a different opinion on actively targeting drug delivery to tumour. In his previous studies [109], the nanoformulation called MCC465, which was liposomal doxorubicin conjugated with anti-GAH, showed excellent anticancer activity in animal studies. However, MCC465 had no objective antitumor response in a phase I clinical trial [110]. Later, he discovered that human malignant tumours contained a rich cancer stroma, and the cancer stroma could act as a barrier and

hinder the ligand of nanoparticles from interacting with tumour cells. As a result, he developed the Cancer Stromal Targeting (CAST) Therapy [111] to enhance the therapeutic effect of drug in low EPR tumours. In brief, they conjugated monomethyl auristatin E to the fibrin antibody through a Val-Leu-Lys linker, and then this antibody drug conjugate (ADC) can specifically bind to the insoluble fibrin of cancer stromal and release the carried drug by plasmin cleavage.

The above two active targeting strategies are based on the EPR effect to preferentially accumulate nanocarriers in tumour tissue, and then the antibodies can actively bind with their targets to exert their functions. However, in low or no EPR tumours of patients, the effectiveness of these strategies will be suppressed to a very low level. Based on the fundamental research of the tumour microenvironment (TME), tumour cells and nearby tissues live in a nutrition deficient, acidic and hypoxic environment [112–114]. The TME of tumour tissues is different with the environment of healthy tissues. So, under these abnormal stimuli, cells have to develop some different genes to express specific proteins to fit the hypoxic stress and acidic environment when compared with the normal cells in the healthy tissues. For example, the tumour vascular endothelial cells will generate EndoPDI mRNA and then the expressed endothelial protein-disulfide isomerase can exert the protective function to avoid the apoptosis induced by hypoxia [115]. Moreover, some expressed receptors only exist in tumour endothelium and are absent in adult healthy tissues [116], such as

roundabout-4 (ROBO4) and endomucin. Thus, TME induced receptors are promising specific targets for drug delivery. Chen et al. [117] believed that tumour vasculature targeting has a greater potential for the clinical translation than targeting tumour cell delivery. In their research, they selected the endoglin (CD105) as the biomarker of the tumour neovasculature due to the tumour angiogenesis, the proliferating endothelial cells highly expressed endoglin [118]. They conjugated the endoglin antibody TRC105 to the mesoporous silica ($mSiO_2$) nanoparticle and exploited the ^{64}Cu radiolabelling to visualize the biodistribution of their nanoparticles in the 4T1 tumour-bearing mice by PET imaging, as shown in ***Fig 11***. According to their PET images, the position of the 4T1 tumour was clearly visualized after the intravenous injection of TRC105-conjugated silica nanoparticles with ^{64}Cu radiolabelling (***Fig 11. a***) when compared with the normal silica nanoparticles with ^{64}Cu radiolabelling (***Fig 11. b***). To further confirm the specific binding between the CD105 receptor and TRC105-silica nanoparticles, they injected the CD105 antibody alone to the 4T1 tumour bearing mice to prior block the CD105 receptors, and then TRC105-silica nanoparticles were injected. In ***Fig 11. c***, the signal emitted from the ^{64}Cu-TRC105 conjugated silica nanoparticles at the tumour site was largely suppressed with the prior injection of the antibody TRC 105. Based on the results of their *in vivo* experiments, tumour vascular targeting is indeed a very promising strategy for the actively targeted delivery of therapeutic agents.

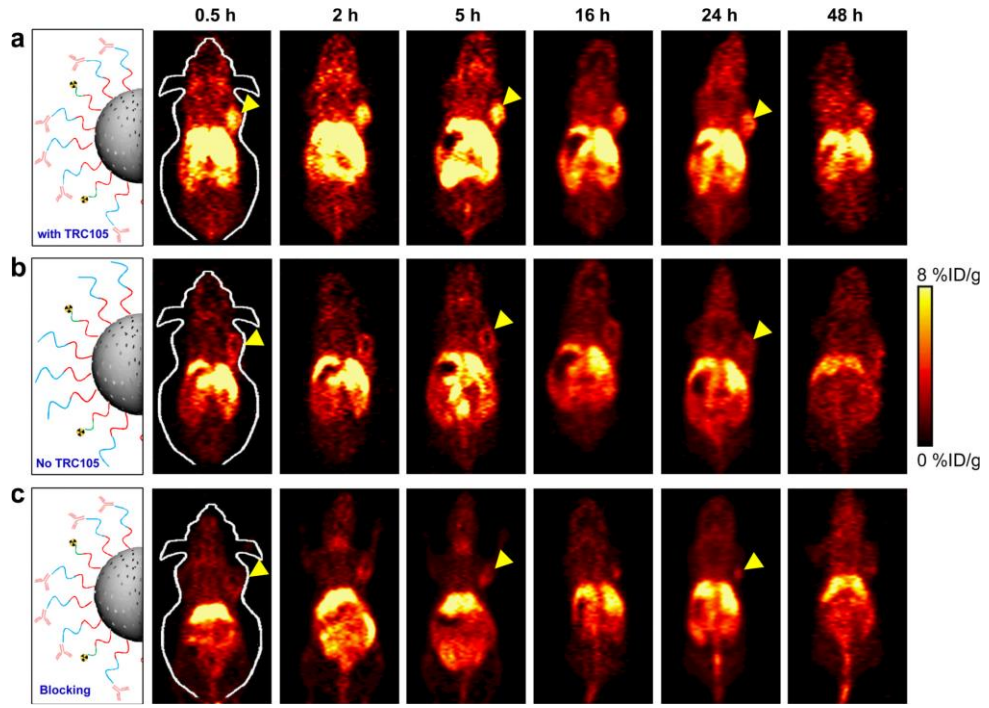

Fig 11. PET images of biodistribution of ^{64}Cu radiolabelled nanoparticles in 4T1 tumour bearing mice at different time points. (a) The biodistribution of the intravenously injected TRC105 tagged silica nanoparticles at different time points. **(b)** The contrast group, 4T1 tumour bearing mice were injected with normal silica nanoparticles. **(c)** 4T1 tumour bearing mice were pre-treated with the antibody TRC105 to block the CD105 receptor, then the uptake of TRC105-silica nanoparticles was significantly inhibited. The yellow triangle indicated the position of 4T1 tumour. Reprinted with permission from Chen, F.; Hong, H.; Zhang, Y.; Valdovinos, H. F.; Shi, S.; Kwon, G. S.; Theuer, C. P.; Barnhart, T. E.; Cai, W. In Vivo Tumor Targeting and Image-Guided Drug Delivery with Antibody-Conjugated, Radiolabeled Mesoporous Silica Nanoparticles. ACS Nano 2013, 7 (10), 9027–9039. https://doi.org/10.1021/nn403617j. Copyright (2013) American Chemical Society.

For targeted cancer therapy and targeting tumour tissue-related cells, scientists also developed a targeting strategy in which they intentionally activate the immune system in order to distinguish cancer cells [119]. Tumour associated antigens can be encapsulated into nanocarriers and delivered to antigen-presenting cells (APC) in a targeted manner to activate the immune system. Antigen-presenting cells [120], including dendritic cells, macrophages and B cells,

express some accessible receptors, such as scavenger receptor, integrins, mannose receptor. By attaching specific antibodies or ligands to the surface of nanocarriers, the tropism of nanocarriers can be thereby altered to target the antigen-presenting cells. Currently, cancer vaccines are mainly used for preventing recurrence. Some clinical trials [121,122] have shown significantly lower cancer recurrence rates in treated patients who received a cancer vaccine compared to the non-vaccinated group. However, the intrinsic immune evasion capacity of cancer cells poses a significant obstacle to the successful translation of therapeutic cancer vaccines from preclinical studies to clinical applications in the treatment of patients with established malignant tumours [123].

Since Paul Ehrlich pioneered the era of targeted therapy in the 1890s and 1900s, scientists have made remarkable achievements in the basic research of the interaction between nanoparticles and cells. As a result, many active targeting strategies have been developed and successfully applied into animal models. Furthermore, more than two hundred clinical trials associated with antibody containing formulations have been carried out [124]. With substantial pre-clinical and clinical studies, the understanding of the relationships between nanoparticles, the immune system and cancer has been summarised and updated by numerous scientists. Although achieving true targeted delivery of drugs to tumors clinically remains challenging, the concept of the 'magic bullet' continues to be the ultimate goal for the design of nanomedicine.

Other strategies to increase therapeutic effect

In addition to exploiting the EPR effect and targeting tumour-associated cells, researchers have explored various other strategies to enhance the effectiveness of nanocarrier drug delivery systems.

Xu and colleagues [125] utilized the inherent tropism of mesoporous silicon microparticles, which preferentially accumulate in the liver and lungs, to target and treat metastatic breast cancer murine models. This approach takes advantage of the natural distribution of the microparticles to deliver therapeutic agents specifically to the desired sites. Palanikumar et al. [126] employed the polymer PLGA as a scaffold for a pH-sensitive nanocarrier. The drug doxorubicin-triphenylphosphine (DOX-TPP) was encapsulated within the nanocarrier, and its release was triggered by the low pH environment found in tumour microenvironments and cellular endosomes and lysosomes. This pH-sensitive nanosystem allows for controlled drug release, maximizing the therapeutic effect in the acidic tumour environment.

Beyond these strategies, there are many other diverse approaches [127–129] to enhance the delivery effectiveness of nanocarriers. These include photo-responsive drug delivery, where light is used to trigger drug release; ROS-responsive drug delivery, which utilizes reactive oxygen species to activate drug release; and magnetic-responsive drug delivery, where magnetic fields are employed to direct the nanocarriers to specific sites.

Over the past few decades, substantial progress has been achieved in the field of cancer nanomedicine. From 2000 to 2021, approximately fifty thousand articles in the cancer nanotechnology field have been published according to the PubMed database [130]. The growth in studies on cancer nanotechnology has been particularly remarkable since 2010. In terms of clinical translation, a survey conducted in 2019 [131] revealed that 75 nanomedicine candidates used for cancer therapy were under clinical evaluation, and 190 relevant clinical trials were being conducted. The pass rate of nanomedicine candidates for phase I clinical trial was high at 94%, with these candidates showing improved pharmacokinetics profiles compared to free drug formulations. However, the pass rate decreased to 48% in phase II and only 14% in phase III clinical trials. The major reason for the failure of these nanomedicines was their low efficacy in patients. Consequently, enhancing the effectiveness of nanoformulations remains a critical task for successful clinical translation. Nevertheless, the high pass rate in phase I clinical trials also highlights the significant advantage of nanoformulations in terms of safety and reduced toxicity compared to free drug formulations. The failures of nanomedicines in clinical trials provide valuable information and insights for future research. As concluded from this survey [131], most of the nanoplatforms used in the phase 1 to 3 clinical trials were liposomes or polymer based nanoparticles. It is clear that the efficacy of passively targeted and tumour cell-targeted nanomedicines heavily relies on the EPR effect in cancer patients,

which explains why many of these formulations failed in large and randomized phase III clinical trials. It is recommended that the therapeutic effect of the passively targeted nanomedicines might be improved by combining the EPR enhancement measures listed in the '***Strategies - EPR effect enhancement***' section of this chapter. The near total annihilation of passively targeted nanomedicines in clinical phase III also illustrates the need to increase the effective delivery of drugs to tumours by other means when designing nano-anti-cancer drugs.

The failures in clinical trials do not diminish the potential of nanomedicines. They are opportunities for learning and further progress. While low efficacy leading to the failure of phase III clinical trials is a challenge, it is not insurmountable. With continued advancements and innovations, cancer nanotechnology still holds immense promise in realizing the vision of curing cancer. The journey to harnessing the full potential of nanomedicines for cancer treatment continues, and the field remains a highly promising tool in the fight against cancer.

1.6 Motivation and Rationale of this PhD project

Inspired by the great success of Abraxane®, it is evident that albumin nanoparticles offer a suitable method for delivering hydrophobic drugs. Abraxane® (albumin-paclitaxel nanoparticle) is a well-known cancer nanomedicine used to treat advanced breast cancer, non-small cell lung cancer and pancreatic cancer [132]. Its unique paclitaxel protein-bound, solvent-free manufacturing technique eliminates the need for toxic excipients present in the Taxol® formulation, which is made up of paclitaxel and a mixture of toxic Cremophor oil and ethanol [63].

Clinical trials of Abraxane® have demonstrated its safety and biocompatibility in advanced cancer patients, with a higher maximum tolerated dose (MTD) of paclitaxel compared to Taxol®. The phase I trial showed that Abraxane® can be administered at 300 mg/m^2 over a 30-minute infusion without premedication, whereas Taxol® requires 175 mg/m^2 over a 3-hour infusion with premedication to reduce hypersensitivity reactions [133]. The higher paclitaxel MTD of Abraxane® without acute hypersensitivity reaction in the clinical trial implies that albumin nanoparticles as the carriers of paclitaxel are safe and biocompatible for human use. Additionally, the phase III clinical trial of Abraxane® demonstrated significantly higher response rates (39%) in metastatic cancer patients compared to Taxol® (19%), further confirming the improved antitumor response of

Abraxane® [134]. The improved antitumour response of Abraxane® in metastatic cancer patients has proven that exploiting albumin nanoparticles as the nanocarrier is a successful approach for clinical translation.

Taxol® is the first-generation formulation of paclitaxel injection [135]. This micellar formulation of paclitaxel is made up of a mixture of the nonionic surfactant polyoxyethylated castor oil and absolute ethanol. The FDA approved Taxol® for the treatment of advanced ovarian cancer in 1992 and later for numerous cancers, including metastatic breast cancer [136]. It is notable that Taxol® was once the best-selling anti-cancer drug, with annual sales reaching $1.6 billion in 2000 [70]. However, due to the Cremophor oil-induced acute toxicity, patients need to be pre-treated with histamine H1/2 blockers and corticosteroids to reduce the hypersensitivity reaction before the infusion of Taxol® [137]. As a result, its acute systemic toxicity limited the maximum tolerated dose of paclitaxel and therapeutic effect for patients. Therefore Taxol® has been gradually replaced by Abraxane® in the clinical treatment of advanced cancers.

However, it must be acknowledged that poor colloidal stability, limited efficacy and low payload are some of the shortcomings associated with albumin-based nanoparticles [138]. Thus, many research groups [139] have attempted to address these drawbacks, and then numerous studies and methods have been published. Among the developed methods, desovlation [140,141] is the most commonly used for fabricating albumin nanoparticles. However, the functional

groups of albumin proteins are largely occupied by crosslinking in the last step of the desolvation method and the poor colloidal stability at low concentrations is also not improved.

So, in this work, the human serum albumin (HSA) is selected as the nanoparticle scaffold to fabricate novel nanocarriers with high colloidal stability and high drug payload for a variety of hydrophobic small molecules and details are discussed in the following chapters. This endogenous protein was chosen to produce more biocompatible species that may be possibly translated to clinical applications, as it was hypothesised that biomolecules would be less toxic than a variety of synthetic polymers and circumvent protein corona formation and thus more likely to be working in the clinic. To be precise, albumin is a generic term for a family of specific globular proteins. Albumins can be found in the blood of human and animal species, milk, egg whites and plant proteins [142]. In this thesis, human serum albumin is referred to as albumin or HSA for short.

Serum albumin is extensively investigated as a material for making nanocarriers to deliver active ingredients in cancer therapy. Due to the great commercial success achieved by Abraxane® (with annual sales of approximately $1.2 billion in 2020), human serum albumin has attracted great attention in the delivery of chemotherapeutic agents.

Human serum albumin is constituted of 20 types of amino acids without addition of metal ions, a single chain comprising 585 amino acids is folded in a heart

shaped crystal structure with a molecular weight of 66.5 kDa [143], as shown in ***Fig 12***. The structure of the 20 essential amino acids is shown in ***Fig 13*** and the amino acid sequence of HSA is listed in ***Fig 14***. Human serum albumin is the most abundant protein in plasma with an approximate 50 g/L concentration and it can be easily obtained at a low cost, making it a cost-effective nanomaterial [144]. Moreover, as an endogenous protein, albumin is water-soluble, nontoxic, biocompatible and biodegradable, thus the toxicity of albumin nanoparticles is expected to be decreased to a very low level. In addition, according to the complete amino acid sequence of HSA listed in ***Fig 14***, HSA contains 59 free amine groups from lysine side chains, 97 carboxylic acid groups from the side chains of aspartic acid and glutamic acid, 17 disulfide bonds and one free sulfhydryl group from the side chain of cysteine (position 34 in amino acid sequence, also known as Cys-34). This makes albumin easily functionalized, as the amine groups, carboxylic acid groups, and thiol groups can be readily modified via NHS-ester reactions, esterification reactions, and maleimide reactions, respectively. Meanwhile, albumin also has many hydrophobic amino acids and aromatic amino acids, these functional groups can provide hydrophobic interaction and π-π stacking interaction to facilitate the carrying and delivery of hydrophobic small molecules in the bloodstream. Thus, HSA is an excellent starting polymer for use in drug delivery.

Therefore, in this PhD project, a novel albumin-based nanocarrier (HSA-PLA

nanoparticle) with a high colloidal stability and a high payload has been created by a covalent binding of the poly(lactic acid) (PLA) to the albumin cysteine residues. In order to further enhance the colloidal stability of the HSA-PLA nanoparticles, a step of acetylation on the albumin L-lysine residues was carried out to create the acetylated HSA (Ac-HSA).The polymer PLA was then conjugated to the Ac-HSA, resulting in the formation of Ac-HSA-PLA polymeric micelles. A variety of hydrophobic small molecules have been encapsulated into these albumin nanoparticles: paclitaxel, docetaxel, curcumin, as well as some hydrophobic fluorescent dyes like coumarin 6 and cyanine derivatives. The resulting nanosystems have shown good colloidal stability for long-term storage. Notably, Ac-HSA-PLA nanoparticles showed a highly enhanced uptake in MDA-MB-231 cells (human TNBC cell line) when compared with HSA standard and HSA-PLA nanoparticles. The synthesis and characterization details of the HSA-PLA nanoparticles are introduced in ***Chapter 2***. Then the characterization, *in vitro* and *in vivo* evaluations of paclitaxel loaded HSA-PLA nanoparticles are demonstrated in ***Chapter 3***. The ***Chapter 4*** includes the synthesis method and characterization of the Ac-HSA-PLA nanoparticles and ***Chapter 5*** covers and explains the enhanced uptake of the Ac-HSA-PLA nanoparticles in MDA-MB-231 cells based on the data obtained from the *in vitro* and *in vivo* studies.

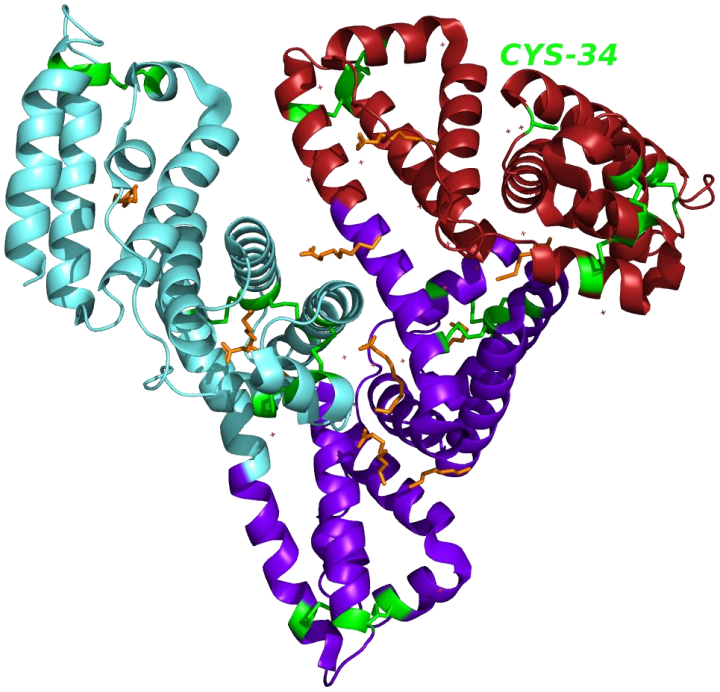

Fig 12. Crystal structure of human serum albumin (HSA, PDB 1e7e). The domain I, II, III were coloured in Red, Purple and Cyan, respectively. The orange labelled fatty acid molecules were distributed in the albumin's hydrophobic pockets. Disulphide bridges were emphasized in green sticks and position of cysteine 34 was labelled as CYS-34. This image was created through The PyMOL Molecular Graphics System, Version 1.2r3pre, Schrödinger, LLC.

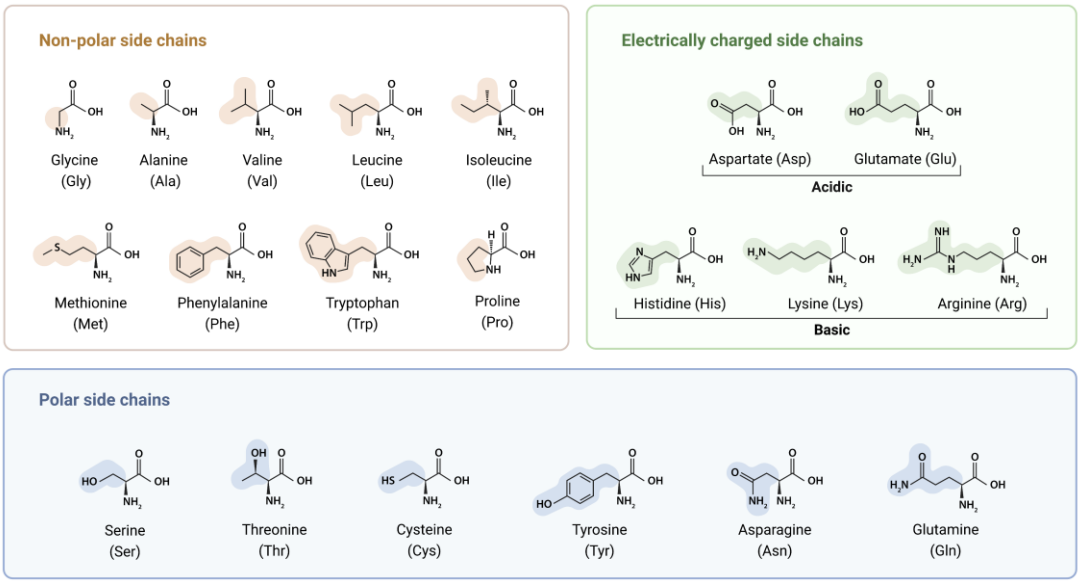

Fig 13. Structure of 20 essential amino acids. These amino acids are categorized into three types according to their side chain chemical property. Adapted from "Amino Acid Chart", by BioRender.com (2023). Retrieved from https://app.biorender.com/biorender-templates.

			3			6			9			12			15
1	Asp	Ala	**His**	Lys	Ser	**Glu**	Val	Ala	**His**	Arg	Phe	**Lys**	Asp	Leu	**Gly**
16	Glu	Glu	**Asn**	Phe	Lys	**Ala**	Leu	Val	**Leu**	Ile	Ala	**Phe**	Ala	Gln	**Tyr**
31	Leu	Gln	**Gln**	Cys	Pro	**Phe**	Glu	Asp	**His**	Val	Lys	**Leu**	Val	Asn	**Glu**
46	Val	Thr	**Glu**	Phe	Ala	**Lys**	Thr	Cys	**Val**	Ala	Asp	**Glu**	Ser	Ala	**Glu**
61	Asn	Cys	**Asp**	Lys	Ser	**Leu**	His	Thr	**Leu**	Phe	Gly	**Asp**	Lys	Leu	**Cys**
76	Thr	Val	**Ala**	Thr	Leu	**Arg**	Glu	Thr	**Tyr**	Gly	Glu	**Met**	Ala	Asp	**Cys**
91	Cys	Ala	**Lys**	Glu	Gln	**Pro**	Glu	Arg	**Asn**	Glu	Cys	**Phe**	Leu	Gln	**His**
106	Lys	Asp	**Asp**	Asn	Pro	**Asn**	Leu	Pro	**Arg**	Leu	Val	**Arg**	Pro	Glu	**Val**
121	Asp	Val	**Met**	Cys	Thr	**Ala**	Phe	His	**Asp**	Asn	Gln	**Glu**	Thr	Phe	**Leu**
136	Lys	Lys	**Tyr**	Leu	Tyr	**Glu**	Ile	Ala	**Arg**	Arg	His	**Pro**	Tyr	Phe	**Tyr**
151	Ala	Pro	**Glu**	Leu	Leu	**Phe**	Phe	Ala	**Lys**	Arg	Tyr	**Lys**	Ala	Ala	**Phe**
166	Thr	Glu	**Cys**	Cys	Glu	**Ala**	Ala	Asp	**Lys**	Ala	Ala	**Cys**	Leu	Leu	**Pro**
181	Lys	Leu	**Asp**	Glu	Leu	**Arg**	Asp	Glu	**Gly**	Lys	Ala	**Ser**	Ser	Ala	**Lys**
196	Gln	Arg	**Leu**	Lys	Cys	**Ala**	Ser	Leu	**Gln**	Lys	Phe	**Gly**	Glu	Arg	**Ala**
211	Phe	Lys	**Ala**	Trp	Ala	**Val**	Ala	Arg	**Leu**	Ser	Gln	**Arg**	Phe	Pro	**Lys**
226	Ala	Glu	**Phe**	Ala	Glu	**Val**	Ser	Lys	**Leu**	Val	Thr	**Asp**	Leu	Thr	**Lys**
241	Val	His	**Thr**	Glu	Cys	**Cys**	His	Gly	**Asp**	Leu	Leu	**Glu**	Cys	Ala	**Asp**
256	Asp	Arg	**Ala**	Asp	Leu	**Ala**	Lys	Tyr	**Ile**	Cys	Glu	**Asn**	Gln	Asp	**Ser**
271	Ile	Ser	**Ser**	Lys	Leu	**Lys**	Glu	Cys	**Cys**	Glu	Lys	**Pro**	Leu	Leu	**Glu**
286	Lys	Ser	**His**	Cys	Ile	**Ala**	Glu	Val	**Glu**	Asn	Asp	**Glu**	Met	Pro	**Ala**
301	Asp	Leu	**Pro**	Ser	Leu	**Ala**	Ala	Asp	**Phe**	Val	Glu	**Ser**	Lys	Asp	**Val**
316	Cys	Lys	**Asn**	Tyr	Ala	**Glu**	Ala	Lys	**Asp**	Val	Phe	**Leu**	Gly	Met	**Phe**
331	Leu	Tyr	**Glu**	Tyr	Ala	**Arg**	Arg	His	**Pro**	Asp	Tyr	**Ser**	Val	Val	**Leu**
346	Leu	Leu	**Arg**	Leu	Ala	**Lys**	Thr	Tyr	**Glu**	Thr	Thr	**Leu**	Glu	Lys	**Cys**
361	Cys	Ala	**Ala**	His	Asp	**Pro**	Tyr	Glu	**Cys**	Ala	Ala	**Lys**	Val	Phe	**Asp**
376	Glu	Phe	**Lys**	Pro	Leu	**Val**	Glu	Glu	**Pro**	Gln	Asn	**Leu**	Ile	Lys	**Gln**
391	Asn	Cys	**Glu**	Leu	Phe	**Glu**	Gln	Leu	**Gly**	Glu	Tyr	**Lys**	Phe	Gln	**Asn**
406	Ala	Leu	**Leu**	Val	Arg	**Tyr**	Thr	Lys	**Lys**	Val	Pro	**Gln**	Val	Ser	**Thr**
421	Pro	Thr	**Leu**	Val	Glu	**Val**	Ser	Arg	**Asn**	Leu	Gly	**Lys**	Val	Gly	**Ser**
436	Lys	Cys	**Cys**	Lys	His	**Pro**	Glu	Ala	**Lys**	Arg	Met	**Pro**	Cys	Ala	**Glu**
451	Asp	Tyr	**Leu**	Ser	Val	**Val**	Leu	Asn	**Gln**	Leu	Cys	**Val**	Leu	Glu	**His**
466	Lys	Thr	**Pro**	Val	Ser	**Asp**	Arg	Val	**Thr**	Lys	Cys	**Cys**	Thr	Glu	**Ser**
481	Leu	Val	**Asn**	Arg	Arg	**Pro**	Cys	Phe	**Ser**	Ala	Leu	**Glu**	Val	Asp	**Glu**
496	Thr	Tyr	**Val**	Pro	Lys	**Gln**	Phe	Asn	**Ala**	Glu	Thr	**Phe**	Thr	Phe	**His**
511	Ala	Asp	**Ile**	Cys	Thr	**Leu**	Ser	Glu	**Lys**	Glu	Arg	**Gln**	Ile	Lys	**Lys**
526	Gln	Thr	**Ala**	Leu	Val	**Glu**	Leu	Val	**Lys**	His	Lys	**Pro**	Lys	Ala	**Thr**
541	Lys	Glu	**Gln**	Leu	Lys	**Ala**	Val	Met	**Asp**	Asp	Phe	**Ala**	Ala	Phe	**Val**
556	Glu	Lys	**Cys**	Cys	Lys	**Ala**	Asp	Asp	**Lys**	Glu	Thr	**Cys**	Phe	Ala	**Glu**
571	Glu	Gly	**Lys**	Lys	Leu	**Val**	Ala	Ala	**Ser**	Gln	Ala	**Ala**	Leu	Gly	**Leu**

Fig 14. The complete amino acid sequence of human serum albumin. 585 amino acids are consisted of Ala (62), Arg (24), Asn (17), Asp (36), Cys (35), Gln (21), Glu (61), Gly (12), His (16), Ile (8), Leu (61), Lys (59), Met (6), Phe (31), Pro (24), Ser (24), Thr (28), Trp (1), Tyr (18) and Val (41).

1.7 Aims of project

In this project, we have focused on increasing the efficacy of albumin-based nanoformulations, particularly in the context of delivering the model drug paclitaxel (PTX). To achieve this goal, we have developed two strategies and demonstrated their effectiveness:

- Fabrication of HSA-PLA nanoparticle: We have created HSA-PLA nanoparticles and formulated PTX with these blank nanoparticles, resulting in a novel PTX nanoformulation. Our investigation has primarily focused on evaluating the colloidal stability of the HSA-PLA (PTX) nanoformulation.
- Acetylation and hydrophilization of human serum albumin: To further enhance the efficacy of albumin-based nanoformulations, we have acetylated and hydrophobized human serum albumin. By doing so, we have prepared a novel PTX formulation known as Ac-HSA-PLA (PTX). Our research has explored the cellular uptake of these nanoparticles in triple-negative breast cancer cells and their ability to efficiently deliver PTX to tumours in a murine tumour model.

Chapter 2. Synthesis and characterization of the highly colloid-stable albumin-polylactic acid (HSA-PLA) nanocarriers

2.1 Introduction

This chapter covers the synthesis method of the amphiphilic polymeric conjugate, HSA-PLA, and a series of related characterization studies. According to our hypothesis, HSA-PLA amphiphilic polymers self-assemble into polymeric micelles with high colloidal stability (low critical micelle concentration) in the aqueous medium. Here, MALDI-TOF (mass spectrometry) was used to determine the molecular weight of human serum albumin standard and the HSA-PLA conjugate, and thus the number of PLA molecules linked to albumin was estimated. The FT-IR technique was employed to ascertain the presence of the characteristic absorption peak of PLA molecules in the HSA-PLA spectrum, which was absent in the HSA spectrum. Furthermore, the protein secondary structure parameters of both HSA and the HSA-PLA conjugate were measured through the technique of circular dichroism. Then the critical micelle concentration of the HSA-PLA conjugate was obtained in fluorescence experiments using pyrene as a probe. At last, DLS and TEM were applied to demonstrate the morphology of the HSA-PLA nanoparticles as nanoscale spherical.

2.1.1 Amphiphilic polymeric micelle

Polymeric micelles [145] refer to shell-core structured nanocarriers constructed by the self-assembly of block copolymers above the critical micelle concentration in aqueous media. The geometry of polymeric micelles depends on the ratio of the thickness of the hydrophilic shell to the radius of the inner core [146]. If this ratio > 1, the resulting polymeric micelle will have a spherical appearance; otherwise, it will form a non-spherical structure [147], such as a rod or lamellae.

In comparison to low-molecular-weight surfactant micellar systems, polymeric micelles have a lower critical micelle concentration (CMC). This indicates that polymeric micellar systems are more stable than surfactant micellar systems at low concentrations [148]. Colloidal stability of nanocarriers at low concentrations is crucial for drug delivery, as robust nanocarriers can withstand disintegration caused by the dilution effects of body fluids (e.g., blood).

In the case of amphiphilic polymeric micelles, the formation of the inner core in aqueous medium is driven by hydrophobic interactions between the lipophilic segments of amphiphilic copolymers [149]. A schematic illustration is provided in ***Fig 15***. Once the concentration of amphiphilic polymers exceeds the CMC, these polymers self-assemble into a shell-core structure, reducing the interfacial area between hydrophobic blocks and the aqueous medium, thereby minimizing interfacial free energy [150].

Beside amphiphilic polymeric micelles, scientists have developed other types of polymeric micelles, such as polymer-metal complex micelles and polyion complex micelles, which also play important roles in drug delivery systems. In this thesis, HSA-PLA polymeric micelles belong to the family of amphiphilic polymeric micelles.

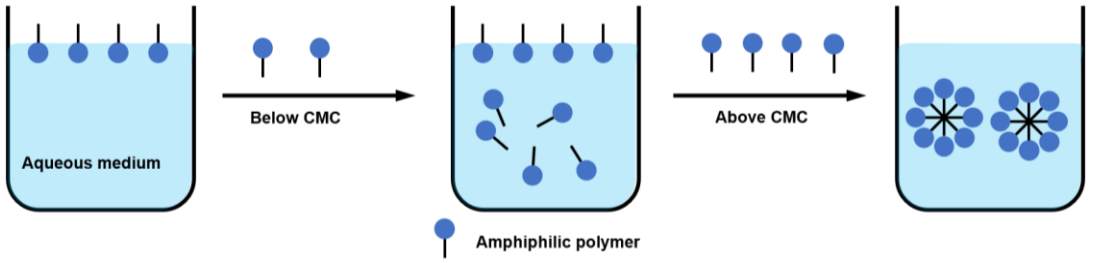

Fig 15. Schematic illustration of the formation of polymeric micelles by hydrophobic interactions. CMC represents critical micelle concentration of amphiphilic polymer.

In this work, we have devised a novel approach for creating albumin nanoparticles. Our hypothesis centred on the potential for these newly devised constructs to exhibit heightened colloidal stability and carry a substantial payload. Essentially, we achieved this by modifying the sulfhydryl group of human serum albumin with a hydrophobic polymer. The resultant HSA-polymer conjugates then self-assembled into polymeric micelles with nanoscale diameters. This polymeric micellar nanosystem has shown a higher payload and stability when employed for delivering paclitaxel, surpassing even the performance of the Abraxane®. Meanwhile, the presence of PTX molecules in the hydrophobic core of the HSA-PLA micelles contributes to the additional stabilization of the entire nanosystem. This is facilitated through intermolecular interactions, such as hydrophobic

interactions and π-π stacking. More specifically, the maleimide terminated PLA molecules were covalently bound to the Cys-34 side chains of reductively processed human serum albumins. The resulting HSA-PLA conjugates self-assembled into polymeric micelles within aqueous environments, as depicted in ***Fig 16***, with a nanoscale diameter as observed in TEM images.

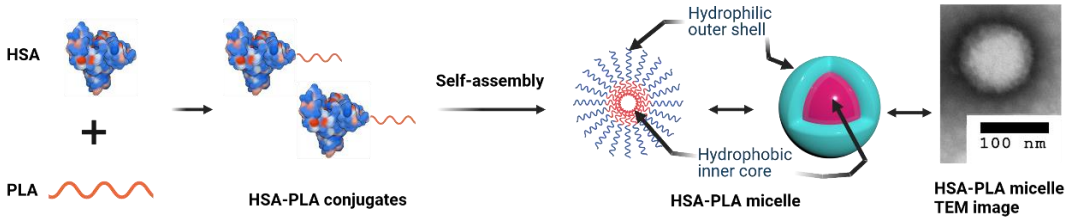

Fig 16. Schematic illustration of the preparation process of HSA-PLA polymeric micelles. Created with BioRender.com.

2.1.2 Introduction: MALDI-TOF

Mass spectrometry is an analytical technique used to measure the mass-to-charge ratio of analyte ions or to analyse the chemical structure of unknown compounds [151]. The analytes are ionized before entering the gaseous mobile phase. By applying an electric or magnetic field to the ionized sample, analyte ions with different sizes can be detected by the detector in a specific order. The resulting signals are then converted into a mass spectrum [152].

The initial step in mass spectrometry involves the desorption and ionization of

analytes. Different ionization methods have been developed based on the physicochemical properties of samples, such as molecular weight, polarity, and volatility [153]. Common ionization methods include electron impact (EI), electrospray ionization (ESI), and matrix-assisted laser desorption ionization (MALDI). These methods are frequently employed in mass spectrometry. After ionization, the ions are directed to a mass analyser for separation according to their mass-to-charge ratios (m/z). A common mass analysis method is time-of-flight (TOF), often used in combination with MALDI or LC-MS. The separation of ions in a TOF mass analyser [154] relies on their different flight times in a long TOF chamber. Accelerated with the same kinetic energy, smaller ions reach the detector first over the same distance, while heavier ions are detected later.

Consequently, a MALDI-TOF mass spectrometer utilizes MALDI ionization techniques to desorb and ionize analytes, with a TOF mass analyser for subsequent ion separation. Typically, MALDI-TOF is suitable for analysing samples with poor thermostability, non-volatility, and high molecular weight, such as proteins, peptides, oligosaccharides, and oligonucleotides.

In the preparation of samples for MALDI-TOF, the sample is dissolved in distilled water and then mixed with a matrix solution. The resulting sample-matrix solution is deposited onto a MALDI metal plate. After the water and solvent naturally evaporate, the remaining sample and matrix create a thin film on the MALDI-TOF sample plate. A laser is then employed to irradiate the matrix-sample thin film on

the metal plate. The matrix absorbs the laser energy, converting it into excitation energy that ionizes the samples, either positively or negatively charged, depending on the matrix type. The ratio of matrix to sample also influences mass spectrum resolution.

In the selection of MALDI-TOF mode, either positive or negative ionization can be used for MALDI, detected in linear or reflector mode. For instance, protein samples embedded in an acidic matrix (e.g., sinapinic acid) are subjected to positive ionization, while negative ionization is common for oligonucleotide and oligosaccharide samples with proton-accepting matrices [155], like 2-amino-5-nitropyridine and 6-aza-2-thiothymine. In the linear mode of the TOF mass analyser (***Fig 17***), ions travel in a straight line toward the detector, separated by their flight speed (proportional to molecular weight). However, their different starting positions in the accelerating field can lead to broader peaks and low-resolution signals in the mass spectrum [152]. Reflector mode (***Fig 18***), utilized in this study, accelerates the matrix-protein sample ions in an electric field, guiding them to the TOF chamber. Inside the chamber, ions are reflected by an ion mirror before detection. The longer ion path in the reflector mode enhances the separation of ions with varying flight speeds and minimizes the impact of differing spatial distributions of the same ions, resulting in increased mass spectrum resolution.

To calibrate the MALDI-TOF mass spectrometer, a suitable standard can be used

as an external calibrator, run beforehand, or combined with samples and embedded in the matrix as an internal calibrator. In this study, the internal calibration mode was adopted, using aldolase as the calibration standard.

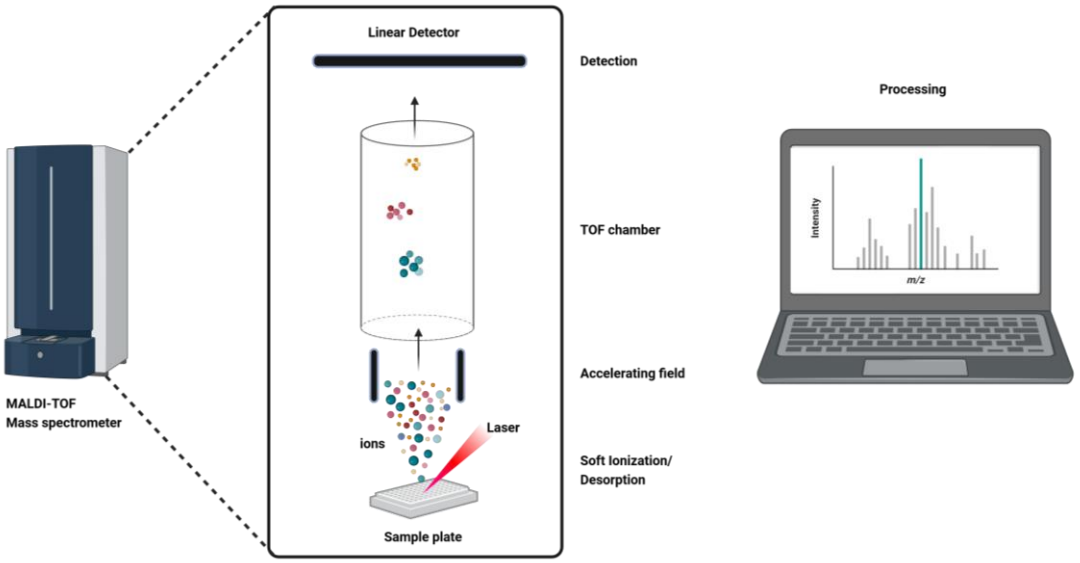

Fig 17. Linear mode of MALDI-TOF. After the ionization of sample and the resulting ions are accelerated in an electric field and then enter the TOF chamber, ions are separated based on the different flight times in TOF chamber and detected by the linear detector. Created with BioRender.com.

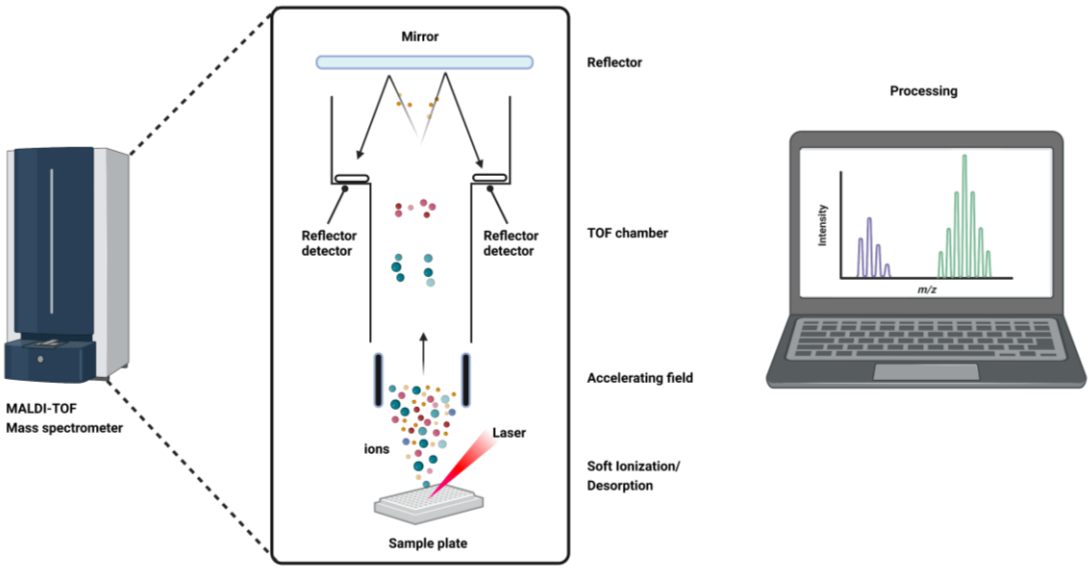

Fig 18. Reflector mode of MALDI-TOF. Samples are ionized by laser bombardment and the resulting ions are accelerated in an electric field and then enter the TOF chamber, where they are then reflected by the ion mirror at the end of the TOF chamber and detected by the reflector detectors. A longer ion path can help to better separate ions when they have different flight speeds and to reduce the impact of different spatial distributions of same ions. As a result, resolution of mass spectra of samples can be increased. Created with BioRender.com.

2.1.3 Introduction: FT-IR

Fourier-transform infrared spectroscopy (FT-IR) is a rapid, convenient and accurate analytical technique to obtain a specific infrared spectrum of an analyte. The resulting IR spectrum serves as a molecular fingerprint for the analyte, which can be used to characterize new compounds or identify the unknown sample by comparing them with existing IR spectra [156].

Before delving into the fundamentals of FT-IR spectroscopy, the concept of '**light**' is first introduced. Throughout history, scientists have made efforts to describe and explain the nature of light, proposing various hypotheses [157], including

electromagnetic radiation, photons, and quantum theory. Maxwell depicted light as propagating waves consisting of electric and magnetic fields [158]. Building upon the theory of electromagnetic waves, light can be categorized by its frequency and wavelength, as demonstrated in the electromagnetic spectrum shown in ***Fig 19***. For example, visible light falls within a wavelength range of 400 to 700 nanometres. The energy of light is linked to its wavelength and frequency, with longer wavelengths generally corresponding to lower energy. This energy carried by light can be transferred to objects when they are illuminated, potentially triggering a series of photoreactions. This principle explains various phenomena, including how plants generate energy through photosynthesis. It also applies to the human visual system, essentially acting as a form of spectrophotometry. The photoreceptor cells in human eyes, such as rod cells and cone cells, get excited by light within the visible spectrum (400 – 700 nm), allowing humans to perceive and differentiate objects based on their appearances and colors.

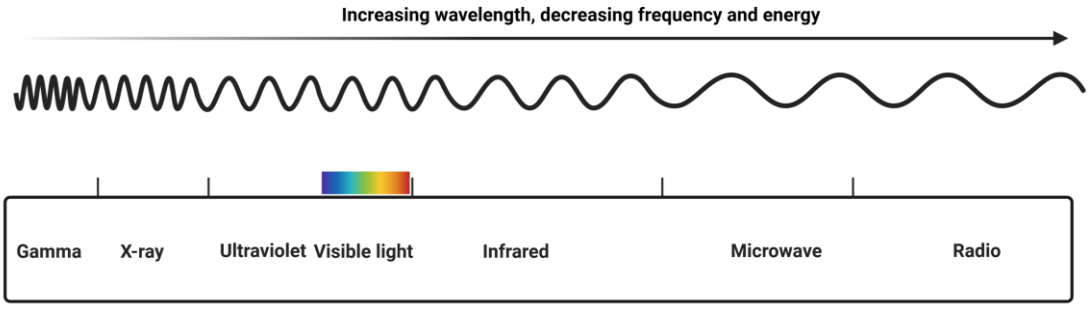

Fig 19. Schematic diagram of electromagnetic spectrum. Energy of light is proportional to frequency and negative correlated with wavelength of light. Created with BioRender.com.

Based on the theory of electromagnetic radiation, infrared spectroscopy was developed to visualize the molecular bonds and functional groups of molecules in the form of an infrared spectrum. The energy of IR radiation at specific wavelength can be absorbed by molecules in accordance with their molecular bonds, inducing bond vibrations including stretching and bending. An IR spectrometer captures the variation in light intensity as light passes through a sample before and after absorption. For example, the carbonyl group (C=O) in an ester strongly absorbs light around 1750 cm^{-1}, yielding a distinct absorption signal in the IR spectrum .

On the basis of the IR spectroscopy, scientists developed the FT-IR (Fourier-transform infrared) technique to gather spectral data across all infrared wavelengths. Unlike the older IR method that measured light absorption one wavelength at a time, the FT-IR spectrometer employs a Michelson interferometer [159] to collect all transmitted light at once, as shown in ***Fig 20***. The interferometer divides produced infrared light, directing portions toward both a fixed mirror and a movable mirror. After reflection, the beams are combined and directed through the sample. By this means, the detector collects transmitted light across all wavelengths, resulting in an FT-IR spectrum .

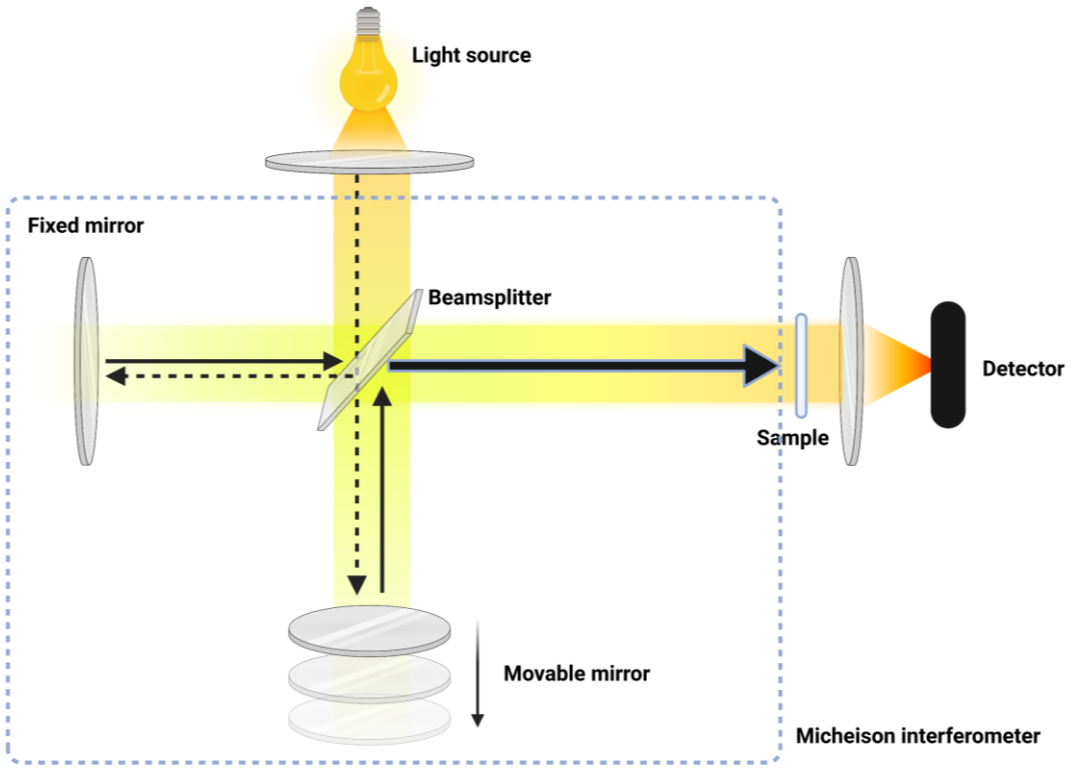

Fig 20. Schematic diagram of Fourier-transform infrared (FT-IR) spectrometer. The infrared light is split to a fixed mirror and a movable mirror by beamsplitter in the Michelson interferometer. The reflected beam can then be combined to pass through the sample. The all-wavelength transmitted light can then be collected by detector. Created with BioRender.com.

2.1.4 Introduction: Circular dichroism

A circular dichroism spectrophotometer is an analytical tool used to measure the sample absorption difference between left and right circularly polarized ultraviolet light [160]. Within the circular dichroism spectrophotometer, ultraviolet light is polarized in both right- and left-circular directions. Due to the tertiary structure of proteins (α-helices and β-sheets), the chromophores of peptide bonds exhibit

differing absorption characteristics for left and right circularly polarized ultraviolet light. After a series of calculations, a graph of delta epsilon (Δ ε) as a function of wavelength (nm) can be obtained by the software. Subsequently, protein secondary structure parameters can be calculated using online calculators (e.g., http://cbdm-01.zdv.uni-mainz.de/~andrade/k2d3/). As a result, CD proves to be a robust technique for analysing conformational changes in proteins.

2.1.5 Introduction: DLS

The dynamic light scattering (DLS) technique is employed to determine the hydrodynamic diameter (D_H) of particles suspended in a medium [161]. In DLS, a laser beam is directed at a colloidal suspension, and a portion of the light scatters when encountering the moving particles. Variations in the intensity of the scattered light are influenced by the speed of Brownian motion of the particles. Smaller particles exhibit faster diffusion and more rapid fluctuations in intensity. The analysis of these fluctuations in dynamically scattered light intensity allows the investigation of the random Brownian motion of particles in the medium. Consequently, the correlator can calculate the particles' diffusion coefficient.

The hydrodynamic diameters of the mobile entities can be computed based on the Stokes-Einstein equation [162] outlined below:

Stokes – Einstein equation: $D_H = \frac{kT}{3\pi\eta D_f}$

Where D_H is the hydrodynamic diameter, k is the Boltzmann's constant, T represents the absolute temperature, η denotes the viscosity of solvent and D_f signifies the diffusion coefficient of particles.

However, it's important to note that the DLS instrument estimates and calculates hydrodynamic diameters from sets of scattered light intensities. Thus, the instrument cannot differentiate between individual dispersed particles and agglomerated particle clusters (***Fig 21***). Additionally, the presence of a hydration layer around particles [163], implies that the actual particle sizes are likely smaller than the measured hydrodynamic diameters.

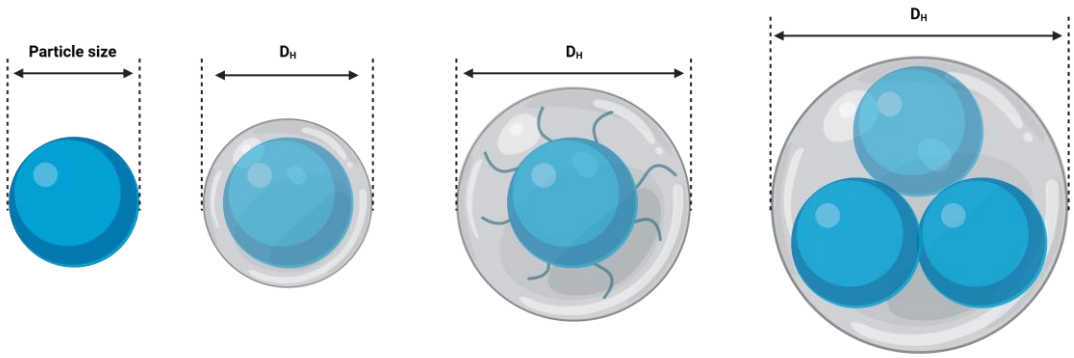

Fig 21. Schematic illustration of the difference between particle sizes and hydrodynamic diameters of particles. The measured hydrodynamic diameters can be influenced by the hydration layer or the hydrophilic chains around the particle surface or the particle clusters. Created with BioRender.com.

2.1.6 Introduction: TEM

Transmission electron microscopy (TEM) is a type of electron microscope used to obtain high-resolution images of samples [164]. Therefore, TEM may be used to image nanoparticles to acquire precise information about the morphology and particle size of nanoparticles.

In contrast to the techniques described above, transmission electron microscopy does not rely on light for imaging. In the 19th century, scientists designed an innovative microscope based on electron imaging technology, which boasted much higher resolution compared to optical microscopes of the same era [165]. Drawing from the principles of matter and wave-particle duality, as well as Einstein's equation ($E = mc^2$), Louis de Broglie formulated an equation stating that wavelength is inversely proportional to mass when velocity remains constant.

Louis de Broglie equation: $\lambda = \frac{h}{mv}$

Where *h* = Planck's constant, *m* = mass of particles, and *v* = velocity of particles. As the mass of an electron is much greater than that of a photon, once this electron has been accelerated to a high speed, the wavelength of the electron will be very small, allowing for a highly improved resolution of the image.

Based on the above theories, scientists developed the TEM microscopy, as shown in ***Fig 22***. The electron gun produces an electron beam and electrons are accelerated from cathode to anode. Condenser lenses are used to focus these

electrons onto the sample. Due to electrons are not photons, TEM condenser lenses are electromagnetic lenses rather than the optical lenses. Once the electrons interact with the sample, and some of electrons are absorbed by the sample. The dark areas of TEM images are areas where electrons are largely absorbed and few electrons are transmitted. To enhance clarity in TEM images of biological samples, staining agents like uranyl acetate are often applied prior to imaging. Subsequently, the transmitted electrons are collected and concentrated by the objective lens. The magnification is then adjusted using a projector lens. After undergoing transformations, 2D images of the sample are visualized on a screen.

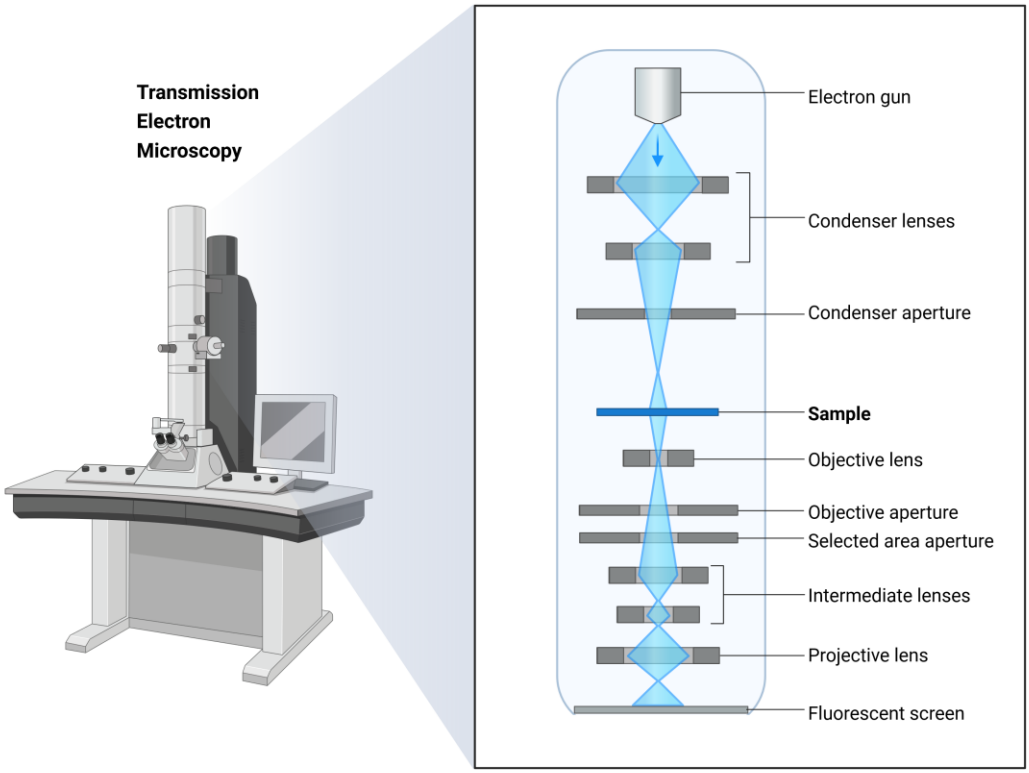

Fig 22. Schematic illustration for the working principle of transmission electron microscopy. Electrons from the electron gun are accelerated from cathode to anode. Condenser lenses focus the electrons on to the sample. Part of electrons will be absorbed by the sample**.** Next, the transmitted electrons are collected and focused by the objective lens. At last, the projective lens are used to adjust the magnification. After transformation, TEM images of sample can be seen on the screen. Adapted from "Transmission electron microscopy (TEM)", by BioRender.com (2023). Retrieved from https://app.biorender.com/biorender-templates.

2.2 Materials

Table 3. Materials used in the synthesis and characterization of HSA-PLA nanoparticle.

Supplier	Materials
Merck UK	Acetone puriss ACS reagent
	Dimethyl sulfoxide (DMSO)
	5,5'-Dithiobis (2-nitrobenzoic acid) 99%
	Ethylenediaminetetraacetic acid (EDTA)
	L-cysteine hydrochloride monohydrate (reagent grade)
	Human serum albumin (HSA) essentially fatty acid free
	Methanol puriss ACS reagent
	Phosphotungstic acid hydrate for microscopy
	Poly(L-lactide) N-2-hydroxyethylmaleimide terminated Mn 2000
	Pyrene, puriss. p.a for fluorescence ≥99.0%
	Sodium phosphate monobasic dihydrate (≥99.0%)
	Sodium phosphate dibasic heptahydrate (98-102%)
	Syringe-driven filter units (0.45µm)
Generon UK	Tris(2-carboxyethyl) phosphine Hydrochloride (TCEP•HCl)
Thermo Fisher Scientific UK	Acetonitrile (ACN, ≥99.9%, HPLC Gradient grade)
	3,5-Dimethoxy-4-hydroxycinnamic acid, 98%
	Slide-A-Lyzer™ Dialysis Cassettes 20K MWCO
	Trifluoroacetic acid (TFA, 99%)
Biosynth Carbosynth	4-azidobenzoic acid (ABA)
ELGA PURELAB®	Distilled water

All chemicals, reagents and solvents were used as purchased without any purification.

2.3 Experimental methods

2.3.1 Preparation of HSA-PLA polymeric micelles

All solutions used in the synthesis were degassed overnight. Also all reactions described in this section were carried out under the nitrogen protection.

Step 1: Reduction of human serum albumin

An amount of 800 mg of HSA powder was dissolved in 120 mL of 0.1 M sodium phosphate buffer solution (pH 6.8, 1 mM EDTA), followed by the addition of 7 mL of a TCEP solution (10 mg/mL in water) to the HSA solution. The resulting mixture was stirred using a magnetic stirrer for 4 hours while placed in an ice bath and under nitrogen protection.

Step 2: Quenching TCEP reduction

A total of 0.5 mL of DMSO containing 50 mg of 4-azidobenzoic acid was added drop by drop to the previously mentioned mixture. Following a 10-minute quenching period, 40 mL of 0.2 M sodium phosphate buffer (pH 9.3) was introduced to the mixture to neutralize any acidic by-products.

Step 3: Conjugating MAL-PLA to the reduced HSA

Maleimide-PLA (540 mg, Sigma-Aldrich, UK) was dissolved in 15 mL of DMSO and subsequently added to the previously reduced HSA solution. The resultant mixture was stirred using a magnetic stirrer for 4 hours at 37°C in an oil bath, all

while being protected with nitrogen.

Step 4: Purification and lyophilization

After the conjugation, the mixture was subjected to centrifugation for 5 minutes at 6000 rpm (5 cycles) using a Hermle Z232K Centrifuge (Hermle Labortechnik FmbH, Germany). The resulting supernatant was carefully transferred to a dialysis cassette with a molecular weight cut-off of 20K. After 2 days of dialysis against distilled water, the nanosuspension underwent centrifugation once more for 5 cycles at 6000 rpm for 5 minutes. The purified nanoparticle suspension was rapidly frozen in a -20°C medium containing 25% (w/v) NaCl, followed by a subsequent 48-hour lyophilization process utilizing a freeze dryer (ALPHA 1-4 LDplus, Martin Christ, Germany). The resulting lyophilized powder was collected and stored in a glass vial at room temperature.

2.3.2 Ellman's colorimetric assay

Ellman's colorimetric assay was utilized to quantify the presence of free sulfhydryl groups in both albumin standards and the reduced albumins.

Step 1: Determination of free sulfhydryl groups of albumin standards

The free sulfhydryl groups of commercially available albumin proteins (HSA-A1887, A3782, A8763; and BSA-A2153, Sigma-Aldrich, UK) were quantified by using the Ellman's assay. Briefly, albumin and Ellman's reagent (5,5-dithio-bis-(2-

nitrobenzoic acid), DTNB) powder were dissolved in degassed 0.1 M sodium phosphate buffer solution (pH 8.0, 1 mM EDTA), respectively. Subsequently, the Ellman's reagent solution was added to the albumin solutions, and the resulting mixtures were stirred under the protection of nitrogen for 15 minutes at room temperature. The concentrations of the albumins and Ellman's reagent in the mixtures were equivalent to 0.025 mM and 0.5 mM, respectively. An instrument (UV-1650PC, Shimadzu, Japan) was used to measure the absorbance of reactants at wavelengths from 400 nm to 450 nm.

Step 2: Determination of free sulfhydryl groups of reduced albumins

The assessment of free sulfhydryl groups in the reduced albumins (listed in method 2.3.1) was conducted at predetermined time points (10 min, 30 min, 1, 2, and 4 hours). The final concentrations of the reduced HSA and the DTNB were 0.025 mM and 1.0 mM, respectively. The mixture was stirred for the designated times (as specified above) within an ice bath and under a continuous stream of nitrogen. Prior to this, TCEP within the mixture had been inactivated using 4-azidobenzoic acid, and the pH was adjusted to pH = 8. The UV-1650PC instrument (Shimadzu, Japan) was once again employed to measure reactant absorbance across wavelengths ranging from 400 nm to 450 nm.

2.3.3 Matrix-assisted laser desorption ionization time-of-flight

The molecular weights of both HSA standards and the HSA-PLA conjugates were determined by a Matrix-Assisted Laser Desorption-Time of Flight (MALDI-TOF) Mass Spectrometer (Bruker Daltonics, BD, Bremen, Germany). The saturated matrix solution was prepared by dissolving an excess of 3,5-dimethoxy-4-hydroxycinnamic acid (sinapinic acid) in a solution consisting of 50% distilled water and 50% ACN (0.2% v/v TFA). Protein samples (100 pmol/μL) were diluted with the freshly made matrix solution (1: 9). Then, 1 μL of the resulting mixture was carefully deposited onto a MALDI sample plate. Additionally, 1 μL of an aldolase standard solution (A9096, Sigma Aldrich, UK) was deposited at the same site, serving as an internal calibration standard. Reflector mode was selected to achieve a higher resolution mass spectrum.

2.3.4 Fourier-transform infrared spectroscopy, FT-IR

Functional group information of the samples was acquired through FT-IR Spectrometry using a Perkin Elmer-FTIR Spectrum-100 instrument (Perkin Elmer, Germany). To perform this, either the HSA standard or HSA-PLA powder was placed onto the mounting plate to ensure detector coverage. The pressure level was regulated to approximately 120 by adjusting the pressure arm knob. The scanning process covered a range from 400 to 4000 cm^{-1}, and each spectrum was generated by conducting 16 scans.

2.3.5 Circular dichroism, CD

The JASCO J-720 Spectropolarimeter (JASCO, JAPAN) instrument was utilized to assess the secondary structure of both HSA and HSA-PLA. For this purpose, the HSA standard and lyophilized powder of HSA or HSA-PLA were dissolved in phosphate buffer (pH 7.4, without sodium chloride) at a concentration of 0.5 mg/mL. These sample solutions were placed within 0.22 mm pathlength demountable cuvettes (Hellma®) and subjected to scanning from 300 nm to 180 nm at room temperature. Each sample underwent three separate scans, and the acquired spectra were processed using the CDtools software. The α-helix and β-sheet data for each sample were computed through the K2D3 web calculator (http://cbdm-01.zdv.uni-mainz.de/~andrade/k2d3/).

2.3.6 Dynamic light scattering, DLS

The hydrodynamic diameter, zeta potential, and polydispersity index (PDI) of both the HSA standard and the HSA-PLA nanoparticles were assessed using dynamic light scattering (DLS) through a Malvern Nano-ZS instrument. For each analysis, 2 mg of the lyophilized sample was dispersed in 2 mL of distilled water. The pH value of both the albumin solution and the HSA-PLA nanosuspension was maintained at 7 (pH = 7). To ensure accuracy, each sample underwent three measurements.

2.3.7 Critical micelle concentration assessment

To determine the critical micelle concentration of the HSA-PLA nanoparticles, the pyrene fluorescence method was employed. Here's the procedure in detail:

1. Preparation of pyrene solution:

- Dissolve 1.2 mg of pyrene in 1 mL of MeOH, creating a 5.93 mM pyrene solution.
- Dilute this solution with MeOH to yield a 593 μM pyrene solution.

2. Preparation of pyrene stock solution:

- Take 0.1 mL of the 593 μM pyrene solution and place it in an empty amber bottle.
- Allow this to dry in a fume hood for 30 minutes.
- Fill the dried amber glass vial with 100 mL of distilled water, resulting in a 593 nM pyrene stock solution.

3. Preparation of HSA-PLA nanoparticle dispersions:

- Create HSA-PLA nanoparticle dispersions at concentrations of 0.02, 0.2, 2, 20, 60, 100, 200, and 2000 μg/mL.

4. Mixing pyrene stock solution with nanoparticle dispersions:

- Add 1 mL of the pyrene stock solution to each glass vial.
- To each vial, slowly introduce 1 mL of the corresponding HSA-PLA nanoparticle dispersion while employing magnetic stirring.

5. Spectra measurement:

- The concentration of pyrene in each sample vial is now 297 nM, and the HSA-PLA polymer concentrations range from 0.01 to 1000 µg/mL.
- Record the spectra (water background subtracted) using an LS 45 luminescence spectrometer (Perkin Elmer, Germany).
- The parameters for the measurement are: excitation wavelength 340 nm, emission wavelength from 365 to 415 nm, scan speed 20 nm/min, and 5 repeated scans per sample.

This procedure allows for the assessment of the critical micelle concentration of the HSA-PLA nanoparticles using the pyrene fluorescence method, providing insight into the self-assembly behaviour of the nanoparticles.

2.3.8 Transmission electron microscopy, TEM

A drop of HSA-PLA nanosuspension at a concentration of 5 mg/mL and a drop of HSA standard solution at a concentration of 5 mg/mL were applied to TEM grids. After a 5-minute interval, excess water on the TEM grid was absorbed by tissue paper. Subsequently, a drop of 1% (w/v) neutral phosphotungstic acid solution was added to each TEM grid. Following a 1-minute staining period, distilled water was utilized to wash each copper grid and remove excess staining agent. The prepared TEM samples were stored in a dark environment until imaging.

2.3.9 Statistics

Data are presented as the means ± SD (standard deviation). The student's t-test was used in this chapter for the statistical analysis by Prism software. A value of $p < 0.05$ was considered to be a significant difference between the two sets of data.

2.4 Results and discussion

2.4.1 Synthesis of HSA-PLA conjugates

In this study, it is aimed to link a hydrophobic polymer to the cysteine-34 (Cys-34) sulfhydryl group of HSA. As reported previously [166], there is a free sulfhydryl group (Cys-34) at the surface of HSA (***Fig 13***). However, in fact, the Cys-34 thiol groups of commercial albumins are often occupied, because albumin also acts as the plasma antioxidant [167], and thus these Cys-34 thiol groups are susceptible to be oxidized in the blood circulation or manufacturing processes. Consequently, the Cys-34 of commercial albumin might not be reactive, necessitating an additional reduction step to eliminate any unknown compounds bound to the Cys-34 side chain prior to the PLA conjugation.

TCEP [(tris(2-carboxyethyl)phosphine)] is a frequently used reductant in the biological chemistry. The inert phosphate oxide (oxidized TCEP) was formed when HSA was reduced by the TCEP (***Fig 23***). Furthermore, the excess TCEP was able to be inactivated and quenched by the addition of 4-azidobenzoic acid. Simultaneously, the utilization of a degassed buffer and the inclusion of EDTA in the reaction medium were undertaken to mitigate any potential unexpected side reactions. These precautions aimed to counteract events such as the oxidative modification of sulfhydryl groups and the binding of thiol groups to metals.

After the reduction of the HSA, 4-azidobenzoic was added to neutralize the excess TCEP. Based on the previous discussion, the TCEP could be transformed to the unreactive phosphine oxide through the Staudinger reaction [168]. Moreover, the acidic by-product, 4-aminobenzoic acid, could provide the additional protons to protect the reduced sulfhydryl groups (from thiolate anion state to sulfhydryl state) during the quenching step.

For the subsequent conjugation step, an alkaline buffer solution was added to neutralize the acidic by-products and activate the sulfhydryl groups of the reduced HSA (-SH to -S−). Subsequently, Following this, a solution of maleimide-polylactide (MAL-PLA) in dimethyl sulfoxide (DMSO) was added to the reduced albumin solution. The water-insoluble complex formed by MAL-PLA and DMSO was then dispersed within the aqueous basic reaction medium. This dispersion enabled the MAL-PLA molecules to interact with and conjugate to the cysteine side chains of albumins. As a result, the HSA-PLA conjugates formed and underwent self-assembly into polymeric micelles. Since MAL-PLA molecules do not dissolve readily in the aqueous reaction medium, the efficiency of conjugation of MAL-PLA to HSA was notably low. Consequently, a surplus amount of MAL-PLA molecules had to be added to ensure sufficient conjugation occurred.

Despite the release of multiple thiol groups per albumin due to the action of TCEP, the polymer MAL-PLA was still highly conjugated to the side chain of the Cys-34. This phenomenon has been substantiated and verified in subsequent chapters.

The occurrence can be attributed to the steric hindrance effect [169,170], which dictates that the dispersed micron-sized clusters of MAL-PLA can exclusively interact with the thiol group of Cys-34 located on the surface of HSA. Notably, the amphiphilic nature of the resulting HSA-PLA conjugates, which share identical critical micelle concentration and surface tension in the given aqueous environment [171], greatly contributes to the formation of exceptionally uniform nanoparticles.

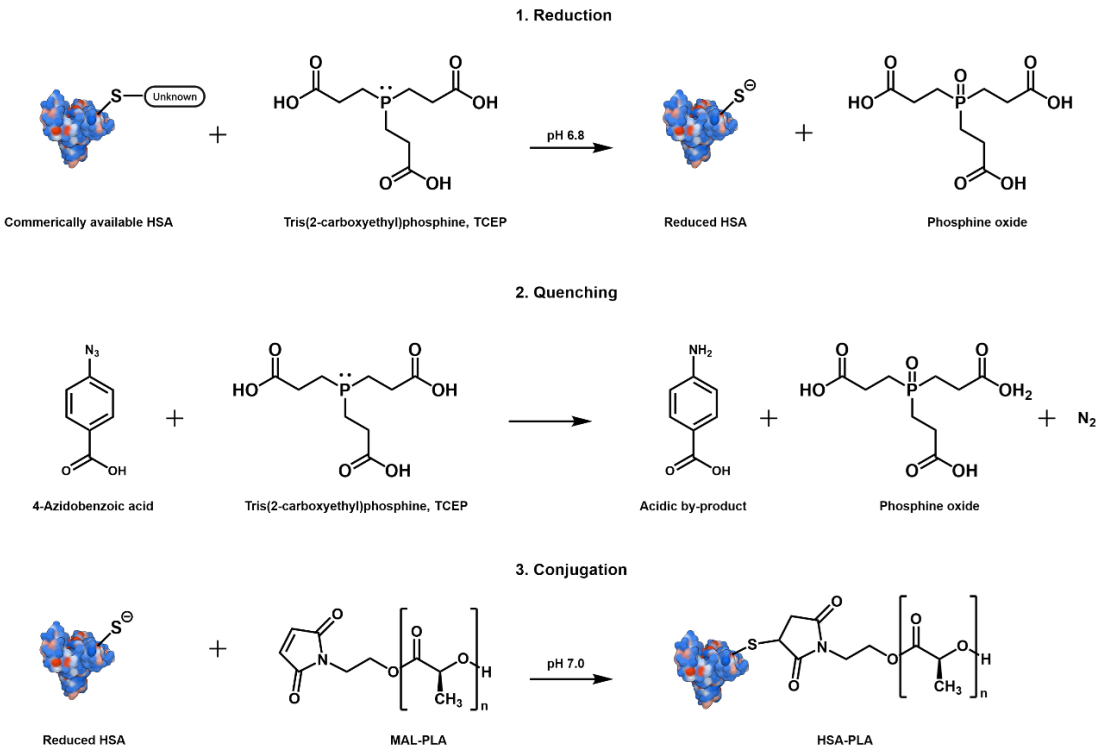

Fig 23. Synthetic process of HSA-PLA conjugates including reducing, quenching and conjugation steps. TCEP was used to release the sulfhydryl group of Cys-34, then 4-azidobenzoic acid was added to neutralize the excess TCEP. At last, a hydrophobic polymer MAL-PLA was conjugated to the reduced HSA via the maleimide reaction.

2.4.2 Confirmation of the synthesis of HSA-PLA conjugates

The synthesis of the HSA-PLA conjugates was confirmed through a series of analytical methods, including the Ellman's colorimetric assay, MALDI-TOF, FT-IR, and circular dichroism studies.

Ellman's colorimetric assay

The hypothesis underlying this study was that the hydrophobic polymer PLA would be conjugated with the free sulfhydryl group (Cys-34) of HSA. To investigate this, the Ellman's assay was initially employed to quantify the availability of free sulfhydryl groups in the HSA obtained from Sigma Aldrich, UK. Various types of albumin, including three bottles with different product numbers (A1887, A3782, and A8763) of HSA and one bottle of BSA (A2153), were selected to assess the occupancy status of their Cys-34 side chains. Though the nucleophilic substitution reaction (***Fig 24. A***) between the thiolate anion and DTNB [Ellman's reagent, 5,5'-Dithio-bis-(2-nitrobenzoic acid)], the absorbance of the resulting TNB^- at a wavelength of 412 nm was recorded by a UV-VIS spectrophotometer. The concentration of TNB^- molecules served as an indicator of the concentration of free sulfhydryl groups. Approximately, according to the Ellman's assay results (***Fig 24. B***), 65% of the Cys-34 side chains of the human serum albumins (Sigma Aldrich, UK) were blocked, and 50% of the Cys-34 thiol groups of bovine serum albumins were occupied. Consequently, an additional

reduction step for HSA was deemed necessary to release the sulfhydryl groups for the conjugation. The curve depicting the released thiol groups over the course of albumin reduction time (***Fig 24. C***) indicated that the TCEP reduction method did not break all disulphide bridges within the HSA molecules. Given that HSA protein contains 35 cysteine residues, the maximum number of thiol groups released per albumin molecule was 7. In ***Fig 24. D***, the lower absorbance intensity at 412 nm represents a lower concentration of thiol groups in the solution. Notably, the HSA-PLA sample exhibited nearly no free thiol groups in comparison to the HSA standard. This result indicates that the free thiol groups released from the Cys-34 of albumins were fully occupied after the conjugation reaction.

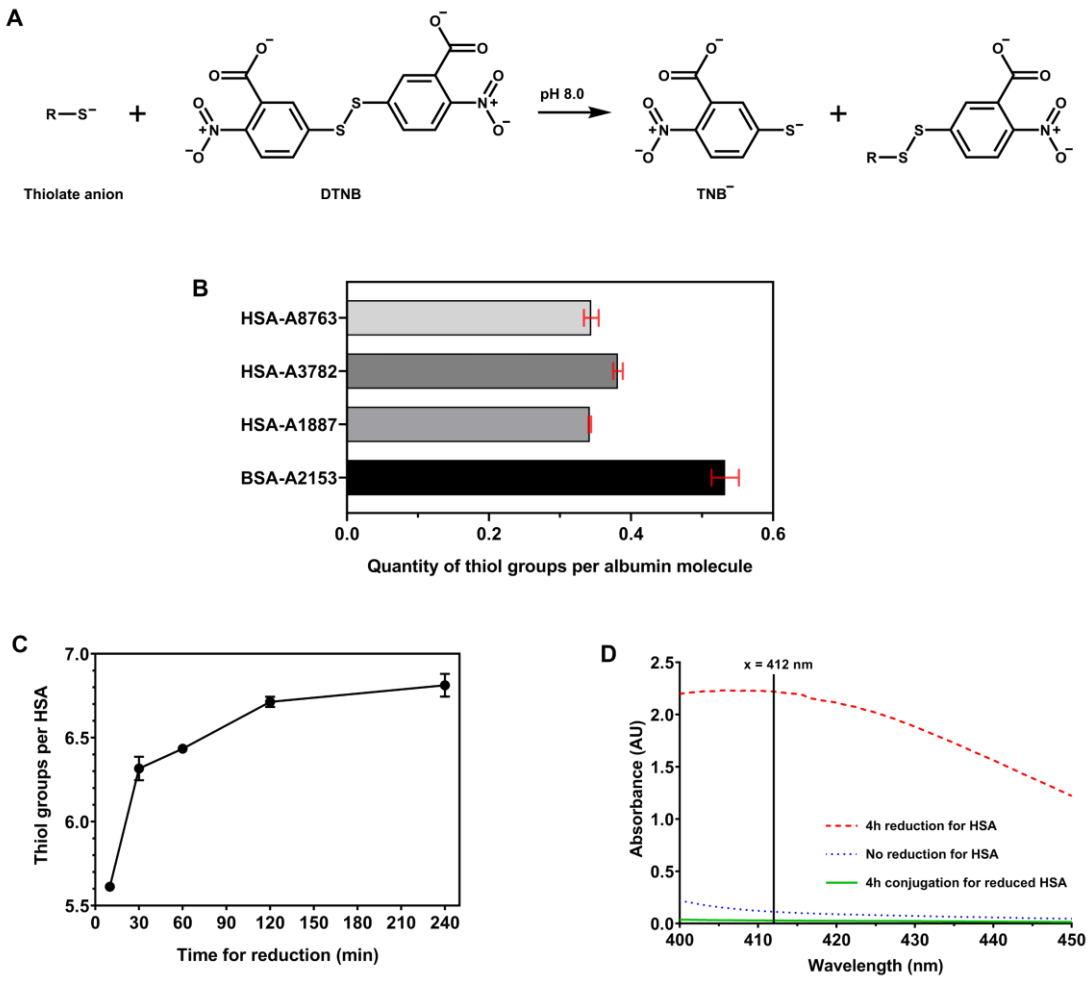

Fig 24. The Ellman's colorimetric assay was used to quantify the free sulfhydryl groups of albumins. (A) An nucleophilic substitution reaction between the thiolate anion and DTNB. **(B)** Free sulfhydryl groups of different commercially available albumins. **(C)** The number of released thiol groups at different pre-determined TECP reduction time points. **(D)** The comparison of UV-VIS spectra, the absorbance intensity at 412 nm of each albumin sample is proportional to its concentration of free sulfhydryl groups. No free thiol group was left after the 4-hour conjugation reaction of MAL-PLA with the reduced HSA in comparison to the HSA standard.

Fourier-transform infrared spectroscopy

Fourier-transform infrared spectroscopy (FT-IR) was applied to check if the polymer MAL-PLA was conjugated to the reduced albumin. The stacked FT-IR spectra (***Fig 25***) clearly showed an absorption peak at 1756 cm^{-1} corresponding to the carbonyl group of PLA in the HSA-PLA spectrum, contrasting with the FT-IR spectrum of the HSA standard. Based on the results of the Ellman's assay and the FT-IR studies, it is concluded that the MAL-PLA was effectively conjugated to the reduced HSA, and this conclusion was further corroborated through subsequent analyses (as detailed below).

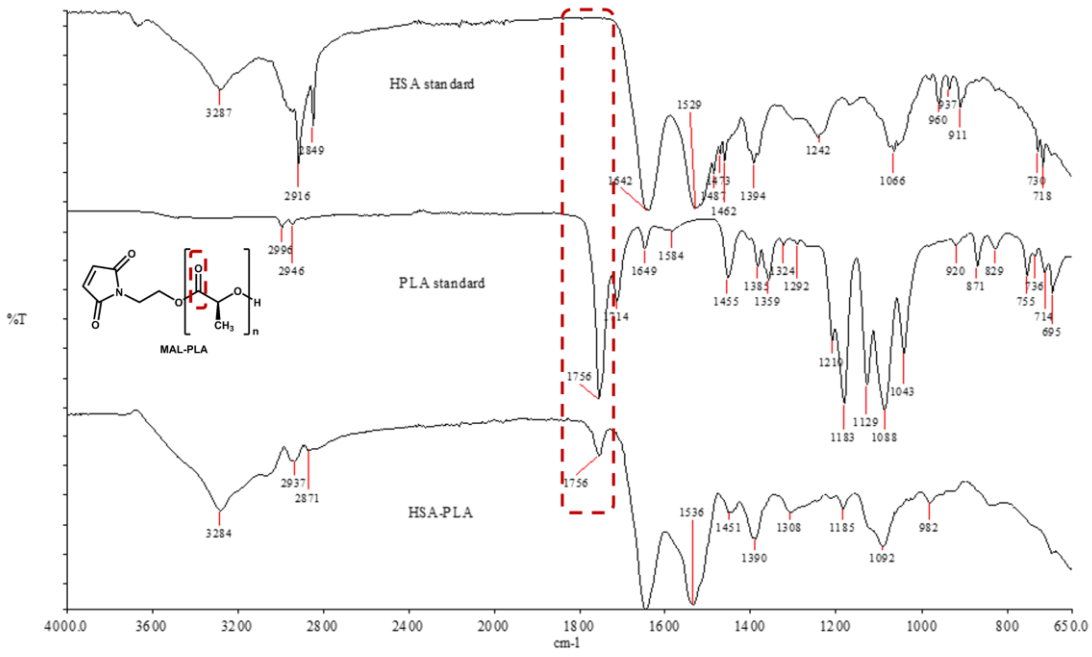

Fig 25. FT-IR spectra of HSA standard, MAL-PLA standard and HSA-PLA lyophilized powder. The polymer MAL-PLA has one characteristic absorption peak at 1756 cm^{-1} of ester carbonyl group (C = O), which is present in the HSA-PLA FT-IR spectrum and absent in the HSA standard spectrum.

Matrix-assisted laser desorption ionization time-of-flight

The MALDI-TOF mass spectrometer was used to measure the molecular weights of HSA standards and HSA-PLA conjugates. The mass spectra of the HSA standard and the HSA-PLA conjugate are shown in ***Fig 26***. Furthermore, the quantity of PLA molecules covalently bound with the HSA can be estimated according to the difference in the molecular weights between the HSA standards and the HSA-PLA conjugates.

The aldolase standard (A9096) was purchased from Sigma Aldrich and used as the internal calibrator in the measurement of the molecular weights of the HSA standards and the HSA-PLA conjugates. The obtained HSA molecular weight results (66479 ± 35 Da) align with the literature-recorded molecular weight of HSA (66.5 kDa), affirming the suitability of the MALDI-TOF method and instrument for subsequent HSA-PLA measurements.

The measured molecular weights of the HSA standards and the HSA-PLA conjugates were 66479 ± 35 Da and 67863 ± 282 Da, respectively ($p < 0.01$). With the average molecular weight of the MAL-PLA polymer (Sigma Aldrich, UK) approximately 2000 Da, we inferred that, on average, each HSA molecule had received one MAL-PLA molecule.

As a summary, it was hypothesized that the polymer MAL-PLA was linked with the Cys-34 residue of HSA. Despite the release of approximately 7 free sulfhydryl groups from each albumin molecule following the TCEP reduction, the presence

of steric hindrance effects implies that Cys-34 on the HSA surface is likely the only point of reactivity with the micron-sized dispersed MAL-PLA segments. As a result, from a theoretical standpoint, no significant alteration in the secondary structure of the HSA-PLA conjugates was anticipated when compared to the HSA standards.

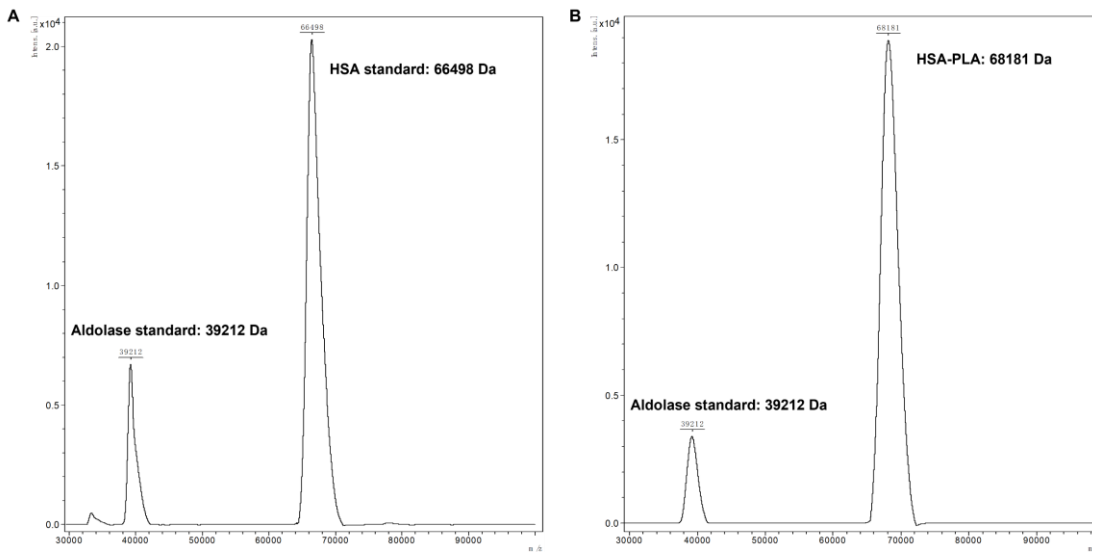

Fig 26. MALDI-TOF spectra. Aldolase (39212 Da) was used as internal calibrator. (A) Mass spectrum of HSA standard. (B) Mass spectrum of HSA-PLA conjugate. The molecule weights of the HSA standards and the HSA-PLA conjugate are 66479 ± 35 Da and 67863 ± 282 Da, respectively ($p < 0.01$).

Circular dichroism

To confirm our hypothesis on the synthesis, the circular dichroism technique was applied to evaluate the secondary structure of HSA standards, lyophilized HSA and lyophilized HSA-PLA. It must be acknowledged that the secondary/ tertiary structure of proteins may be influenced during the process of lyophilization [172]. HSA, a typical alpha-helical protein [173], has negative bands at 222 nm and 208 nm and a positive peak at 193 nm in the far-UV CD spectrum (***Fig 27***). In theory, the endogenous human serum albumin presents as a heart-shaped structure consisting of a single polypeptide chain with 68% α-helix and zero β-sheet [166]. According to the Sigma Aldrich product information [174], the α-helix and β-sheet content of the commercial HSA is 45% and 15%, respectively. Evidently, the secondary structural information of the HSA provided by Sigma Aldrich was not corresponding with the literature records of the endogenous HSA.

Consequently, the secondary structure of the HSA obtained from the Sigma Aldrich, UK was evaluated and tested to verify the reproducibility of their reported data. Moreover, an additional dissolving-freeze-drying cycle was conducted on the HSA standard obtained from the Sigma Aldrich to ascertain whether the lyophilization process could alter the protein's secondary structure. Based on the data listed in ***Table 4***, the lyophilization did significantly alter the secondary structural of the HSA [α-helix (%) decreased from 44.52 ± 0.62 to 16.90 ± 0.32, $p < 0.0001$; β-sheet (%) increased from 12.89 ± 0.12 to 27.06 ± 0.28, $p < 0.0001$].

It is noteworthy that the administration of denatured albumin through intravenous injection might trigger immune response-related side effects [175]. Notably the secondary structure data (α-helix and β-sheet) of HSA-PLA conjugates are not statistically different with the additionally lyophilized human serum albumin. This observation potentially indicates that the site of PLA conjugation to HSA is the Cys-34 residue of HSA.

In summary, findings from the Ellman's assay, FT-IR, MALDI-TOF, and CD studies collectively support the notion that the MAL-PLA has been selectively conjugated to the Cys-34 residue of HSA using this synthesis approach.

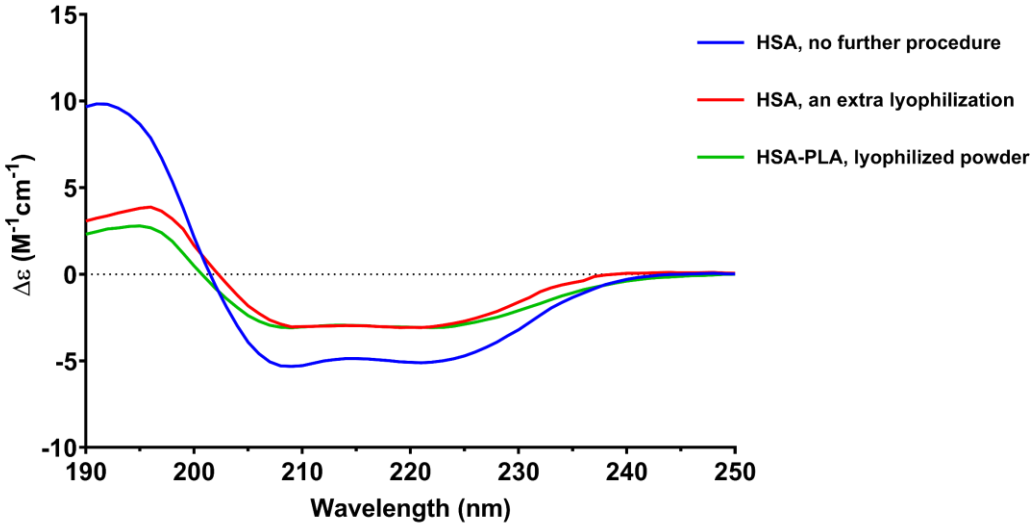

Fig 27. CD spectra of albumins. The secondary structure of human serum albumin (untreated and lyophilized) received from Sigma Aldrich, UK and the HSA-PLA conjugate. Lyophilization did significantly alter the secondary structural of HSA based on the spectra. The structure information obtained from the CD spectra of HSA-PLA was similar to that of lyophilized human serum albumin.

Table 4. Secondary structure information of albumins. Data are presented as mean ± SD, n = 3. ****, $p < 0.0001$. vs HSA standard.

	α-helix (%)	β-sheet (%)	Ref
Endogenous HSA	68	0	[173]
HSA (Sigma product sheet)	45	15	[174]
HSA standard	44.52 ± 0.62	12.89 ± 0.12	Data
Lyophilized HSA	16.90 ± 0.32****	27.06 ± 0.28****	Data
HSA-PLA	16.94 ± 0.32****	26.85 ± 0.15****	Data

2.4.3 Characterization of HSA-PLA nanoparticles

Here, a Malvern Nano-ZS instrument was used to determine the hydrodynamic diameters and zeta-potentials of HSA standards and HSA-PLA nanoparticles in distilled water at a concentration of 1 mg/mL. The morphology of the HSA-PLA nanoparticles was visualized by the TEM microscopy. Additionally, the pyrene fluorescence method was utilized to determine the critical micelle concentration of HSA-PLA conjugates, thereby confirming the polymeric micelle nature of the HSA-PLA nanoparticles.

Hydrodynamic diameter, polydispersity index and zeta-potential

Dynamic Light Scattering (DLS) is a robust technique employed for characterizing macromolecules and nanoparticles. By monitoring the random Brownian motion

of substances within a medium, it's possible to estimate the hydrodynamic diameters of these moving entities. In this context, the DLS technique was employed to differentiate between HSA proteins and HSA-PLA nanoparticles in an aqueous medium (distilled water), focusing on aspects like size distribution, polydispersity index (PDI), and zeta-potential. In ***Fig 28. A and B***, the size distribution graphs of the HSA standard and the HSA-PLA nanoparticles imply that HSA protein aggregates exhibited a multi-distribution pattern in water, while HSA-PLA nanoparticles showed a mono-distribution in water. As shown in ***Table 5***, the average hydrodynamic diameter of the HSA standards and the HSA-PLA nanoparticles was 14 ± 8 nm and 170 ± 7 nm, respectively, $p < 0.0001$. A higher PDI value of the HSA standard (0.57 ± 0.23 for HSA standards and 0.15 ± 0.05 for HSA-PLA nanoparticles) also indicates that the size distribution of the HSA proteins was significantly broader than that of the HSA-PLA nanoparticles, $p < 0.05$. In addition, the zeta-potential of the HSA-PLA nanoparticles was more negative than the zeta potential of the HSA standard, -26.3 ± 0.5 mV versus -12.6 ± 3.3 mV, $p < 0.01$ respectively.

Given that the polymer MAL-PLA was linked to the Cys-34 side chain of the HSA, and considering that HSA-PLA conjugates would self-assemble into polymeric micelles, it's noteworthy that an HSA consists of a single polypeptide chain containing 585 amino acids. Therefore, the amino acids surrounding Cys-34 would be enclosed within the hydrophobic core of the HSA-PLA nanoparticles.

Based on the structure of the HSA (***Fig 13***), this hydrophobic core should encompass PLA polymers and amino acids within domain I and part of domain II (***Fig 74***, page 263). According to this hypothesis, the number of positively charged amino acids was tabulated (see ***Table 13***, page 264), specifically arginine (Arg) and histidine (His), spanning the 1st to the 210th amino acid of the HSA (***Fig 14***). Notably, 35.9% of HSA's amino acids (the initial 210 out of 585) accounted for 45.8% of HSA's arginine (11 out of 24) and 43.8% of HSA's histidine (7 out of 16). In contrast, within the first 210 amino acids of the HSA, negatively charged amino acids—specifically aspartic acid and glutamic acid—constituted 38.9% and 36.1%, respectively, of the entire pool of HSA's aspartic acid and glutamic acid. Consequently, more positively charged amino acids were incorporated into the core of the HSA-PLA nanoparticles compared to the negatively charged ones. This resulted in the more negative zeta-potential of the HSA-PLA nanoparticles compared to the free HSA.

In conclusion, based on the differences in hydrodynamic diameter, PDI, and zeta-potential between the HSA standards and the HSA-PLA nanoparticles, it can be inferred that the successful conjugation of the polymer MAL-PLA to the Cys-34 of the HSA potentially facilitated the formation of mono-distributed albumin-based nanoparticles, namely, the HSA-PLA nanoparticles.

Table 5. Hydrodynamic diameter (D_H), polydispersity index (*PDI*) and zeta-potential of human serum albumin standard and HSA-PLA nanoparticles. Data are presented as mean ± SD (n = 3). *, $p < 0.05$. **, $p < 0.01$. ****, $p < 0.0001$. vs HSA standard.

Samples	D_H (nm)	*PDI*	Zeta potential (mV)
HSA standard	14 ± 8	0.57 ± 0.23	-12.6 ± 3.3
HSA-PLA NPs	170 ± 7****	0.15 ± 0.05*	-26.3 ± 0.5**

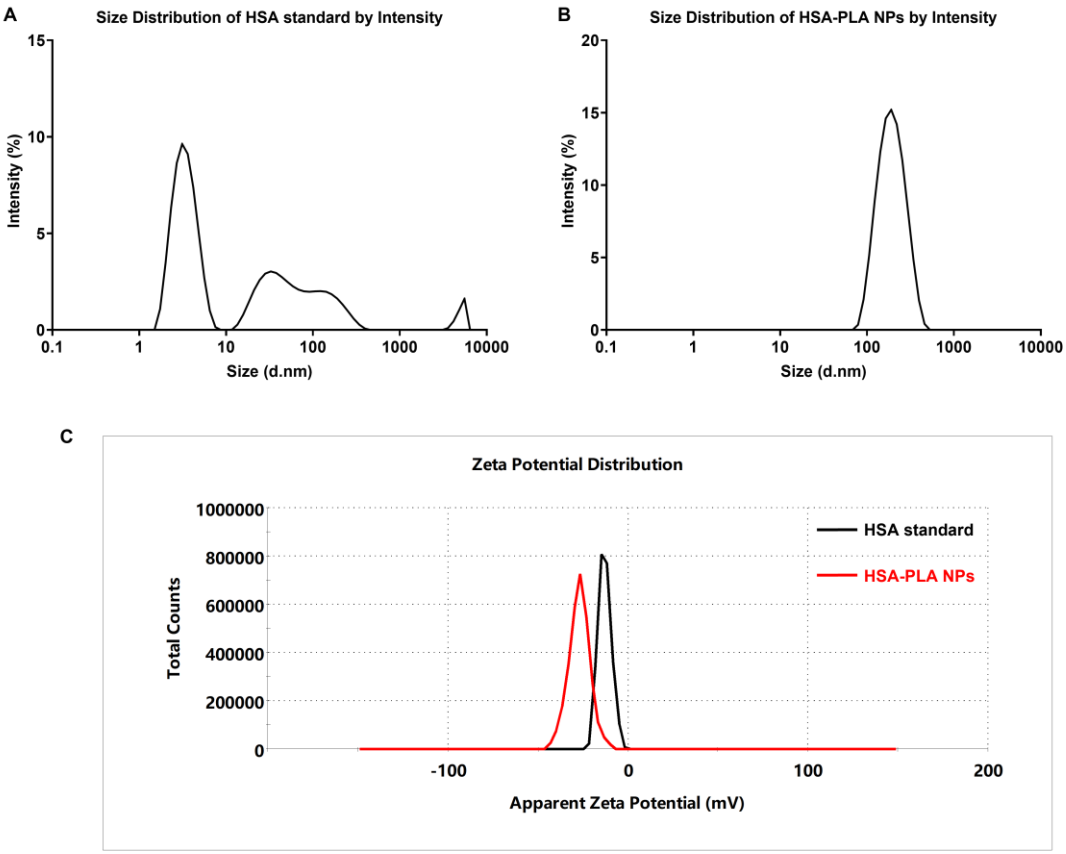

Fig 28. Characterization of HSA-PLA nanoparticles in the aspects of size distribution and zeta-potential. The hydrodynamic diameter distribution of **A**) HSA standard and **B**) HSA-PLA NPs and **C**) zeta potential distribution of HSA standard and HSA-PLA NPs were obtained through a Malvern Nano-ZS instrument. The size distribution of HSA molecules in water was multi-distributed. While after the conjugation of MAL-PLA to HSA, the size distribution of HSA-PLA nanoparticles was mono-distributed. HSA-PLA nanoparticles exhibited a larger size and more negative zeta potential when compared with HSA standard.

TEM images of HSA standard and HSA-PLA nanoparticles

The TEM image of the HSA standard (***Fig 29***) shows the small size of the free HSA and some large aggregates of the denatured HSA. It is corresponding with the above DLS results that the size distribution of the HSA in water was multi-distributed. In the TEM image of the HSA-PLA nanoparticles (***Fig 30***), the HSA-PLA nanoparticles are visualized in the form of a spherical appearance and some particle clusters. The morphology, distribution, and size of the HSA-PLA nanoparticles in their TEM images distinctly contrast with those of the HSA standard.

HSA standard

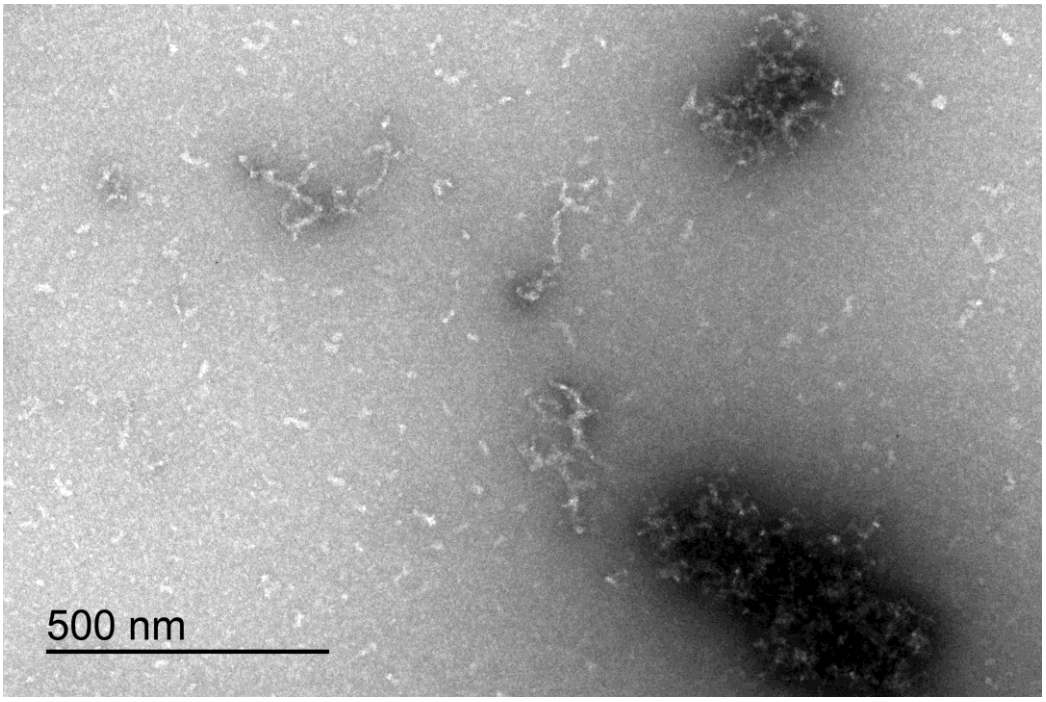

Fig 29. TEM image of human serum albumin molecules. The HSA proteins show a filamentous appearance and large aggregates in this TEM image.

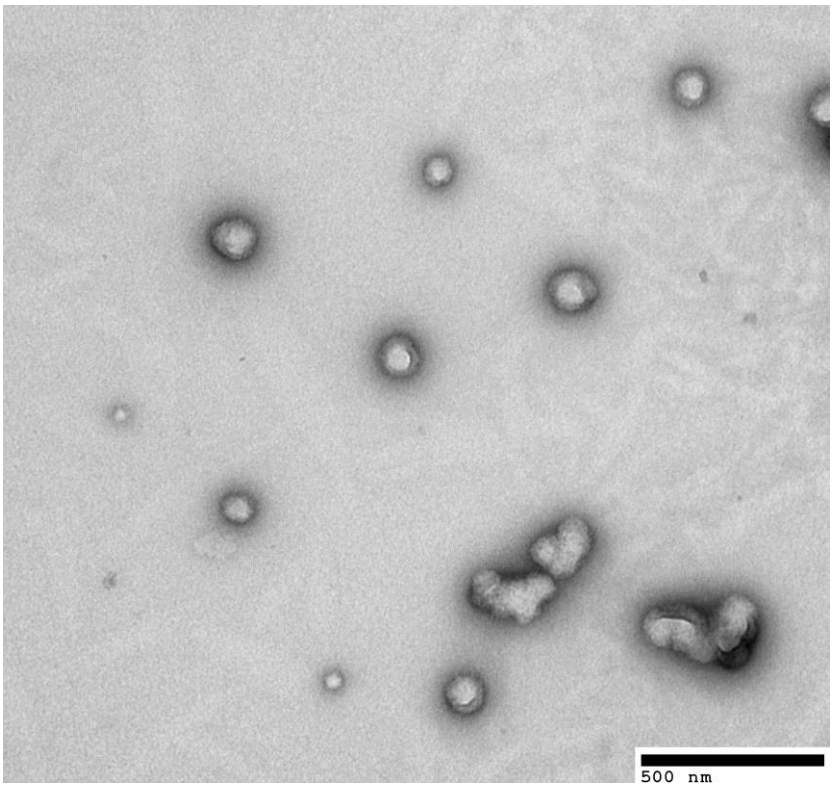

Fig 30. TEM image of HSA-PLA nanoparticles. Spherical nanoparticles and some particle clusters can be observed in this TEM image.

CMC determination of HSA-PLA nanoparticle

The critical micelle concentration (CMC) of the HSA-PLA blank nanoparticles was measured through the well-documented pyrene fluorescence method. In this approach, the fluorescence intensity ratio of the peak at 372 nm (I_{372}) to the peak at 384 nm (I_{384}) was calculated. The resulting values were then used to plot the curve of I_{372}/I_{384} against polymer concentrations through Boltzmann-Sigmoidal fitting (***Fig 31. a***). The CMC of the HSA-PLA polymeric micelles is 37.15 ± 3.31 mg/L, around 0.5 μM of the HSA-PLA conjugates. Normally, the CMC of a

surfactant such as sodium dodecyl sulphate is around 9 mM [176]. Therefore, in comparison to low molecular weight micelles, the polymeric micelles demonstrate significantly enhanced colloidal stability at these low concentrations (0.5 μM vs. 9 mM). In addition, the redshift of the peaks (I_{372} and I_{384}) observed with increasing polymer concentration (***Fig 31. b***) indicates the process of HSA-PLA polymeric micelle formation [177].

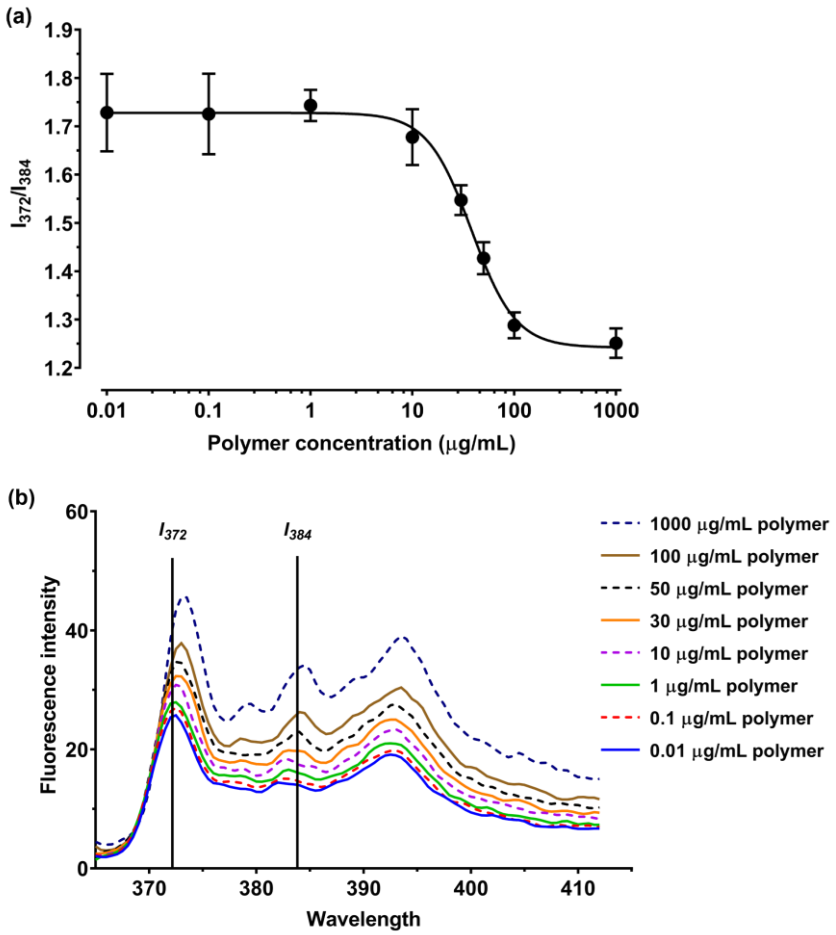

Fig 31. Critical micelle concentration measurements of HSA-PLA polymeric micelles. **(a)** A Sigmoidal-Boltzmann fitting curve of the fluorescence intensity ratio I_{372}/I_{384} versus the HSA-PLA polymer concentration. **(b)** Fluorescence emission spectra of the probe pyrene in HSA-PLA polymer aqueous solutions. The redshift of five emission peaks along with the increasing polymer concentration implied the incorporation process of pyrene in HSA-PLA polymeric micelles.

2.5 Conclusion

To sum up, a completely new synthetic method was designed for producing the self-assembling HSA-PLA conjugates. The decorated albumin has been created by the covalently binding of polylactides to the albumin Cys-34 residues (HSA-PLA). The Ellman's assay confirmed that the Cys-34 sulfhydryl group in commercial human serum albumins is not available for derivatization. Consequently, reduction of HSA is necessary to release free sulfhydryl groups for successful conjugation. The MALDI-TOF and FT-IR techniques were used to prove that polymer MAL-PLA had been successfully conjugated to the reduced HSA. The molecular weight of the HSA-PLA conjugates is 67863 ± 282 Da.

Through TEM, DLS, and CMC studies, it was established that the HSA-PLA nanoparticles exhibit spherical polymeric micelle morphology with nanoscale diameters. These nanoparticles displayed an exceptionally low critical micelle concentration of around 0.5 μM in distilled water. Notably, the hydrodynamic diameter of a single HSA-PLA nanoparticle (170 ± 7 nm) appeared larger than the actual particle size evident in the TEM images (50 nm - 100 nm). This disparity can be attributed to nanoparticle agglomeration in water, resulting in observable clusters in the TEM images.

To reduce the nanoparticle agglomeration, strategies such as pegylation of the HSA-PLA nanoparticles or decorating negatively charged molecules onto the

nanoparticle surface could be employed to decrease surface tension. The zeta-potential of the HSA-PLA nanoparticles is -26.3 ± 0.5 mV, which is significantly more negative than that of the HSA standard -12.6 ± 3.3 mV, $p < 0.01$. As the conjugation of the MAL-PLA to the side chain of Cys-34 facilitates the formation of shell-nucleus nanoparticles, a large amount of positively charged amino acids in the vicinity of the Cys-34 may be encapsulated within the inner core. Meanwhile, considering that 45.2% of HSA's phenylalanine and 38.9% of HSA's tyrosine are situated within the first 210 amino acids, the HSA-PLA nanoparticles might be suitable for encapsulating paclitaxel due to the abundance of aromatic functional groups within their core.

Chapter 3. Drug loading and characterization of the PTX-loaded HSA-PLA nanoparticles.

3.1 Introduction

This chapter involves the optimization of a drug loading method for HSA-PLA nanoparticles, coupled with various characteristic studies aimed at confirming the encapsulation of the drug paclitaxel (PTX) within the HSA-PLA nanoparticles. In addition, diverse colloidal stability tests have been carried out on the HSA-PLA (PTX) in this work. The reasons behind the heightened colloidal stability of the HSA-PLA (PTX) in comparison to Abraxane® were elucidated, drawing upon thermodynamics and the DLVO theory.

In this section, the drug PTX was encapsulated into the HSA-PLA blank nanoparticles with the aid of probe ultrasonication. The reverse phase high performance liquid chromatography (RP-HPLC) method was used to determine the drug loading efficiency and drug loading capacity associated with this drug loading method. X-ray powder diffraction technique was applied to validate the encapsulation of paclitaxel within the core of the HSA-PLA nanoparticles. Afterwards, DLS and TEM techniques were exploited to determine the size distribution and morphology of the PTX-loaded HSA-PLA nanoparticles. At last, the colloidal stability of the HSA-PLA (PTX) was evaluated through room

temperature storage assessments, evaluation of performance in biological media, and tests involving large volume dilutions.

3.1.1 Introduction: Paclitaxel (PTX)

Paclitaxel (PTX) is a broad-spectrum drug employed for the treatment of diverse cancers and it is the frequently used as a chemotherapeutic agent in the treatment of advanced breast cancer [178]. The chemical structure and chemical properties of PTX are shown in ***Fig 32***.

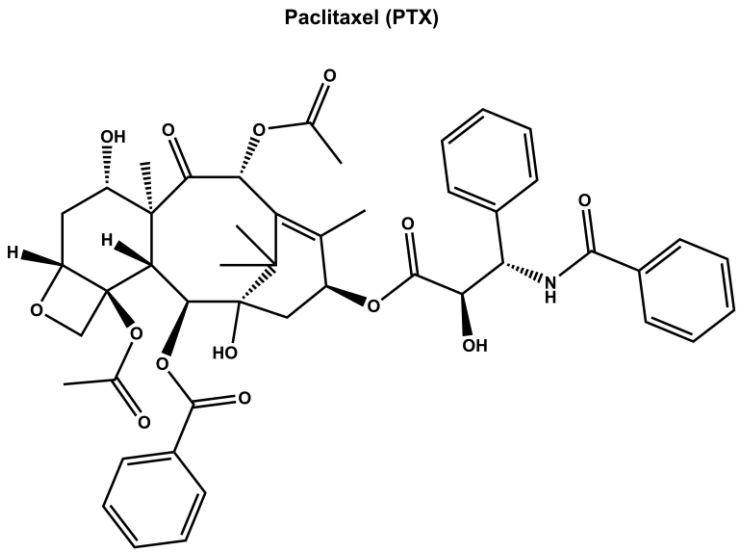

Fig 32. Chemical structure of paclitaxel. The molecular weight of PTX is 854 g/mol. Paclitaxel has a log P value of approximately 4. It is a hydrophobic small molecule, the water solubility of PTX is lower than 0.1 µg/mL.

Paclitaxel is used as an effective inhibitor of cell differentiation and proliferation in the clinic. Its mechanism of action involves binding to β-tubulin within cellular microtubules, thus stabilizing them and preventing their disassembly [179]. Microtubules are elongated, fibrillar, pipe-shaped protein polymers that play a

critical role in the cytoskeleton's structure and function. During the final phase of the cell cycle, paclitaxel's ability to stabilize microtubules leads to the cessation of cell division (mitosis) and prompts ongoing growth of the microtubules, ultimately triggering apoptosis. As the infinite proliferation is a hallmark of aggressive cancer cells, paclitaxel proves highly effective in inhibiting the growth of such cancer cells *in vitro*.

3.1.2 Introduction: Drug loading method

In this work, the drug paclitaxel was encapsulated into the blank HSA-PLA nanoparticles under the action of probe ultrasonication. As the HSA-PLA nanoparticles are protein-based nanoparticles, the use of organic solvents should be limited when designing drug loading methods. This makes many conventional drug loading techniques, such as the thin-film hydration method and dialysis method, unsuitable for the HSA-PLA nanoparticles [180].

More specifically, the PTX powder was dissolved in methanol at a concentration of 20 mg/mL. This methanolic solution of PTX was then added to an aqueous nanosuspension of HSA-PLA (at a concentration of 3.5 mg/mL) in a weight ratio of 10 mg nanoparticles to 2 mg PTX. The function of the methanol could be seen as a small surfactant or emulsifier to reduce the interfacial tension between the PTX particles and water when a small volume of the methanolic paclitaxel

solution was added to water, as illustrated in ***Fig 33***. This process initially forms unstable and temporary MeOH-PTX micellar systems. However, these simple micellar systems were highly unstable due to the substantial interfacial tension between the MeOH-PTX micelles and the water phase, driving them to aggregate and ultimately coagulate to minimize the high surface energy ***Fig 34***. As can be seen from the photographs in ***Fig 34***, what appears is not a paclitaxel precipitation, but a typical colloidal suspension appearance, with colloidal coagulation of the PTX micelles after 1 minute..

Therefore, the probe ultrasonicator was used to separate the aggregated MeOH-PTX micelles. Then these resulting nanoscale PTX particles could be encapsulated into the hydrophobic cores of the HSA-PLA blank nanoparticles to reduce their high surface intension in water. Thereby, PTX-loaded HSA-PLA nanoparticles were formed in water.

It is necessary to create the temporary and separated nanoscale PTX particles, otherwise PTX cannot be encapsulated in the HSA-PLA nanoparticles. This is due to the impossibility of loading micron-sized hydrophobic drug masses into a nanoscale carrier in a water medium. Notably, any residual methanol within the core of HSA-PLA nanoparticles can be eliminated during the freeze-drying of the HSA-PLA (PTX) nanosuspension.

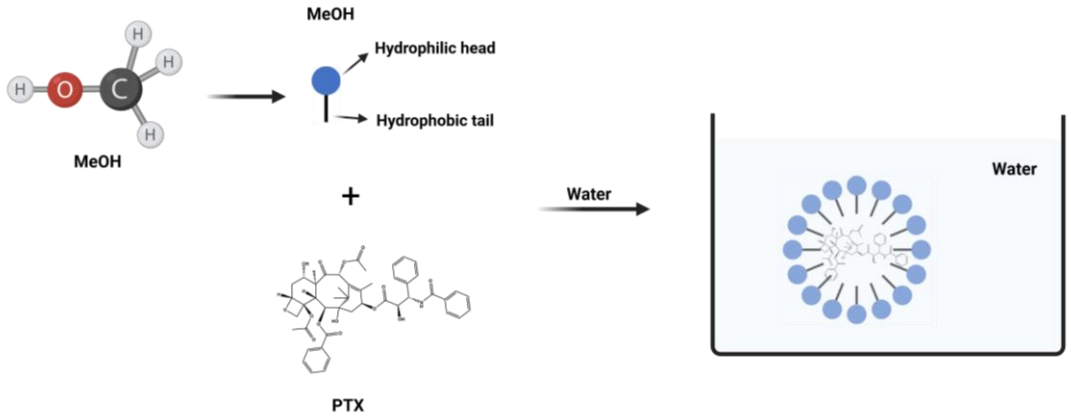

Fig 33. Schematic illustration for the formation of single MeOH-PTX micelle in water. The methyl group (CH_3) of MeOH can be seen as a hydrophobic tail and the hydroxy group (OH) can be considered as a hydrophilic group. Then methanol can be used as a surfactant or stabilizer to create a temporary MeOH-PTX micellar system in water. Created with BioRender.com.

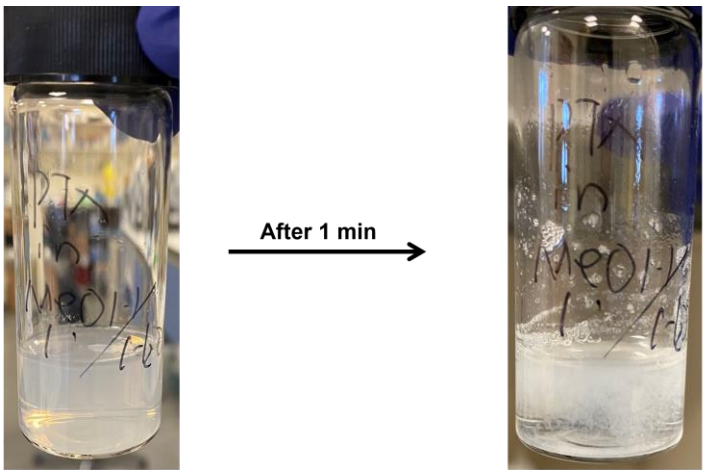

Fig 34. Appearance of MeOH-PTX micellar systems in water and the coagulation of MeOH-PTX micelles. Due to the high interfacial tension between the MeOH-PTX micelles and water phase, this MeOH-PTX micellar system was very unstable. Thus the MeOH-PTX micelles tended to aggregate into the clusters to decrease their contact areas with water. Therefore, in order to reduce the high interfacial tension, more and more MeOH-PTX micelles spontaneously aggregated to increase size and reduce surface free energy until coagulation.

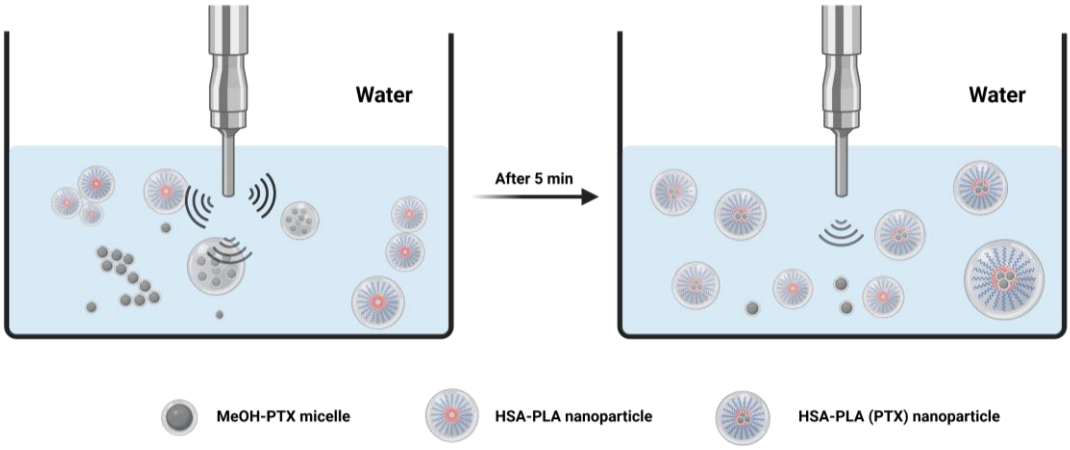

Fig 35. Schematic illustration for encapsulating paclitaxel in HSA-PLA nanoparticles through the probe ultrasonication. The aggregated MeOH-PTX micelles can be re-dispersed to the separated MeOH-PTX particles. Then nanoscale MeOH-PTX particles can be delivered into the hydrophobic cores of HSA-PLA nanoparticles during the probe sonication. Created with BioRender.com.

3.1.3 Introduction: RP-HPLC

High-performance liquid chromatography (HPLC) is a widely used analytical technique to analyze the known or unknown compounds qualitatively and quantitively [181]. The fundamental components of an HPLC system encompass a mobile phase, a pump, a sample injector, a stationary phase (referred to as an HPLC column), a detector, and a computer for data processing. Depending on the analysis's objective and the chemical characteristics of the analyte, the stationary phase can be either hydrophilic for normal phase HPLC or hydrophobic for reverse-phase HPLC. The selection of a suitable mobile phase is crucial, primarily for its role in dissolving the analytes, as it acts as the carrier for the

analytes throughout the HPLC system. Insoluble analytes can lead to clogging of downstream HPLC components due to deposition.

The choice between normal phase and reverse phase HPLC hinges on the analyte's chemical properties and the analysis's purpose. In the context of this study, the goal is to separate and quantify paclitaxel within a mixture. To achieve efficient separation of paclitaxel, reverse-phase high-performance liquid chromatography (RP-HPLC) was employed. Utilizing a hydrophobic column, such as a C18 column, facilitates the adsorption of paclitaxel from the mobile phase, effectively prolonging its elution time. This strategic approach results in the separation of paclitaxel from other impurities and minimizes potential negative impacts from impurities during quantitative analysis.

The workflow of the RP-HPLC is schematically shown in ***Fig 36***. Generally, the solvents constituting the mobile phase are pumped from solvent reservoirs through the sample injector, column, UV detector, and subsequently delivered to a waste container once the sample is eluted. The injected PTX sample is effectively dissolved within the flowing solvent comprising the mobile phase. The duration of PTX elution from the column was contingent upon its interaction with the stationary and mobile phases. To elaborate, when the column material is hydrophilic and PTX is hydrophobic in nature, a lack of interaction between PTX and the column material leads to swift elution, rendering such conditions unsuitable for accurate PTX analysis. Consequently, a hydrophobic column was

deliberately chosen to extend the retention time of PTX. This was achieved through the hydrophobic interaction between PTX and the column matrix, effectively slowing the movement of PTX molecules in relation to the flow rate of the mobile phase. The retention of PTX can also be prolonged by using a longer column, reducing the flow rate of mobile phase or increasing the polarity of mobile phase. Once a completely separated chromatographic peak of PTX was obtained, then the concentration of PTX could be determined according to a predetermined PTX calibration curve. As the peak area of PTX is proportional to the PTX concentration. This analytical approach enables accurate quantification of PTX content in the sample under investigation.

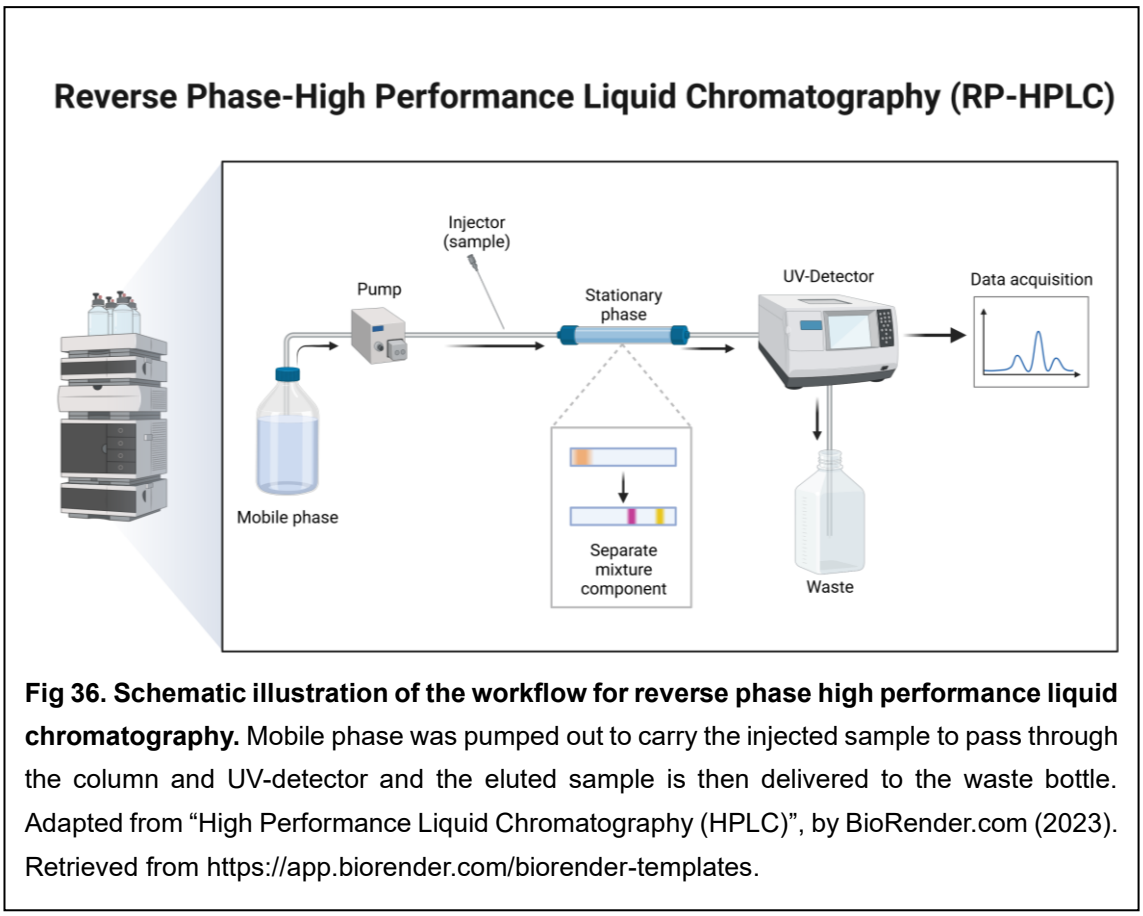

Fig 36. Schematic illustration of the workflow for reverse phase high performance liquid chromatography. Mobile phase was pumped out to carry the injected sample to pass through the column and UV-detector and the eluted sample is then delivered to the waste bottle. Adapted from "High Performance Liquid Chromatography (HPLC)", by BioRender.com (2023). Retrieved from https://app.biorender.com/biorender-templates.

3.1.4 Introduction: XRD

The X-ray Powder Diffraction (XRD) technique is based on the collection of diffracted X-rays at pre-determined angles to determine the crystallographic structure of solid materials. In crystalline solids, molecules or atoms are systematically arranged within, yielding a uniform internal structure. Consequently, when crystalline solids are exposed to X-rays, their internal molecules or atoms can absorb the X-ray energy and reemit it symmetrically, as shown in ***Fig 37***. Contrarily, when the amorphous solids receive the X-rays, due to the random arrangement of internal molecules, the X-rays are scattered over a wide area (***Fig 38***), while the detector can receive a low intensity of X-rays.

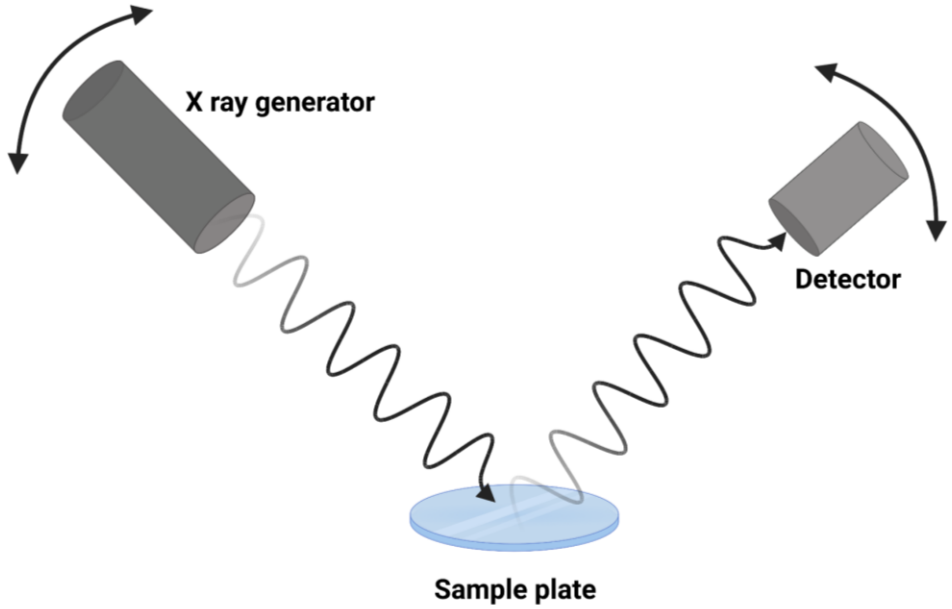

Fig 37. Schematic illustration of the X-ray powder diffraction of crystalline solid. The uniformly arranged atoms absorb the X-rays and release them in the symmetrical direction with high intensity. Created with BioRender.com.

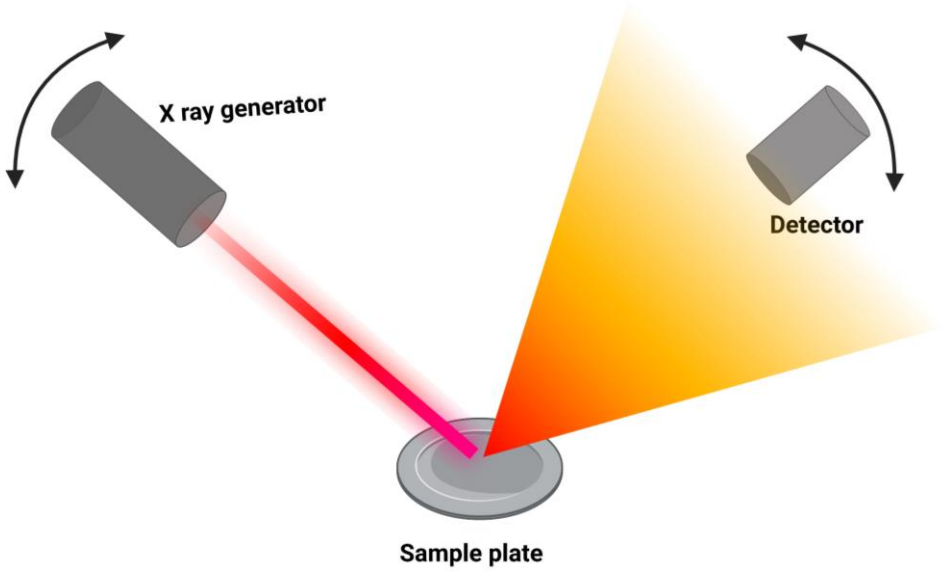

Fig 38. Schematic illustration of the X-ray powder diffraction of amorphous solid. Due to the molecular arrangement of amorphous solid is random, X-rays are thus scattered in a broad range. Therefore, detector can only receive low intensity X-rays and signals can be detected in the broad angles. Created with BioRender.com.

3.2 Materials

Table 6. Materials used in the synthesis and characterization of HSA-PLA nanoparticle.

Supplier	Materials
Merck UK	Human serum
	Phosphotungstic acid hydrate for microscopy
	Syringe-driven filter units (0.45μm)
Generon UK	Paclitaxel (PTX)
Thermo Fisher Scientific UK	Acetonitrile (ACN, ⩾99.9%, HPLC Gradient grade)
	Phosphate Buffered Saline PBS pH7.4
	PTFE hydrophobic syringe filters, 0.22 μm
	Trifluoroacetic acid (TFA, 99%)
University College London Hospital	Taxol®
	Abraxane®
ELGA PURELAB®	Distilled water

All chemicals, reagents, and solvents were used in their as-purchased state, without undergoing any purification processes.

3.3 Experimental methods

3.3.1 Preparation of paclitaxel-loaded nanoparticles

HSA-PLA nanoparticle lyophilized powder (100 mg) was dispersed in 35 mL distilled water. To this dispersion, 1 mL of methanol (MeOH) containing 20 mg of paclitaxel was added drop by drop. Probe sonication (Soniprep 150plus, MSE, UK) was exploited to encapsulate PTX into the HSA-PLA nanoparticles. The process involved 2 cycles, where each cycle consisted of 5 minutes of sonication (5 amplitudes) followed by 3 minutes of rest, all performed in an ice bath. After sonication, the resulting colloidal liquid containing paclitaxel-loaded nanoparticles was filtered using a 0.45 μm syringe filter for purification. Multiple formulations of the HSA-PLA (PTX) were prepared in triplicate using different batches of the HSA-PLA blank nanoparticles. The most effective probe sonication method for drug loading was also determined.

Subsequently, the filtrate was frozen at -20°C. The frozen drug loaded nanoparticles must be lyophilized (ALPHA 1-4 LDplus, Martin Christ, Germany) in a cold environment (at 0°C). The residual MeOH was removed in the vacuum environment during the lyophilization. The lyophilized powder of the PTX-loaded NPs was stored in glass vials at room temperature for the further analysis and stability tests.

3.3.2 Drug encapsulation efficiency and drug loading capacity

The drug encapsulation efficiency (DEE%) and drug loading capacity (DLC%) were calculated by the following equations:

$$\boldsymbol{DEE}\% = \frac{Weight\ of\ PTX\ in\ nanoparticles}{Weight\ of\ PTX\ added} \qquad \boldsymbol{DLC}\% = \frac{Weight\ of\ PTX\ in\ nanoparticles}{Weight\ of\ polymer\ and\ PTX}$$

The lyophilized powder (2 mg) of the HSA-PLA (PTX) nanoparticle was dissolved in 5 mL of a 60% (v/v) acetonitrile aqueous solution. The resulting mixture was subjected to 2 minutes of vortex mixing and bath sonication. Afterward, the mixture was filtered using a 0.2 μm PTFE filter.

The PTX concentration in the filtrate was quantified using a high-performance liquid chromatography (HPLC) system (Agilent Technologies 1200 series, USA) equipped with a reversed-phase column (XBridge Shield RP 18, 250 × 4.60 mm, 3.5 μm). The mobile phase consisted of 40% water and 60% acetonitrile. The flow rate was set at 0.8 mL/min, and the analytes were detected at a wavelength of 227 nm. A volume of 10 μL of the drug sample was injected onto the HPLC column. The calibration curve for PTX concentration was determined as y = 25377x, with a correlation coefficient of 1.0. Using this calibration curve, the concentration of PTX in the sample could be quantified, which is essential for calculating the drug encapsulation efficiency and drug loading capacity of the nanoparticles.

3.3.3 X-ray powder diffraction, XRD

The X-ray powder diffraction (XRD) was used to detect the crystalline state and amorphous state of PTX to check whether the paclitaxel was encapsulated into nanoparticles or not. Briefly, HSA-PLA blank nanoparticle powder, PTX-loaded nanoparticle powder, PTX standard powder, PTX + HSA-PLA NPs powder mixtures and Abraxane® powder were finely ground and placed on the sample holders, respectively. Samples were scanned by an X-ray diffractometer (MiniFlex 600, Rigaku®, Germany). The specific parameters: angle 2θ scanned from 3° to 60°, step size = 0.02°, rate of scan = 10 degree/min, X-rays (λ = 1.5418 Å) generated by a CuKα tube at 40 kV and 15 mA.

3.3.4 Dynamic light scattering, DLS

The hydrodynamic diameters, zeta potentials and polydispersity index of Taxol®, blank nanoparticles and PTX-loaded nanoparticles were determined using the dynamic light scattering (DLS) technique with a Malvern Nano-ZS instrument. A quantity of 2 mg from each lyophilized sample was dispersed in 2 mL of distilled water, while the Taxol® solution was diluted with distilled water to achieve a PTX concentration of 1 mg/mL. Each sample was measured in triplicate, and three distinct batches of samples were examined.

3.3.5 Transmission electron microscopy, TEM

In short, a droplet of 5 mg/mL HSA-PLA nanosuspension, HSA-PLA (PTX), and Abraxane® nanoparticle suspensions were placed onto separate TEM grids. After 5 minutes, any excess water on the TEM grids was removed with tissue paper. Next, a droplet of 1% (w/v) neutral phosphotungstic acid solution was added to each TEM grid. After 1 minute of staining, the grids were washed with distilled water to remove excess staining agent. The prepared TEM samples were stored in a dark location until imaging.

3.3.6 Colloidal stability

Storage stability

The lyophilized powder of HSA-PLA (PTX) nanoparticles was stored at room temperature. The storage stability parameters (DLC%, D_H, zeta potential and *PDI*) of the samples were tested on day 1, 7, 15, 30 and 60, respectively.

Colloidal stability in aqueous media

The colloidal stabilities of the HSA-PLA (PTX) nanoparticles in phosphate buffered saline and human blood serum (diluted with PBS to a concentration of 20% v/v) were monitored for 7 days at 37°C. Changes in the hydrodynamic diameter of the HSA-PLA (PTX) nanoparticles were recorded.

Colloidal stability at low concentration

The parameters of hydrodynamic diameters and width of size distribution (PDI) of PTX loaded nanoparticles at different concentrations in phosphate buffered saline (0.001, 0.01, 0.05, 0.1, 0.3, 0.5, 1, 5, and 10 mg/mL) were measured to evaluate the colloidal stability of the Abraxane® and the HSA-PLA (PTX) nanoparticles at low concentrations.

3.3.7 Statistics

Data are presented as the means ± SD (standard deviation). The student's t-test, one-way ANOVA and two-way ANOVA were used for the relative statistical analysis in Prism software. A $p < 0.05$ value represents the significant difference between the two data sets.

3.4 Results and discussion

3.4.1 Optimization of the drug loading method

As outlined in the previous discussion in this chapter (section 3.1.2), many common drug loading methods could not be used in this work. As HSA-PLA conjugates are albumin-based polymers, the presence of high concentrations of organic solvents could potentially disrupt the hydrophobic interactions between amino acid side chains and alter the protein's primary structure. Consequently, methods like the thin film hydration method or dialysis method, which involve organic solvents, are unsuitable for loading drugs onto protein nanoparticles.

Therefore, we have developed an ultrasonication-based drug loading method for the HSA-PLA blank nanoparticles, as described in section 3.1.2. The fundamental of this method is to create the unstable and temporary micellar system, MeOH-PTX micelles. Subsequently, probe ultrasonication was employed to disperse the aggregated MeOH-PTX micelles. Consequently, the resultant nanoscale PTX systems were encapsulated into the hydrophobic cores of the HSA-PLA blank nanoparticles. Otherwise, paclitaxel cannot be encapsulated in the HSA-PLA polymeric micelles without the presence of MeOH in practise. Self-assembling nanoscale systems, such as HSA-PLA nanoparticles, are unable to encapsulate microscale paclitaxel solids, due to their size incompatibility. Thus, a preliminary

step in formulating a temporary nanoscale paclitaxel system was deemed indispensable. Methanol and ethanol are good candidates to be selected as the stabilizer for PTX in water. However, in practise, it was found that the temporary PTX micellar systems created by ethanol were more stable than those of methanol. This enhanced stability can be attributed to ethanol's higher hydrophobic nature. When the ethanol was removed during the freeze drying, the HSA-PLA (PTX) systems were broken up as well. This problem is absent in the MeOH-based drug loading method. Thus, methanol is selected as the stabilizer in our drug loading method.

The second variable factor in this drug loading method is the duration of probe sonication. Thus, the drug content (% w/w) of the HSA-PLA (PTX) nanoparticles produced at different probe sonication times was selected as a criterion for assessing the drug loading method, as shown in ***Fig 39***. Notably, at 5 and 60 minutes of probe sonication, the drug loading capacity (%) of the HSA-PLA nanoparticles was considerably lower than that at 10 minutes. Thus, a probe ultrasound processing time of 10 minutes emerged as the most suitable for this drug loading method. Based on the concentration of the PTX measured by the HPLC, the drug loading efficiency and drug loading capacity of this drug loading method for the HSA-PLA nanoparticles were calculated.

Drug loading efficiency % = 91.2 ± 1.6 %

Drug loading capacity % = 15.2 ± 0.3 %

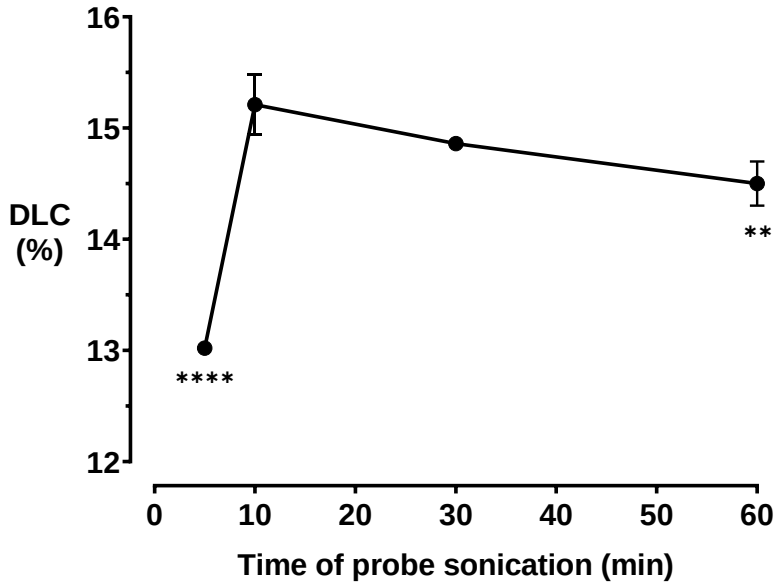

Fig 39. Relationship between the drug loading capacity (DLC%) of HSA-PLA nanoparticles and different times of probe sonication. Data are presented as means ± SD, n = 3. **, $p < 0.01$. ****, $p < 0.0001$ vs. DLC% of 10 min probe sonication.

3.4.2 X-ray powder diffraction, XRD

The X-ray Powder Diffraction is an analytical technique used to determine the crystallographic structure of solid materials. In this study, the XRD technique was used to determine the crystallographic structure of paclitaxel in the HSA-PLA (PTX) nanoparticles. According to the obtained XRD patterns (***Fig 40***), the drug loaded albumin nanoparticles [HSA-PLA (PTX) and Abraxane®] and albumin blank nanoparticles (HSA-PLA) are all amorphous solids. Contrarily, paclitaxel powder exhibited its crystalline nature with three characteristic peaks at 5.6°, 8.9° and 12.5°. Meanwhile, if PTX was not encapsulated in the HSA-PLA

nanoparticles, characteristic signals of the PTX should be detected, as seen in the XRD data of PTX + HSA-PLA mixtures.

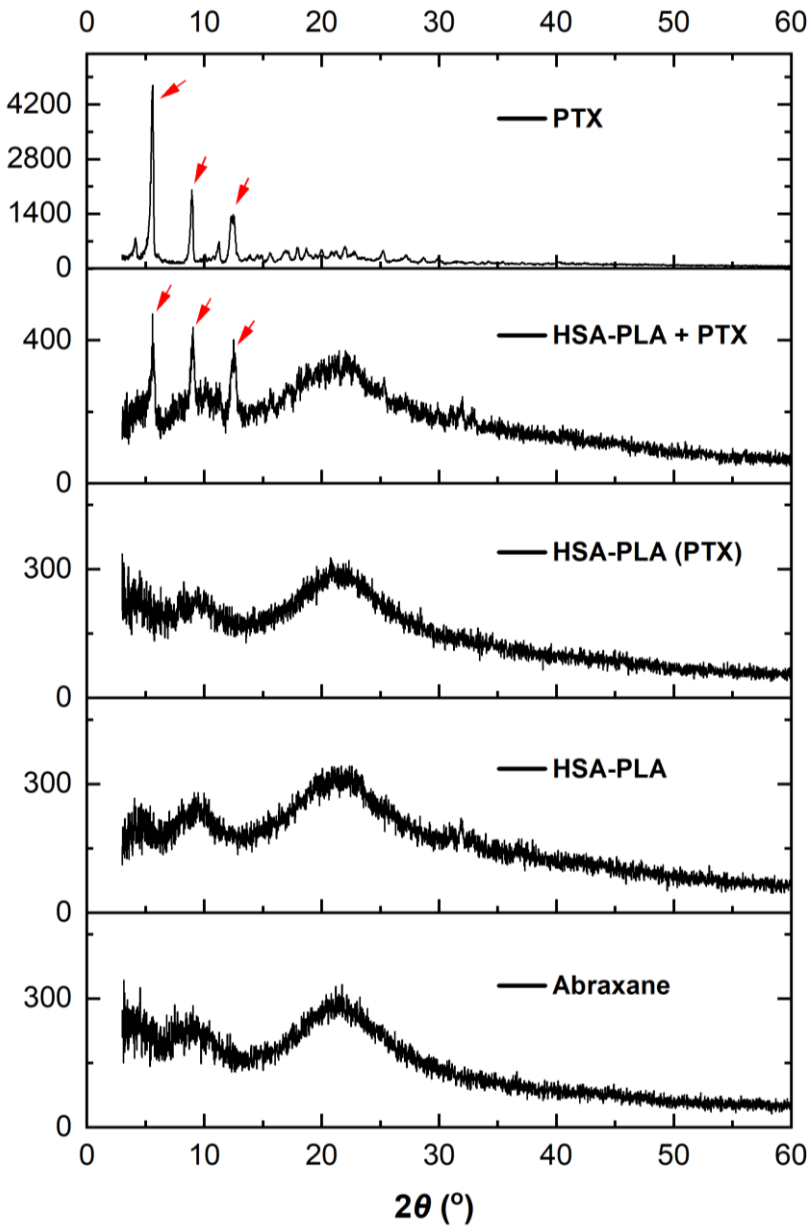

Fig 40. XRD patterns of samples. From top to bottom, the XRD patterns represent these samples in order of PTX standard, PTX+HSA-PLA nanoparticle mixture (1:9 w/w), PTX loaded HSA-PLA nanoparticles, HSA-PLA blank nanoparticles and Abraxane® nanoparticles. Red arrows indicate the characteristic peaks of the crystalline paclitaxel.

3.4.3 Characterization of PTX-loaded HSA-PLA nanoparticles

By using the RP-HPLC, the PTX drug contents of the HSA-PLA (PTX) nanoparticles were determined to be 15.2 ± 0.3 % w/w. Meanwhile, the signals corresponding to crystalline paclitaxel were not detected in the XRD pattern of the HSA-PLA (PTX), indicating successful encapsulation of PTX within the nanoparticles. This drug loading approach proved effective. To provide additional evidence for the PTX encapsulation, the HSA-PLA (PTX) nanoparticles were subjected to characterization in terms of their visual appearance, DLS parameters in water, and morphologies observed in TEM images. These analyses collectively affirm that the HSA-PLA (PTX) nanoparticles indeed represent a nanoformulation of PTX.

Appearance of nanosuspensions (Tyndall scattering)

The HSA-PLA and HSA-PLA (PTX) nanoparticle aqueous dispersions showed a milky white appearance, distinguishing them from a simple albumin solution in water, as shown in (***Fig 41. A***). To differentiate between an aqueous solution of solutes and a colloidal suspension, a straightforward Tyndall scattering test was employed [182]. The path of the red-light beam (***Fig 41. B***) is visible when the red laser passing through the colloidal suspensions of Abraxane®, HSA-PLA (PTX) and HSA-PLA nanoparticles, because of the light scattering induced by the suspended particles. In contrast, the optical path is invisible in water and HSA

water solution. Therefore, it is confirm that the HSA-PLA (PTX) nanoparticles were dispersed in distilled water in the same way as Abraxane®.

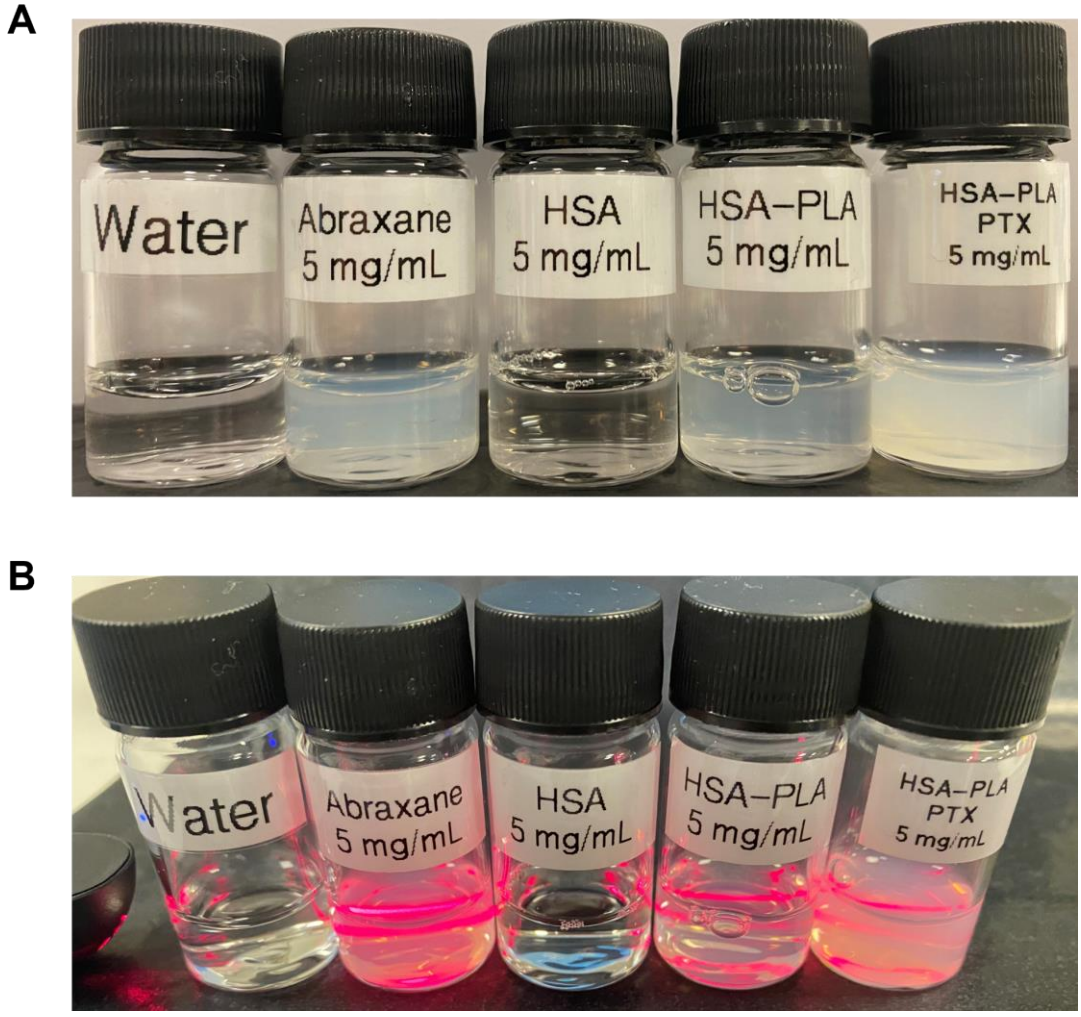

Fig 41. Photographs of the distilled water, albumin water solution and albumin nanosuspensions. (A) Appearances of the Abraxane®, HSA-PLA and HSA-PLA (PTX) nanosuspensions were milky, off-white liquid while water and an HSA solution in water were both colourless liquids. Photograph **(B)** showed the Tyndall effect within the colloidal suspensions, path of red laser was visible in Abraxane®, HSA-PLA and HSA-PLA (PTX) colloidal suspensions and invisible in water and HSA solution when the red laser passed through these aqueous media.

Dynamic light scattering, DLS parameters

The hydrodynamic diameters of these suspended particles were determined by the technique of dynamic light scattering (DLS). The DLS results of each nanosuspension are listed in ***Table 7***. The average hydrodynamic diameters of HSA-PLA, HSA-PLA (PTX) and Abraxane® nanoparticles in distilled water are 170 ± 7 nm, 174 ± 7 nm and 157 ± 2 nm, respectively. Their size distribution graphs and low *PDI* values presented in ***Fig 43. B&C*** provided clear indications of monodispersed nanoparticles. The principle of DLS technique has been comprehensively introduced in ***Chapter 2*** section 2.1.5. By recording the random Brownian motion of nanoparticles in the medium, the DLS instrument could estimate the size of the moving entities. It's worth noting that due to variations in ionic strengths, nanoparticle agglomeration, and media viscosity, the recorded hydrodynamic diameters for the same sample in different media displayed differences, as observed in ***Table 7***. This discrepancy in D_H readings for the same sample in both distilled water and phosphate-buffered saline could be attributed to these factors.

The zeta-potentials of different nanoparticles in distilled water (***Fig 43. D***) were measured as well. The average zeta potentials of Abraxane®, HSA-PLA and HSA-PLA (PTX) nanoparticles in pH = 7 aqueous media are -13.43 ± 3.73, -26.29 ± 0.52 and -34.38 ± 1.01 mV, respectively. The zeta-potentials of the HSA-PLA and the HSA-PLA (PTX) nanoparticles are significantly more negative than the

Abraxane® nanoparticles ($p < 0.01$). In accordance with several literature sources [183–186], an absolute zeta potential value above 20 mV (either less than -20 mV or more than +20 mV) is considered acceptable for colloidal suspensions. However, the absolute zeta potential value for Abraxane® nanoparticles falls below 20 mV, which contributes to the explanation of their instability at low concentrations.

According to the DLVO (**D**erjaguin–**L**andau–**V**erwey–**O**verbeek) electrostatic theory (***Fig 42***), the nanoparticles in a stable colloidal system should have a strong electrostatic repulsion to counteract the Van der Waals attractive force, thus avoiding aggregation and sedimentation of the nanoparticles [184]. In practice, the absolute zeta potential value of nanoparticles serves as a representation of the strength of electrostatic repulsive forces among them. A higher absolute zeta potential value signifies more potent electrostatic repulsion. Consequently, the colloidal stability and agglomeration tendencies of nanoparticles can be evaluated and understood based on their zeta potential values [183,187].

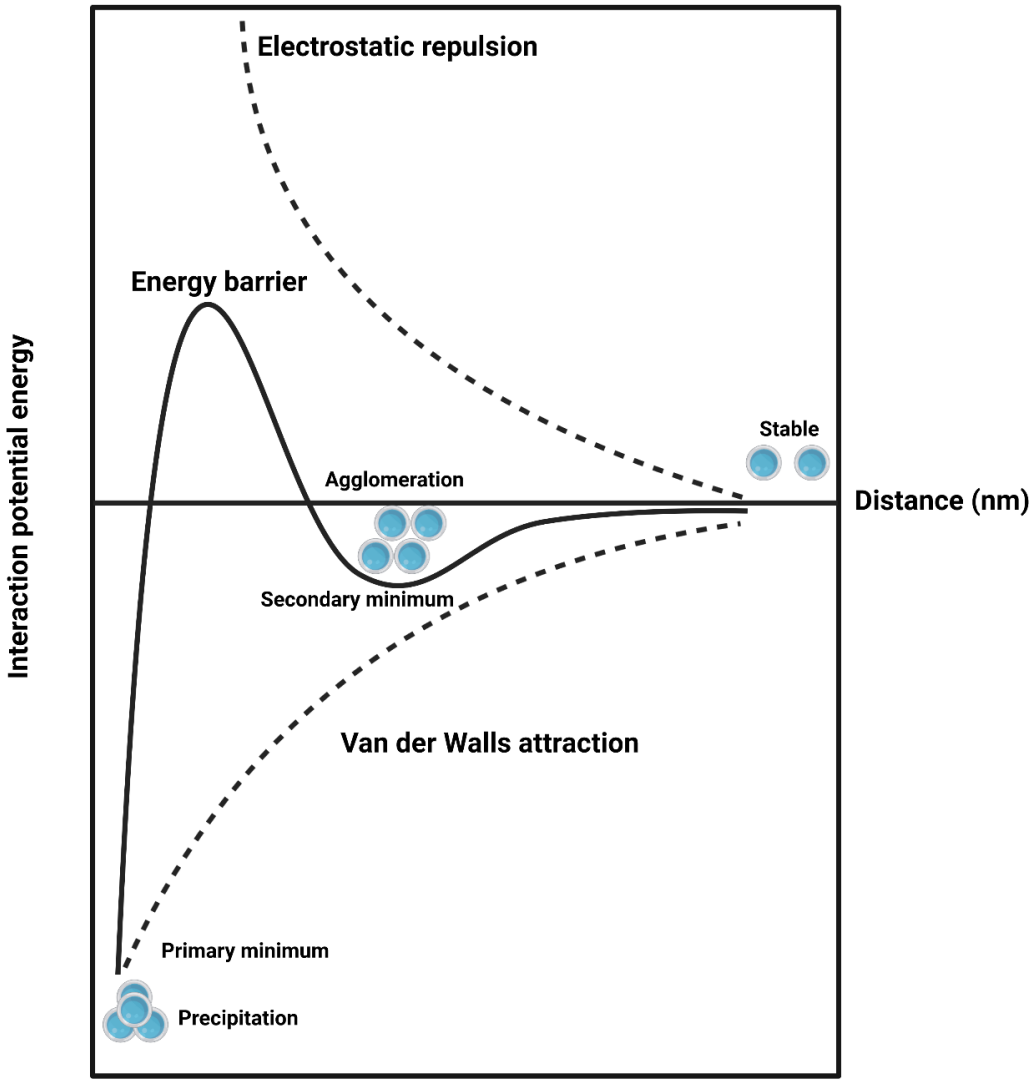

Fig 42. The DLVO theory. This is a graph of the sum of potential energies based on the intermolecular forces between different particles at different distances. The electrostatic double layers of particles provide the electrostatic repulsions between particles, while the surface of particles can also create the attractive forces between particles – van der Waals interactions. The attractive forces drive the aggregation of dispersed particles if the electrostatic repulsions between particles are not strong in the colloidal system. Created with BioRender.com.

Table 7. DLS results, D_H, *PDI* and zeta potential, of various nanoparticles in distilled water and saline media. Data are presented as mean ± SD (n = 3). *, $p < 0.05$. **, $p < 0.01$. ***, $p < 0.001$. ****, $p < 0.0001$. vs Abraxane®.

Media	Samples	D_H (nm)	*PDI*	Zeta potential (mV)
In distilled water	HSA-PLA	170 ± 7	0.15 ± 0.05	-26.29 ± 0.52**
	HSA-PLA (PTX)	174 ± 7	0.07 ± 0.01	-34.38 ± 1.01****
	Taxol®	12 ± 3	0.12 ± 0.01	N/A
	Abraxane®	157 ± 2	0.09 ± 0.01	-13.43 ± 3.73
In PBS saline	HSA-PLA	133 ± 2	0.18 ± 0.01	N/A
	HSA-PLA (PTX)	145 ± 6	0.06 ± 0.01	N/A
	Taxol®	11 ± 4	0.17 ± 0.01	N/A
	Abraxane®	125 ± 4	0.05 ± 0.01	N/A

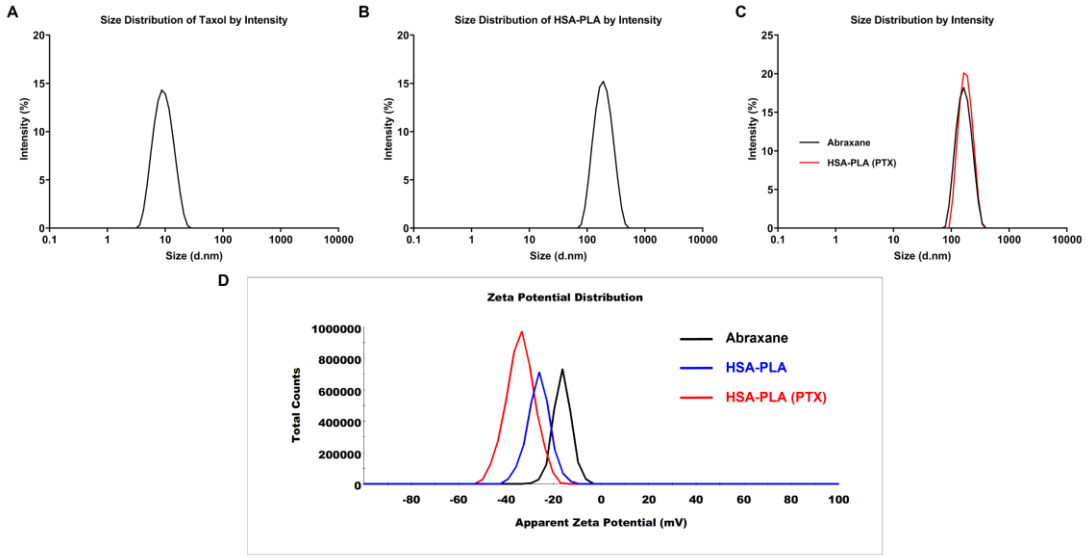

Fig 43. DLS results of each nanosuspension. Hydrodynamic diameter distributions of **A**) Taxol®, **B**) HSA-PLA blank nanoparticles, **C**) Abraxane® and HSA-PLA (PTX) in distilled water. The zeta potential distributions of Abraxane® nanoparticles, HSA-PLA blank nanoparticles and HSA-PLA (PTX) nanoparticles in distilled water were presented in graph (**D**).

Transmission electron microscopy images

The morphologies of Abraxane® nanoparticles, HSA-PLA nanoparticles and HSA-PLA (PTX) nanoparticles were visualized by the TEM technique, as shown in ***Fig 44***, ***Fig 46***. All these nanoparticles exhibited a spherical shape based on the TEM images. Notably, it's intriguing to observe that the morphology of the Abraxane® nanoparticles in our TEM images is totally different with the current view on the morphology of the Abraxane® (spherical particles with a diameter of around 130 nm). The TEM images of the Abraxane® nanoparticles (as shown in ***Fig 44. a, b & c***) revealed heavy agglomeration, forming irregularly shaped clusters with an approximate diameter of 130 nm. Other publications, such as [188,189], also presented cryo-EM images of Abraxane®, showing irregularly shaped shadows (***Fig 45***) that corresponded closely to the irregular clusters of tiny particles in our TEM images. In reality, our high-resolution TEM images unveiled that the actual Abraxane® nanoparticles comprised numerous tiny spherical particles with an approximate average diameter of 40 nm. In contrast, the HSA-PLA blank nanoparticles and the HSA-PLA (PTX) nanoparticles exhibited spherical shapes with an average diameter of approximately 100 nm.

A proposed explanation for the agglomeration behaviour of Abraxane® nanoparticles centred around the considerations of thermodynamics and the DLVO theory in this study. From the aspect of thermodynamics [190], the lowest free energy of a system is the favourable state to keep the colloidal system in a

stable state. Consequently, the agglomeration of unstable nanoparticles becomes a spontaneous process, reducing their surface free energy and minimizing the overall free energy of the colloidal system, in accordance with the second law of thermodynamics and the Gibbs free energy graph, as shown in ***Fig 47***. Therefore, the spatial distributions of nanoparticles presented in the HSA-PLA and the HSA-PLA (PTX) TEM images (***Fig 46***) are less agglomerated than the Abraxane® nanoparticles due to their lower surface-to-volume ratios and the lower surface energy of each nanoparticle.

Moreover, considering the DLVO theory as discussed earlier, the zeta potential values played a role. The zeta potential of Abraxane® nanoparticles (-13.43 ± 3.73 mV) indicated weaker electrostatic repulsion between them compared to the zeta potentials of HSA-PLA nanoparticles and HSA-PLA (PTX) nanoparticles (-26.29 ± 0.52 and -34.38 ± 1.01 mV, respectively). This contributed to the greater agglomeration of Abraxane® nanoparticles in water, as evidenced by the TEM and cryo-EM images.

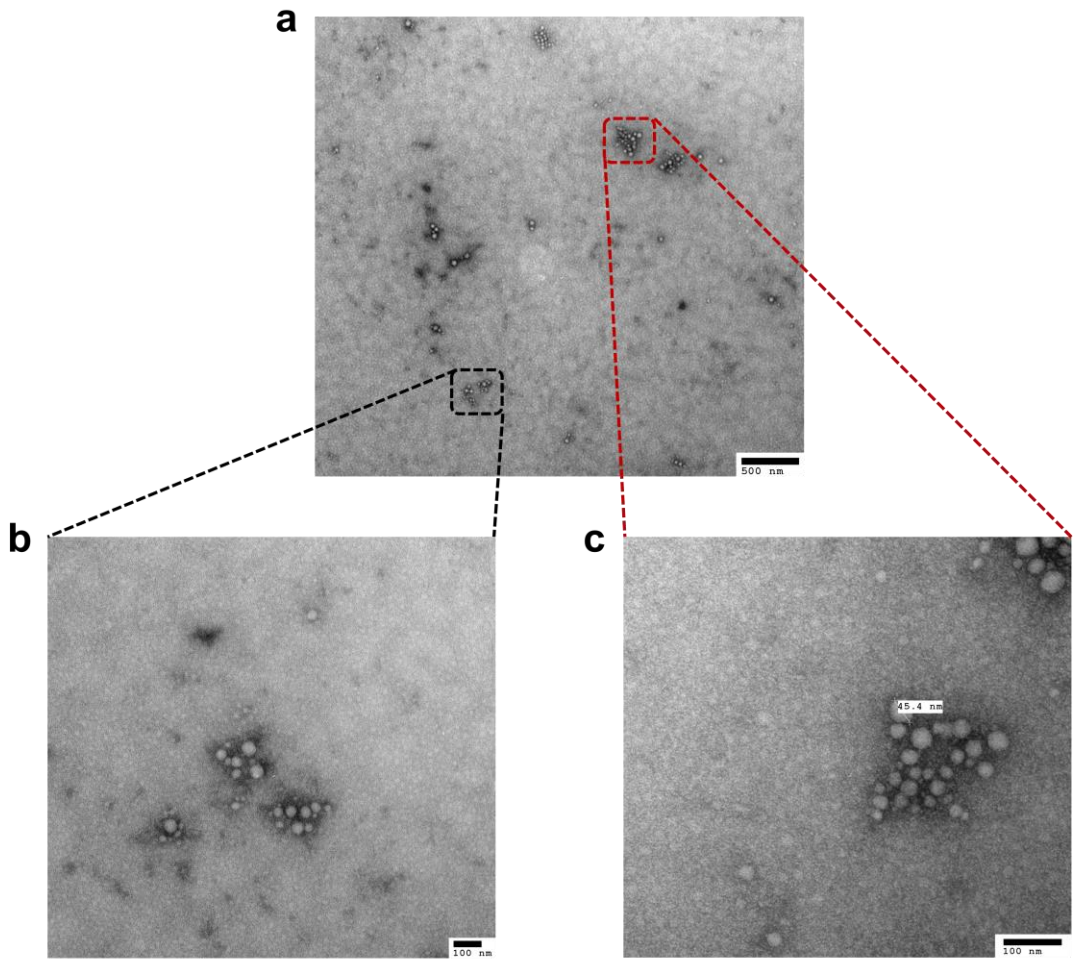

Fig 44. Transmission Electron microscopy images of Abraxane® nanoparticles. TEM images **(a, b & c)** of Abraxane® nanoparticles at different magnifications. The actual Abraxane® nanoparticles are constituted with many tiny spherical particles with a diameter around 40 nm, which is different from the conceptual form of the Abraxane® nanoparticle (a spherical particle of around 130 nm in diameter). In addition, the Abraxane® tiny particles agglomerate into several irregularly shaped clusters, which are highly corresponding with the irregularly shaped shadows in the Abraxane's cryo-EM images, see **Fig 45**.

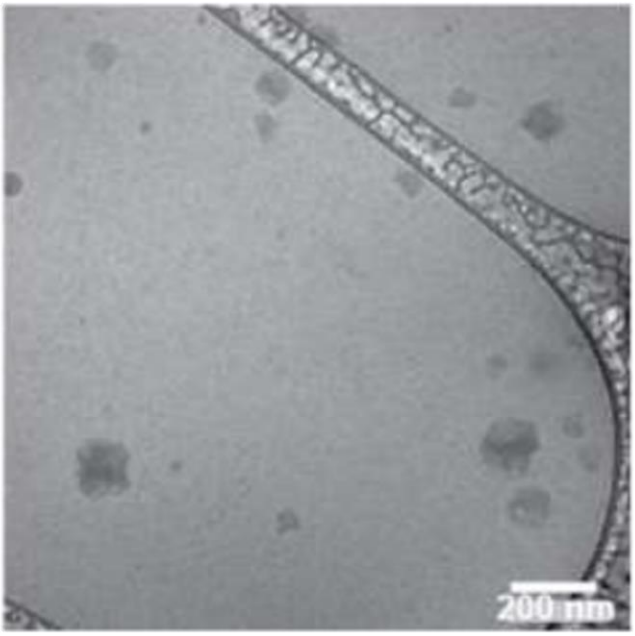

Fig 45. Cryogenic electron microscopy (Cryo-EM) image of Abraxane® nanoparticles. The cryo-EM image of Abraxane® was reproduced with permission from Springer Nature, Bhattacharyya, J.J. Bellucci, I. Weitzhandler, J.R. McDaniel, I. Spasojevic, X. Li, C.-C. Lin, J.-T.A. Chi, A. Chilkoti, A paclitaxel-loaded recombinant polypeptide nanoparticle outperforms Abraxane in multiple murine cancer models, Nat Commun. 6 (2015) 7939.

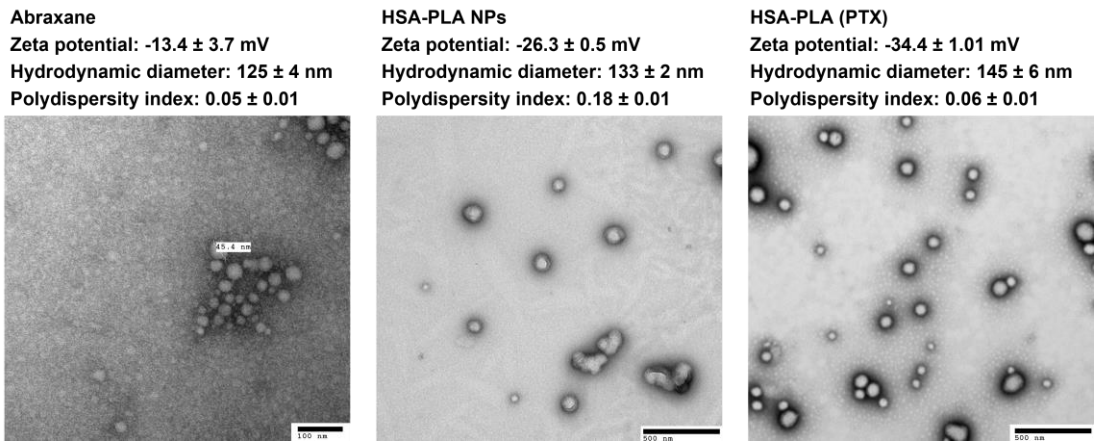

Fig 46. The comparison of the Abraxane® nanoparticles, HSA-PLA nanoparticles and HSA-PLA (PTX) nanoparticles in terms of morphology, D_H, *PDI* and zeta-potential. The agglomeration of Abraxane® nanoparticles indicate that the Abraxane® nanoparticles need to reduce surface free energy by more aggregation in comparison of HSA-PLA (PTX) nanoparticles. Moreover, the more negative zeta-potential of PTX-loaded HSA-PLA nanoparticles (-34 mV) should confer a higher colloidal stability compared with Abraxane (-13mV).

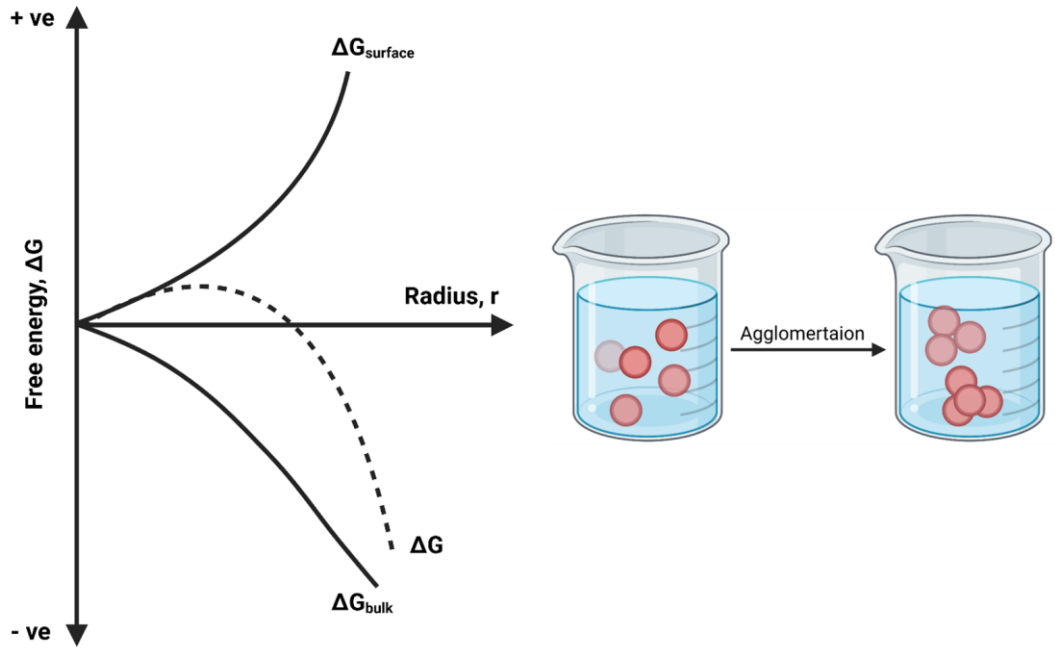

Fig 47. Schematic illustration of the relationship between Gibbs free energy of entity and its size. The Gibbs free energy change (ΔG) is equal to the sum of the surface free energy change ($\Delta G_{surface}$) and the bulk free energy change ((ΔG_{bulk}). The dashed curve of ΔG refers to the Gibbs free energy change as a function of the particle radius. According to the aspects of thermodynamics, the formation of nanoparticles is to decrease the Gibbs free energy of the bulk materials in the media. Meanwhile, the positive surface free energy is introduced during the formation of nanoparticles. The lower free energy of the resulting colloidal system indicates a higher colloidal stability. Therefore, the morphology of the most nanoparticle is spherical, due to the fact that spheres have the smallest surface area compared to other shapes of the same volume. The agglomeration of nanoparticles is a spontaneous process to increase the particle size and decrease the relative interface area between the media and nanoparticles for reducing the free surface energy to achieve the favourable state for the colloidal system. Created with BioRender.com.

3.4.4 Colloidal stability

Here, a series of systematic colloidal stability tests were carried out to evaluate the HSA-PLA (PTX) nanoparticles. These tests included a two-month storage stability test, a 7-day stability test of HSA-PLA (PTX) nanoparticles in various physiological media, and a lateral comparison of the hydrodynamic diameter changes between Abraxane® and HSA-PLA (PTX) at low concentrations in phosphate-buffered saline.

Storage stability of the HSA-PLA (PTX)

The storage stability of the HSA-PLA (PTX) nanoparticle lyophilized powder was evaluated at room temperature for two months without the addition of any excipients or surfactants. Relevant storage stability indicators, including the hydrodynamic diameters and the zeta potentials of the HSA-PLA (PTX) nanoparticles in distilled water, the PDI (size distribution) of the HSA-PLA (PTX) nanoparticles in distilled water, and the drug contents (% w/w) of PTX-loaded HSA-PLA nanoparticles were tested and listed in ***Table 8***. Upon subjecting these results to one-way ANOVA statistical analysis, it was found that there were no significant alterations observed in these indicators over the two-month storage period. As a result, it can be concluded that the HSA-PLA (PTX) powder remained stable during the two-month storage duration.

Table 8. Storage stability indicators for the HSA-PLA (PTX) nanoparticle powder during a two-month storage period at room temperature. Data are presented as mean ± SD, n = 3.

Indicators		D_H (nm)	*PDI*	Zeta-potential (mV)	DLC% (w/w)
HSA-PLA (PTX)	Day 1	167 ± 5	0.08 ± 0.01	-32.5 ± 2.0	15.2 ± 0.6
	Day 7	170 ± 4	0.08 ± 0.02	-32.9 ± 1.1	14.8 ± 0.2
	Day 15	167 ± 4	0.10 ± 0.01	-31.4 ± 1.2	15.6 ± 0.6
	Day 30	164 ± 4	0.11 ± 0.01	-33.9 ± 0.7	14.8 ± 0.2
	Day 60	171 ± 1	0.09 ± 0.01	-32.7 ± 1.3	15.3 ± 0.3

The lyophilized powder of HSA-PLA (PTX) nanoparticles was stored at room temperature without the addition of any excipients or surfactants. When compared with the parameters on Day 1, there was not any significant alteration of these indicators over a two-month storage period after the one-way ANOVA statistical analysis.

Colloidal stability of HSA-PLA (PTX) in aqueous media

The lyophilized powder of the HSA-PLA (PTX) nanoparticles was dispersed in phosphate buffered saline (PBS, pH = 7.4), as well as in a PBS solution containing human blood serum (20% v/v). Subsequently, the mixture was stored in a 37°C water bath for a duration of 7 days. Over this period, the hydrodynamic diameters and the PDI of the HSA-PLA (PTX) nanosuspensions were continuously monitored for 7 days and recorded as a graph illustrating the relationship between hydrodynamic diameter/PDI and time.

During the 7-day storage period, there were no significant alterations observed in the hydrodynamic diameter and the PDI of the HSA-PLA (PTX) nanoparticles in

both aqueous media, as shown in ***Fig 48. A***.

Colloidal stability at low concentrations

The colloidal stability of the Abraxane® nanoparticles and the HSA-PLA (PTX) nanoparticles at low concentrations was also evaluated. Based on the previous discussion, the heavy agglomeration of the Abraxane® nanoparticles in the TEM images and the weak zeta-potentials of the Abraxane® nanoparticles indicate that the potential instability of the Abraxane® nanoparticles at low concentrations. Therefore, the hydrodynamic diameter alternations of the Abraxane® nanoparticles and the HSA-PLA (PTX) nanoparticles after different dilutions were recorded, as shown in ***Fig 48. B***. The hydrodynamic diameter of the Abraxane® nanoparticles is approximately 130 nm in water at a concentration of 1 mg/mL. But, according to the above TEM and cryo-EM images of the Abraxane® nanoparticles, the 130 nm-Abraxane® nanoparticles were composed of many tiny particles with a diameter of around 40 nm. As presented in the ***Fig 48. B***, clusters of the Abraxane® nanoparticles began to rapidly dissociate into smaller nanoparticles approximately from 130 nm to 20 nm at a concentration of 0.3 mg/mL in water, and further details can be found in reference [191]. Then, at a concentration of 0.1 mg/mL Abraxane® nanoparticle in water, the unstable small Abraxane® nanoparticles (approx. 40 nm in diameter) disintegrated into several albumin molecules with a hydrodynamic diameter of 20 nm, which was corresponding with the hydrodynamic diameter of the HSA standard, see ***Table***

5. In comparison to the Abraxane®, the HSA-PLA (PTX) nanoparticles are still stable at a concentration of 0.01 mg/mL.

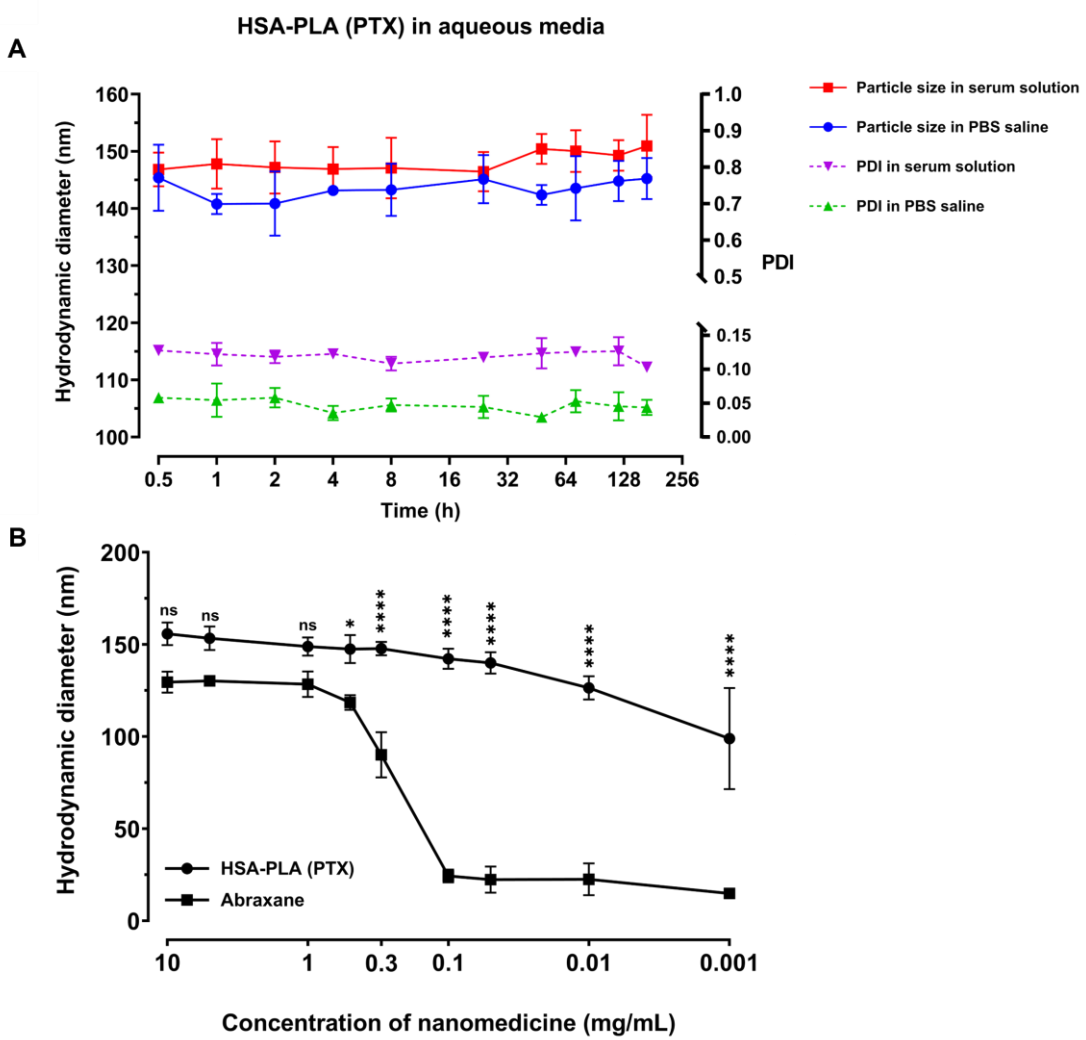

Fig 48. Colloidal stability tests of the HSA-PLA (PTX) nanoparticles in aqueous media. The changes of hydrodynamic diameters and polydispersity indices of the HSA-PLA (PTX) nanosuspensions in a 37 °C water bath were monitored for 7 days and recorded as the graph of the hydrodynamic diameter/PDI versus time **(A)**. Hydrodynamic diameters of the Abraxane® and HSA-PLA (PTX) nanoparticles at different concentrations **(B)**. Abraxane® nanoparticles were unstable at the concentration of 0.3 mg/mL while the HSA-PLA (PTX) nanoparticles were even stable at a concentration of 0.01 mg/mL. After the two-way ANOVA statistical analysis, the hydrodynamic diameters of the HSA-PLA (PTX) nanoparticles were significantly different with the hydrodynamic diameters of the Abraxane® nanoparticles at low concentrations. *, $p < 0.05$. ****, $p < 0.0001$. vs Abraxane® at corresponding concentrations, ns = not significant.

3.5 Conclusion

Overall, a drug loading method was developed for the encapsulation of the PTX into the HSA-PLA polymeric micelles, resulting in the fabrication of a novel paclitaxel nanoparticle formulation, HSA-PLA (PTX) nanoparticles. The drug content of the PTX in the HSA-PLA (PTX) nanoparticles and the Abraxane® nanoparticles is approximately 15% w/w and 10% w/w, respectively. The hydrodynamic diameter of the HSA-PLA (PTX) nanoparticles in phosphate buffered saline is around 145 nm.

Based on the theories of the thermodynamics and the DLVO, combined with the data of the TEM images and zeta-potential of the Abraxane® and the HSA-PLA (PTX) nanoparticles, it is possible to explain why the stability of the Abraxane® nanoparticles is significantly lower than that of the HSA-PLA (PTX) nanoparticles at low concentrations. Additionally, the high colloidal stability of the HSA-PLA (PTX) nanoparticles has been proved in terms of the storage of lyophilized powders and nanosuspension in biological media at 37^{o}C.

In this section, a novel paclitaxel nano-formulation was created with a higher cargo and a greater colloidal stability when compared to those of the Abraxane®.

Chapter 4. *In vitro* and *In vivo* evaluations of PTX-loaded HSA-PLA nanoparticles

4.1 Introduction

As previously mentioned, breast cancer holds the highest incidence among cancers, with triple-negative breast cancer standing out as its most aggressive subtype. Furthermore, metastatic triple negative breast cancer (mTNBC) patients have the lowest five-year survival rate of all advanced breast cancers based on several clinical investigations, see ***Chapter 1*** section 1.4 Breast cancer. Currently, systematic chemotherapy remains the major treatment option for the mTNBC patients.

During 1960-1981 [192], a collaborative programme initiated by the National Cancer Institute (NCI) and the United States Department of Agriculture (USDA) conducted a plant screening project. The aim was to gather and evaluate extracts from 15,000 plants, resulting in a collection of 115,000 extracts. The purpose of this project was to identify potential natural compounds possessing anti-cancer activity.

In 1967, scientists isolated and confirmed an active ingredient with anti-cancer activity from the bark extract of the *Taxus brevifolia* and named this substance as

taxol, also known as paclitaxel (PTX). Later, in 1971, the chemical structure of PTX was published for the first time [193]. Schiff et al. proposed a mechanism for PTX-induced cell apoptosis in 1979 based on their *in vitro* study [194]. By promoting and stabilizing the assembly of cellular tubulins, the growth and formation of cellular microtubules are accelerated in the presence of PTX. The stabilizing function provided by paclitaxel (PTX) prevents the disassembly of microtubules required for cell division, leading to a halt in the cell cycle at the mitotic step. Meanwhile, the polymerization of tubulins cannot be stopped by cells, which triggers the cell apoptosis. As the rapid proliferation is one major feature of aggressive cancer cells, PTX can thereby largely inhibit the growth of most cancer cells *in vitro*.

Therefore, scientists decided to formulate PTX for the treatment of various cancers. Taxol® is the first-generation formulation of PTX injection [135], this micellar formulation of PTX is prepared by dissolving PTX in a mixture of nonionic surfactant polyoxyethylated castor oil and absolute ethanol. In 1992, the FDA approved Taxol® for the treatment of advanced ovarian cancer, and later it was also approved to treat numerous cancers including metastatic breast cancer [136]. It is notable that Taxol® became the best-selling anti-cancer drug at the time, with the annual sales of $1.6 billion in 2000 [70].

However, due to the acute toxicity induced in patients by Cremophor oil, patients need to be pre-treated with histamine H1/2 blockers and corticosteroids to reduce

hypersensitivity reaction before the infusion of Taxol® [137]. Consequently, the acute systemic toxicity induced by Taxol® restricts the maximum tolerated dose of PTX and limits therapeutic outcomes for patients. As a result, Taxol® has been gradually replaced by the Abraxane® as the first-line treatment of advanced cancers.

Abraxane® is the second-generation of formulation of PTX injection as well as the latest version currently on the market. This albumin-paclitaxel nanoparticle formulation is a renowned cancer nanomedicine used in treating advanced breast cancer, non-small cell lung cancer, and pancreatic cancer [132].

In clinical practice, both Taxol® and Abraxane® can be used to treat metastatic breast cancer patients. In ***Chapter 2*** and ***Chapter 3***, we have thoroughly elucidated why the colloidal stability of the HSA-PLA (PTX) is significantly higher than that of the Abraxane® at low concentrations in aqueous media. In our hypothesis, a higher colloidal stability of a nanomedicine in physiological fluids may enhance the effectiveness of chemotherapy for cancer patients.

To validate this hypothesis, the performance of the HSA-PLA (PTX) nanoparticles was evaluated in animal models. Firstly, the murine triple negative breast cancer cell line – 4T1 was selected to observe cellular uptake of the HSA-PLA nanoparticles in the 4T1 cells and ascertain the mechanism of uptake. Subsequently, pharmacokinetics profiles of the HSA-PLA (PTX) nanoparticles, the Taxol® and the Abraxane® were investigated and compared in rats. The *in*

vivo behaviors of the HSA-PLA (PTX) nanoparticles, the Taxol® and the Abraxane® were studied in terms of biodistribution and tumoricidal activity in 4T1 tumour-bearing mice (tumours were implanted in the right flanks of BALB/c mice). Based on the results of these *in vivo* studies, the HSA-PLA (PTX) nanoparticles exhibited improved pharmacokinetics profiles and superior tumoricidal effects in the 4T1 tumour-bearing mice when compared to the Abraxane®. The enhancement of colloidal stability in albumin-based nanomedicine correlates with heightened PTX delivery effectiveness.

4.1.1 Introduction – Confocal Laser Scanning Microscope

Confocal laser scanning microscopy (CLSM) is a powerful tool for visualizing cellular structures, organelles, and the localization of nanoparticles within cells through appropriate fluorescent staining. As the previous discussion of light in ***Chapter 2***, it can be regarded as propagating electromagnetic waves, with light or photons bearing energy. When atoms absorb energy from photons, they transition to an excited state. After excitation, these excited atoms may return to the ground state and emit the light at longer wavelengths (lower energy). This principle is applicable to fluorescent dyes, where fluorophores within fluorescent dye molecules can be excited by visible light. Following excitation, these fluorescent dyes emit visible light at longer wavelengths (lower energy).

Based on this excitation-emission principle, fluorescent microscopy was designed to observe samples labelled with fluorescent dyes. The technique involves capturing emitted light from these fluorophores. In order to achieve the higher resolution fluorescent images of cells, confocal microscopy was designed to increase the signal-to-noise ratios of images through a number of subtle designs, such as employing a pinhole to suppress out-of-focus fluorescence signals, see ***Fig 49***. With ongoing advancements and enhancements in confocal microscope technology, it has become possible to obtain three-dimensional perspectives of cells. Consequently, confocal laser scanning microscopy was employed in our in vitro studies, specifically for investigating cellular uptake and intracellular tracking of nanoparticles within 4T1 cells.

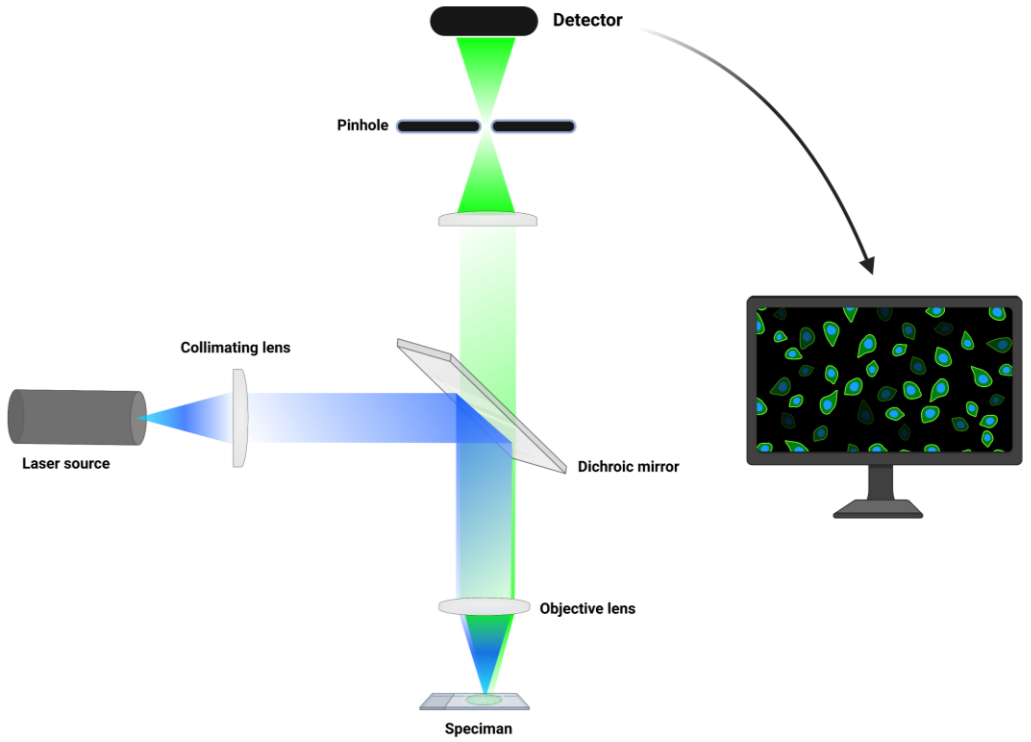

Fig 49. A simple diagram of the workflow for confocal laser scanning microscope. A specific visible laser is generated by a laser diode in a laser source. After passing through the collimating lens and being reflected by a dichroic mirror, the laser is focused on the same plate by the objective lens with adjustable magnification. Then after excitation, the emitted light from sample is concentrated to pass through the pinhole and detected. Meanwhile, the unwanted noise may be filtered by the pinhole. Created with BioRender.com.

4.1.2 Introduction – Cellular uptake pathways of nanoparticles

The limited solubility of PTX in aqueous media prompted us to employ HSA-PLA nanoparticles for encapsulating PTX, thereby indirectly enhancing its aqueous incorporation. To exert the tumoricidal function of PTX, the HSA-PLA (PTX) nanoparticles need to be delivered into the tumour cells for releasing PTX to promote and stabilize the polymerization of tubulins (microtubules) in cells. As a

result, the inhibition of cancer cell growth and the induction of apoptosis in tumour cells may be achieved.

To validate the uptake of HSA-PLA (PTX) nanoparticles by 4T1 cells and identify potential internalization pathways, a confocal laser scanning microscopy experiment was conducted. The principal mode of nanoparticle entry into cells is endocytosis, which can be further categorized into different types. The endocytosis of nanoparticles can then be subdivided into several types. The study of endocytosis is a constantly evolving field, and thus outdated perceptions and misconceptions about endocytic mechanisms are consistently being rectified and updated. For example, the endocytic pathways [195,196] of nanoparticles were previously identified as macropinocytosis, phagocytosis, clathrin – mediated endocytosis, cavolae – mediated endocytosis, clathrin/caveolae – independent endocytosis. While the current consensus classification of the endocytic pathways [197,198] encompasses clathrin and dynamin dependent endocytosis, fast endophilin – medicated endocytosis, CLIC/GEEC pathway, macropinocytosis and phagocytosis. Another example is that the receptor – medicated endocytosis was considered to be equal to the clathrin – mediated endocytosis previously [197]. However, the receptor-ligand interactions can also drive the endocytosis of nanoparticles in other pathways, such as the CLIC/GEEC pathway [199]. In addition, the entry of nanoparticles to cells through caveolae is currently controversial [200,201]. The characteristics of each endocytic pathway of

nanoparticles are generally introduced below.

Clathrin – mediated endocytosis

The clathrin-mediated endocytosis is an important pathway for cells to collect nutrients and cell signalling from the extracellular matrix, primarily reliant on the activation of diverse receptors. Receptors commonly involved in clathrin-mediated endocytosis [197] encompass transferrin receptors, low-density lipoprotein receptors, and certain G protein-coupled receptors [202]. Upon capturing their corresponding ligands, these receptors stimulate intracellular proteins to aggregate around the cell membrane at the point of interaction, setting the stage for endocytosis. The ligands captured in this process are subsequently internalized into cells, enclosed within vesicles resembling a lattice structure that forms through invagination of the cell membrane coated with lectin proteins, as shown in the TEM images [203] in ***Fig 50***. Subsequently, the mature latticed vesicles containing the internalized substances are detached from the cell membrane through the action of dynamin [204]. The lattice structure of these vesicles is constructed from symmetrical three-legged biomolecules known as clathrin triskelions. A clathrin triskelion is composed of three clathrin proteins. As of now, the precise mechanism through which clathrin-based vesicles form, involving the interplay between clathrin triskelions and various adaptor proteins [205], remains to be fully understood.

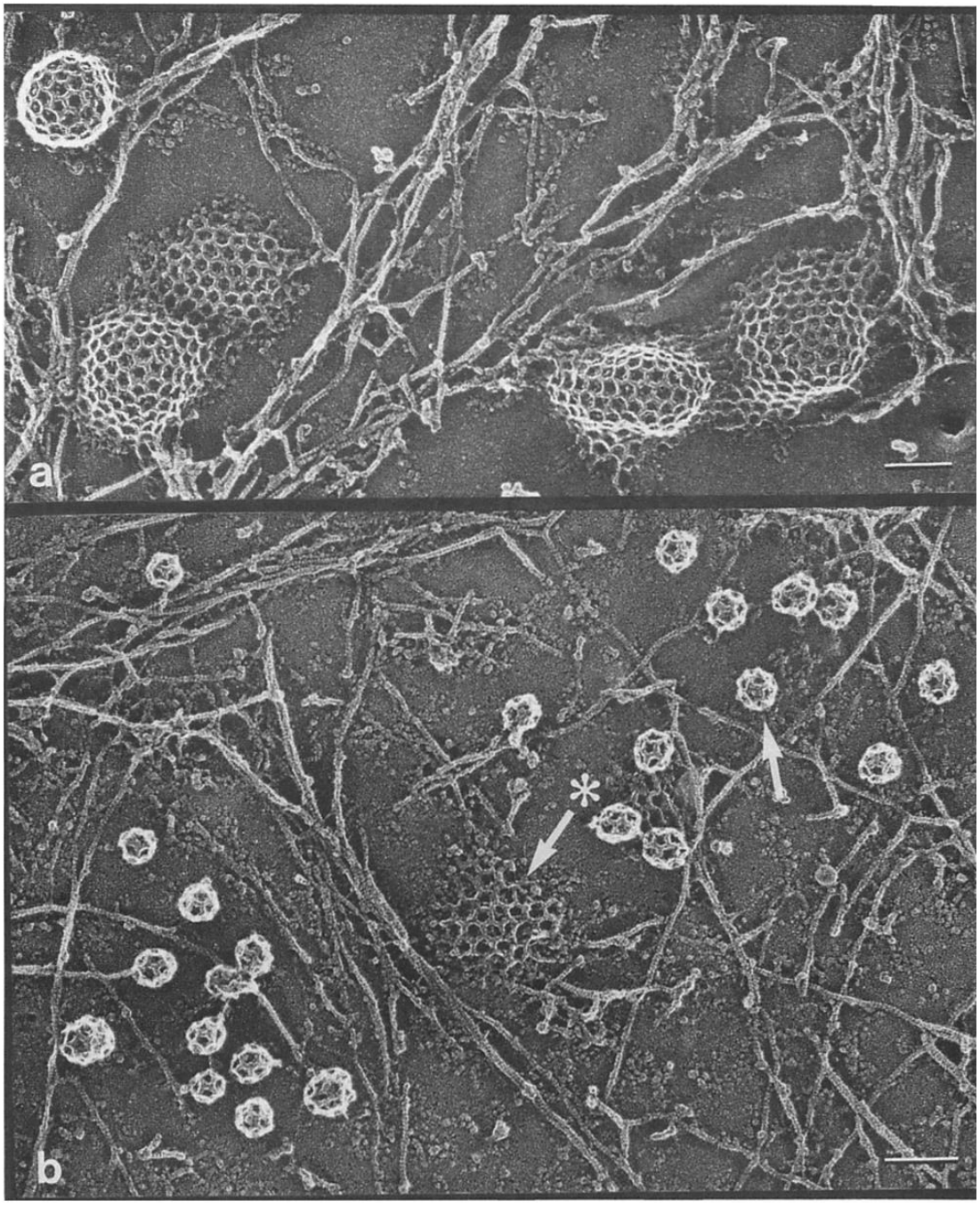

Fig 50. TEM images of the inner cell membrane of a normal chick fibroblast. The formed nanoscale clathrin-coated vesicles at various stages. Bar = 100 nm. "Used with permission of Rockefeller University Press, from Heuser JE, Anderson RG. Hypertonic media inhibit receptor-mediated endocytosis by blocking clathrin-coated pit formation. J Cell Biol. 1989 Feb;108(2):389-400; permission conveyed through Copyright Clearance Center, Inc."

Fast endophilin-mediated endocytosis

The fast endophilin-mediated endocytosis (FEME) is a form of clathrin-independent endocytosis. This mechanism involves the generation of nanoscale tubular pits on the cellular membrane under the mediation of endophilins, following the linkage of FEME cargoes with specific receptors. The resulting tubular vesicles are then disconnected from the cell membrane by the action of the protein dynamin and subsequently transported along microtubules by dynein [206]. The identified receptors [197] involved in the FEME pathway include some G-protein-coupled receptors and growth factor receptors, such as EGFR, β1-adrenergic receptors and acetylcholine receptor.

CLIC/GEEC pathway

The CLIC/GEEC (CG) pathway [197] represents an endocytic pathway that operates independently of clathrin and dynamin. This pathway involves the formation of clathrin-independent carriers (CLIC), which arise through the invagination of cell membranes triggered by the interaction between ligands and receptors. These carriers subsequently mature into tubular early endocytic compartments, also recognized as glycosylphosphatidylinositol-anchored protein-enriched compartments (GEEC). Notably, the receptors internalized within this endocytic pathway can be efficiently and promptly recycled back to the cell membrane (***Fig 51***). Consequently, the CLIC/GEEC endocytic pathway

functions as a recurring and continuous route for the uptake of proteins and other macromolecules. Therefore, this endocytic pathway is largely exploited by the aggressive cancer cells to rapidly grab nutrients from the extracellular matrix for supporting their rapid proliferation. Well-known receptors related to tumour cells[199], including CD44, folate receptor α [207] and integrins, undergo internalization via the CLIC/GEEC pathway.

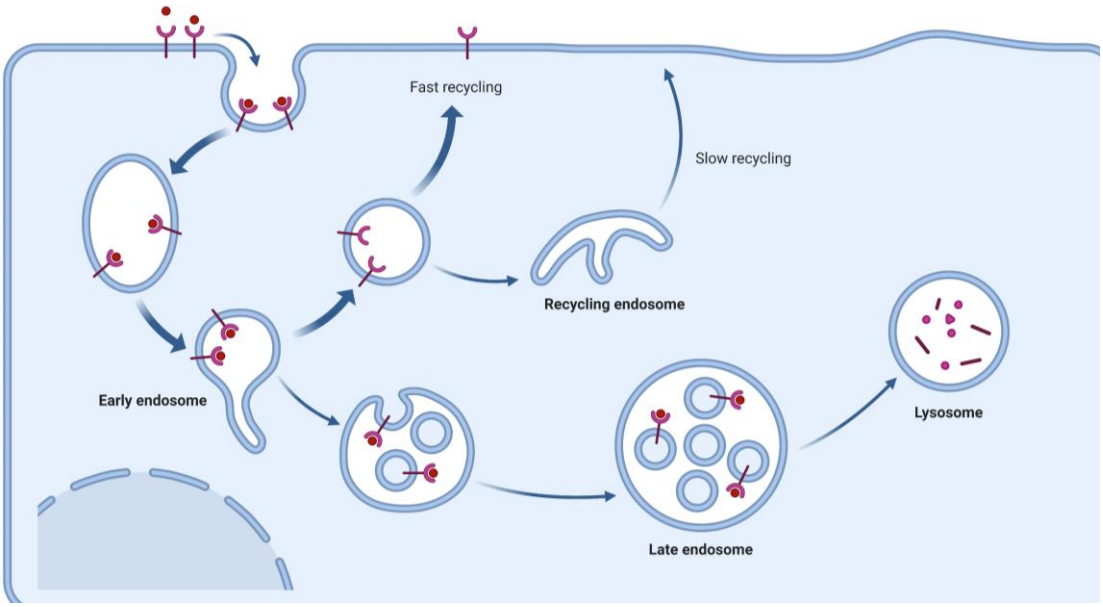

Fig 51. A schematic diagram of the internalization of nutrients via the CLIC/GEEC endocytic pathway. The CLIC/GEEC pathway is a clathrin-independent and dynamin-independent endocytic pathway. Clathrin-independent carriers (CLIC) formed by the invagination of the cell membrane triggered by the binding of ligands and receptors, subsequently mature into the tubular early endocytic compartments, also known as glycosylphosphotidinositol- anchored protein enriched compartment (GEEC). Rapidly recyclable receptors promote the abundant uptake of nutrients from the extracellular matrix in a recurrent manner. Created with BioRender.com.

Macropinocytosis

Macrophagocytosis is a type of clathrin-independent and dynamin-independent endocytic pathway. Within this process, macromolecules, nutrients, and antigens from the extracellular environment are internalized through non-specific encapsulation within macropinosomes. The formation of marcopinosomes involves an actin-driven stretching of the plasma membrane, and then as the stretched membrane folds back, a large amount of extracellular fluid is subsequently encapsulated in a large vesicle, see TEM image [208] of macropinocytosis in ***Fig 52***. The size of macropinsomes can vary from 0.2 μm to 5 μm in diameter [209].

Phagocytosis

Phagocytosis is a process characterized by cells engulfing large exosomes through membrane extension, enclosing the exosomes within phagosomes. Subsequently, these formed phagosomes undergo fusion with lysosomes for the digestion of the engulfed exosomes. The initiation of particle phagocytosis occurs upon binding of the particles to corresponding receptors, including the scavenger receptors on the surface of the professional phagocytes or non-professional phagocytes [210].

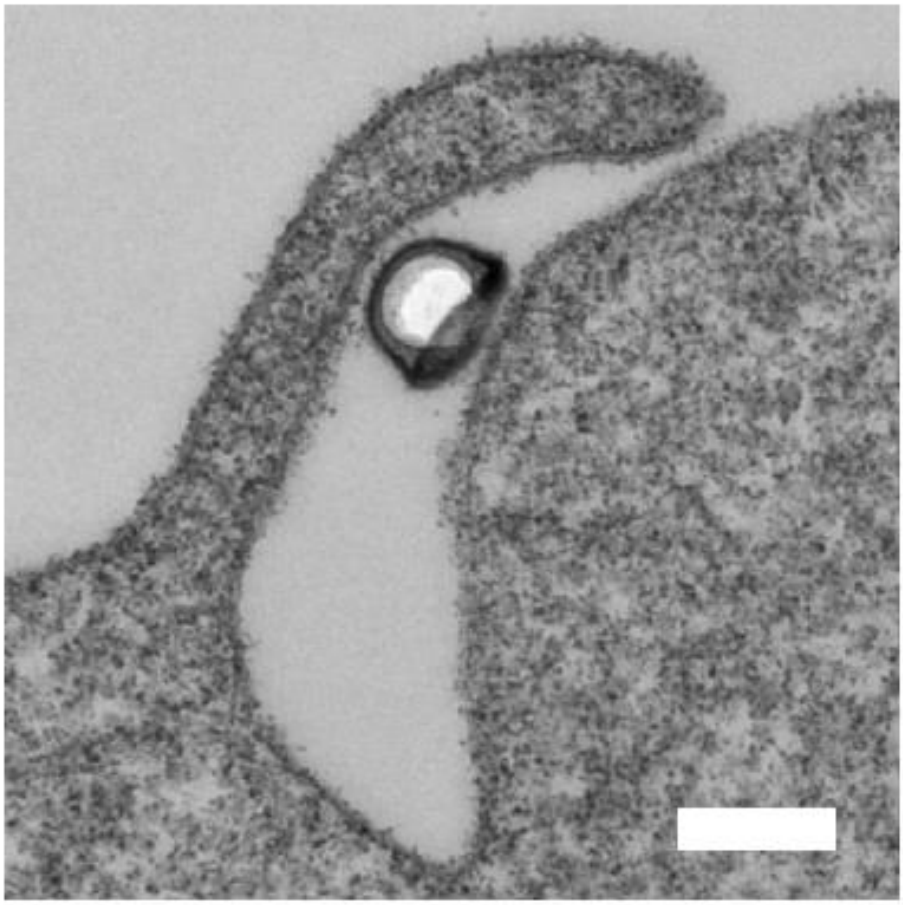

Fig 52. TEM image of a macrophage cell-RAW264.7. A nanoparticle was being internalized through the endocytic pathway – macropinocytosis. The large macropinosome was forming to carry the internalized nanoparticle. The scale bar = 200 nm. This cell TEM image was adapted from an open-access article with a *Creative Commons Attribution-NonCommercial license*. Citation: Y. Hui, X. Yi, D. Wibowo, G. Yang, A. P. J. Middelberg, H. Gao, C.-X. Zhao, Nanoparticle elasticity regulates phagocytosis and cancer cell uptake. *Sci. Adv.***6**, eaaz4316 (2020).

4.1.3 Introduction – LC-MS/MS

LC-MS/MS is a bioanalytical technique belonging to the family of liquid chromatography tandem mass spectrometry techniques. In LC-MS/MS, analytes can be separated by a column in the liquid chromatography system, and the eluted analytes are then detected in a triple quadrupole mass spectrometer. The principle of the liquid chromatography has been illustrated in the section of RP-HPLC in ***Chapter 3***. The mechanism of the detection of samples by a triple quadrupole mass spectrometer is entirely different from the UV detector of HPLC. UV detection is based on the collection of the emitted light from the excited chromophores of samples. In other words, if the sample can't absorb enough energy from the UV light, the sample does not emit the light that can be detected by the UV detector. For example, methanol cannot be detected by the UV detector. In the case of the triple quadrupole mass spectrometer, the detection of sample is based on the collection of ions of ionized analytes. Concretely, the acidic or basic mobile phase of the LC system can ionize the injected samples. The selection of an acidic or basic mobile phase depends on the chemical properties of the analyte of interest. After the separation of analytes in the stationary phase (column), the mobile phase carries the analytes to the electrospray ionization (ESI) compartment. In the ESI compartment, the mobile phase and analytes are sprayed out as aerosols and the size of droplets depends on the nebulization

pressure, conductivity and flow rate of the mobile phase. In order to achieve the optimal ionization of the analytes, the droplets of aerosols should be as small as possible. In the ESI compartment, solvent in the aerosols can be evaporated by the flow of heated inert gas and the remaining ions are aspirated into the electrically charged capillary. The ions are then delivered to the octupole to be accelerated before entering into the first quadrupole (Q1). Based on the selected mode for the ion detection (a full MS scan, a selected MS range scan or a selected ion scan), ions can be selectively allowed to pass through the first quadrupole (Q1). The most sensitive mode of the triple quadrupole mass spectrometer is the selected reaction monitoring (SRM) or multiple reaction monitoring (MRM). Since the sensitive detection technique of the LC-MS/MS, the lower limit of detection of an LC-MS/MS instrument can be improved at least 1000-fold compared to the HPLC technique.

In this work, the selected MS range scan mode was used to detect and determine the ions of PTX molecules within the range from 200 to 900 m/z, as shown in ***Fig 53***. Then, ions with m/z values of 854.2 and 569.2 were selected as the precursor ions for the MRM method to quantify PTX, with their respective product ions chosen as 286.1 and 509.2 m/z. More specifically, as seen in ***Fig 54***, PTX was ionized in ESI compartment, by applying a proper fragmentor voltage and the resulting ions were then delivered to the accelerator. After acceleration, the predetermined ions (854.2 m/z and 569.2 m/z) passed through the Q1 ion filter

and entered into the Q2 collision cell. Subsequently, by applying an appropriate collision energy, these precursor ions were fragmented into the smaller ions in the collision cell. Next, only the selected product ions (286.1 m/z and 509.2 m/z) could pass through the Q3 ion filter and reach the detector to generate the corresponding response value. The resulting peak area of product ions is proportional to the concentration of PTX.

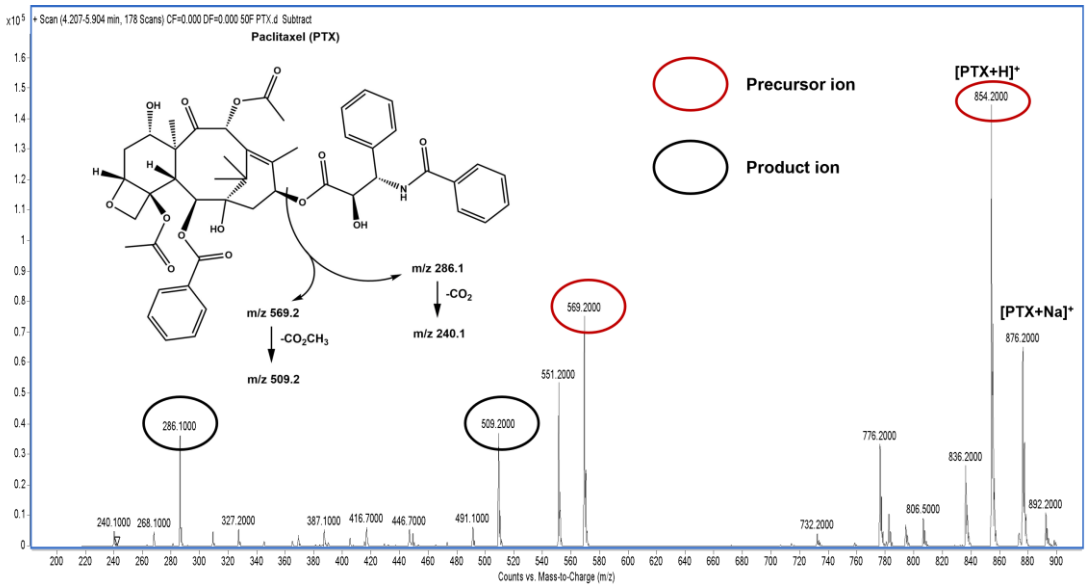

Fig 53. Mass spectrum of paclitaxel under all scan mode. Based on the structure of the fragments of paclitaxel, two groups of ions are selected for the MRM mode method. The first precursor ion is 854.2 m/z and its product ion is 286.1 m/z. The second precursor ion is 569.2 m/z and its product ion is 509.2 m/z.

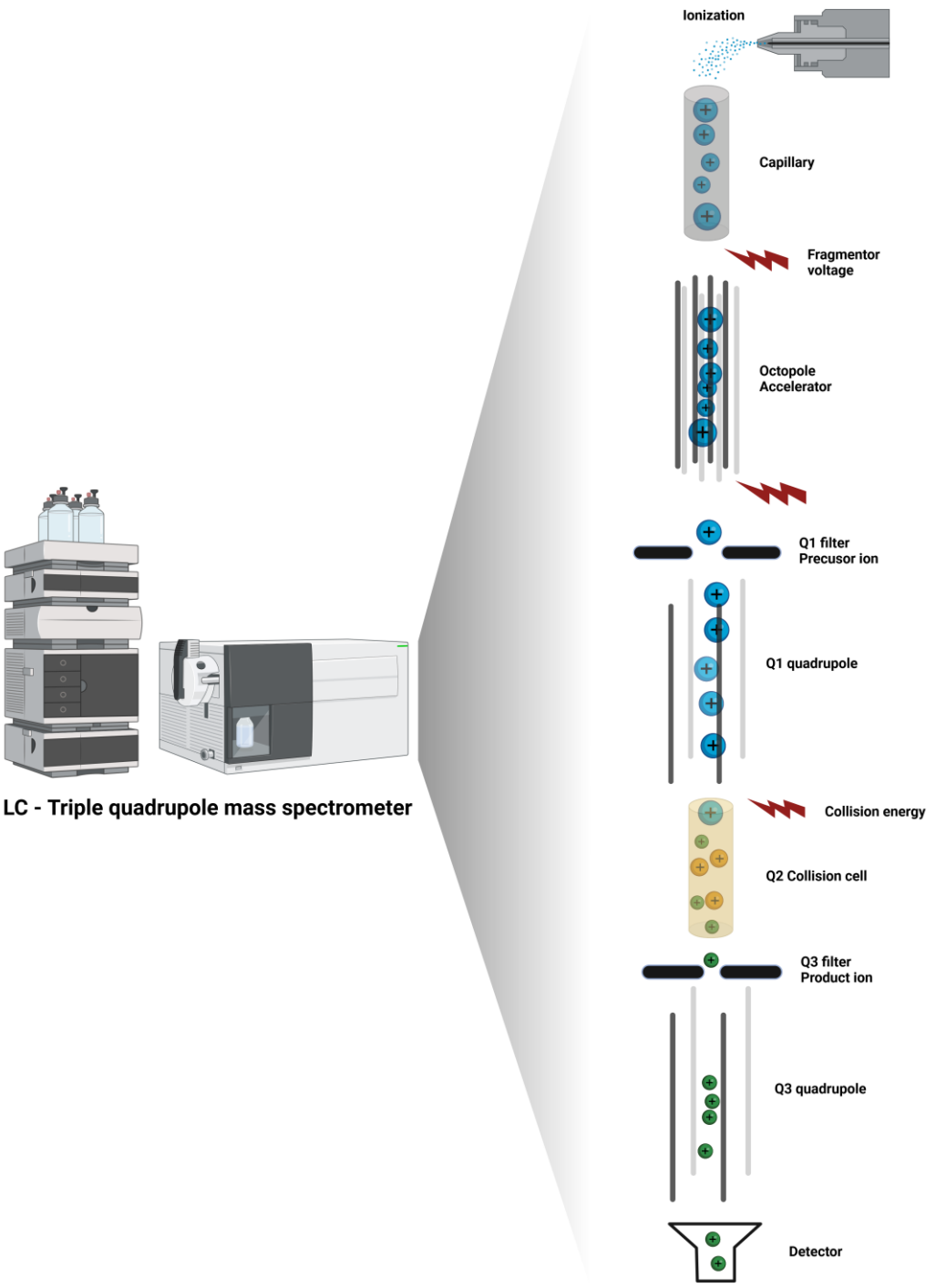

Fig 54. Schematic diagram of the working mechanism of the triple quadrupole mass spectrometer. In MRM mode, the predetermined precursor ions can pass through the Q1 ion filter according to the m/z value. In Q2 collision cell, these precursor ions are fragmented into the smaller ions by applying a collision energy. Then the selected smaller ions can pass through the Q3 ion filter and generate response at the site of detector. The response value is proportional to sample concentration. This MRM method can largely suppress the influences of impurities in biological samples and even quantify the sample at a concentration of 1 ng/mL. Created with BioRender.com.

4.2 Materials, cell line and animals

Table 9. Materials, cell line and animal models used in the *in vitro* and *in vivo* studies of HSA-PLA (PTX) nanoparticle.

Supplier	Materials, cell line and animals
Thermo Fisher Scientific UK	Acetonitrile (ACN, ⩾99.9%, HPLC Gradient grade)
	Advanced RPMI 1640 Medium
	Collagen Type I Cellware 22 mm round Coverslips
	GlutaMAX™ Supplement 100X
	Immersion Oil™ 518F,
	Methyl-Tert-Butyl Ether MTBE Extra Pure
	NucBlue™ Live ReadyProbes™ Reagent (Hoechst 33342)
	Penicillin-Streptomycin solution 100X
	Phosphate Buffered Saline PBS pH7.4
	PTFE hydrophobic syringe filters, 0.22 µm
	Paraformaldehyde Solution 4% in PBS
	Recovery™ Cell Culture Freezing Medium
	Trifluoroacetic acid (TFA, 99%)
	TrypLE™ Express Enzyme (1X) no phenol red
	Water with 0.1% Formic acid Optimal LC/MS grade
Merck UK	Acetonitrile with 0.1% FA LC-MS grade
	Coumarin 6 (≥99%)
	1,1′-Diethyl-2,2′-dicarbocyanine iodide
	Dimethyl sulfoxide (DMSO)
	Fetal Bovine Serum Heat Inactivated non-USA origin sterile-filtered
	Heparin sodium salt

	Human serum albumin (HSA) essentially fatty acid free
	Methanol puriss ACS reagent
	Syringe-driven filter units (0.45µm)
	Tetramethylrhodamine isothiocyanate–Dextran, average mol wt 20,000
Generon UK	Paclitaxel (PTX)
University College London Hospital	Taxol®
	Abraxane®
ELGA PURELAB®	Distilled water
ATCC	4T1 (ATCC CRL-2539)
Charles River Laboratories	BALB/c female mice (6 weeks)
	Sprague Dawley female rats (200 g)

All chemicals, reagents and solvents were used as purchased without any purification.

4.3 Experimental methods

4.3.1 Cell culture of 4T1 cells

4T1 cells were cultured in a tissue culture flask with a vented cap using a complete medium composed of Advanced RPMI 1640 Medium supplemented with 10% (v/v) heat-inactivated FBS, 1% (v/v) Glutamax, and 1% (v/v) penicillin/streptomycin. The cells were maintained at 37°C in a humidified incubator with 5% CO_2.

4.3.2 Cellular uptake and intracellular tracking of HSA-PLA nanoparticles

Cellular uptake

The cyanine dye 1,1′-Diethyl-2,2′-dicarbocyanine iodide (Sigma Aldrich, UK) was dissolved in methanol at a concentration of 1 mg/mL. A volume (1 mL) of methanol containing 1 mg of 1,1′-Diethyl-2,2′-dicarbocyanine iodide (Cy Red) was dropwise added to the HSA-PLA nanosuspension (100 mg powder of the HSA-PLA nanoparticles in 35 mL distilled water). After subjecting the HSA-PLA nanoparticles and cyanine dye mixture to probe sonication for 2 cycles (5 min sonication followed by 3 min of rest as one cycle) at level 5 amplitudes in an ice bath, the resulting Cy Red-loaded nanoparticle colloidal liquid was filtered using

a 0.45 μm syringe filter to purify it. Then the filtrate was frozen in a tube silicone freezer mould at -20ºC. The frozen Cy-Red loaded nanoparticles were subsequently lyophilized (ALPHA 1-4 LDplus, Martin Christ, Germany) in a cold environment (0°C), and any residual MeOH was removed in the vacuum environment during the lyophilization process. The lyophilized powder of the Cy-Red loaded NPs was stored in glass vials at room temperature for further analysis. The Collagen Type I Cellware 22 mm round Coverslips were placed in a 6-well plate (SARSTEDT, Germany). Approximately 1×10^5 4T1 cells were seeded per well in the aforementioned 6-well plate with 4 mL of complete medium per well, and the plate was incubated at 37°C until the cells reached 80% confluence. The previous complete medium was replaced with fresh FBS-free medium (3 mL). Cells were subjected to two cold PBS washes (5 mL each, pH 7.4) after 3 hours of starvation at 37°C in the incubator. Following this, FBS-free medium (3 mL) containing 0.5 mg/mL HSA-PLA (Cy Red) was added to each well and incubated with the cells for 1 hour at 37°C. The medium containing nanoparticles was then aspirated, and the cells were washed with cold PBS twice (5 mL each, pH 7.4). Next, FBS-free fresh medium (3 mL) was added to each cell well, and 6 drops of Hoechst 33342 solution were introduced into each well for cell nuclei staining. After a 30-minute staining period, the FBS-free medium was removed, and the cells were washed with cold PBS twice (5 mL each, pH 7.4). Subsequently, the coverslips were removed, washed with cold PBS (pH 7.4), and placed in a new

6-well plate. The cells on the coverslips were fixed with 4% paraformaldehyde solution (2 mL) for 15 minutes on ice. One drop of mounting medium was placed on a microscope slide, and a washed coverslip was positioned on the mounting medium and sealed with nail oil. Fluorescent cell images were acquired using a confocal microscopy (ZEISS LSM 710).

Intracellular tracking

The fluorescent dye Coumarin-6 was encapsulated in the HSA-PLA nanoparticles in the same way as described above and recorded as HSA-PLA (Cou-6). The cell seeding procedures were consistent with those used in the cellular uptake experiments. After a 3-hour starvation period at 37°C in the incubator, FBS-free medium (3 mL) containing 0.5 mg/mL HSA-PLA (Cou-6) and tetramethyl rhodamine dextran (TRITC-dextran) was added to each well and incubated with the cells for 0.5 hour at 37°C. Subsequently, the medium containing the dyes was aspirated, and the cells were washed twice with 2 mL of cold PBS. FBS-free medium (3 mL) was then introduced to each cell well, followed by the addition of 6 drops of Hoechst 33342 solution to each well for cell nuclei staining. After a 30-minute staining period at room temperature, the same fixation, mounting, and sealing procedures used in the cellular uptake experiments were applied. A confocal microscopy (ZEISS LSM 710) was employed to capture cell images featuring distinct fluorescent dyes.

4.3.3 Pharmacokinetics study in rats

Nine healthy female Sprague-Dawley (SD) rats (7-8 weeks old, weighing 220 ± 20g) were randomly allocated into 3 groups, each consisting of 3 SD female rats (n = 3). Taxol® liquid was diluted with 0.9% NaCl saline to achieve a PTX concentration of 2.2 mg/mL. The lyophilized powders of Abraxane® nanoparticles and HSA-PLA (PTX) nanoparticles were dispersed in 0.9% NaCl saline to obtain a PTX concentration of 2.2 mg/mL for each formulation. Subsequently, 1 mL of the aforementioned PTX formulations was intravenously administered to the SD rats via the tail vein, resulting in an equivalent PTX dose of 10 mg/kg for each group. Blood samples were collected from the tail vein at various time points: 0.25, 0.5, 1, 2, 4, 8, 24, and 72 hours post-injection. These samples were temporarily preserved in heparin-treated Eppendorf tubes. Following a 10-minute centrifugation at 3000 rpm using a Bench Top Refrigerated Microlitre Centrifuge (Biofuge® Fresco, Heraeus®, Germany), 100 µL of plasma samples (400 µL for the 72-hour time point group) were stored in a -20°C freezer until quantification could be performed using LC-MS/MS.

4.3.4 Biodistribution study in mice

Female BALB/c mice (6-8 weeks, 20 ± 2 g) were subcutaneously injected with 4T1 cells ($2x10^6$cells/100 µL of DPBS) at the right flank sites. Ten days after the injection of the 4T1 cells, tumour volume reached approximately 200 mm^3. The

Taxol® liquid was diluted with the 0.9% NaCl saline to a concentration of PTX 4 mg/mL. The lyophilized powders of the Abraxane® nanoparticles and the HSA-PLA (PTX) nanoparticles were dispersed in the 0.9% NaCl saline according to a concentration of PTX 4 mg/mL, respectively.

These mice were then randomly divided into groups of three mice each and were intravenously administered 0.1 mL of the prepared PTX injections, resulting in an equivalent PTX dosage of 20 mg/kg for each group. Subsequently, the mice were anesthetized and sacrificed at specific time points: 1, 3, 8, 24, and 72 hours after the injection of the paclitaxel preparations. Blood samples were obtained from the mice via heart puncture, and the organs were flushed with 50 mL of PBS saline through cardiac perfusion to remove residual blood. After perfusion, tumours, hearts, livers, spleens, lungs, and kidneys were extracted, rinsed with PBS, and then stored in a -20°C freezer.

The frozen tissue samples were thawed using a 37°C water bath, and the organs and tumours were sectioned into smaller pieces, while removing vessels, ducts, ligaments, fibrous appendages, and fats within the tissues. Subsequently, these tissue pieces were weighed and suspended in PBS saline (100 mg of tissue per mL of PBS). After 10 minutes of probe sonication at an amplitude of 9, the tissue pieces were homogenized to create a tissue suspension. Finally, 0.1 mL of the tissue suspension (0.4 mL for the 72-hour group) was aliquoted and stored at -20°C until further MTBE liquid-liquid extraction .

4.3.5 MTBE liquid-liquid extraction

The frozen plasma or tissue suspension samples from above were defrosted in a 37°C water bath. The defrosted samples were treated with 100 µL of 60% ACN and vortexed for 2 minutes. Subsequently, another 100 µL of ACN was added for protein precipitation, and the tissue suspension was vortexed for an additional 2 minutes. Following this, a volume of 2 mL of MTBE was added to the treated tissue suspension for the first extraction and vortexed for 5 minutes. The mixture was then subjected to centrifugation at 10,000 rpm for 5 minutes. The resulting supernatant was collected and transferred to a glass vial.

For the second extraction, another 2 mL of MTBE was added to the pellet obtained from the first extraction. The suspension was vortexed for 5 minutes and then subjected to centrifugation at 10,000 rpm for 5 minutes. The second supernatant was combined with the first supernatant, and the MTBE solvent was removed using rotary evaporation. The residue was dissolved in 1 mL of ACN (0.5 mL ACN for the 72-hour rat plasma samples and 0.2 mL ACN for the 72-hour mouse plasma samples) through vortexing and bath sonication.

After dissolving the residue, 0.2 µm PTFE syringe filters were employed to filter the samples. Subsequently, the samples were subjected to quantification of PTX using LC-MS/MS (Agilent Technologies, 6460 Triple Quad LC/MS).

4.3.6 In vivo anticancer study

Twenty BALB/c female mice (6-8 weeks) were subcutaneously injected with 4T1 cells ($2x10^6$ cells per 100 µL of DPBS). When the tumour volume was approximately 100 mm^3, these mice were divided into four groups with 5 mice in each group (n = 5). The groups were as follows: HSA/saline (400 mg/kg) serving as the control group, Taxol® (equivalent to PTX 20 mg/kg), Abraxane® (equivalent to PTX 40 mg/kg), and HSA-PLA (PTX) (equivalent to PTX 40 mg/kg). Each group of mice received an intravenous injection of the corresponding treatment on Day 0 and another injection on Day 3, totalling two injections per mouse. The tumour volume was measured daily using a vernier calliper and the tumour volume was calculated through the formula, tumour volume = 0.5 × length × $width^2$. Mice were euthanized if the tumour volume reached around 1000 mm^3, if there was a body weight loss exceeding 15%, or if tumour ulceration persisted for more than 3 days.

4.3.7 Statistics

Data are presented as the means ± SD (standard deviation). The student's t-test, one-way ANOVA and two-way ANOVA were used for the relative statistical analysis in Prism software. A value of $p < 0.05$ indicates a significant difference in the data.

4.4 Results and discussion

4.4.1 Cellular uptake study of HSA-PLA nanoparticles

The fluorescent dye, 1,1′-Diethyl-2,2′-dicarbocyanine iodide, was encapsulated in the HSA-PLA nanoparticles by using the same method employed for PTX drug loading. The weight ratio of the HSA-PLA nanoparticles to the cyanine dye was maintained at 100 to 1. This formulation of cyanine dye-loaded HSA-PLA nanoparticles was denoted as HSA-PLA (Cy Red) nanoparticles.

The cell nuclei of 4T1 cells were stained with the Hoechst 33342. The fluorescent dye Hoechst 33342 was excited by the light with a wavelength of 405 nm and the emitted blue light was collected by the detector of the confocal laser scanning microscopy. The cyanine dye labelled HSA-PLA nanoparticles was excited by the light at a wavelength of 633 nm and thereby the red emission light was detected. As shown in ***Fig 55***, blue spots represented the cell nuclei of 4T1 cells and the red stain was due to the emitted light from the HSA-PLA (Cy Red) nanoparticles. The cell images captured at various magnifications (10X, 20X, and 40X) exhibited clear evidence of 4T1 cells internalizing the HSA-PLA (Cy Red) nanoparticles, with the red emitted light from the intracellular nanoparticles illuminating the entire cell. Meanwhile, the bright cell images indicated that the 1,1′-diethyl-2,2′-dicarbocyanine iodide could produce very strong fluorescent intensity after

excitation. This dye may also be potentially used for *in vivo* imaging. Additionally, this fluorescent dye has not been reported to be used for biological application in previous publications. Therefore, its utilization for both cell imaging and in/ex vivo imaging represents a pioneering endeavour.

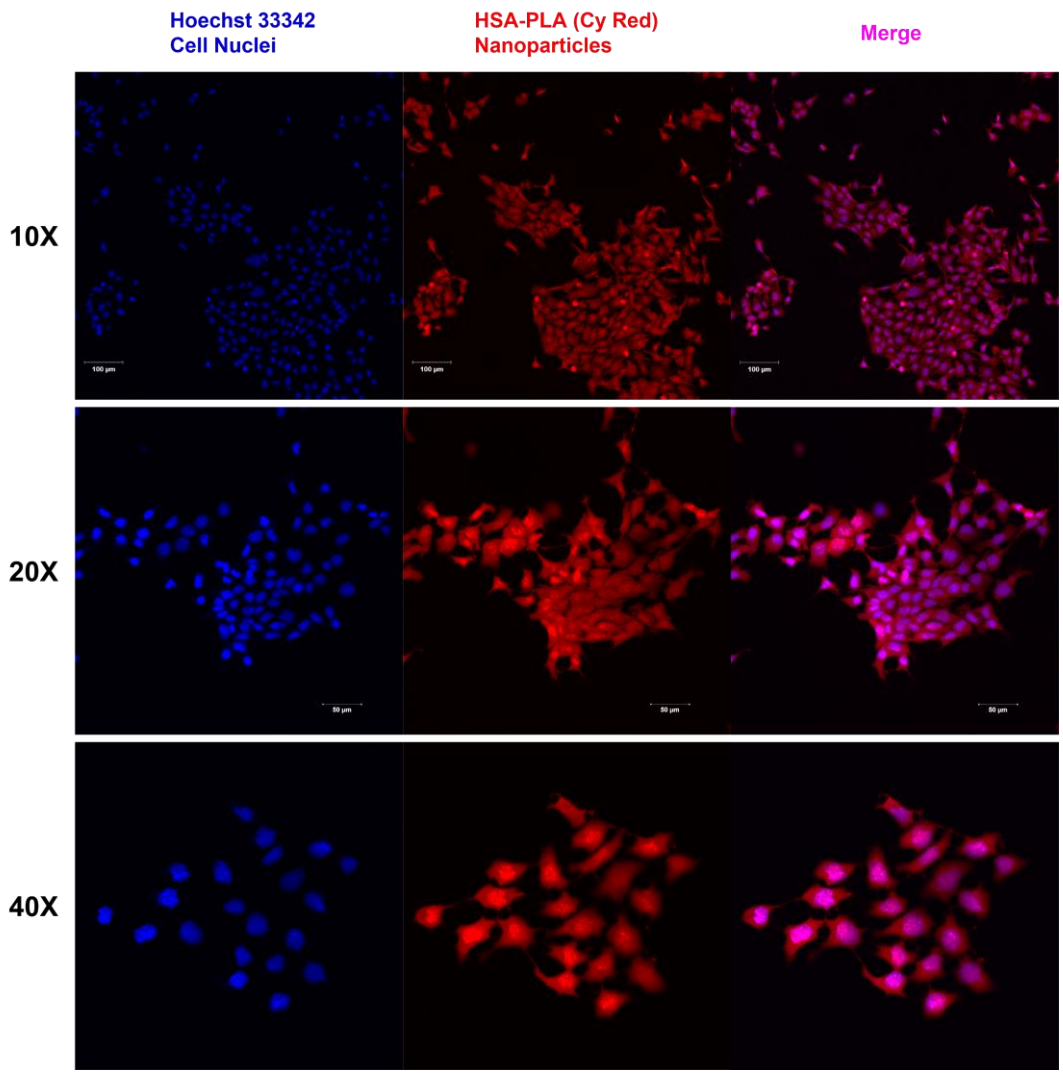

Fig 55. Cellular uptake study of HSA-PLA (Cy Red) nanoparticles in 4T1 cells after 1-h incubation at 37ºC. From top to bottom, cell images are presented at 10x, 20x and 40x magnification, respectively. The Hoechst 33342 is used to stain cell nuclei and emits blue light after the excitation of light at a wavelength of 405 nm. HSA-PLA (Cy Red) nanoparticles are taken by 4T1 cells and the red emitted light from the intracellular nanoparticles illuminates the whole cell.

4.4.2 Intracellular tracking of HSA-PLA nanoparticles

The cyanine dye we used in the cellular uptake study demonstrated robust fluorescence suitable for cell imaging and potentially in vivo imaging. However, a limitation of this dye lies in its broad excitation and resulting emission range; it can be excited at 488 nm and emits green light at around 520 nm.

Thus, for the intracellular tracking study, the coumarin-6 was encapsulated in the HSA-PLA nanoparticles at an HSA-PLA coumarin-6 weight ratio of 100 to 1. Then tetramethylrhodamine isothiocyanate–dextran (TRITC-dextran) was used to label the macropinosome [211]. Following a 30-minute incubation of 4T1 cells with HSA-PLA (Cou-6) nanoparticles and TRITC-dextran, the resulting cell image from confocal laser scanning microscopy is illustrated in ***Fig 56***. During imaging, the HSA-PLA (Cou-6) nanoparticles were excited using a 458 nm wavelength laser, generating green emission (500 nm) that was subsequently detected. In parallel, TRITC-dextran was excited using light with a wavelength of 595 nm, with emitted light being detected at 620 nm.

HSA-PLA nanoparticles and TRITC-dextran were taken by 4T1 cells via macropinocytosis and then entrapped in the macropinosomes, which were around 2 μm in diameter, shown in ***Fig 56***. Moreover, through the creation of a 3D cell image via Z-stacks scanning, it was evident that the macropinosome was positioned above the cell nucleus and had yet to merge with the lysosome.

Considering the current understanding of nanoparticle endocytic pathways as discussed in section 4.1.2, microscale vesicles are produced only through the macropinocytosis of extracellular fluids. As such, it can be inferred that macropinocytosis likely constitutes one of the key endocytic pathways for the internalization of the HSA-PLA nanoparticles into 4T1 cells.

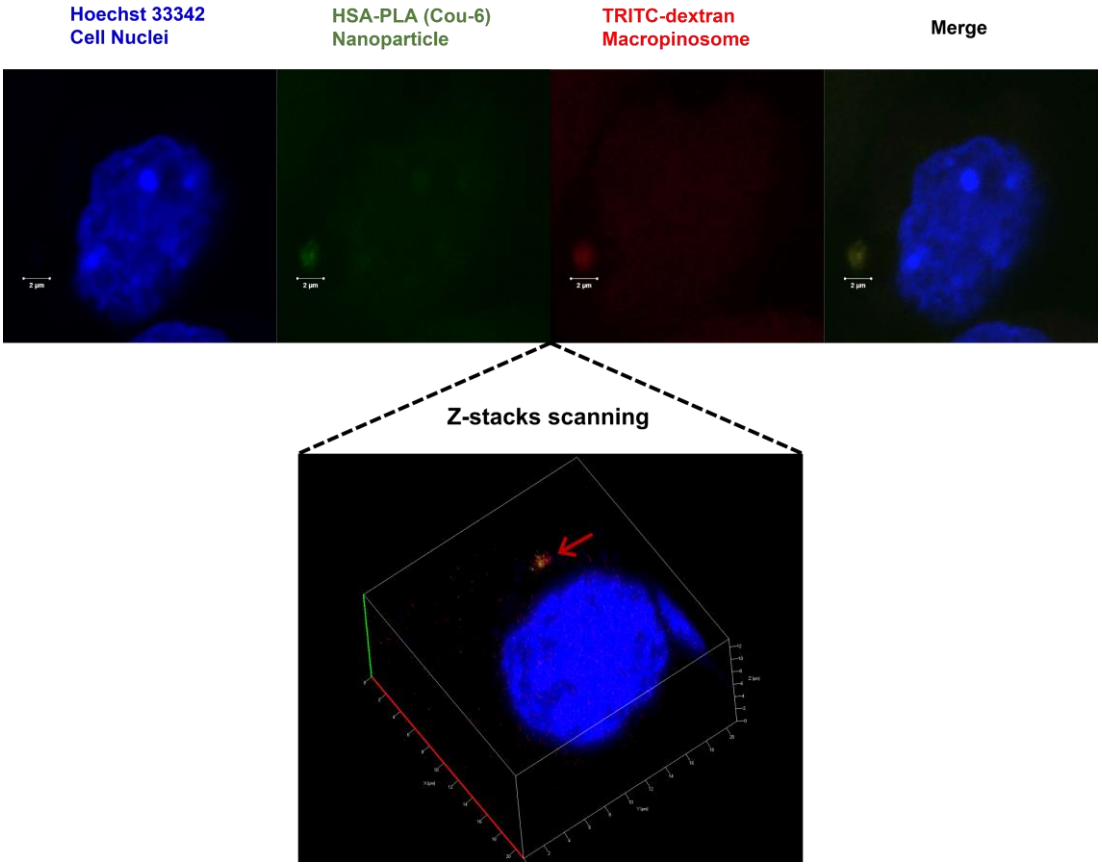

Fig 56. Endocytic pathway of HSA-PLA nanoparticles entering 4T1 cells. Coumarin-6 is encapsulated in HSA-PLA nanoparticles, recorded as HSA-PLA (Cou-6). TRITC-dextran is used to label macropinosomes of 4T1 cells. The microscale vesicle containing HSA-PLA (Cou-6) nanoparticles and TRITC-dextran proves that HSA-PLA nanoparticles are internalized in 4T1 cells through the macropinocytosis.

4.4.3 Pharmacokinetics study in rats

Following the *in vitro* studies of the HSA-PLA nanoparticles in terms of the cellular uptake and the endocytic pathway studies, the *in vivo* performance of the HSA-PLA (PTX) nanoparticles was investigated. This involved conducting a pharmacokinetics study of the HSA-PLA (PTX) nanoparticles in rats and comparing the obtained data with the pharmacokinetic (PK) profiles of Taxol® and Abraxane® in the same animal model.

In this part, Taxol®, Abraxane® and HSA-PLA (PTX) nanoparticles were intravenously injected to the Sprague-Dawley (SD) rats at a PTX dose of 10 mg/kg. The PK profiles, depicting the PTX concentration in plasma over time post-injection, are illustrated in ***Fig 57***. Noncompartmental pharmacokinetic parameters of each PTX formulation in rats were calculated by the PKSolver, including the terminal half-life ($t_{1/2}$), time of peak concentration (T_{max}), peak concentration (C_{max}), extrapolated concentration at time 0 (C_0), the area under the concentration-time curve from 0-72 h ($AUC_{0\text{-}72h}$), extrapolated area under the concentration-time curve from 0 to ∞ (AUC_{∞}) , Volume of distribution (V_d) is the ratio of dose of injected PTX to C_0, and total body clearance (CL). The results of these PK parameters were listed in ***Table 10***. In terms of the PK parameters and the PK profiles of Taxol®, Abraxane® and HSA-PLA (PTX) nanoparticles in rats, the rapid decline of PTX in rat plasma at the initial stage and the parameters such

as the large V_d of these three PTX formulations indicated that most of the injected PTX left the bloodstream rapidly and was distributed to the tissue compartments, such as liver. The plasma concentrations of these PTX preparations ranged from 1 ng/mL to 10 ng/mL after 72 hours of injection, which were far lower than the PTX contents in the organs of rats at the same time, see ***Fig 57***. A 72-hour post-injection biodistribution study reaffirmed that most injected PTX distributed to tissues and organs. In addition, according to the ***Fig 57. B***, the PTX concentrations of the Taxol® injection in rat hearts were significantly higher than those of the Abraxane® and the HSA-PLA (PTX) in rat hearts. This observation aligns with published reports of severe cardiotoxicity issues linked to Taxol® [212]. What is still striking in this rat pharmacokinetics study is the difference between the $AUC_{0\text{-}72h}$ values of Taxol®, Abraxane® and HSA-PLA (PTX) injections. A higher AUC value indicates that a PTX formulation results in reduced elimination and prolonged circulation of paclitaxel in the bloodstream. Although the $AUC_{0\text{-}72h}$ of the Taxol® injection in rats was 32.0 ± 7.5 μg*h/mL, significantly higher than the $AUC_{0\text{-}72h}$ of the Abraxane® injection in rats (2.2 ± 0.5 μg*h/mL, $p < 0.01$), the acute toxicity and severe side-effect (e.g. haematuria) caused by the Taxol® limited its maximum tolerated dose of PTX to rats. The $AUC_{0\text{-}72h}$ of the HSA-PLA (PTX) injection in rats was 4.0 ± 1.0 μg*h/mL, statistically higher than that of the Abraxane® injection ($p < 0.05$), which indicated that more paclitaxel molecules from the HSA-PLA (PTX) nanoparticles have a higher possibility to access the

tumour through the EPR effect.

It is worth noting that the data from our pharmacokinetic studies of PTX formulations in rats are consistent with the data from the nanomedicine report of the Nanotechnology Characterization Laboratory (NCL, Novel Method to Determine Bioequivalence of Nanomedicines) as well as the data of the preclinical research of the Taxol® and the Abraxane® [213]. To further interpret and track the distribution and elimination of the injected PTX in animal models, a biodistribution study and an anti-cancer study in 4T1 tumour bearing mice were carried out to track the injected PTX in mice and evaluate the tumoricidal activity of the HSA-PLA (PTX) injection by comparing those with the Taxol® and Abraxane® injections.

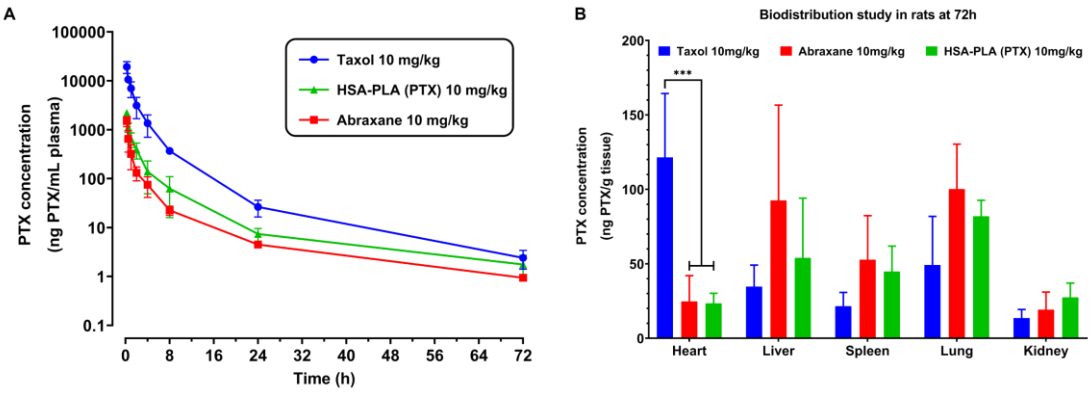

Fig 57. Pharmacokinetics study of Taxol®, Abraxane® and HSA-PLA (PTX) in SD rats. **(A)** Profiles of the PTX concentration in rat plasma versus time since the injection following intravenous administration of Taxol®, Abraxane® and HSA-PLA (PTX) at a PTX dose of 10 mg/kg. **(B)** PTX contents in the hearts, livers, spleens, lungs and kidneys of rats after 72 h of injection with PTX formulations. The PTX concentrations of the Taxol® injection in rat hearts are significantly higher than the Abraxane® and HSA-PLA (PTX) levels in rat hearts ($p < 0.001$), which is consistent with the published severe cardiotoxicity problems induced by the administration of the Taxol®.

Table 10. Pharmacokinetics profiles of Taxol®, Abraxane® and HSA-PLA (PTX) in rats. Data are presented as mean ± SD (n = 3) and analysed by the two-tailed Student's t-test. *, $p < 0.05$. **, $p < 0.01$ vs. Abraxane®. ##, $p < 0.01$ vs. HSA-PLA (PTX).

Drugs / Parameters	Taxol®	Abraxane®	HSA-PLA (PTX)
$t_{1/2}$ (h)	8.2 ± 1.7	14.3 ± 0.5	11.8 ± 3.7
T_{max} (h)	0.25	0.25	0.25
C_{max} (μg/mL)	19.4 ± 5.3	1.5 ± 0.3	2.2 ± 0.1
C_0 (μg/mL)	36.5 ± 16.5	3.9 ± 2.1	4.6 ± 1.7
$AUC_{0\text{-}72h}$ (μg*h/mL)	32.0 ± 7.5**##	2.2 ± 0.5	4.0 ± 1.0*
AUC_{∞} (μg*h/mL)	32.1 ± 7.5**	2.2 ± 0.5	4.0 ± 1.0*
V_d (mL/kg)	327.6 ± 182.2*	3029.9 ± 1452.8	2356.8 ± 720.0
CL (L/kg/h)	0.3 ± 0.1**	4.8 ± 1.2	2.6 ± 0.7*

Where **$t_{1/2}$** represents the terminal half-life, **T_{max}** stands for the time of peak concentration, **C_{max}** signifies the peak concentration, **C_0** corresponds to the extrapolated concentration at time 0, **$AUC_{0\text{-}72h}$** denotes the area under the concentration-time curve from 0 to 72 hours, **AUC_{∞}** represents the extrapolated area under the concentration-time curve from 0 to infinity, **V_d** is the volume of distribution, and **CL** refers to the total body clearance.

4.4.4 Biodistribution study in 4T1 tumour-bearing mice

In this study, the 4T1 tumour-bearing mice were intravenously injected with Taxol®, Abraxane® and HSA-PLA (PTX) at a PTX dose of 20 mg/kg, respectively. The equipment LC-MS/MS was used to detect and quantify the PTX levels extracted from the plasma, tumours, hearts, livers, spleens, lungs and kidneys of mice at 1, 3, 8, 24 and 72-h post-injection of each PTX formulation, respectively. To achieve a precise quantification of PTX contents in tissues, a highly reproducible method was designed to prepare samples for LC-MS/MS analysis, including heart perfusion, tissue homogenization and MTBE liquid-liquid extraction.

Heart perfusion

In theory, the average volume of circulating blood in a mouse is 72 mL/kg [214]. So, a 20 g mouse should have a total of approximately 1.44 mL of blood. However, in practice, a maximum volume of about 0.4 mL of blood was withdrawn from a mouse by cardiac puncture, which indicated that approximately 1 mL of blood remained in the tissues and organs. According to the PK profiles of Taxol®, Abraxane® and HSA-PLA (PTX) in rats, see ***Fig 57***, the presence of PTX in rat plasma was still detectable up to 72 hours after injection through our LC-MS/MS detection method. In order to get the accurate PTX levels in tissues, the blood in the organ should be removed to minimize the influence coming from the PTX in blood. Therefore, the operation of heart perfusion with 50 mL of phosphate

buffered saline was performed to the mice to remove blood from the tissues. Photographs (***Fig 58***) of the organs treated with or without heart perfusion have clearly displayed the difference in the appearance of the organs with and without blood inside. The excessive saline in and around the tissues was meticulously absorbed and desiccated using absorbent papers. Subsequently, the dried organs and tumours were meticulously collected and stored within a -20°C freezer until the subsequent steps involving tissue homogenization .

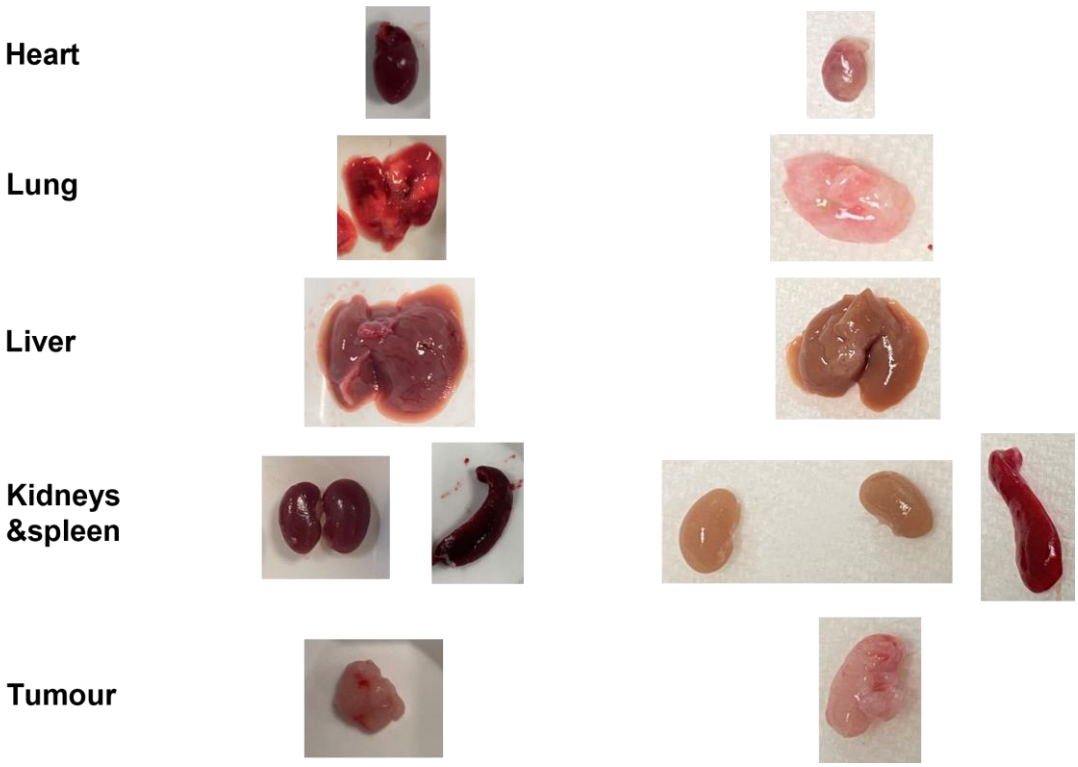

Fig 58. Appearance of organs and tumours with and without heart perfusion of saline. The colour of organs is significantly altered after the heart perfusion with saline when compared with the group without heart perfusion. The blood within different organs has been removed by the heart perfusion of saline.

Tissue homogenization

The organs and tumours were sectioned into small pieces, and concurrently, the vessels, ducts, ligaments, fibrous appendages, and fats were meticulously removed from the organs. The weights of these minced organs and tumours were accurately recorded. Subsequently, phosphate-buffered saline was employed to create a suspension of the organ fragments, maintaining a ratio of 100 mg tissue per 1 mL PBS saline. Following this, a 10-minute probe sonication process was applied to achieve thorough homogenization of the organ or tumour suspensions. A portion (0.1 mL) of the resulting tissue suspension was then extracted and stored for subsequent MTBE liquid-liquid extraction. This homogenization technique guarantees the absence of tissue chunks in the suspensions, ensuring a uniform homogenization process for both tumours and organs. As a result, exceptional reproducibility in PTX content measurements within organs and tumours was achieved.

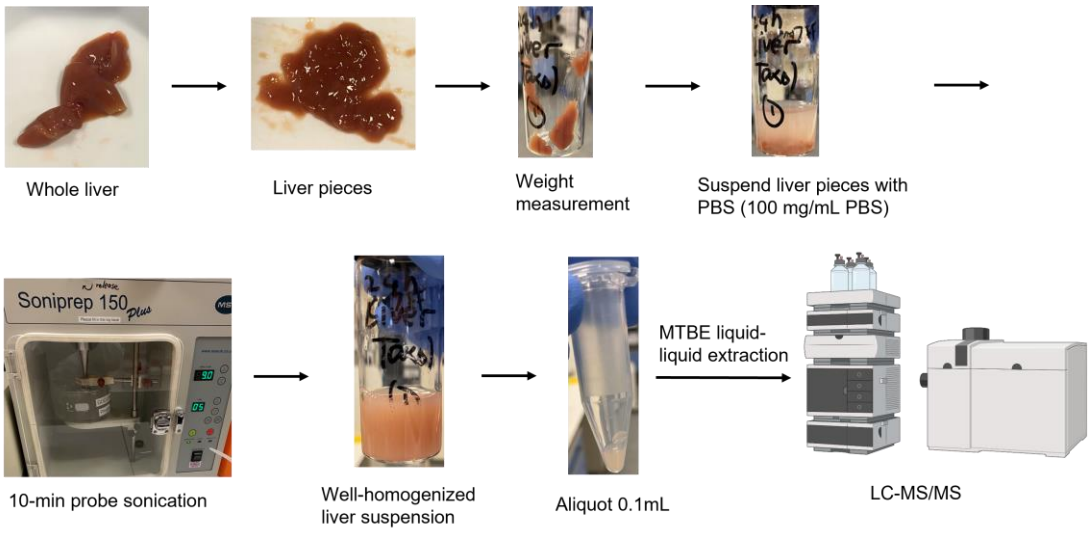

Fig 59. Workflow of the tissue homogenization. Here, the mouse liver is used as an example to demonstrate this method of tissue homogenization. Created with BioRender.com.

MTBE liquid-liquid extraction

To achieve a complete extraction of PTX from both plasma and tissue suspensions, a MTBE liquid-liquid extraction method was developed and illustrated in ***Fig 60***. The initial step of this extraction method involved adding 100 µL of a 60% (v/v) aqueous ACN solution to the thawed plasma and tissue suspensions. This addition aimed to dissolve and disperse any potential clumps that might arise during the thawing process, as protein aggregates could form in the suspensions. Subsequently, 100 µL of pure ACN was introduced to precipitate the proteins. MTBE was used for the first extraction of hydrophobic substances in the plasma and tissue suspensions. To enhance the recovery rate of the extraction process, the MTBE extraction step was repeated, allowing for a second extraction cycle. The extraction method's recovery rate was determined by

spiking PTX into blank plasma and subsequently comparing the quantity of extracted paclitaxel with the quantity of paclitaxel added .

Employing this extraction approach for preparing LC-MS/MS samples significantly reduced impurities and effectively suppressed the baseline noise in the spectra to a minimal level. The removal of hydrophilic impurities from biological samples is crucial, as their presence could lead to denatured proteins in the ESI compartment due to the elevated temperature environment. This, in turn, could render the baseline noise unsuitable for the sensitive detection of low concentrations of paclitaxel, such as 1 ng/mL.

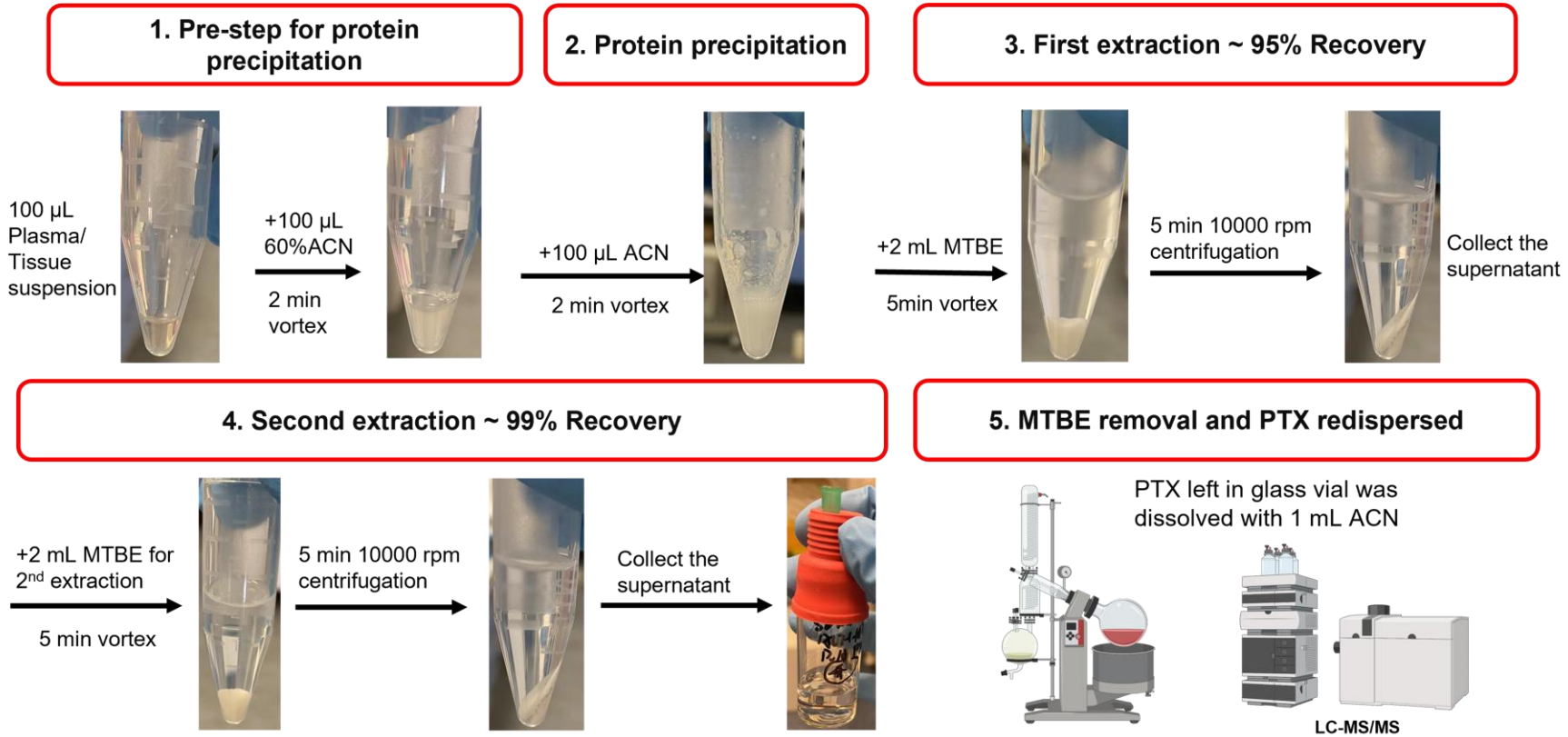

Fig 60. MTBE liquid-liquid extraction of paclitaxel from biological samples. Due to the complex hydrophilic impurities in the plasma and tissue suspensions are removed in this method, the contamination of the ESI compartment (by the denatured proteins) was avoided. Thereby, the limit of detection of PTX in the LC-MS/MS is improved to be lower than 1 ng/mL. Created with BioRender.com.

Results obtained from LC-MS/MS

For the LC-MS/MS detection method of PTX, the ion 854.2 m/z was selected as the precursor ion and this ion $(PTX+H)^+$ was mainly fragmented into a product ion 286.1 m/z by adjusting the collision energy. Based on this combination of precursor-product ions, a calibration curve of paclitaxel in acetonitrile was established, y = 222.52 x, ranging the concentration of PTX from 1 ng/mL to 10,000 ng/mL with a correlation coefficient value of 0.9996 (R^2 = 0.9996). Due to the fact that the detection of PTX by mass spectrometry is based on the ionization of analytes, the ionization of PTX in different tissue compartments might be different. In order to reduce the influence from this variable factor on the quantification of PTX, the different calibration curves of PTX in ACN spiked with plasma, tumour or organs were created, see ***Fig 61***. The equations for these calibration curves, used for quantifying PTX in plasma, tumour, heart, liver, spleen, lung, and kidney, are listed below:

Plasma: y = 223.04x R^2 = 1

Tumour: y = 229.4x R^2 = 1

Heart: y = 197.08x R^2 = 0.9985

Liver: y = 240.72x R^2 = 0.9997

Spleen: y = 228.84x R^2 = 0.9996

Lung: y = 211.43x R^2 = 0.9999

Kidney: y = 212.69x R^2 = 0.999

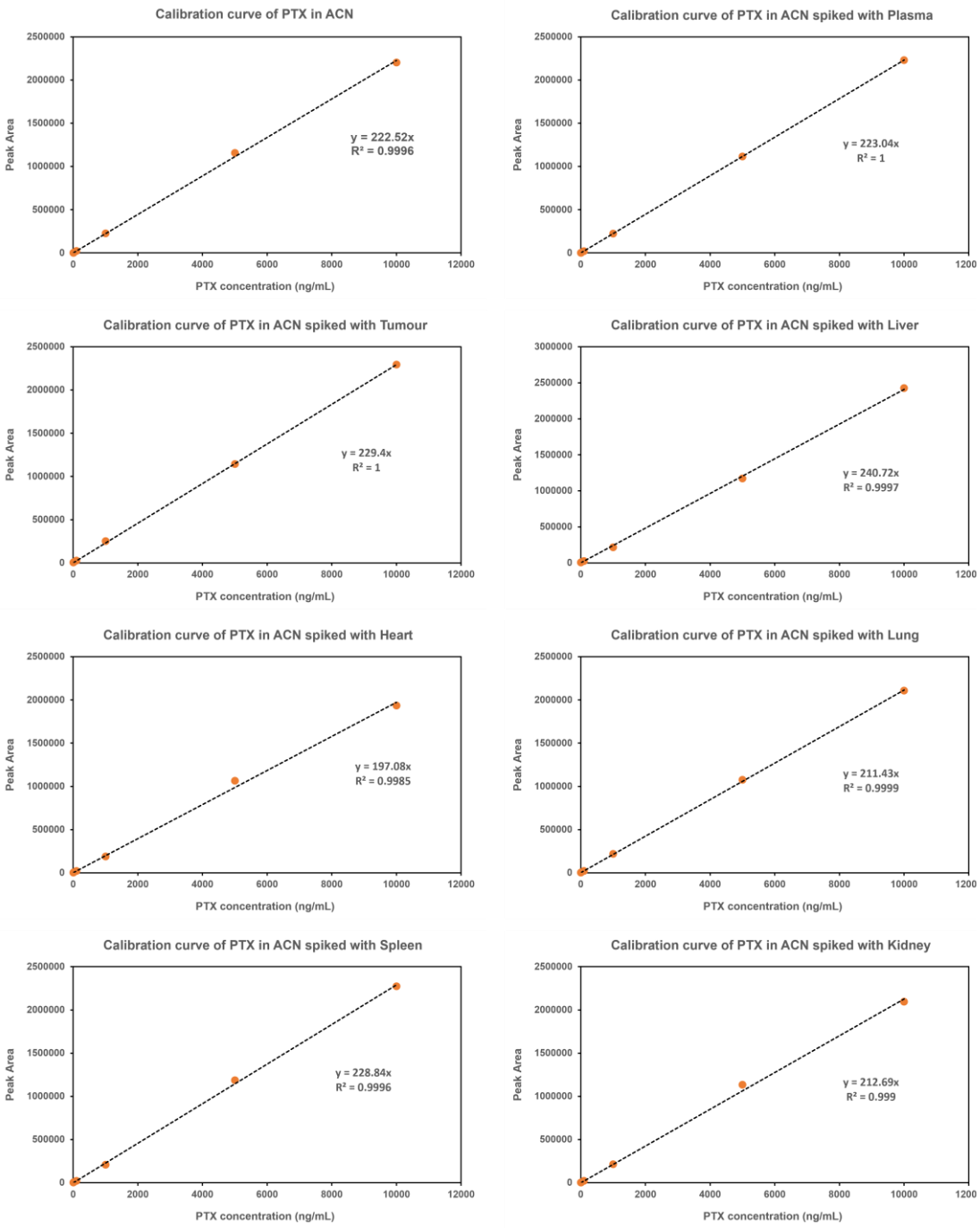

Fig 61. Calibration curves of PTX in different media for the LC-MS/MS detection method. Due to the different ionization of PTX may affect the final response in mass spectrometer, the different calibration curves of PTX in different media are developed for the specific quantification of PTX from different tissue compartments.

Based on the above calibration curves of PTX, the PTX contents in plasma, tumour and organs were determined. These determinations were then used to generate concentration-versus-time curves for PTX post-injection (see ***Fig 62***). Additionally, bar charts were constructed to illustrate the percentage of injected PTX per gram of tissue at various post-injection time points (***Fig 63***). Based on the curves of PTX concentration versus time post-injection of PTX formulations, the PK parameter, $AUC_{0\text{-}72h}$, of PTX in different compartments were calculated, as shown in ***Table 11***.

Apparently, the injected PTX from Taxol®, Abraxane® and HSA-PLA (PTX) formulations was systemically spread in the mice, as PTX was detected in and not limited to the mice plasma, tumours, hearts, livers, spleens, lungs and kidneys. The average 4T1 tumour weight in this biodistribution study was lower than 300 mg, therefore, only a small portion (less than 1%) of the injected PTX from three PTX formulations was delivered to the tumour site based on the bar chart of the 1-h post injection in ***Fig 63***. This underutilization of hydrophobic therapeutic ingredients is a common and significant issue in therapy. Literature reports suggest that nearly 99% of the injected nanomedicine dose is eliminated by the liver and spleen [215,216].

At the 1-hour post-injection of the PTX formulations (***Fig 63***), around 15% of the injected Taxol® and more than 20% of the injected Abraxane® and HSA-PLA (PTX) were captured by the liver (liver weights were around 1 gram). A noteworthy study

[89] has revealed the mechanism for the clearance of the nanoparticles by the liver, where scientists consider that the flow velocity of the nanoparticles in the liver blood vessels is retarded up to 1000 fold in comparison to the blood flow in the normal systemic circulation. As a result, the frequency of the interaction between nanoparticles and hepatic cells is sharply increased. Meanwhile, in their study [89], they found that the uptake of nanoparticles by the hepatocytes was associated with the particle size and the larger nanoparticles were preferentially taken up by the hepatocytes. Their findings offer an explanation for the lower volume of distribution of PTX from Taxol® injections in rats and mice compared to other paclitaxel formulations at the same dose , see ***Table 10***.

The plasma $AUC_{0\text{-}72h}$ values of the Taxol® injection in rats and mice are statistically higher than the plasma $AUC_{0\text{-}72h}$ values of the Abraxane® and the HSA-PLA (PTX) in rats and mice, respectively, ($p < 0.01$). The smaller hydrodynamic diameter of the Taxol® micelles in aqueous media (11 ± 4 nm, see ***Table 7***) may contribute to the less sequestration of PTX in the liver, thereby the circulation time of the Taxol® micelles is prolonged. Consequently, more injected PTX from the Taxol® is allowed to be delivered to the tumour via the EPR effect when compared with the Abraxane® (125 ± 4 nm). The tumour $AUC_{0\text{-}72h}$ value of the Taxol® injection is 120.27 ± 4.35 μg.h g^{-1}, significantly higher than the tumour $AUC_{0\text{-}72h}$ value of the Abraxane® injection 90.05 ± 12.4 μg.h g^{-1}, $p < 0.5$. A higher tumour $AUC_{0\text{-}72h}$ value of the injected PTX indicated that the tumour is exposed

to more paclitaxel molecules. Consequently, in tumour-bearing mice models, intravenous administration of Abraxane® did not exhibit a superior tumoricidal effect compared to intravenous administration of Taxol® at the same PTX dose, which is consistent with the *in vivo* data of the publication [136] of Yuan et al. as well as our pilot anticancer study.

The current hypothesis aims to create a nanocarrier with higher colloidal stability compared to the Abraxane®, reducing unnecessary loss upon dilution in the bloodstream. The DLVO theory is used to explain the poor colloidal stability of the Abraxane® nanoparticles at low concentrations. The changes in the hydrodynamic diameter of the Abraxane® nanoparticles with the decreasing concentration have been recorded in ***Fig 48. B***. The Abraxane® nanoparticles start to disintegrate below a concentration of 0.3 mg/mL (eq. PTX 30 µg/mL). Therefore, the Abraxane® nanoparticles become unstable when its concentration falls below 0.3 mg/mL (eq. PTX 30 µg/mL), while the HSA-PLA (PTX) nanoparticles remain stable at a concentration of 0.01 mg/mL.

As a result, the plasma $AUC_{0\text{-}72h}$ values for the HSA-PLA (PTX) in rats (4.0 ± 1.0 µg.h mL^{-1}) and mice (23.02 ± 1.71 µg.h mL^{-1}) are significantly higher ($p < 0.5$) than the plasma $AUC_{0\text{-}72h}$ values of the Abraxane® in rats (2.2 ± 0.5 µg.h mL^{-1}) and mice (16.12 ± 2.46 µg.h mL^{-1}). Consequently, the HSA-PLA (PTX) nanoparticles are able to deliver a significantly higher amount of PTX to tumours when compared to the Abraxane®, the tumour $AUC_{0\text{-}72h}$ value of the HSA-PLA

(PTX) (128.64 ± 3.41 μg.h g^{-1}) is significantly higher ($p < 0.01$) than the tumour $AUC_{0\text{-}72h}$ value of the Abraxane® (90.05 ± 12.4 μg.h g^{-1}). Moreover, the HSA-PLA (PTX) nanoparticles exhibit a similar organ clearance pattern to the Abraxane® nanoparticles. As shown in ***Fig 62***, the clearance rate of the injected Taxol® in different organs was significantly lower than that of the injected Abraxane® and HSA-PLA (PTX) nanoparticles. This suggests that Taxol® potentially induces higher systemic toxicity and more severe organ damage compared to Abraxane® and HSA-PLA (PTX) nanoparticles. Furthermore, the clearance rates of the HSA-PLA (PTX) nanoparticles from mice's hearts, livers, spleens, lungs, and kidneys are similar to those of the injected Abraxane® nanoparticles, indicating that the HSA-PLA (PTX) nanoparticles may also offer the advantage of low systemic toxicity.

Table 11. The pharmacokinetic parameter, $AUC_{0\text{-}72h}$, of different paclitaxel formulations in terms of mice plasma, tumours and organs. Data are expressed as mean ± SD (n = 3). *, $p < 0.05$. **, $p < 0.01$ vs Abraxane®. ##, $p < 0.01$ vs. HSA-PLA (PTX).

$AUC_{0\text{-}72h}$	Units	Taxol®	Abraxane®	HSA-PLA (PTX)
Plasma	µg.h mL^{-1}	52.91 ± 10.56**##	16.12 ± 2.46	23.02 ± 1.71*
Tumour	µg.h g^{-1}	120.27 ± 4.35*	90.05 ± 12.4	128.64 ± 3.41**
Heart		106.50 ± 28.74	41.53 ± 11.75	34.32 ± 3.03
Liver		466.75 ± 75.87	237.51 ± 55.15	254.95 ± 13.23
Spleen		157.87 ± 15.64	41.16 ± 5.96	43.35 ± 3.00
Lung		94.81 ± 7.83	26.14 ± 3.39	35.95 ± 2.05
Kidney		198.98 ± 33.78	63.13 ± 9.73	66.56 ± 8.11

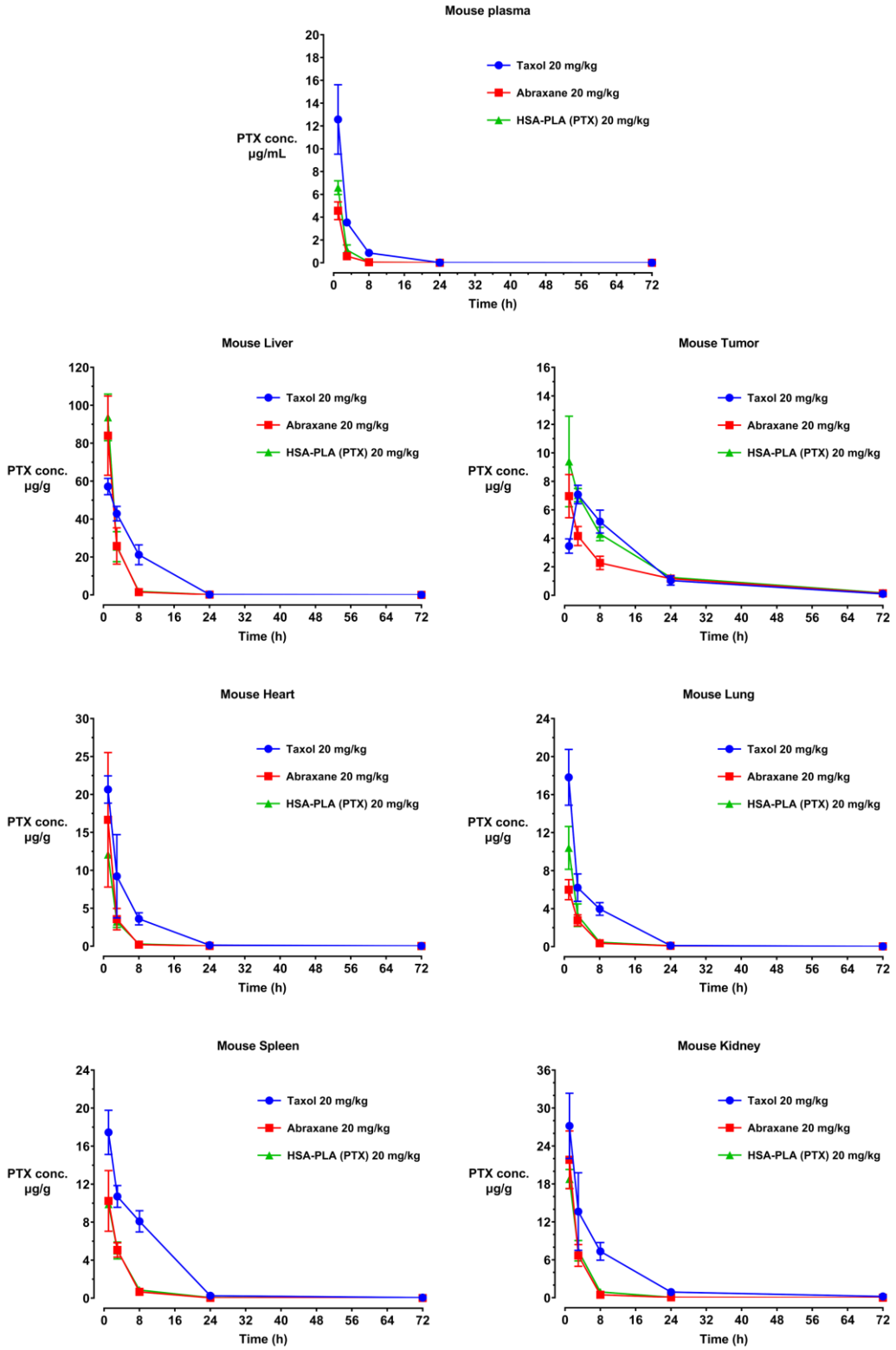

Fig 62. Pharmacokinetic profiles of PTX concentration versus time post-injection for mice plasma and different tissue compartments. 4T1 tumour-bearing mice were intravenously injected with Taxol®, Abraxane® and HSA-PLA (PTX) at 20 mg kg^{-1} PTX, respectively. Data are expressed as mean ± SD, n = 3.

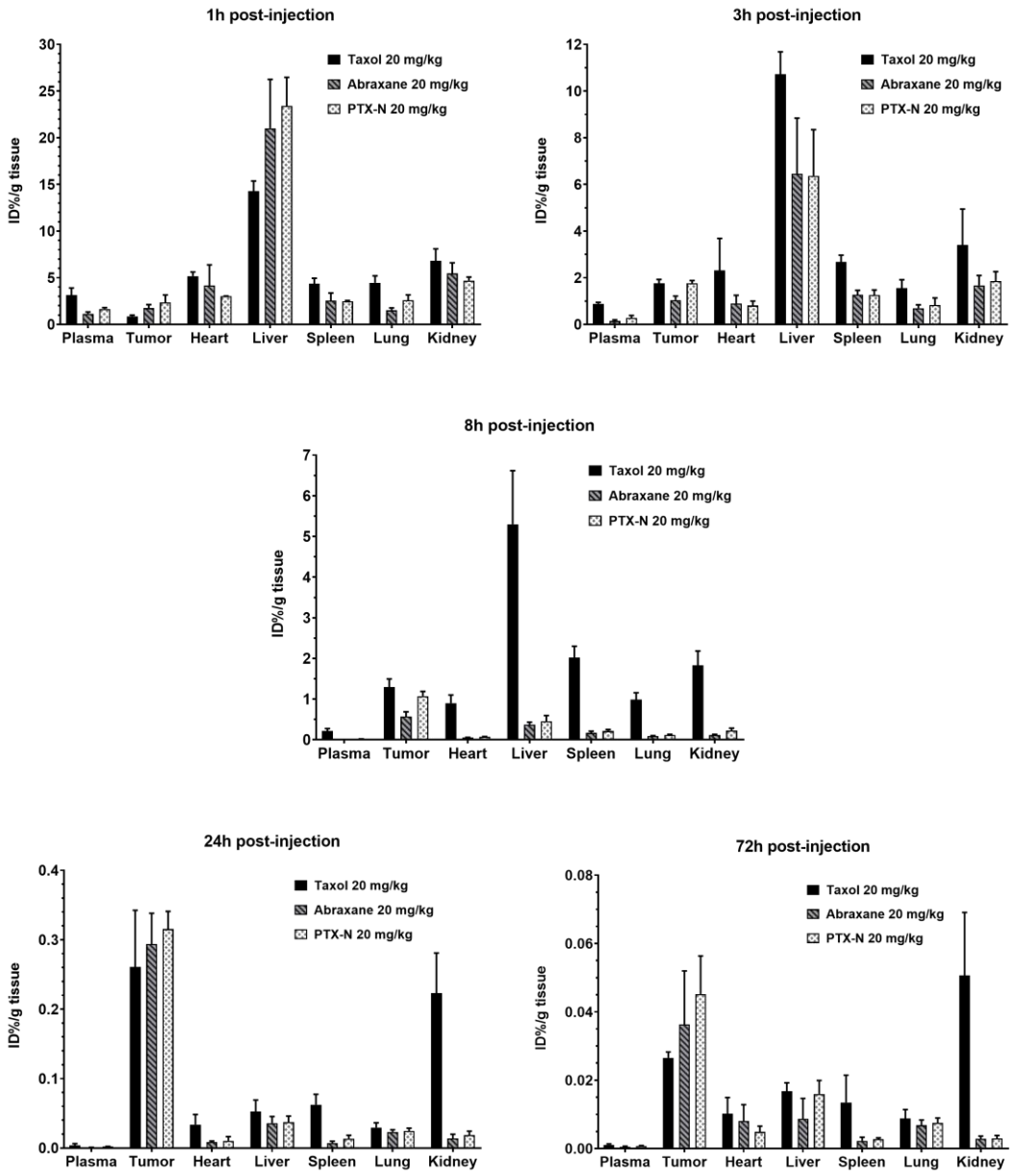

Fig 63. Bar charts of the percentage of the injected PTX in per gram tissue at different time points post-injection. The biodistribution of the injected Taxol®, Abraxane® and HSA-PLA (PTX) nanoparticles in 4T1 tumour-bearing mice at different time points after the intravenous administration of each PTX formulation at the dose of PTX 20 mg/kg. Due to the EPR effect, the PTX levels in tumour are higher than PTX contents in organs at the 24-h and 72-h post-injection. Data are expressed as mean ± SD, n = 3.

4.4.5 In vivo anti-tumour study

To further evaluate the potential influence of nanoparticles' colloidal stability on the tumoricidal effects of albumin-based nanomedicine, an *in vivo* anti-tumour study involving Taxol®, Abraxane®, and HSA-PLA (PTX) was conducted on mice bearing 4T1 tumours. Determined by the preliminary investigation, the maximum tolerated dose of Taxol® administered intravenously to mice with 4T1 tumours was established at 20 mg/kg PTX per dose. It was also noted that multiple IV injections of HSA/saline, Taxol®, HSA-PLA (PTX), or Abraxane® (three or more separate injections) might potentially lead to fatal anaphylactic shock in BALB/c female mice.

Therefore, in the formal study, each mouse received only two injections of the PTX formulation to prevent triggering a severe immune response. The general method of this *in vivo* anticancer study, including the tumour implantation and the treatment regimes, are illustrated in ***Fig 64***.

Based on the PK studies of the Taxol® and the Abraxane® in rats and mice and a pilot anticancer study, it was established that the superiority of the Abraxane® over the Taxol® in non-immunodeficient animals primarily stemmed from its reduced toxicity rather than its effectiveness in delivering PTX. Consequently, the injection doses for Abraxane® and HSA-PLA (PTX) nanosuspensions in tumour-bearing mice were increased to 40 mg/kg PTX. Conversely, the dose for Taxol®

remained at 20 mg/kg due to its heightened toxicity.

According to the tumour growth curves (***Fig 65. A***), mice treated with the HSA-PLA (PTX) at PTX 40 mg/kg experienced significant suppression of tumour growth compared to those treated with the Abraxane® at the same PTX dose. The final tumour weight in the HSA-PLA (PTX) group measured 239.8 ± 43.0 mg, which was statistically smaller than the Abraxane® group's weight of 340.6 ± 62.8 mg ($p < 0.5$, ***Fig 65. C***). The reason for the better tumoricidal activity of the injected HSA-PLA (PTX) was explained in the pharmacokinetic studies, as the HSA-PLA (PTX) nanoparticles could deliver more paclitaxel to the tumours compared with the injected Abraxane® at an equivalent PTX dose. Although the tumour growth of the Taxol® treated group was inhibited when compared to the control group (HSA/saline), the body weights of mice in the Taxol® treated group continuously decreased due to the heightened systemic toxicity associated with the administration of Taxol® (***Fig 65. B***).

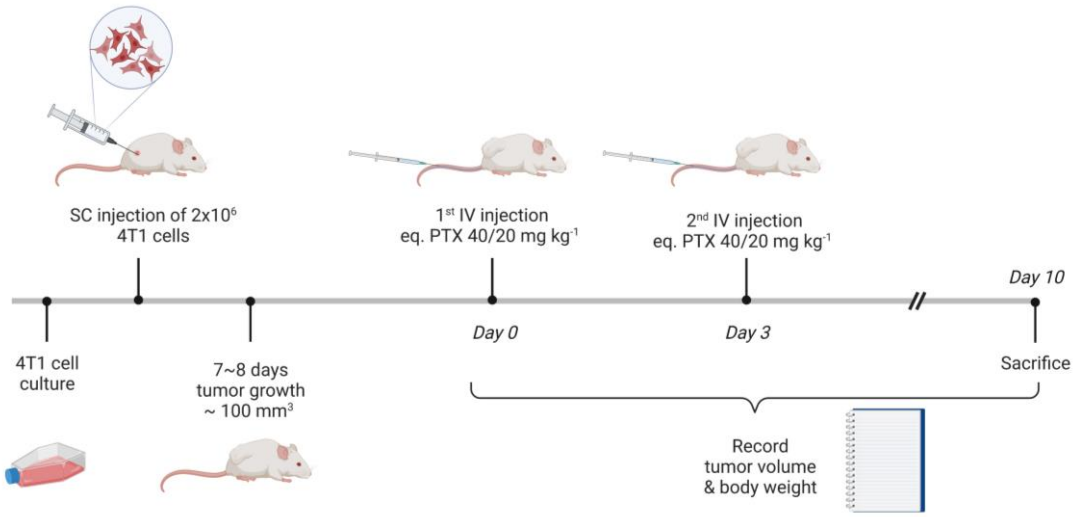

Fig 64. Schematic representation of the methodological flow of the *in vivo* anti-tumour study. The harvested 4T1 cells were subcutaneously injected at the right flank sites of BALB/c female mice. When the tumour volume was around 100 mm^3, the 4T1 tumour-bearing mice were treated with Taxol® (eq. PTX 20 mg/kg), Abraxane® (eq. PTX 40 mg/kg) and HSA-PLA (PTX) nanoparticles (eq. PTX 40 mg/kg) at Day 0 and 3, respectively. Note: the maximum tolerated dose (MTD) of the Taxol® to mice is 20 mg/kg PTX. While the MTDs of the Abraxane® and the HSA-PLA (PTX) nanoparticles to mice are higher than 50 mg/kg PTX. The difference of the MTDs between the Taxol® and the Abraxane® in this *in vivo* study is consistent with the clinical practice guidelines for the intravenous infusion of the Taxol® (175 mg/m^2) and the Abraxane® (300 mg/m^2) on patients. Created with BioRender.com.

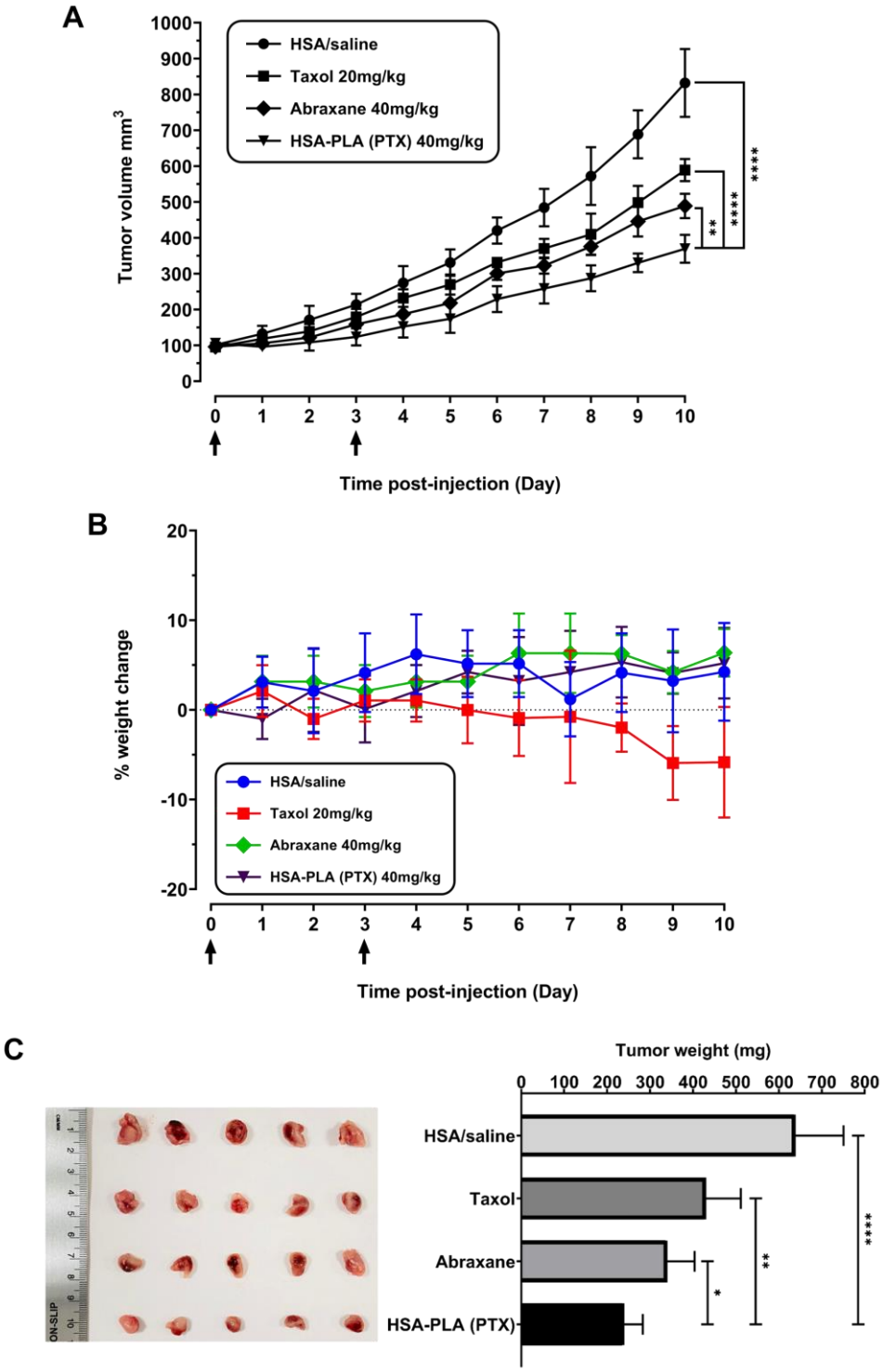

Fig 65. *In vivo* anti-tumour study. (**A**) Tumour growth curves of the 4T1 tumour-bearing mice with different treatments. (**B**) Percent weight change in mice after the first injection, where positive changes indicate weight gain and negative changes mean mice weight loss compared to their body weight at the time of the first injection. (**C**) Tumour size and weight in different treatment groups 10 days after injection. Data are expressed as mean ± SD (n=5). *, $p < 0.05$. **, $p < 0.01$. ***, $p < 0.001$. ****, $p < 0.0001$.

4.5 Conclusion and outlook

To sum up, the decorated albumin nanocarrier (HSA-PLA polymeric micelle) has shown an outstanding colloidal stability when delivering paclitaxel. The higher colloidal stability of the HSA-PLA (PTX) nanoparticles improves the delivery efficacy of PTX to tumours when compared with the Abraxane®. Consequently, the tumoricidal efficacy of the injected HSA-PLA (PTX) nanoparticles has surpassed that of the injected Abraxane® when equal doses of paclitaxel are administered intravenously to mice with 4T1 tumours. Furthermore, in this part, Furthermore, this section has conclusively demonstrated, through the *in vivo* studies, that the therapeutic impact of Abraxane® on 4T1 tumour-bearing mice does not surpass that of Taxol® at the same PTX dose.

The high comparability of our PK studies with the NCL's nanomedicine report and the PK results from the preclinical studies with Taxol® and Abraxane® demonstrates the reliability of our data and methodology. The rapid decline of the injected PTX in experimental rats and mice and patient plasma indicates that Abraxane® does not inherit the long systemic circulation function of albumin. In the pilot anticancer study, multiple injections of the Abraxane® to mice might induce the fatal immune response on mice. By combining the data of the circular dichroism experiments (see ***Table 4***), it is evident that albumins underwent denaturation during the manufacturing and lyophilization processes, leading to

rapid elimination of PTX within albumin carriers in the bloodstream due to the mice's immune system being stimulated. The severe systemic toxicity induced by the injected Taxol® resulted in the weight loss of mice as well as a low maximum tolerated dose on mice.

Based on the findings of these in vivo studies, it is determined that the primary advantage of the injected Abraxane® over the injected Taxol® in cancer therapy is its reduced systemic toxicity rather than its efficiency in delivering PTX to tumours. It's noteworthy that our PTX formulation, HSA-PLA (PTX), not only shares the low toxicity attributes of the Abraxane®, but also exhibits similar PTX tumour deposition to that of Taxol® at equivalent PTX doses. This is attributed to the heightened colloidal stability of the HSA-PLA (PTX) nanoparticles.

For the future work, the stealth polymers can be used to coat the surface of the HSA-PLA (PTX) nanoparticles to prolong the blood circulation time of the encapsulated PTX. Suitable options include polyethylene glycol, EK10 polypeptide, dextran, or polyglycerol. Leveraging the amine groups on the surface of the HSA-PLA nanoparticles holds potential for linking with ligands that target tumours, thereby increasing PTX deposition within tumours. In addition, there's potential to encapsulate various other hydrophobic drugs within the HSA-PLA nanoparticles for different medical needs.

Chapter 5. Synthesis, characterization and *in vitro* and *in vivo* evaluation of a novel tumour targeted nanocarriers

5.1 Introduction

In 1986, Matsumura and Maeda [72] discovered an important phenomenon that the macromolecules preferentially accumulated in the tumour tissue and were slowly cleared from the tumour in animal models, an observation that they named the EPR (enhanced permeation and retention) effect. They also speculated that the EPR effect could extend to cancer patients with malignant tumours, presenting an opportunity to enhance the efficacy of chemotherapy. Indeed, numerous clinical studies [74] have since confirmed the existence of the EPR effect in cancer patients. Since the 1990s, the US Food and Drug Administration and the European Medicines Agency have already approved several nanomedicines [104] for the oncotherapy based on exploiting the EPR effect of malignant tumours to deliver active ingredients in a passively targeted manner.

However, the EPR effect in the malignant tumours is heterogeneous among cancer patients [73]. Moreover, currently available commercial nanomedicines offer limited benefits in terms of survival for cancer patients with low or negligible EPR effects [217]. Therefore, the heterogeneity of the EPR effect has been

proposed as an explanation for the different patient responses to nanomedicines. Furthermore, a meta-analysis focused on investigating nanoparticle delivery to tumour sites in animal models [215] revealed that approximately less than 1% of injected nanoparticles were actually present at the tumour locations. As a result, enhancing the delivery of active ingredients within tumours remains a significant challenge in the field of nanomedicine development [75]. This challenge underscores the reason why researchers have developed various strategies aimed at improving the delivery efficiency of nanomedicines.

In this chapter, a novel tumour-tropism drug delivery system was developed to increase the delivery of therapeutic payloads to malignant tumours. In 1897, Paul Ehrlich [102] proposed the ‘Side-Chain Theory’ to describe the phenomenon of a specific interaction between a particular substance and a cell surface side chain. Ehrlich later refined his theory in 1900, giving rise to the 'Receptor-Ligand Theory,' which forms the basis for targeted therapy. As time has progressed, targeted cancer therapies have become widely recognized. The current strategies for the targeted therapies are primarily based on the Ehrlich’s Receptor-Ligand Theory, and thus scientists have developed diverse nanocarriers decorated with different ligands to specifically bind with the receptors of target. Over the past decade, more than forty thousand research reports about actively targeted delivery have been published [98]. Nonetheless, it's notable that, excluding Antibody-drug conjugates, none of these targeted drug delivery systems have successfully

transitioned into clinical practice.

In this work the hydrophobic PLA chain was introduced to albumin cysteine groups to create HSA-PLA conjugates. Additionally, acetyl groups were introduced to the albumin L-lysine groups independently, serving to heighten the colloidal stability of the nanoparticles through the reduction of surface energy. These combined modifications resulted in the development of the Ac-HSA-PLA tumour-targeted drug delivery system, as shown in ***Fig 66***.

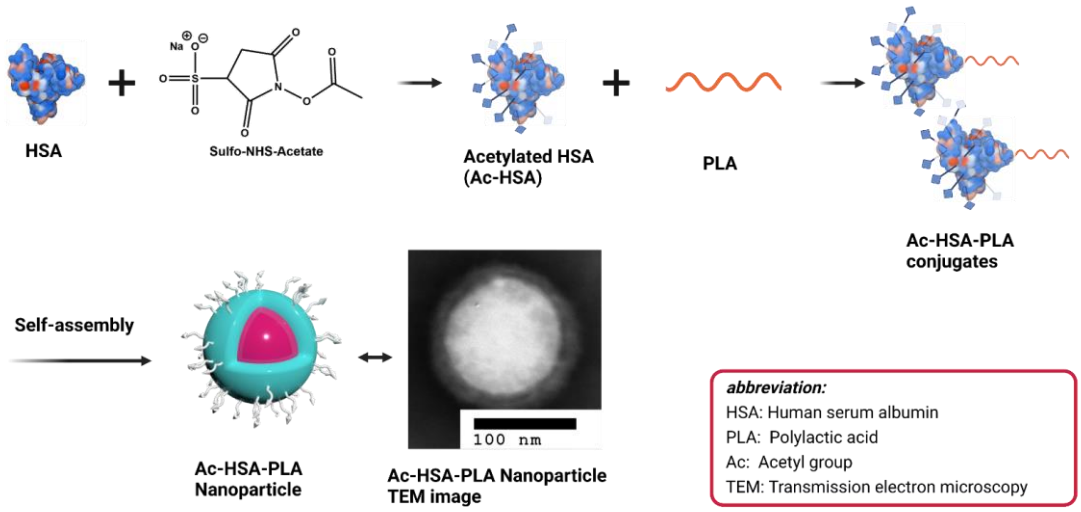

Fig 66. Schematic illustration for the preparation process of Ac-HSA-PLA polymeric micelles. After the acetylation of human serum albumin (Ac-HSA), the decorated albumin (Ac-HSA) can then interact with cell receptors, such as CD44 and folate receptors. By conjugating the hydrophobic polymer (PLA) to the acetylated albumin (Ac-HSA), the novel tumour-tropism nanocarriers, Ac-HSA-PLA nanoparticles, are created. Created with BioRender.com.

The initial hypothesis centred around acetylating the L-lysine groups of HSA to occupy the available free amine groups, ultimately leading to a more negatively charged protein structure. It was hypothesized this acetylated albumin (Ac-HSA) may be conjugated with the hydrophobic polymers (PLA) to create the amphiphilic

conjugates, Ac-HSA-PLA. These resultant Ac-HSA-PLA conjugates were expected to self-assemble into polymeric micelles, forming Ac-HSA-PLA polymeric micelles with a more negative zeta potential than their HSA-PLA counterparts. According to the DLVO theory, the colloidal stability of albumin nanoparticles would be thereby increased by making the particles more negative in their zeta potential. Notably, this hypothesis was proven and verified in this chapter.

What is even more remarkable is the discovery of the excellent cancer cell targeting affinity exhibited by the Ac-HSA-PLA nanoparticles. From the *in vitro* studies, it has been found that the cellular uptake of the Ac-HSA-PLA nanoparticles in the CD44 and folate receptor-enriched cells is largely enhanced when compared to HSA standards and albumin-based nanoparticles. This work is the first to discover that the acetylated albumins target uptake to MDA-MB-231 cells.

In this chapter, the synthetic process details, principles and the theoretical basis are introduced and discussed. The characterization of the Ac-HSA-PLA conjugates and the Ac-HSA-PLA polymeric micelles was determined by studies of MALDI-TOF, DLS, protein gel electrophoresis and TEM. The CMC of the Ac-HSA-PLA nanoparticles was also determined. The enhanced cellular uptake of the Ac-HSA-PLA nanoparticles in MDA-MB-231 cells (enriched with folate and CD44 receptors) was quantified by flow cytometry and visualized through

fluorescence microscopy. In addition, the enhanced MDA-MB-231 tumour uptake of the acetylated HSA-PLA nanoparticles was visualized by the IVIS® *in vivo* imaging system.

Techniques like MALDI-TOF, DLS, CMC measurements and TEM have been introduced in previous chapters. Generally, besides the zeta potential results from DLS, the native polyacrylamide gel electrophoresis (PAGE) protein separation technique was used to visually present the difference in net charges between the HSA-PLA and the Ac-HSA-PLA conjugates.

5.1.1 Introduction – Native polyacrylamide gel electrophoresis protein separation

Polyacrylamide gel electrophoresis (PAGE) techniques have been developed as highly reliable and common methods for isolating, identifying, and characterizing proteins and other biomacromolecules. Electrophoresis separates charged substances based on an electric field. In the case of PAGE, protein separation occurs due to the distinct electrophoretic mobilities of individual proteins under the same electric field [218]. Theoretically, proteins can be effectively separated during their migration from a cathode to an anode. The rate of movement for a charged analyte in the presence of an applied electric field is referred to as the electrophoretic velocity, v_{ep}.

Electrophoretic velocity: $v_{ep} = \mu_{ep}E$

Where μ_{ep} refers to the electrophoretic mobility of the sample and E is the magnitude of the applied electric field.

Electrophoretic mobility (μ_{ep}) is defined as the average electrophoretic migration rate of charged ions per unit field strength.

Electrophoretic mobility: $\mu_{ep} = \frac{q}{6\pi\eta r}$

Where *q* means the net charge of the analyte, η is the viscosity of medium, and *r* is the radius of the sample.

According to the equations of the electrophoretic mobility and velocity, two parameters, *q* and *r,* come from the intrinsical physicochemical properties of the analysed proteins. Therefore, on the basis of exploiting the molecular weights and net charges of proteins, the PAGE gel electrophoresis techniques have been developed into an SDS-PAGE application and a native PAGE application.

For the SDS-PAGE technique used in the separation of proteins, a surfactant, sodium dodecyl sulphate (SDS), is used to bind with the denatured proteins to create the negatively charged complexes. The addition of SDS leads to the similarity in net charges among various SDS-protein complexes during PAGE gel electrophoresis. Consequently, the separation of distinct proteins during electrophoresis relies on their respective molecular weights or sizes. Therefore, a denatured protein with a larger size migrates slower towards the anode.

In the application of the native PAGE, proteins are not denatured, and the surfactant is not used to homogenize the net charges of proteins. Therefore, the separation of different native proteins in the native PAGE gel electrophoresis is dependent on the ratios of their net charges to their sizes. As shown in ***Fig 67***, when the molecular weights of the analysed proteins are comparable, those with higher negative charges will exhibit a faster migration towards the anode from the cathode.

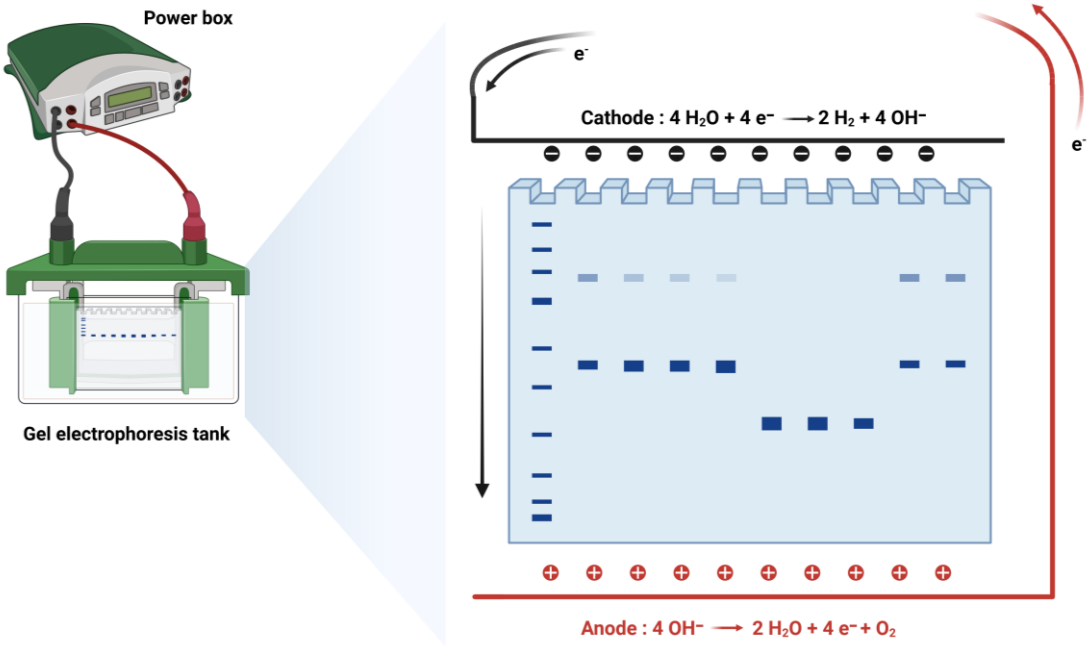

Fig 67. Schematic illustration of the protein separation in the gel electrophoresis tank. For the SDS-PAGE application, the separation of proteins is based on their molecular weights, smaller proteins move faster to the anode. In the native PAGE application, migration rates of the proteins are based on the ratios of the net charges to the mass of proteins. For example, when molecular weights of the proteins are similar, more negatively charged proteins will move faster to anode. Created with BioRender.com.

5.1.2 Introduction – Fluorescence microscopy

Fluorescence microscopy is an extensively used tool to rapidly image cells containing fluorescent information, including the detection of fluorescent proteins (green fluorescent protein) and the illumination of fluorescently labelled nanoparticles and organelles in cells. As shown in ***Fig 68***, the light from the LED passes through the excitation filter, illuminating a wide field within cells and exciting the fluorophores of fluorescent substances. The resulting intense emitted light is then collected by the detector.

Compared with a confocal laser scanning microscopy, the EVOS fluorescence microscopy possesses the ability to excite a wider cell area and capture a broader area of emitted light. Employing this technique allows for visualizing the cellular uptake of fluorescently labelled nanoparticles from a wider area of cells. This enhances the capacity to compare the cellular uptake of normal nanoparticles versus actively targeted nanoparticles, resulting in more robust cell images for analysis, without being confined to a small cell count.

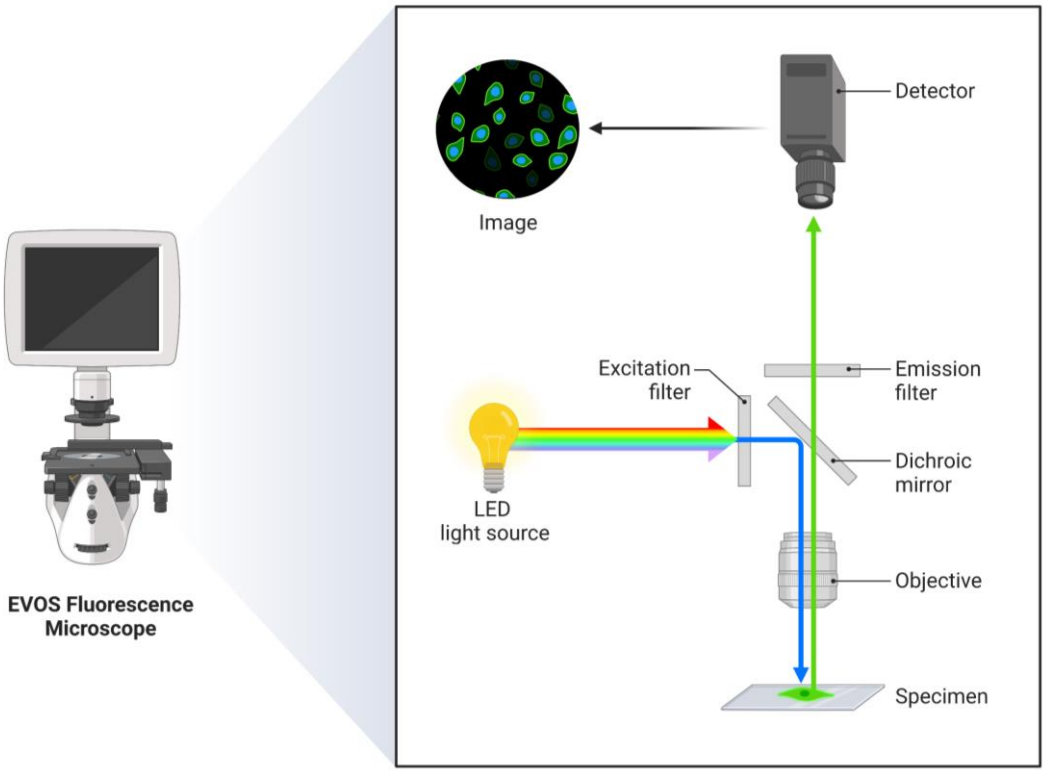

Fig 68. Schematic diagram of the workflow of an EVOS fluorescence microscopy. The parallel light beam passes through an excitation filter and then the light is focused on a wide field of sample plate. The resulting emission light is collected by the detector. Created with BioRender.com.

5.1.3 Introduction – Flow cytometry

Flow cytometry is a powerful technique for rapidly analysing the individual cells in terms of cellular size, granularity and fluorescence. The characteristics of each individual cell, such as its size, shape, and fluorescence intensity across various channels, are recorded and presented as events in a scatter plot within flow cytometry. The process of counting cells in a flow cytometer is depicted in the schematic workflow shown in ***Fig 69***. Cells from the injected cell suspension are

detected individually through the function of a fluidics system. Upon contact with the transmitted laser light, the cell's scattered laser light is received by a forward scatter (FSC) detector and a side scatter (SSC) detector, capturing information about the cellular size and shape. Concurrently, the fluorophores within the cells are excited by the laser, and the emitted light is detected by photomultiplier tube (PMT) detectors across different channels, where the fluorescence intensity of the emitted light is recorded.

Based on the recorded information of an individual cell, this data is represented as an independent event and visualized as a single point in the scatter plot of SSC versus FSC in flow cytometry. A larger FSC value indicates a bigger cell size, while the SSC value correlates positively with the cell's granularity or internal complexity. By combining the FSC and SSC measurements of a cell, the cell's morphology can be broadly described and classified within the scatter plot.

In this work, a fluorescent dye, fluorescein isothiocyanate (FITC), was used to covalently label the nanoparticles. By reading the fluorescence intensity of cells that treated with different FITC labelled nanoparticles, the association between different nanoparticles and cells was quantified and compared. By circling the population of live cell events in the SSC-FSC scatter plot, the average FITC fluorescence intensity of cells can be read as a specific number. Thus, a higher FITC fluorescence intensity reading in a cell suggests a more intense interaction between nanoparticles and cells.

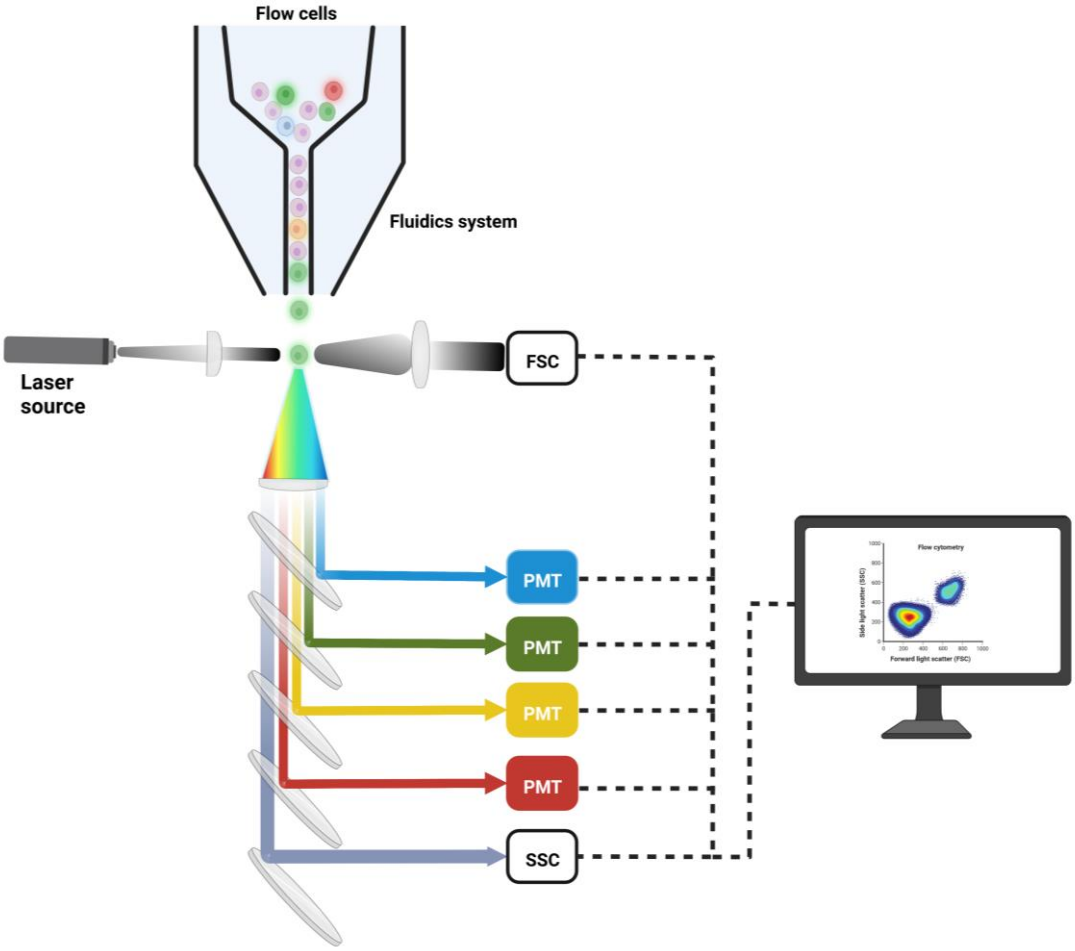

Fig 69. Schematic diagram of the workflow of a flow cytometer when counting cells and recording cellular information. By using a fluidics system, the injected cells pass through the detector one by one. The scattered light is received in a forward scatter and side scatter detectors, which encode the information into the size and granularity of the cells. Meanwhile, the emissions from the different fluorescent dye treated cells are recorded by different PMT detectors in different channels. As a result, the fluorescence intensity of the cells is recorded and converted into a specific number. Created with BioRender.com.

5.1.4 Introduction – IVIS Spectrum Imaging System

The IVIS® spectrum imaging system is used for non-invasive detection and quantification of fluorescence or bioluminescence signals emanating from animals, tissues, or cells. The IVIS® spectrum imaging system is commonly utilized for applications involving 2D/3D bioluminescence imaging and 2D/3D fluorescence imaging.

For using the application of bioluminescence imaging, mice typically need to be transfected with a luciferase-expressing cell line. Subsequently, the Luc2-transfected cells in the mice can produce luciferase. The chemical luciferin is then specifically oxidized by the enzyme luciferase into oxyluciferin, emitting light at a wavelength of 560 nm during this oxidation process. Therefore, for bioluminescence imaging, mice need to be injected with the luciferin solution, and the resulting emission can be detected by a charge-coupled device (CCD) camera. Consequently, there is no requirement to use excitation light during bioluminescence imaging, and the autofluorescence of the animal does not need to be taken into account.

For the application of fluorescence imaging in the IVIS® Spectrum imaging system, the fluorophores of the injected fluorescent dyes need to be excited by an excitation light. Subsequently, the emitted light is captured by a CCD camera, as shown in ***Fig 70***. In order to minimize the influence from the autofluorescence

of the animal fur, the near infrared (NIR) fluorescent dyes are more suitable for the *in vivo* and *ex vivo* fluorescence imaging.

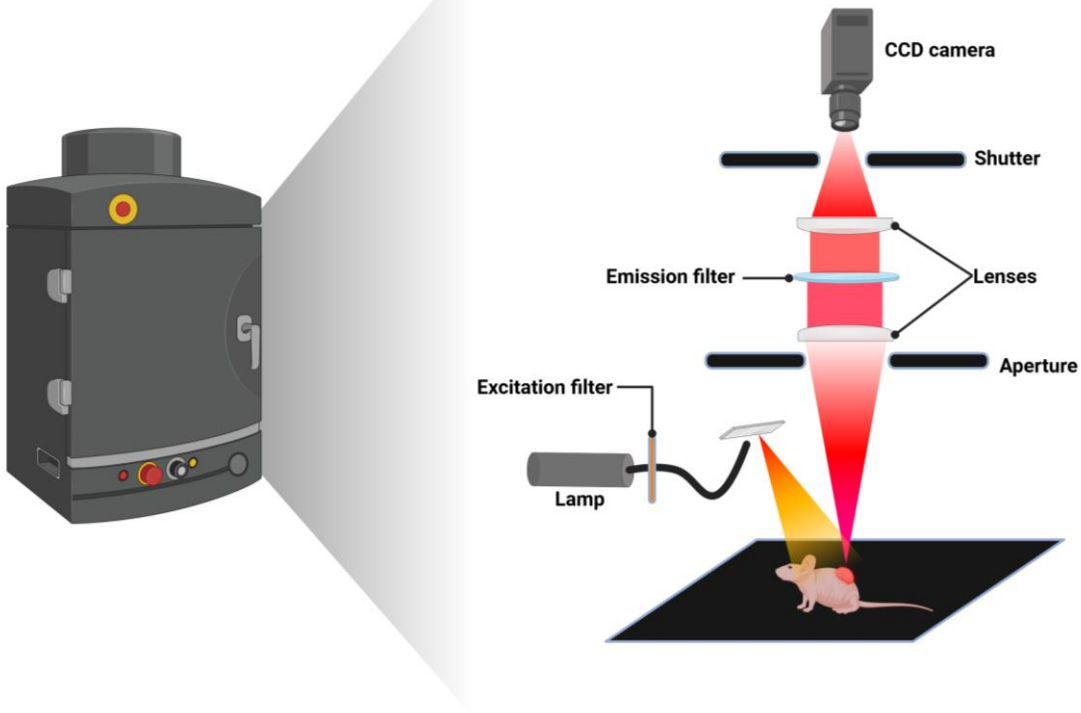

Fig 70. Schematic diagram for the fluorescence imaging of a tumour bearing nude mouse in the IVIS® spectrum imaging system. The generated excitation light is focused on the specific area, the resulting emission light from sample is collected by a CCD camera. A shutter is used to control the exposure time. Aperture settings are related with the resolution of the final image. Created with BioRender.com.

5.2 Materials, cell line and animal

Table 12. Materials, cell line and animal model used in the synthesis, characterization, *in vitro* and *in vivo* evaluation studies of the Ac-HSA-PLA nanoparticles.

Supplier	Materials, cell line and animal
Merck UK	Acetone puriss ACS reagent
	Coomassie Brilliant blue R 250
	Dimethyl sulfoxide (DMSO)
	3,5-Dimethoxy-4-hydroxycinnamic acid
	1,1′-Diethyl-4,4′-dicarbocyanine iodide
	Ethylenediaminetetraacetic acid (EDTA)
	Fetal Bovine Serum Heat Inactivated non-USA origin sterile-filtered
	Folic acid
	Human serum albumin (HSA) essentially fatty acid free
	Hyaluronic acid sodium salt from Streptococcus equi, mol wt 30-50k
	Phosphotungstic acid hydrate for microscopy
	Poly(L-lactide) N-2-hydroxyethylmaleimide terminated Mn 2000
	Pyrene, puriss. p.a for fluorescence ≥99.0%
	Sodium phosphate monobasic dihydrate (≥99.0%)
	Sodium phosphate dibasic heptahydrate (98-102%)
	Syringe-driven filter units (0.45µm)
Generon UK	Tris(2-carboxyethyl) phosphine Hydrochloride (TCEP•HCl)
Thermo Fisher Scientific UK	Acetonitrile (ACN, ≥99.9%, HPLC Gradient grade)
	Collagen Type I Cellware 22mm round Coverslips
	3,5-Dimethoxy-4-hydroxycinnamic acid, 98%

	Immersion Oil™ 518F
	Leibovitz's L-15 Medium
	Native Tris-Glycine Sample Buffer (2X)
	Novex Tris-Glycine Gels
	NucBlue™ Live ReadyProbes™ Reagent (Hoechst 33342)
	Paraformaldehyde Solution 4% in PBS
	Penicillin-Streptomycin solution 100X
	Phosphate Buffered Saline PBS pH 7.4
	Recovery™ Cell Culture Freezing Medium
	Slide-A-Lyzer™ Dialysis Cassettes 20K MWCO
	Sulfosuccinimidyl Acetate
	Trifluoroacetic acid (TFA, 99%)
	Tris-Glycine Native Running Buffer (10X)
	TrypLE™ Express Enzyme (1X) no phenol red
Biosynth Carbosynth	4-azidobenzoic acid (ABA)
BioLabs	Color prestained protein standard (11-245kda)
ELGA PURELAB®	Distilled water
ATCC	MDA-MB-231 (ATCC HTB-26)
Charles River Laboratories	NOD *SCID* mice – NOD.CB17-Prkdcscid /NCrCrl

All chemicals, reagents and solvents were used as purchased without any purification.

5.3 Experimental methods

5.3.1 Synthesis of Ac-HSA-PLA conjugates

All solutions used for synthesis were degassed overnight. Also all synthesis reactions in this section were carried out under the nitrogen protection.

Step 1: Acetylation of human serum albumin

A quantity of 1000 mg of HSA was dissolved in 150 mL of a phosphate buffer solution (0.1 mM, pH 8.0). Simultaneously, 1000 mg of sulfo-NHS-acetate was dissolved in 20 mL of distilled water, and this solution was added dropwise to the HSA solution. The resulting mixture was stirred magnetically at room temperature for 2 hours. Following acetylation, the acetylated HSA solution was transferred into a dialysis cassette (20K MWCO) and subjected to dialysis against distilled water for 48 hours. After the dialysis process, the solution was frozen overnight at -20°C, followed by lyophilization. The powder of acetylated HSA (Ac-HSA) was obtained after 48 hours of freeze-drying and was subsequently stored in a glass vial at room temperature.

Step 2: Releasing free sulfhydryl groups

An amount of 800 mg of the Ac-HSA powder was dissolved in 120 mL of a 0.1 M sodium phosphate buffer solution (pH 6.8, 1 mM EDTA), followed by the addition of 7 mL of a TCEP water solution (10 mg/mL) to the Ac-HSA solution. This mixture

was stirred using a magnetic stirrer for 4 hours in an ice bath, while being protected by a nitrogen atmosphere.

Step 3: Quenching TCEP reduction

A volume of 0.5 mL of DMSO containing 50 mg of 4-azidobenzoic acid was added dropwise to the reduced Ac-HSA solution. After allowing 10 minutes for quenching, 40 mL of a 0.2 M sodium phosphate buffer (pH 9.3) was added to neutralize any acidic by-products.

Step 4: Conjugating MAL-PLA to the Ac-HSA

The hydrophobic polymer maleimide-PLA (540 mg, Sigma-Aldrich, UK) was dissolved in 15 mL of DMSO and subsequently added to the reduced Ac-HSA solution mentioned earlier. The resulting mixture was then stirred using a magnetic stirrer for 4 hours in a 37°C oil bath, all while being protected under a nitrogen atmosphere.

Step 5: Purification and lyophilization

After the conjugation, the mixture was subjected to centrifugation for 5 minutes at 6000 rpm in 5 cycles using a Hermle Z232K Centrifuge (Hermle Labortechnik FmbH, Germany). The resulting supernatant was carefully transferred to a dialysis cassette with a molecular weight cutoff (MWCO) of 20K. Following 2 days of dialysis against distilled water, the nanosuspension underwent centrifugation again for 5 cycles at 6000 rpm for 5 minutes each. The purified nanoparticle suspension was rapidly frozen using a -20°C 25% (w/v) NaCl cooling medium.

Subsequently, it underwent a 48-hour lyophilization process in a freeze dryer (ALPHA 1-4 LDplus, Martin Christ, Germany). The resulting lyophilized powder was collected and stored in a glass vial at room temperature.

5.3.2 Determination of the molecular weight of albumin conjugates

The molecular weights of HSA standards, Ac-HSA, and Ac-HSA-PLA conjugates were determined using a Matrix-Assisted Laser Desorption-Time of Flight (MALDI-TOF) Mass Spectrometer (Bruker Daltonics, BD, Bremen, Germany). The matrix solution was prepared by dissolving an excess of 3,5-Dimethoxy-4-hydroxycinnamic acid (sinapinic acid) in a mixture containing 50% distilled water and 50% ACN (0.2% v/v TFA). Samples (100 pmol/μL) were diluted with the freshly prepared matrix solution (1:9 ratio), and then 1 μL of this resulting solution was applied to a MALDI sample plate. Additionally, 1 μL of the aldolase standard solution (A9096, Sigma Aldrich, UK) was also applied to the same site as an internal calibration standard. The reflector mode was selected to achieve a higher resolution mass spectrum.

5.3.3 Native PAGE protein separation

Sample preparation: 0.0125 mg of HSA, HSA-PLA and Ac-HSA-PLA lyophilized powders were dissolved in 1 mL of a 1X-tris-glycine native sample buffer solution (Novex™, Thermo Fisher Scientific Inc, UK), respectively.

Running buffer preparation: 100 mL of the 10X Tris-Glycine Native Running Buffer (Novex™, Thermo Fisher Scientific Inc, UK) was diluted with 900 mL of distilled water to prepare the 1X Native Running Buffer.

After assembling an XCell SureLock™ Mini-Cell gel tank, 5 µL of a ladder solution was added to the first cell of gel and then 40 µL of each sample solution was added to their respective cells of gel. The remaining space in the gel tank was filled with the prepared running buffer. The power was then set to 225V, and the gel electrophoresis was allowed to run for 40 minutes. Following the electrophoresis run, the gel was equilibrated in distilled water for 1 hour. To visualize the protein samples within the gel, a diluted Coomassie Brilliant Blue R-250 solution (light blue) was used for staining.

5.3.4 Determination of D_H, PDI and zeta potential

The hydrodynamic diameter, zeta potential and polydispersity index (*PDI*) of the Ac-HSA conjugate and Ac-HSA-PLA nanoparticles were determined via the dynamic light scattering (DLS) technique by using a Malvern Nano-ZS. A quantity

of 2 mg of each lyophilized sample was dispersed into 2 mL distilled water, the pH value of the acetylated albumin solution and the Ac-HSA-PLA nanosuspension was 7 (pH = 7). Each sample was measured in triplicate, and the testing was conducted across three different batches of samples for increased reliability.

5.3.5 Measurement of CMC of Ac-HSA-PLA polymeric micelles

The critical micelle concentration (CMC) of Ac-HSA-PLA polymeric micelles was determined by using the pyrene fluorescence method. A quantity (1.2 mg) of pyrene was dissolved in 1 mL of acetone to prepare a 5.93 mM pyrene stock solution, and then this solution was diluted to a 0.0593mM pyrene solution with acetone. Then 0.1mL of the 0.0593 mM pyrene solution was added to an empty amber glass vial and this glass vial was placed in the fume hood. After 30 min, the dried amber glass vial was filled with 10 mL of distilled water to prepare a 0.593 μM pyrene solution. A volume (550 μL) of the 0.593 μM pyrene solution was added to a glass cuvette and the Ac-HSA-PLA nanosuspension (at a concentration of 1 mg/mL) was added to this cuvette dropwise to get a series of sample concentrations from 5.425 to 90.91 mg/L. The spectra (water background subtracted) were obtained via an LS 45 luminescence spectrometer (Perkin Elmer, Germany) with the following parameters: excitation wavelength 340 nm, emission wavelength from 365 to 415 nm, scan speed 20 nm/min and 5 repeated scans per sample.

5.3.6 TEM imaging

The lyophilized powder of the Ac-HSA-PLA nanoparticles was dispersed in distilled water at a concentration of 5 mg/mL. A drop of the Ac-HSA-PLA nanosuspension was dripped onto a TEM grid. After 5 minutes, the excess water on the TEM grid was absorbed by the tissue papers. Then a drop of the 1% (w/v) neutral phosphotungstic acid solution was added to this TEM grid. After 1 min staining, distilled water was used to wash this copper grid to remove the excessive staining agent. The prepared TEM sample was stored in a dark place until imaging.

5.3.7 Cell culture of MDA-MB-231 cells

MDA-MB-231 cells were cultivated in a tissue culture flask equipped with a non-filter cap. The flask contained Leibovitz's L-15 medium, which was supplemented with 10% heat-inactivated fetal bovine serum (FBS) and 1% penicillin/streptomycin. The incubation took place in a controlled environment at 37°C, with a CO_2 concentration of 5% and humidity maintained at 95%.

5.3.8 EVOS fluorescence microscopy

The fluorescent dye coumarin-6 was respectively encapsulated in the HSA-PLA and the Ac-HSA-PLA nanoparticles according to a weight ratio of 0.5 mg dye to 10 mg nanoparticles, and the resulting dye loaded nanoparticles were recorded

as HSA-PLA (Cou-6) and Ac-HSA-PLA (Cou-6), respectively.

The collagen type I Cellware 22 mm round coverslips were placed in a 6-well plate (SARSTEDT, Germany). Approximately, 6×10^5 MDA-MB-231 cells in 4 mL of complete medium were seeded in each well of the above 6-well plate. These cells were then incubated at a temperature of 37°C until they achieved 80% confluence. The complete medium was subsequently aspirated, and the cells were washed twice with 5 mL of cold PBS (pH 7.4). Following the washes, a fresh FBS free medium was introduced to each well, with a volume of 3 mL.

After 4 hours starvation of cells at 37°C in an incubator, the coumarin-6 loaded nanoparticles were added to each well according to a final concentration of 0.5 mg nanoparticles per mL FBS free medium. Following a 3-hour incubation of cells with the dye-loaded nanoparticles, the medium containing them was aspirated and replaced with 3 mL of fresh FBS-free medium for each well. Next, 6 drops of a Hoechst 33342 solution were added to each cell well. After allowing 30 minutes for cell nuclei staining, the coverslips were carefully removed, washed with cold PBS (pH 7.4), and placed in a new 6-well plate. Subsequently, the cells on the coverslips were fixed using a 4% paraformaldehyde solution (2 mL) for 15 minutes on ice. A single drop of mounting medium was applied to each microscope slide. The washed coverslip was then positioned onto the microscope slide with the mounting medium and sealed using nail varnish. The cell images were captured using an EVOS Fluorescent Microscope (EVOS FLoid).

5.3.9 Flow cytometry

The MACSQuant® Analyzer 10 Flow Cytometer (Miltenyi Biotec Ltd, Germany) was used to measure the fluorescent intensity of the fluorescein isothiocyanate (FITC) labelled samples in cells.

Preparation of fluorescence-labelled nanoparticles and albumin standard

A quantity of 80 mg of HSA standard, HSA-PLA nanoparticles and Ac-HSA-PLA nanoparticles was dispersed in 10 mL of a phosphate buffer solution (0.1 mM sodium phosphate, pH 8.0), respectively. Subsequently, 2 mL of DMSO containing 2 mg of FITC was added dropwise to the aforementioned solutions. The resulting mixtures were then stirred using a magnetic stirrer at room temperature for a duration of 4 hours. By using the 0.45 μm syringe filters, the insoluble FITC can be removed. The resulting filtrates were respectively injected into a dialysis cassette (20K MWCO) for a 48-h dialysis against distilled water to remove salts, DMSO and the dissolved FITC molecules. Upon completion of the dialysis, the resulting yellow-colored liquids were frozen overnight within a -20°C freezer. Subsequently, a 48-hour lyophilization procedure was conducted using a freeze dryer (ALPHA 1-4 LDplus, Martin Christ, Germany). The resulting lyophilized powder was then collected and stored within an amber glass vial at room temperature.

Time dependent cellular uptake of the FITC labelled samples

The harvested MDA-MB-231 cells were seeded in a 12-wells cell culture plate according to a seeding density of 2 x 10^5 cells in 2 mL complete medium per well. After 15 hours of incubation, 2 mL of the complete medium was replaced with 1.5 mL of FBS-free medium. Subsequently, following a 4-hour incubation within a 37°C incubator, the FITC-labelled samples (FITC-HSA, FITC-HSA-PLA nanoparticles, FITC-Ac-HSA-PLA nanoparticles) were introduced into their respective cell wells at a concentration of 0.5 mg/mL. The FITC-labelled samples were then incubated with the cells for predetermined durations (1h, 3h, 5h, and 7h). Following incubation, the cells were subjected to three washes with PBS (pH 7.4) to eliminate any free FITC-labelled samples. Subsequently, 0.5 mL of TrypLE™ Express Enzyme (1X) was added to each well to detach the cells from the cell culture plate. To neutralize the TrypLE™ Express Enzyme, 1 mL of complete medium was introduced to each well. The resulting cell suspensions were individually filtered through a 40 µm cell sieve. After preparation, the cell samples were placed on ice and analysed using a flow cytometer.

Competitive assay – CD44 receptor

The harvested MDA-MB-231 cells were seeded in a 12-wells cell culture plate according to a seeding density of 2 x 10^5 cells in 2 mL complete medium per well. After 15 hours incubation, 2 mL complete medium was replaced with 2 mL FBS-free medium. Then after 4 hours equilibrium, medium was aspirated out and

replaced with 1 mL FBS-free medium and 0.5 mL PBS (pH 7.4) containing 1 mg FITC-HSA or FITC-HSA-PLA nanoparticles, or FITC-Ac-HSA-PLA nanoparticles and 0.5 mL FBS-free medium containing 0.25 mg, or 0.5 mg, or 1 mg, or 2 mg hyaluronic acid (HA). Following three hours incubation in a 37 ^{o}C incubator, medium was removed and cells were washed three times with PBS (pH 7.4). Next, 0.5 mL TrypLE™ Express Enzyme (1X) was added to each well to detach cells from the cell culture plate. Then 1 mL complete medium was added to each well to neutralize the TrypLE™ Express Enzyme, the resulting cell suspensions were respectively filtered through a 40 μm cell sieve. The prepared cell samples were placed on the ice and analysed by a flow cytometer.

Competitive assay – Folate receptor

Preparation of a folic acid (FA) stock solution: 10 mg of folic acid powder was transferred to 9.5 mL of FBS-free medium, and 0.5 mL of 0.1M NaOH was added to adjust the pH to 7.4 and solubilize the folic acid in the FBS-free medium.

The cell seeding procedures mirrored those described in the above part. After a 4-hour equilibrium period, the medium was aspirated and replaced with a combination of 0.5 mL of FBS-free medium, 0.5 mL of PBS (pH 7.4) containing 1 mg of FITC-HSA or FITC-HSA-PLA nanoparticles, or FITC-Ac-HSA-PLA nanoparticles, and 1 mL of FBS-free medium containing either 0.25 mg, 0.5 mg, or 1 mg of FA. Following three hours incubation, the cell sample preparation procedures were same with the part of ***'Competitive assay – CD44 receptor'***.

5.3.10 IVIS ex vivo imaging

Preparation of NIR dye labelled nanoparticles

The NIR dye used in this study was the 1,1′-Diethyl-4,4′-dicarbocyanine iodide. Through the paclitaxel drug loading approach, the aforementioned NIR dye was encapsulated within HSA-PLA nanoparticles and Ac-HSA-PLA nanoparticles, maintaining a weight ratio of 0.1 to 10 w/w between the NIR dye and nanoparticles. These NIR dye-loaded nanoparticles were denoted as HSA-PLA (Cy) and Ac-HSA-PLA (Cy) nanoparticles, respectively.

Subcutaneous implantation of MDA-MB-231 cells to mice

NOD-*SCID* female mice (6-8 weeks) were subcutaneously injected with MDA-MB-231 cells (2 x 10^6 cells per 100 µL DPBS) at the right flanks.

Preparation of samples for ex-vivo imaging

When the tumour volumes were approximately 500 mm^3, tumour bearing mice (n = 3 per group) were intravenously injected with the HSA-PLA (Cy) and the Ac-HSA-PLA (Cy) nanosuspension at a dose of NIR dye 20 µg per mouse, respectively. After 2h injection of the dye-loaded nanoparticles, mice were euthanatized. Subsequent to a 50 mL PBS heart perfusion, various tissues including plasma, brains, hearts, livers, spleens, lungs, kidneys, bones, and tumors were then extracted and imaged using an excitation wavelength of 700 nm and an emission wavelength of 790 nm in the IVIS® imaging system (IVIS

Lumina XRMS, PerkinElmer, Inc., US).

5.3.11 Statistics

Data are presented as the means ± SD (standard deviation). The student's t-test, one-way ANOVA and two-way ANOVA were used for the relative statistical analysis in Prism software. A value of $p < 0.05$ indicates a significant difference in the data.

5.4 Results and discussion

5.4.1 Synthesis of the Ac-HSA-PLA conjugate

As presented in ***Fig 71***, the NHS ester reaction was employed to bind to the available free amine groups on the lysine side chains of HSA. The acetyl group from the compound sulfo-NHS-acetate underwent a nucleophilic acyl substitution, transferring to the amine groups of HSA and resulting in acetylated HSA (Ac-HSA).

The subsequent synthetic steps followed a methodology similar to the HSA-PLA conjugate synthesis detailed in ***Chapter 2***. Briefly, the oxidated thiol group of the Cys-34 side chain of the Ac-HSA was reduced to a free sulfhydryl group by using a reducing agent TCEP. Then, the excess TCEP was neutralized through the addition of the quencher 4-azidobenzoic acid. Subsequently, the hydrophobic polymer maleimide-PLA was conjugated to the reduced Ac-HSA via a maleimide thiol click reaction to create Ac-HSA-PLA conjugates. The resulting Ac-HSA-PLA amphiphilic polymers self-assembled into polymeric micelles.

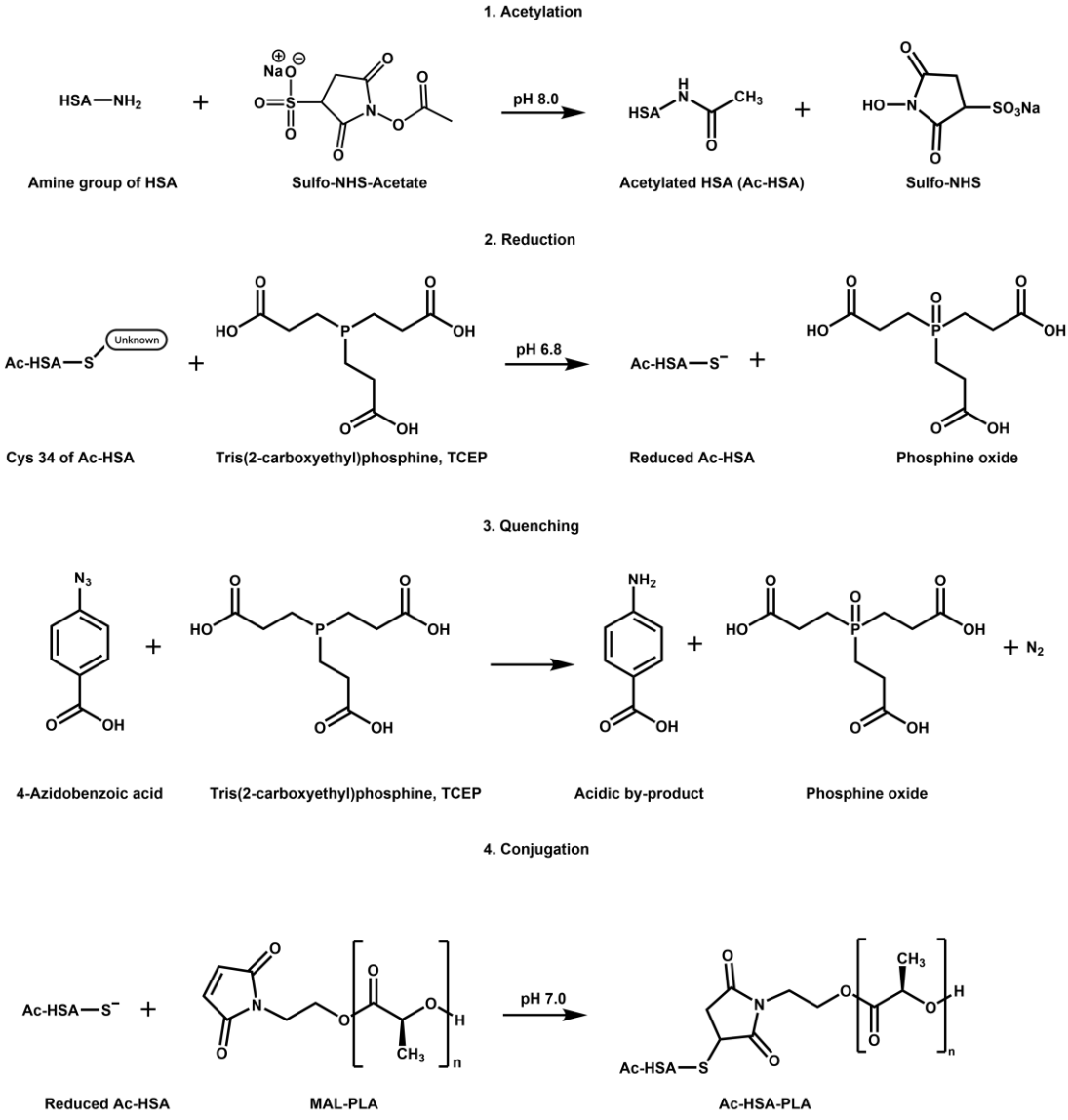

Fig 71. Chemical reactions in the synthetic process of acetylated albumin-polylactic acid conjugates (Ac-HSA-PLA). The sulfo-NHS-acetate is used to acetylate human serum albumin to create the acetylated human serum albumin (Ac-HSA). Next, the occupied Cys 34 side chain was reduced to the free sulfhydryl group by using a reducing agent TCEP. Then 4-azidobenzoic acid is added to neutralize the excess TCEP and release acidic by-products. At last, the hydrophobic polymer maleimide-polylactic acid is conjugated to the reduced Ac-HSA to create the Ac-HSA-PLA conjugates.

5.4.2 Characterization of Ac-HSA-PLA conjugates – MALDI-TOF

In this study, the MALDI-TOF technique was employed to determine the molecular weights of HSA standard, Ac-HSA conjugates, and Ac-HSA-PLA conjugates. The mass spectra representing HSA standard, Ac-HSA, and Ac-HSA-PLA were illustrated in ***Fig 72***. As an internal calibrator for precise molecular weight measurements of the HSA standard, Ac-HSA conjugates, and Ac-HSA-PLA conjugates, the aldolase standard (A9096, Sigma Aldrich, UK) was used. The documented molecular weight of HSA is 66.5 kDa, and the molecular weight of the HSA standard we measured is 66479 ± 35 Da. This high correlation between the documented molecular weight of HSA and molecular weight data of the HSA standard obtained from a MALDI-TOF mass spectrometer indicates that this MALDI-TOF method is suitable for the subsequent measurements of the Ac-HSA conjugates and the Ac-HSA-PLA conjugates.

The molecular weights of the HSA standard, the Ac-HSA conjugates and the Ac-HSA-PLA conjugates are 66479 ± 35 Da, 68374 ± 94 Da and 69638 ± 116 Da, respectively ($p < 0.0001$, see ***Fig 72***). The molecular weight of an acetyl group is 43 g/mol, approximately 45 acetyl groups were covalently bound to 45 amine groups of a human serum albumin molecule in average. (68374 - 66479)/(43-1) = 45.12

The acetylation of the human serum albumin can be controlled by decreasing or

increasing the addition of the sulfo-NHS-acetate. In practise, an *in vitro* pilot study revealed that the cellular uptake of the Ac-HSA-PLA nanoparticles in MDA-MB-231 cells may depend on the acetylation levels of HSA, with a higher acetylation level yielding a higher uptake of the nanocarrier. This finding will be further confirmed in the future work.

Based on the complete amino acid sequence of HSA (see ***Fig 14***), it's evident that an HSA protein encompasses 59 lysine amino acids, signifying the presence of 59 available free amine groups. Therefore, after the acetylation of HSA by the method in this chapter, there should be approximately 14 free amine groups available on an HSA molecule. As the fluorescent dye FITC needs to be covalently bound to the amine groups of the Ac-HSA-PLA nanoparticles in the *in vitro* studies, it is necessary to preserve some available free amine groups on the surface of the Ac-HSA-PLA nanoparticles. In the next chapter, HSA was fully acetylated to achieve an optimal targeting effect, thereby ensuring the highest possible delivery of PTX to MDA-MB-231 tumours *in vivo*.

The average molecular weight of the Ac-HSA-PLA conjugates (69638 ± 116 Da) was significantly increased when compared with the MW of the Ac-HSA conjugates (68374 ± 94 Da, $p < 0.0001$). The conjugation efficiency for the hydrophobic polymer PLA to the Ac-HSA was comparable with the data of the HSA-PLA conjugate synthesis.

In summary, employing this MALDI-TOF method allowed for the quantification

and comparison of increased molecular weights between the Ac-HSA and the Ac-HSA-PLA conjugates.

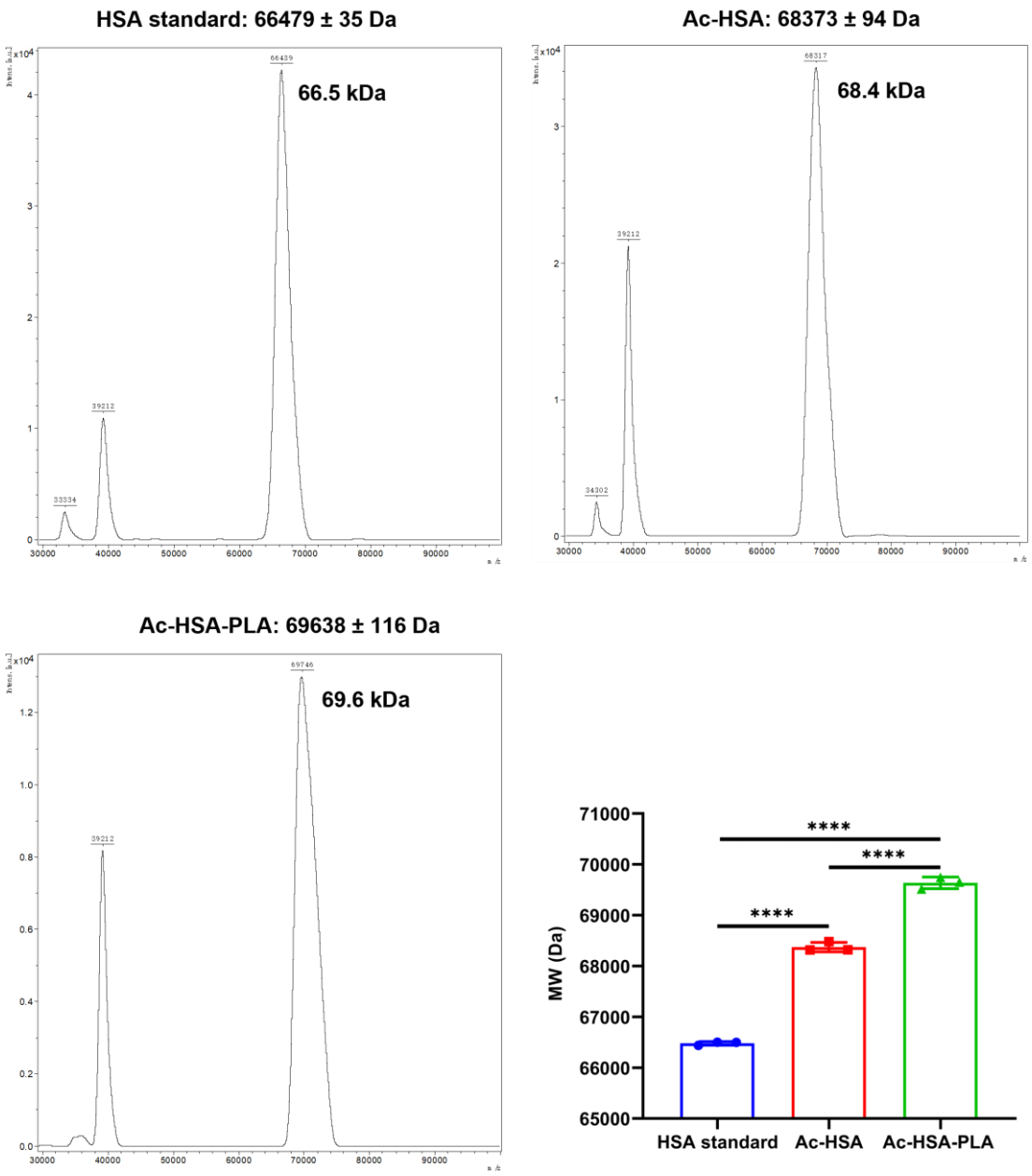

Fig 72. Mass spectra of HSA standard, HSA-PLA conjugate and Ac-HSA-PLA conjugate obtained from a MALDI-TOF mass spectrometer. After the acetylation, the molecular weight of the Ac-HSA is significantly higher than the MW of HSA, 66479 ± 35 Dalton vs. 68374 ± 94 Dalton, $p < 0.0001$. After the conjugation of the PLA to the Ac-HSA, the MW of the Ac-HSA-PLA was 69638 ± 116 Dalton, which is statistically higher than the MW of the Ac-HSA conjugate, $p < 0.0001$. Data are presented as means ± SD, n = 3, ****, $p < 0.0001$.

5.4.3 Characterization of Ac-HSA-PLA conjugates – Native PAGE

Based on the discussion in section ***5.1.1***, the PAGE gel electrophoresis technique can be used to analyse proteins and protein conjugates in terms of their molecular weights and net charges. The separation of proteins in the gel electrophoresis is based on the different electrophoretic mobilities in an applied electric field. The difference of the electrophoretic mobility is due to the different molecular weights and net charges of the different proteins. Therefore, by binding the negative charged surfactant SDS with proteins, the net charges of the different SDS-proteins are similar, and these denatured proteins bound with SDS are separated only according to their molecular weights in the SDS-PAGE applications.

The sample preparation for the native PAGE application excludes the denaturing and SDS-binding steps. Consequently, the separation of proteins in native PAGE gel electrophoresis relies on factors such as sample hydrodynamic size and net charge. In this particular native PAGE method, the sample concentration employed was 12.5 μg/mL, which remained below the CMC of both HSA-PLA conjugates (37 μg/mL) and Ac-HSA-PLA conjugates (35 μg/mL). This lower sample concentration led to the hydrodynamic sizes of HSA standard, HSA-PLA conjugates, and Ac-HSA-PLA conjugates being influenced primarily by their molecular weights. Although the molecular weight of the decorated albumins was

increased after the conjugation of PLA and acetylation steps. However, these molecular weight differences between HSA and HSA conjugates are insignificant in the gel electrophoresis. Therefore, the native PAGE technique could be used to differentiating the albumin conjugates in terms of their net charges, as shown in ***Fig 73***.

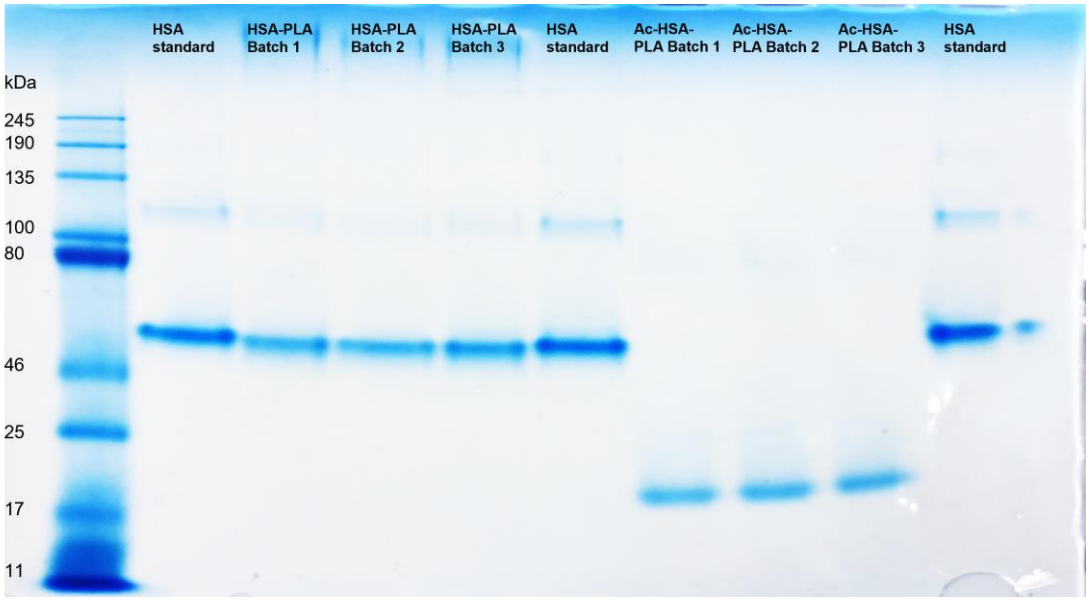

Fig 73. The native PAGE gel electrophoresis of human serum albumin and its conjugates. Proteins are visualized by the Coomassie blue staining.

The HSA standards used in this experiment were sourced from three distinct batches of commercial HSA (HSA-A1887, HSA-A3782, and HSA-A8763). Three major bands of the HSA standards are located between 46 kDa and 80 kDa in the PAGE gel and their dimers can be found between 100 kDa and 135 kDa, which proves that this gel electrophoresis method is reliable for the analysis of HSA and HSA conjugates. The synthesized HSA-PLA conjugates and Ac-HSA-

PLA conjugates from different batches were used to increase the reliability and reproducibility of the data and analysis. The band positions of HSA standards and HSA-PLA conjugates closely aligned, suggesting comparable size and net charge between the HSA-PLA free polymer and the HSA standard.

Contrastingly, the Ac-HSA-PLA conjugates migrated considerably faster than HSA standards and HSA-PLA conjugates, as evident in ***Fig 73***. As too many amine groups of albumins were occupied by the acetyl groups, then the net charges of the Ac-HSA-PLA conjugates were more negative. Thus, the Ac-HSA-PLA conjugates moved towards anode faster than the HSA standards and the HSA-PLA conjugates.

Lots of valuable information can be obtained from ***Fig 73***. Due to the relatively low sample concentration (12.5 μg/mL), HSA-PLA and Ac-HSA-PLA conjugates were represented as free amphiphilic polymers rather than nanoparticles in this study. From the native PAGE image, the band positions of the HSA standards and the HSA-PLA conjugates are similar, which indicate that their net charges are insignificantly different. The zeta-potentials of the HSA standards and the HSA-PLA nanoparticles are -12.6 ± 3.3 mV and -26.3 ± 0.5 mV, respectively ($p < 0.01$), see ***Table 14***. However, the net charge of the HSA standards is similar with the HSA-PLA conjugates. The different net charges of the HSA-PLA nanoparticles and the HSA-PLA conjugates further prove the hypothesis proposed in the ***Chapter 2***, more positively charged amino acids are encapsulated in the

hydrophobic core of the HSA-PLA polymeric micelles. Consequently, the HSA-PLA nanoparticles present a more negative zeta potential than that of the HSA standards. Based on this hypothesis, MAL-PLA was covalently bound with the Cys-34 residues of albumins, and the resulting HSA-PLA conjugates self-assembled into the HSA-PLA polymeric micelles with a CMC at a concentration of 37 μg/mL. Therefore, parts of the HSA adjacent to the PLA position, such as the amino acids from 1 to 210 (***Fig 74***), should be encapsulated within the inner core of the HSA-PLA nanoparticles. Based on the statistics on the amino acid properties of HSA (see ***Table 13***), it has shown that the expression level of the positively charged amino acids (Arg & His) in 1-210 part is higher than an average level (45.8% & 43.8% vs. 35.9%), while the negatively charged amino acids (Asp & Glu) expressed in the 1-210 part is closed to the average level (38.9% & 36.1% vs. 35.9%). In addition, the hydrophilic amino acids are highly expressed in the part of 376-585 (outer layer of the HSA-PLA polymeric micelles). According to these statistics, it is hypothesized that the PLA triggered nanoparticle formation did shield more positively charged amino acids from the contact with the outer environment. Consequently, the net charges of the HSA-PLA nanoparticles are more negative than those of the HSA-PLA conjugates.

Moreover, the band positions of the Ac-HSA-PLA conjugates in the native PAGE gel are horizontal, which imply that the acetylation of HSA is highly reproducible. The faster migration of the Ac-HSA-PLA conjugates indicates that the net charges

of the Ac-HSA-PLA conjugates are more negative than those of the HSA standards, corresponding with the zeta potential results of the HSA standards and the Ac-HSA conjugates, -12.6 ± 3.3 mV vs. -23.2 ± 2.5 mV, $p < 0.5$. Furthermore, the zeta-potential of the Ac-HSA-PLA nanoparticles (-33.5 ± 0.4 mV) is more negative than the Ac-HSA conjugates (-23.2 ± 2.5 mV), $p < 0.01$. Therefore, the negative shift in zeta potential triggered by the PLA conjugation in the synthesis of HSA-PLA nanoparticles is also consistent and repeatable for the synthesis of the Ac-HSA-PLA nanoparticles.

At last, from the results of the MALDI-TOF and the native PAGE gel electrophoresis for both HSA-PLA and Ac-HSA-PLA conjugates, the decorated albumins haven't been crosslinked or degraded in the synthesis. This is evident from the absence of multiple peaks in their mass spectra shown in ***Fig 72*** and the lack of any additional bands in the PAGE gel image in ***Fig 73***.

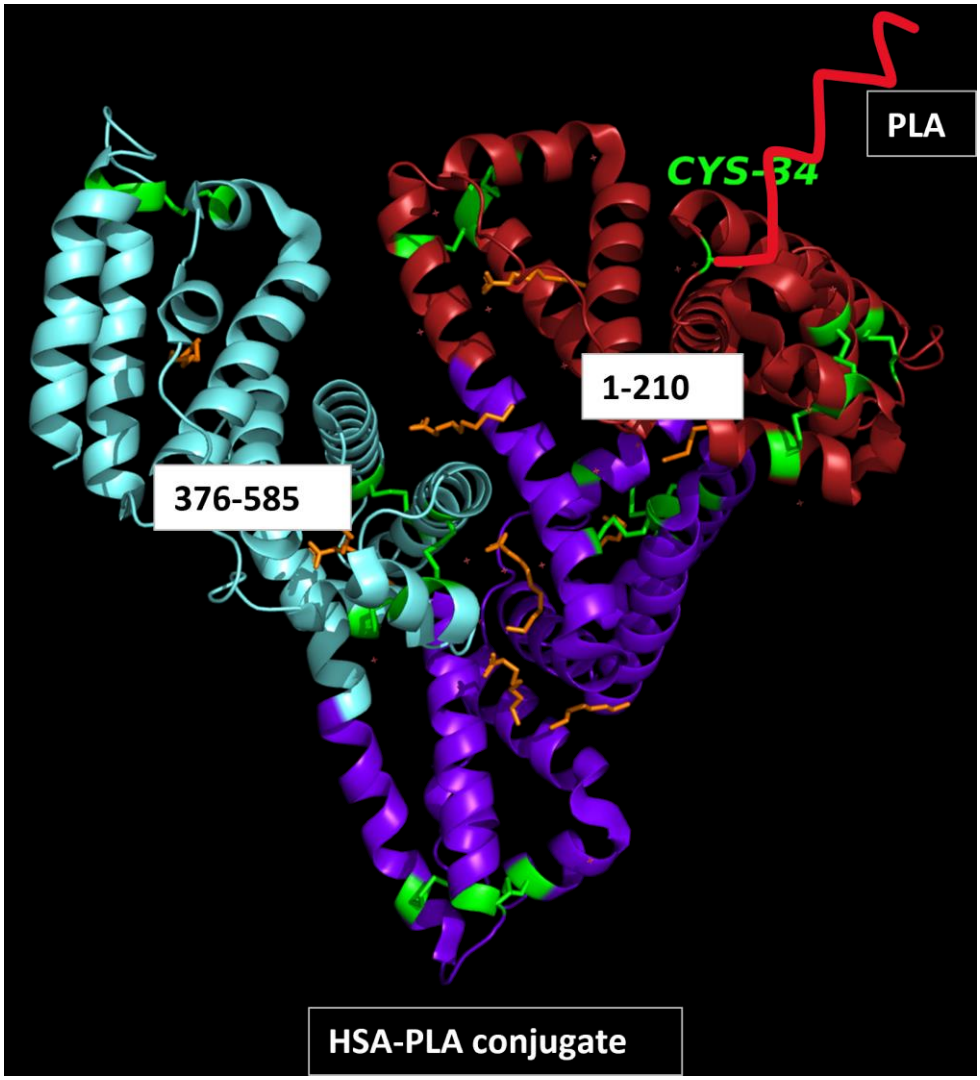

Fig 74. Estimated structure of the HSA-PLA conjugate. The positively charged amino acids are more expressed in the part of amino acid sequence 1-210. Therefore, more positively charged amino acids may be shielded during the formation of HSA-PLA polymeric micelles.

Table 13. Amino acids of HSA – physicochemical properties and position. The backbone of HSA is a single polypeptide chain comprising 585 amino acids.

Function of side chain	Amino acid	Quantity in 1-210	% of HSA Av. 35.9% (210/585)	Quantity in 376-585	% of HSA Av. 35.9% (210/585)
Positive charge	Arginine	11	45.8 (11 of 24)	7	29.2 (7 of 24)
	Histidine	7	43.8 (7 of 16)	4	25.0 (4 of 16)
Amine group	Lysine	19	32.2 (19 of 59)	25	42.4 (25 of 59)
Negative charge	Aspartic acid	14	38.9 (14 of 36)	8	22.2 (8 of 36)
	Glutamic acid	22	36.1 (22 of 61)	22	36.1 (22 of 61)
Thiol group	Cysteine	12	34.3 (12 of 35)	12	34.3 (12 of 35)
Aromatic group (π-π stack)	Phenylalanine	14	45.2 (14 of 31)	10	32.3 (10 of 31)
	Tyrosine	7	38.9 (7 of 18)	4	22.2 (4 of 18)
	Tryptophan	0	0 (0 of 1)	0	0 (0 of 1)
Hydrophobic group	Glycine	5	41.7 (5 of 12)	5	41.7 (5 of 12)
	Alanine	25	40.3 (25 of 62)	17	27.4 (17 of 62)
	Valine	10	24.4 (10 of 41)	20	48.8 (20 of 41)
	Proline	8	33.3 (8 of 24)	10	41.7 (10 of 24)
	Leucine	22	36.1 (22 of 61)	21	34.4 (21 of 61)
	Isoleucine	2	25.0 (2 of 8)	3	37.5 (3 of 8)
	Methionine	2	33.3 (2 of 6)	2	33.3 (2 of 6)
Hydrophilic group	Serine	6	25.0 (6 of 24)	9	37.5 (9 of 24)
	Threonine	9	32.1 (9 of 28)	13	46.4 (13 of 28)
	Asparagine	7	41.2 (7 of 17)	7	41.2 (7 of 17)
	Glutamine	8	38.1 (8 of 21)	11	52.4 (11 of 21)

5.4.4 Critical micelle concentration of Ac-HSA-PLA conjugates

The pyrene fluorescence method was utilized here to determine the critical micelle concentration (CMC) for Ac-HSA-PLA conjugates. By calculating the fluorescence intensity ratio of the peak at 372 nm (I_1) to the peak at 384 nm (I_3) and the curve of the ratio I_1/I_3 versus polymer concentration via a Boltzmann-Sigmoidal fitting was plotted (***Fig 75***).

Following the calculation, the CMC of the Ac-HSA-PLA polymeric micelles was found to be 35.21 ± 4.61 mg/L, which is equivalent to approximately 0.5 μM of Ac-HSA-PLA conjugates. Notably, the acetylation of HSA did not produce a significant alteration in the CMC of the Ac-HSA-PLA polymeric micelles when compared to the CMC of HSA-PLA polymeric micelles (35.21 ± 4.61 mg/L vs. 37.15 ± 3.31 mg/L). This suggests that the introduction of the acetyl group to HSA did not have a substantial impact on the CMC. Consequently, the formation of both HSA-PLA and Ac-HSA-PLA polymeric micelles is predominantly attributed to the conjugation of PLA to the Cys-34 position of the albumins.

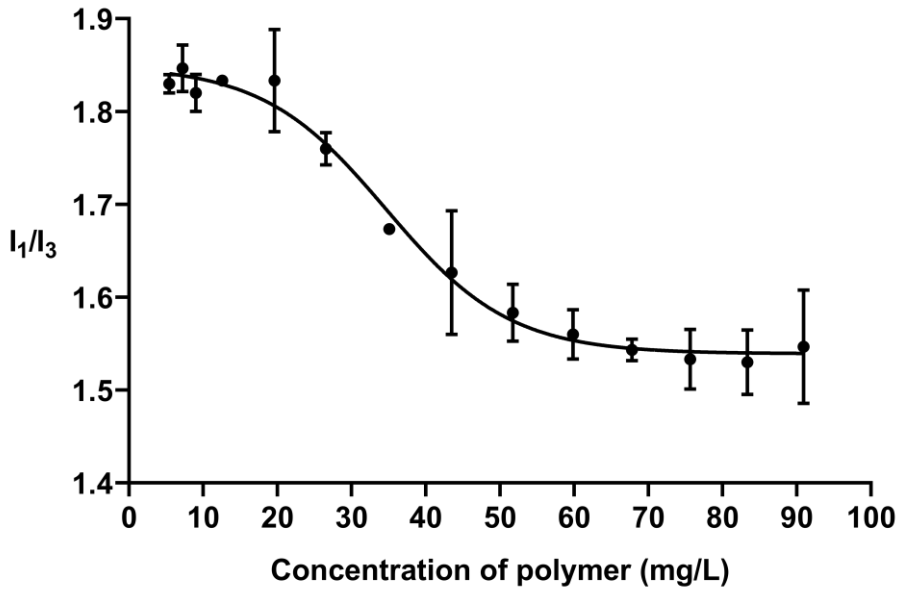

Fig 75. Critical micelle concentration measurements of the Ac-HSA-PLA polymeric micelles. The Sigmoidal-Boltzmann fitting curve of the fluorescence intensity ratio I_{372}/I_{384} versus the Ac-HSA-PLA polymer concentration.

5.4.5 Measurements of D_H, PDI and zeta-potential of albumin conjugates and nanoparticles

The dynamic light scattering (DLS) technique was used here to measure the hydrodynamic diameter (D_H), polydispersity index and zeta potential of the Ac-HSA conjugates and the Ac-HSA-PLA nanoparticles in the distilled water. As listed in ***Table 14***, a notable difference in hydrodynamic diameter was observed between the Ac-HSA-PLA nanoparticles (183 ± 6 nm) and the Ac-HSA conjugates (98 ± 50 nm), with a significance level of $p < 0.5$. The polydispersity index of Ac-HSA-PLA nanoparticles in water (0.05 ± 0.02) exhibited significant enhancement when compared to the polydispersity index of free Ac-HSA polymers in water

(0.45 ± 0.07), reaching a significance level of $p < 0.001$. In the native PAGE part, the fact was discussed that the conjugation of the hydrophobic polymer PLA to HSA did not significantly change the net charge of the HSA-PLA conjugates at low concentrations. The more negative zeta-potentials of the Ac-HSA-PLA nanoparticles than those of the Ac-HSA conjugates indicates that a large proportion of positively charged amino acids of the albumin conjugates were encapsulated in the core of the Ac-HSA-PLA polymeric micelles, -33.5 ± 0.4 mV vs. -23.2 ± 2.5 mV, $p < 0.01$. Compared with the HSA-PLA nanoparticles, more negative zeta potential m contributes to a more uniform dispersion of Ac-HSA-PLA nanoparticles in water, 0.05 ± 0.02 vs. 0.15 ± 0.05, $p < 0.5$.

Table 14. The comparison of the hydrodynamic diameter (D_H), PDI and the zeta-potential between albumin conjugates and nanoparticles. Data are presented as means ± SD (n = 3). *, $p < 0.05$. **, $p < 0.01$. ****, $p < 0.0001$. vs HSA standard. $^{\#}$, $p < 0.05$. $^{\#\#}$, $p < 0.01$. $^{\#\#\#}$, $p < 0.001$. vs the Ac-HSA conjugates.

Samples	D_H (nm)	*PDI*	Zeta potential (mV)
HSA standard	14.3 ± 7.7	0.57 ± 0.23	-12.6 ± 3.3
HSA-PLA NPs	170.0 ± 7.3****	0.15 ± 0.05*	-26.3 ± 0.5**
Ac-HSA conjugates	98.4 ± 50.4	0.45 ± 0.07	-23.2 ± 2.5*
Ac-HSA-PLA NPs	183.4 ± 5.8$^{\#}$	0.05 ± 0.02$^{\#\#\#}$	-33.5 ± 0.4$^{\#\#}$

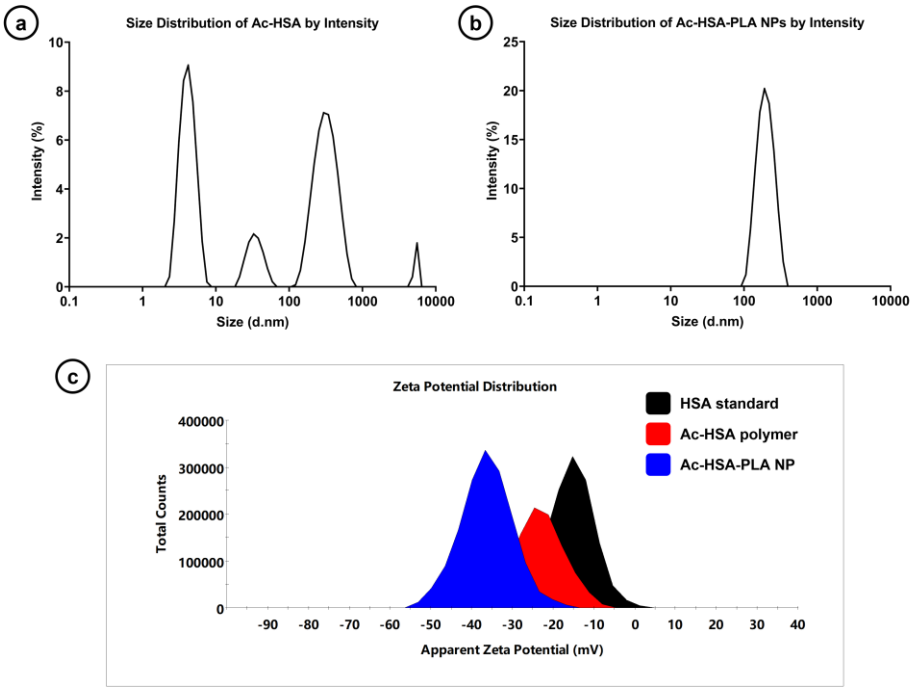

Fig 76. The size and zeta-potential distribution of the Ac-HSA-PLA nanoparticles in comparison of the HSA standard and the Ac-HSA conjugates. The hydrodynamic diameter distribution of **a**) Ac-HSA conjugates and **b**) Ac-HSA-PLA NPs and **c**) the zeta potential distribution of the HSA standard, Ac-HSA conjugates and the Ac-HSA-PLA NPs were obtained through a Malvern Nano-ZS instrument. The Ac-HSA conjugates are polydisperse in water. While after the conjugation of the PLA to the Ac-HSA polymer, the resulting Ac-HSA-PLA nanoparticles are monodispersed in water. The more negative zeta potential of the Ac-HSA-PLA nanoparticles than that of the Ac-HSA conjugates is due to more positively charged amino acids are shielded during the formation of nanoparticles.

5.4.6 TEM images

The wide field 2-D TEM images of the HSA-PLA nanoparticles and the Ac-HSA-PLA nanoparticles have been presented in ***Fig 77***.

Based on the TEM images, the morphology of the HSA-PLA nanoparticle and the Ac-HSA-PLA nanoparticle are spherical. In the ***Fig 77, A***, the TEM image of the HSA-PLA nanoparticles has clearly presented why the PDI of the HSA-PLA

nanoparticles (0.15 ± 0.05) is significantly higher than the PDI of the Ac-HSA-PLA nanoparticles (0.05 ± 0.02), $p < 0.05$. This discrepancy is attributed to the agglomeration of certain HSA-PLA nanoparticles, while others remain separate. This discrepancy in aggregation status results in varying hydrodynamic diameters between individual HSA-PLA nanoparticles and clustered HSA-PLA particle agglomerates, as demonstrated in ***Fig 21***. For the TEM image of the Ac-HSA-PLA nanoparticles, the Ac-HSA-PLA nanoparticles are well separated when compared to the HSA-PLA nanoparticles presented in the TEM image of the HSA-PLA nanoparticles.

The initial purpose for the acetylation of the HSA was to further reduce the surface energy of nanoparticles. As according to the theory of the thermodynamics, the agglomeration of nanoparticles is to reduce the interfacial area between the nanoparticles and media, as a result, the average surface energy for the nanoparticles in the particle cluster can be decreased. In terms of the theories of DLVO and thermodynamics, the more negative zeta potential of the Ac-HSA-PLA nanoparticles can provide a higher electrostatic repulsive force between nanoparticles. The less agglomerated morphology of the Ac-HSA-PLA nanoparticles indicates that the Ac-HSA-PLA nanoparticle may have a better colloidal stability when compared to the HSA-PLA nanoparticles.

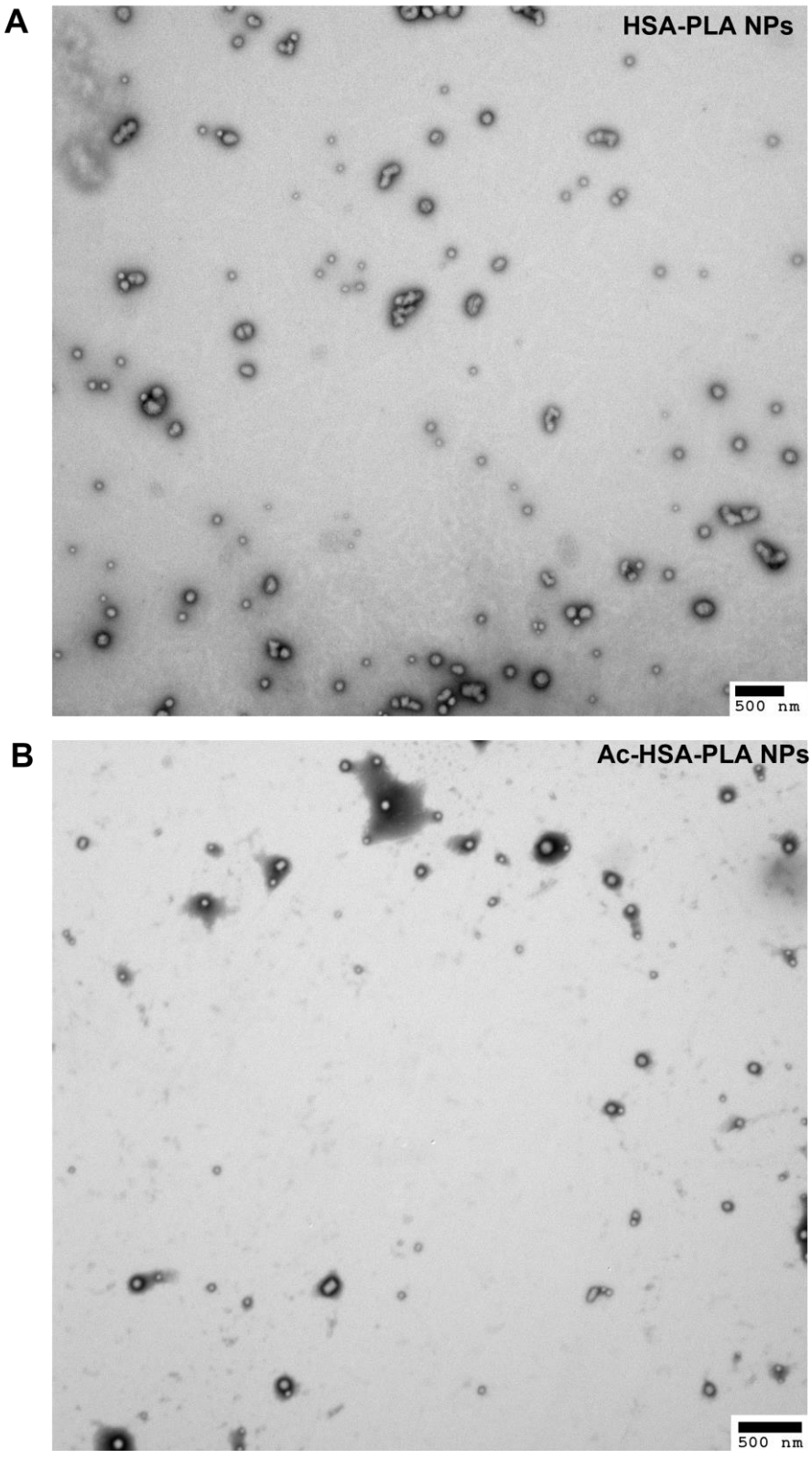

Fig 77. TEM images of the HSA-PLA nanoparticles (top) and the Ac-HSA-PLA nanoparticles (bottom). The lyophilized powders of nanoparticles were dispersed in distilled water at a concentration of 5 mg/mL. The 1% (w/v) neutral phosphotungstic acid solution was added to stain the nanoparticle on the TEM grids.

5.4.7 In vitro studies – Fluorescence imaging

To visualize the cellular uptake of the HSA-PLA nanoparticles and the Ac-HSA-PLA nanoparticles, a hydrophobic fluorescent dye, coumarin-6, was encapsulated in the nanoparticles. Briefly, the same quantity of the coumarin-6 was added to the HSA-PLA and the Ac-HSA-PLA nanoparticles and recorded as HSA-PLA (Cou-6) and Ac-HSA-PLA (Cou-6), respectively. Following a 3-hour incubation period of the fluorescent dye-labeled nanoparticles with MDA-MB-231 cells, EVOS fluorescence microscopy was employed to capture images of the MDA-MB-231 cells, as depicted in ***Fig 78***.

The cell nuclei of the MDA-MB-231 cells were stained with the Hoechst 33342. The Hoechst 33342 was excited by the light of a wavelength of 390 nm and the emitted blue light was filtered and detected by the detector at a wavelength of 446 nm. The coumarin-6 labelled HSA-PLA and Ac-HSA-PLA nanoparticles were excited by the light at a wavelength of 482 nm and thereby the green emission light was detected at a wavelength of 532 nm. As shown in ***Fig 78***, the blue spots represent the cell nuclei of the MDA-MB-231 cells and the green dots are due to the emitted light from the coumarin-6 labelled nanoparticles.

The cellular images clearly indicate the presence of both HSA-PLA (Cou-6) and Ac-HSA-PLA (Cou-6) nanoparticles within the MDA-MB-231 cells. The green signals emitted from the cells treated with the Ac-HSA-PLA (Cou-6) are denser

and stronger than those of the HSA-PLA (Cou-6) treated cells. There are certainly some additional interactions between the Ac-HSA-PLA nanoparticles and the MDA-MB-231 cells compared to the HSA-PLA nanoparticles.

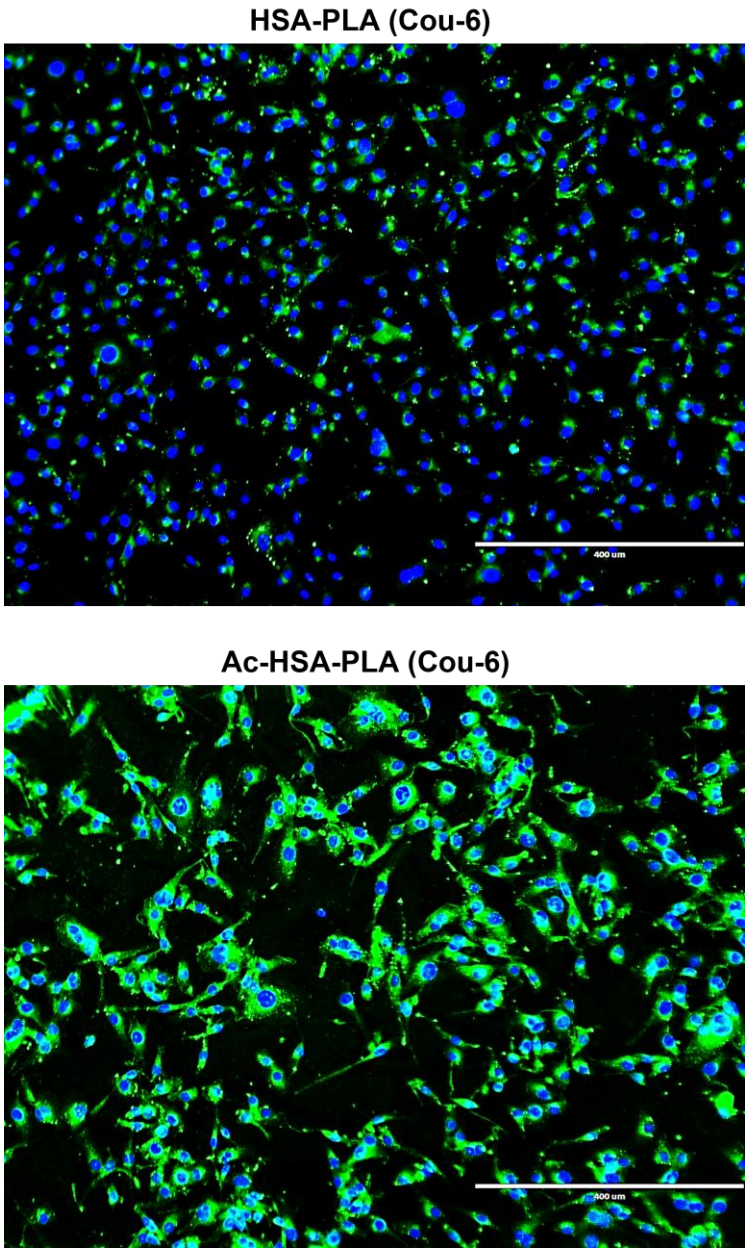

Fig 78. Fluorescence microscopy images of the MDA-MB-231 cells respectively incubated with the Coumarin-6 labelled HSA-PLA nanoparticles and the Coumarin-6 labelled Ac-HSA-PLA nanoparticles. Blue spots = cell nuclei and green dots = dye labelled nanoparticles. Coumarin-6 labelled Ac-HSA-PLA nanoparticles are taken up more efficiently by the cells.

5.4.8 In vitro studies – Flow cytometry

From the cell images of ***Fig 78***, the cellular association between the Ac-HSA-PLA nanoparticles and the MDA-MB-231 cells was enhanced when compared with the HSA-PLA nanoparticles. A flow cytometer was used to quantify the difference between the cellular association of the HSA-PLA nanoparticles and the Ac-HSA-PLA nanoparticles with the MDA-MB-231 cells.

Preparation of fluorescently labelled samples

Briefly, the fluorescent dye, fluorescein isothiocyanate (FITC), has been used to covalently conjugate with the amine groups on the HSA standard (***Fig 79***), the HSA-PLA nanoparticles and the Ac-HSA-PLA nanoparticles. These resulting FITC labelled samples are recorded as FITC-HSA, FITC-HSA-PLA nanoparticles and FITC-Ac-HSA-PLA nanoparticles, respectively. Due to the acetylation step of albumin, approximately 45 amine groups per HSA molecule are occupied. Consequently, the surface of Ac-HSA-PLA nanoparticles possesses a significantly reduced number of free amine groups in comparison to both HSA standard and HSA-PLA nanoparticles. This necessitates careful consideration when designing the FITC labelling procedure, ensuring that the amount of FITC used doesn't surpass what the Ac-HSA-PLA nanoparticles can react with.

Specifically, the HSA standard (80 mg, 1.20 μmol), the HSA-PLA nanoparticles (80 mg, 1.18 μmol) and the Ac-HSA-PLA nanoparticles (80 mg, 1.15 μmol) were

used to react with the FITC (2 mg, 5.1 μmol) in an alkaline buffer solution, respectively. In other words, the 1.2 μmol of the HSA standard is equivalent to the 70.8 μmol amine groups (59 x 1.20 μmol) which can be used to react with the 5.1 μmol isothiocyanate groups of the FITC (2 mg), and the 1.18 μmol of the HSA-PLA nanoparticles approximately have 41.8 μmol free amine groups (excluding the amine groups in the inner core) to react with the 5.1 μmol isothiocyanate groups of the FITC (2 mg), and the 1.15 μmol Ac-HSA-PLA nanoparticles roughly have 9.66 μmol free amine groups (excluding the amine groups in the inner core) to react with the 5.1 μmol isothiocyanate groups. Therefore, in theory, the FITC could be conjugated to the HSA standard, HSA-PLA nanoparticles and the Ac-HSA-PLA nanoparticles at a similar level under a same reaction condition.

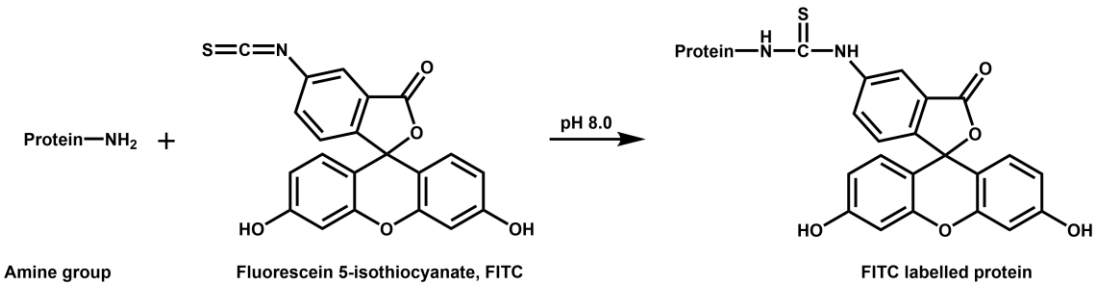

Fig 79. Chemical reaction between amine group and FITC. Under an alkaline condition, the fluorescent dye FITC is covalently bound to the amine groups of proteins.

Cellular uptake studies of different FITC labelled samples

The prepared FITC labelled samples (FITC-HSA, FITC-HSA-PLA nanoparticles and FITC-Ac-HSA-PLA nanoparticles) were used to determine the difference

between the cellular uptake of the HSA-PLA nanoparticles and the Ac-HSA-PLA nanoparticles in the MDA-MB-231 cells, as shown in ***Fig 80***.

To comprehensively evaluate the cellular uptake of the FITC-HSA, FITC-HSA-PLA nanoparticles and the FITC-Ac-HSA-PLA nanoparticles in the MDA-MB-231 cells, a flow cytometer was used to read the fluorescence intensity of cells that were treated with the different FITC labelled samples at predetermined incubation times, see ***Fig 80. A***. Following a two-way ANOVA analysis of the changes in fluorescence intensity of the cells over a seven-hour period, the cellular association of the FITC-Ac-HSA-PLA nanoparticles in the MDA-MB-231 cells is significantly higher than that of the FITC-HSA standard and the FITC-HSA-PLA nanoparticles, $p < 0.0001$. The tendency of the cellular uptake of the FITC-HSA and the FITC-HSA-PLA nanoparticles during a 7 h incubation is comparable. The differences between the FTIC intensity readings of the cells treated with the FITC-HSA and the FITC-HSA-PLA group are not significant, which further confirms that the FTIC was bound to the HSA standard and albumin based nanoparticles at a similar level. Notably, after 3-hour incubation, the fluorescence intensity readings of the cells from the FITC-HSA and the FITC-HSA-PLA groups are steady while the fluorescence intensity readings of the FITC-Ac-HSA-PLA group are decreased as shown in the ***Fig 80. A***. This decline suggests that the Ac-HSA-PLA nanoparticles might escape from the cells following their internalization. This hypothesis could potentially be confirmed through a endothelial permeability

assay in future experiments.

According to the ***Fig 80. A***, it is found that at a 3-hour incubation of the FITC-labelled samples with the MDA-MB-231 cells, the FITC intensity readings reach their peak. Subsequently, a detailed statistical analysis was performed on these readings, as illustrated in ***Fig 80. B & C***. The mean FITC intensity readings of the cells treated with the FITC-HSA, the FITC-HSA-PLA nanoparticles and the FITC-Ac-HSA-PLA nanoparticles are 2.48 ± 0.10, 2.22 ± 0.20 and 24.93 ± 1.06, respectively. The cellular association of the Ac-HSA-PLA nanoparticles with the MDA-MB-231 is more than 10 times higher than that of the HSA standard and the HSA-PLA nanoparticles.

In conclusion, the combination of findings from both fluorescence microscopy imaging and flow cytometry provides clear evidence that the cellular uptake of Ac-HSA-PLA nanoparticles by MDA-MB-231 cells is significantly higher than the uptake of HSA-PLA nanoparticles. As the next step, it becomes meaningful to identify the specific receptors that play a role in the internalization process of the Ac-HSA-PLA nanoparticles within MDA-MB-231 cells. This critical investigation will shed light on the underlying mechanisms driving the enhanced cellular uptake observed with the Ac-HSA-PLA nanoparticles.

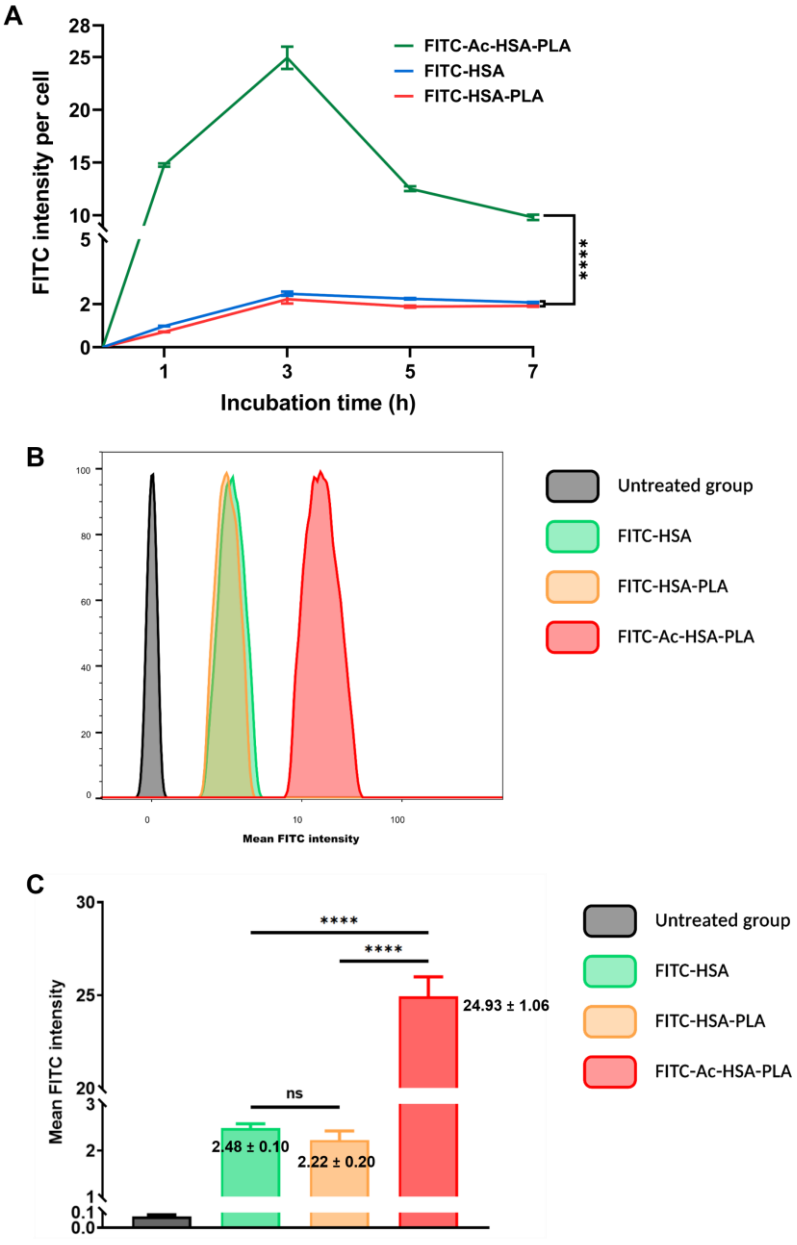

Fig 80. Flow cytometry studies of the MDA-MB-231 cells treated with the fluorescein isothiocyanate (FITC) labelled samples. (A) The mean FITC fluorescent intensity of cells treated with different FITC-labelled samples at different incubation times. **(B)** At a 3-hour incubation time, the flow cytometry histogram of each group (Untreated, FITC-HSA, FITC-HSA-PLA nanoparticles, FITC-Ac-HSA-PLA nanoparticles) has shown higher mean FITC intensity values for the FITC-Ac-HSA-PLA particles indicating higher levels of the FITC-Ac-HSA-PLA nanoparticles are more associated with the cells. **(C)** Statistics analysis of FITC mean fluorescence intensity of each group shows that FITC-Ac-HSA-PLA nanoparticles are more associated with the cells, compared with HSA standard and HSA-PLA nanoparticles. Data are expressed as mean ± SD (n = 3). ****, $p < 0.0001$; ns r = not statistically significant.

5.4.9 Competitive assay

Based on the previous *in vitro* studies, it appears that there are some extra pathways for the internalization of the Ac-HSA-PLA nanoparticles in the MDA-MB-231 cells in contrast with the HSA-PLA nanoparticles. In vitro competitive assays were carried out to screen out some potential receptors which can specifically bind with the Ac-HSA-PLA nanoparticles but do not work on the HSA-PLA nanoparticles. In ***Fig 81***, Non-targeted NP represents the HSA-PLA nanoparticles, Active targeting NP refers to the Ac-HSA-PLA nanoparticles. HA is the abbreviation for Hyaluronic Acid, the ligand of the CD44 receptor. FA stands for Folic Acid, it is a ligand of the folate receptor. As shown in ***Fig 81***, there is no influence on the cell uptake of the HSA-PLA nanoparticles with the addition of HA and FA. However, the cellular uptake of the Ac-HSA-PLA nanoparticles in the MDA-MB-231 cells has been significantly inhibited with the addition of HA and FA. The addition of more HA or FA appears to result in a decrease in the cellular uptake of the Ac-HSA-PLA nanoparticles by MDA-MB-231 cells.

Therefore, based on this preliminary screening outcomes, CD44 and folate receptors of the MDA-MB-231 cells are identified as potential candidates for specific binding with the Ac-HSA-PLA nanoparticles. To corroborate these findings, employing specific antibodies is recommended. Subsequent experiments should involve the use of anti-CD44 and anti-folate receptor

antibodies, coupled with techniques such as confocal laser scanning microscopy or western blotting, to further validate these interactions.

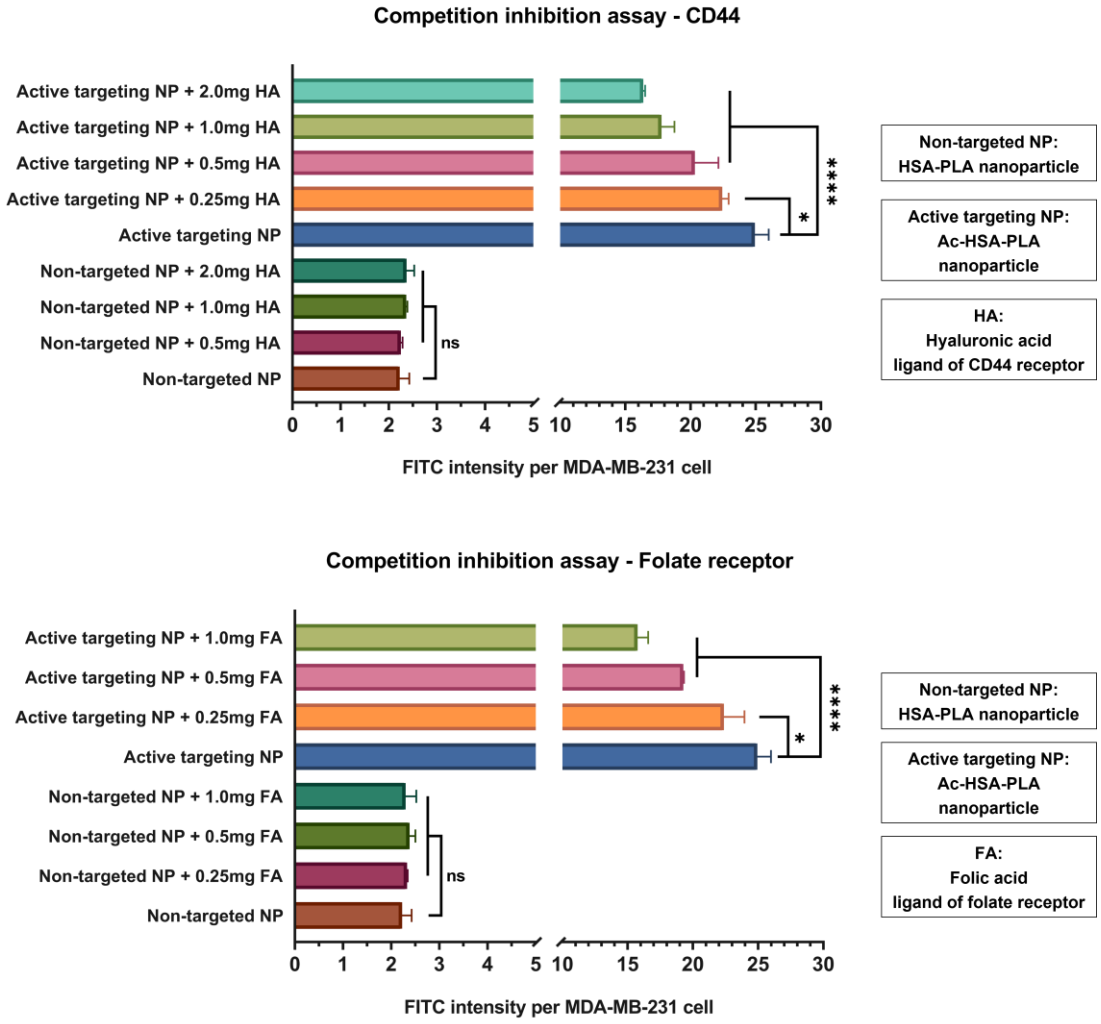

Fig 81. Competition inhibition assays for screening the potential receptors for the Ac-HSA-PLA nanoparticles. After the preliminary screening, it was found that the addition of hyaluronic acid and folic acid did significantly influence the cellular uptake of the Ac-HSA-PLA nanoparticles and did not affect the cellular uptake of the HSA-PLA nanoparticles in the MDA-MB-231 cells. Furthermore, with increasing addition of the folic acid and the hyaluronic acid, less Ac-HSA-PLA nanoparticles were taken by the MDA-MB-231 cells. Data are presented as means ± SD, n = 3. *, $p < 0.05$. ****, $p < 0.0001$; ns r = not statistically significant.

5.4.10 Ex-vivo imaging

The *in vitro* results have demonstrated the remarkable targeting capability of the Ac-HSA-PLA nanoparticles towards MDA-MB-231 cells. Consequently, it is highly valuable to proceed with testing the active targeting potential of these nanoparticles in an *in vivo* study.

Briefly, the near infrared dye, 1,1′-Diethyl-4,4′-dicarbocyanine iodide, was encapsulated in the HSA-PLA nanoparticles and the Ac-HSA-PLA nanoparticles and these resulting NIR dye labelled nanoparticles were recorded as HSA-PLA (Cy) and Ac-HSA-PLA (Cy), respectively. The cyanine dye labelled nanoparticles were intravenously injected to the MDA-MB-231 tumour-bearing mice according to 20 μg dye per mouse. After 2 hours of injection, mice were sacrificed and tissues and tumours were extracted and imaged, as shown in ***Fig 82***.

From the *ex vivo* image (***Fig 82***), the intravenously injected HSA-PLA (Cy) nanoparticles and Ac-HSA-PLA (Cy) nanoparticles are mainly found in the livers. While the Ac-HSA-PLA (Cy) nanoparticles have shown a higher tumour deposition than that of the HSA-PLA (Cy) nanoparticles, as shown in ***Fig 83. A***. Moreover, the uptake ratios of livers to tumours (***Fig 83. B***) for the HSA-PLA nanoparticles are significantly higher than those of the Ac-HSA-PLA nanoparticles, $p < 0.01$. A higher liver-to-tumour uptake ratio indicates that a lesser portion of the injected nanoparticles is being taken by the tumours .

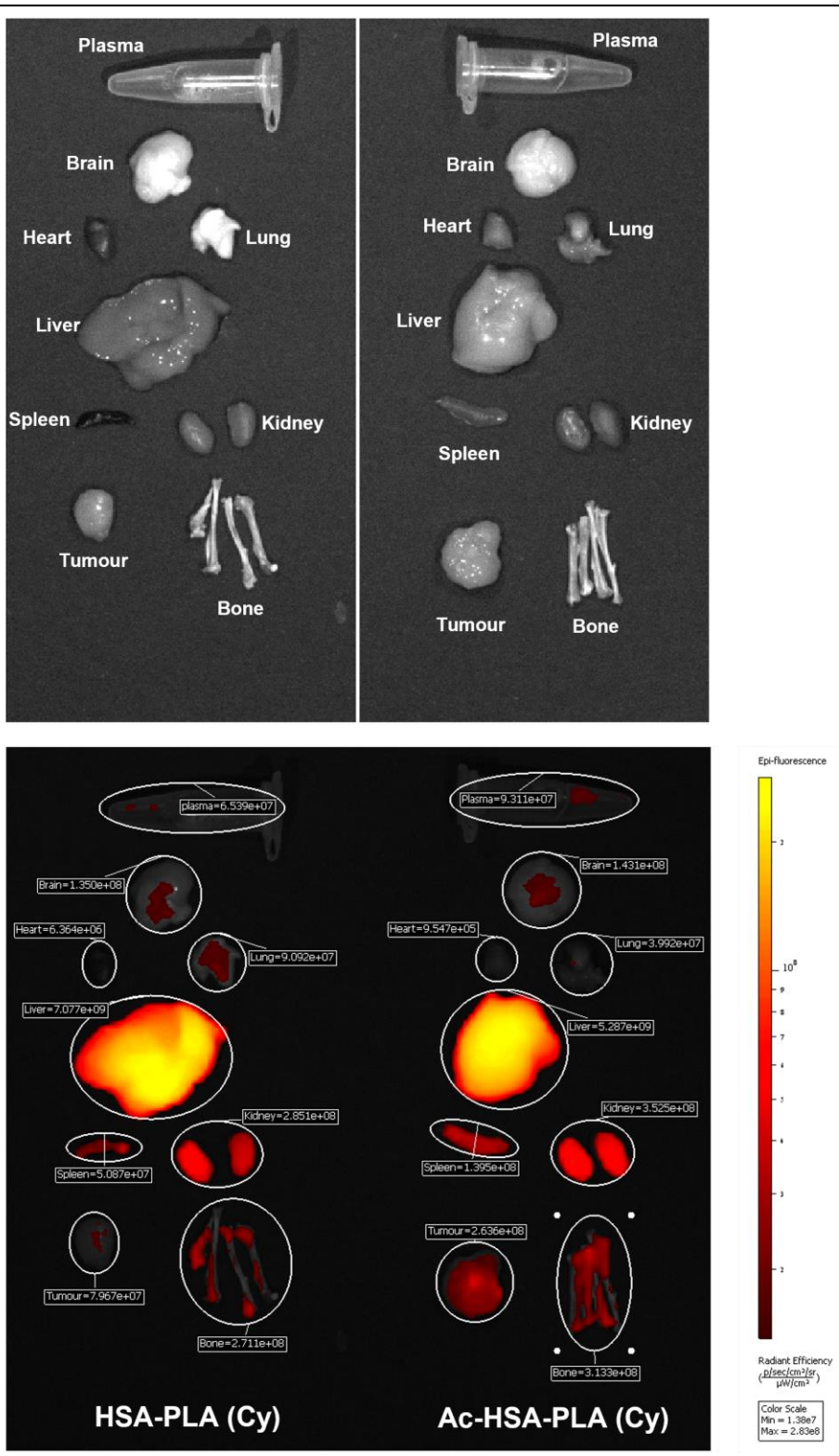

Fig 82. *Ex vivo* imaging study on the active targeting of the acetylated albumin nanoparticles compared with the albumin nanoparticles. After 2 hours injection of the NIR dye labelled nanoparticles, Ac-HSA-PLA (Cy) and HSA-PLA (Cy) nanoparticles, the tissues and tumours were extracted and imaged. A higher number in the graph represents more nanoparticles inside.

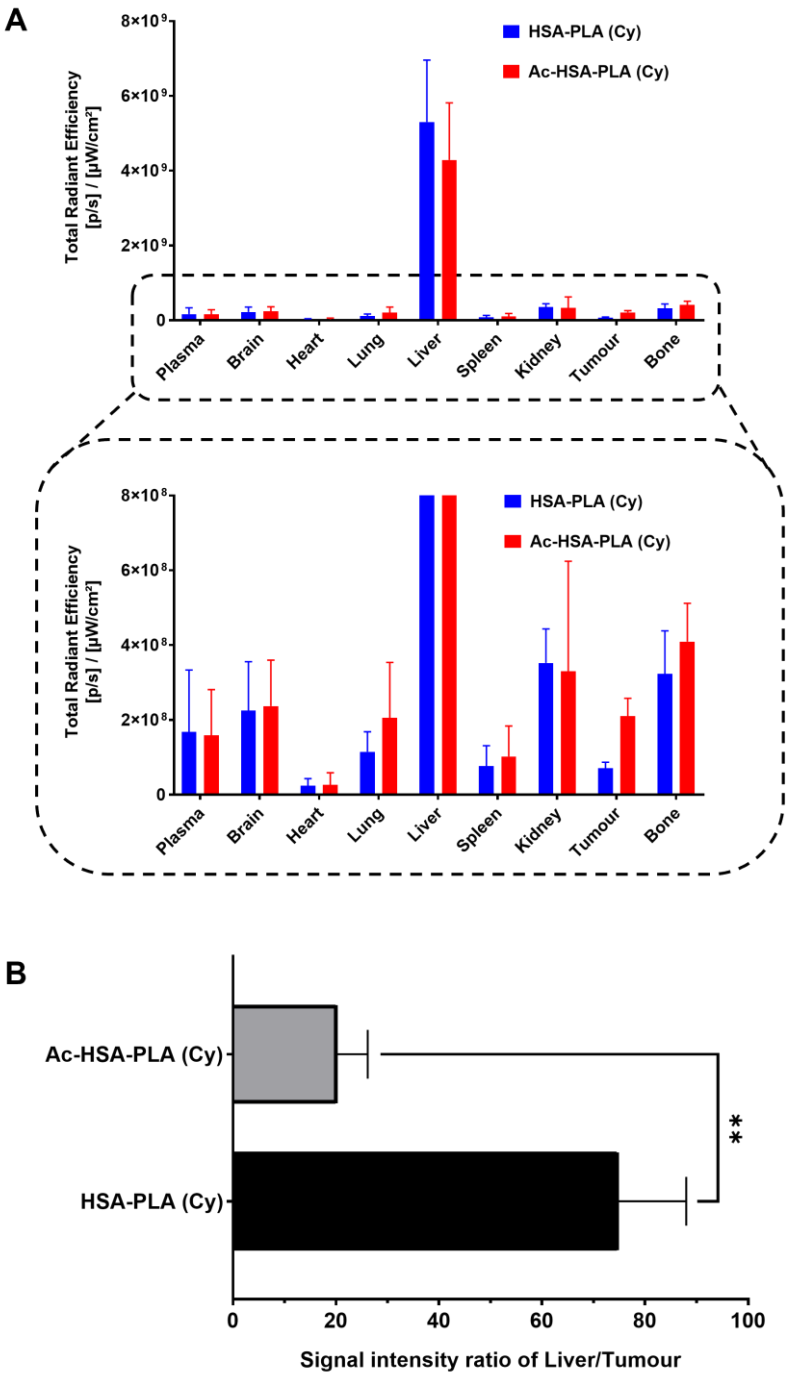

Fig 83. Statistics analysis of the ex-vivo studies. The total radiant efficiency readings of each tissue and tumour were recorded and summarized in the column chart **(A)**. The higher uptake ratio of liver to tumour **(B)** suggests that less of injected nanoparticles were taken by tumour. Data are presented as means ± SD, n = 3. **, $p < 0.01$.

5.5 Conclusion

In this study, the successful acetylation of HSA has significantly enhanced the colloidal stability of the Ac-HSA-PLA nanocarriers, as evidenced by improvements in nanoparticle morphology and net charge compared to the HSA-PLA nanoparticles. Simultaneously, the developed nanocarriers, Ac-HSA-PLA nanoparticles, have exhibited robust targeting towards the triple-negative breast cancer cell line MDA-MB-231 in *in vitro* investigations. Based on the preliminary screening for the interested receptors for the Ac-HSA-PLA nanocarriers, the CD44 and folate receptors are the potential receptors that may provide the fast internalization pathway for the Ac-HSA-PLA nanoparticles, also known as CLIC/GEEC pathway, and these receptors do not work for the internalization of the HSA-PLA nanoparticles. The cellular uptake of the Ac-HSA-PLA nanoparticles in the MDA-MB-231 cells is about 10 times higher than that of the HSA-PLA nanoparticles according to the *in vitro* evaluations. The tumour deposition of the Ac-HSA-PLA nanoparticles is approximately 3-fold higher than that of HSA-PLA nanoparticles after 2 h intravenous injection. Therefore, it is concluded that the acetylation of human serum albumin does provide a constructive solution for improving the colloidal stability of albumin nanoparticles. Moreover, it imparts tumour-tropic properties to human serum albumin, particularly in tumours enriched with CD44 and folate receptors.

Chapter 6. Characterization, *in vitro* and *in vivo* evaluations of the paclitaxel loaded tumour-tropism nanoparticles

6.1 Introduction

When nanotechnology has been applied in the field of pharmaceutics, it offers a new and effective alternative for the formulation of lipophilic, unstable, toxic and metallic drugs. To date, diverse nanomedicines have been developed and approved for the treatment of cancer patients. For example, the anthracycline doxorubicin (DOX) is encapsulated in the liposome nanoparticles for reducing itself cardiotoxicity [219] by altering the biodistribution of the DOX when compared with the traditional doxorubicin formulation (doxorubicin hydrochloride). The commercially available DOX liposomal formulations include Doxil®, Lipodox®, and Myocet®. Additionally, the hydrophobic drug paclitaxel has been formulated as the Abraxane® (albumin-paclitaxel nanoparticles), which has significantly reduced systemic toxicity compared to the first generation of paclitaxel injections - Taxol®.

Most nanomedicines have shown improved pharmacokinetic profiles and a lower systemic toxicity as well as a better therapeutic efficacy in comparison with traditional chemotherapeutic drugs with the same therapeutics. However, based

on substantial clinical and preclinical evidence, the tumour deposition of active ingredients from nanomedicines still falls short in statistically extending the lifespan of metastatic breast cancer patients, in comparison to the formulation of the same drug in a soluble solution [220]. Therefore, improving the effective use of the active ingredients from the nanomedicines *in vivo* remains a major challenge for the nanomedicine formulation design [75]. In response, researchers have developed various strategies aimed at increasing the efficiency of nanomedicines.

Active targeting is a promising strategy to increase the therapeutic payloads delivery by nanocarriers. By anchoring targeting ligands on the nanocarriers, the uptake of the decorated nanoparticles is expected to be increased in the tumour. However, to date, the successful clinical translation of the tumour targeted nanocarriers remains a work in progress. In most cases, the targeting efficiency of the actively targeted nanocarriers is largely restricted within the body [221].

It is hypothesized that serum proteins or opsonins adhere to the surface of nanoparticles, resulting in the formation of a protein layer around the nanoparticles, often referred to as the protein corona [222]. Meanwhile, the targeting ligands on the nanoparticles may be obscured in the protein corona and lose the binding affinity with the cell receptors. In addition, the selection of different ligands can impact the colloidal stability of nanoparticles by altering the surface energy due to ligand-ligand interactions [223]. Furthermore, the

numerous physiological barriers within the body pose significant challenges that must be overcome for tumour-targeted nanocarriers to successfully reach lesions and target tumours.

In this chapter, the PTX was encapsulated in the Ac-HSA-PLA nanocarriers by using a same method introduced in the ***Chapter 3***. The techniques of XRD, DLS and TEM were used to characterize the PTX-loaded Ac-HSA-PLA nanoparticles. The cytotoxicity of the Ac-HSA-PLA (PTX) nanoparticles in the cell lines of the MCF-7, 4T1 and the MDA-MB-231 cells was evaluated. Furthermore, leveraging the heightened receptor-mediated endocytosis of the Ac-HSA-PLA nanocarriers in MDA-MB-231 cells, PTX delivery enhancement in animal models was explored. The tumoricidal activities of the albumin-based PTX nanoformulations were used as control groups .

6.2 Materials, cell lines and animal

Table 15. Materials, cell line and animals used in the characterization, *in vitro* and *in vivo* evaluation studies of the Ac-HSA-PLA (PTX) nanoparticles.

Supplier	Materials, cell line and animal
Merck UK	Cell Proliferation Reagent WST-1
	Dimethyl sulfoxide (DMSO)
	Fetal Bovine Serum Heat Inactivated non-USA origin sterile-filtered
	Insulin solution human sterile-filtered BioXtra suitable for cell culture
	Methanol puriss ACS reagent
	Minimum Essential Medium Eagle
	Phosphotungstic acid hydrate for microscopy
	Syringe-driven filter units (0.45µm)
Generon UK	Paclitaxel (PTX)
Thermo Fisher Scientific UK	Acetonitrile (ACN, ≥99.9%, HPLC Gradient grade)
	Advanced RPMI 1640 Medium
	GlutaMAX™ Supplement 100X
	Leibovitz's L-15 Medium
	PTFE filters
	Penicillin-Streptomycin solution 100X
	Phosphate Buffered Saline PBS pH7.4
	Recovery™ Cell Culture Freezing Medium
	Sodium Pyruvate 100mM
	TrypLE™ Express Enzyme (1X) no phenol red
ELGA PURELAB®	Distilled water
ATCC	MCF-7 (ATCC HTB-22)

	MDA-MB-231 (ATCC HTB-26)
	4T1 (ATCC CRL-2539)
Charles River Laboratories	NOD *SCID* mice – NOD.CB17-Prkdcscid /NCrCrl

All chemicals, reagents, and solvents were used as purchased without undergoing any purification procedures.

6.3 Experimental methods

6.3.1 Preparation of the paclitaxel loaded nanoparticles

A total of 100 mg of lyophilized Ac-HSA-PLA nanoparticle powder was dispersed in 35 mL of distilled water. Subsequently, 1 mL of a methanol solution containing 20 mg of paclitaxel was added drop by drop to the above colloidal dispersion of nanoparticles. Probe sonication (Soniprep 150plus, MSE, UK) was used to encapsulate the PTX into the Ac-HSA-PLA nanoparticles. After subjecting the mixture of the Ac-HSA-PLA nanoparticles and PTX to two cycles of probe sonication (5 minutes of sonication followed by a 3-minute break for each cycle) at a level 5 amplitude, conducted within an ice bath, the resulting suspension of paclitaxel-loaded nanoparticles was subsequently passed through a 0.45 μm syringe filter. This Ac-HSA-PLA (PTX) formulation was replicated in triplicate using distinct batches of Ac-HSA-PLA blank nanoparticles.

Then the filtered nanosuspension was frozen in a -20^{o}C freezer. The frozen drug loaded nanoparticles were then lyophilized (ALPHA 1-4 LDplus, Martin Christ, Germany) in a cold environment (0^{o}C). Residual MeOH was removed in the vacuum environment during the lyophilization. The lyophilized powder of the PTX-loaded NPs was stored in glass vials at room temperature for further characterization, stability tests, and both *in vitro* and *in vivo* evaluations.

6.3.2 Drug encapsulation efficiency and drug loading capacity

The drug encapsulation efficiency (DEE%) and drug loading capacity (DLC%) were calculated by the following equations:

$$\boldsymbol{DEE}\% = \frac{Weight\ of\ PTX\ in\ nanoparticles}{Weight\ of\ PTX\ added}$$

$$\boldsymbol{DLC}\% = \frac{Weight\ of\ PTX\ in\ nanoparticles}{Weight\ of\ polymer\ and\ PTX}$$

A quantity of 2 mg of lyophilized Ac-HSA-PLA (PTX) nanoparticle powder was dissolved in 5 mL of a 60% (v/v) acetonitrile aqueous solution. Following a 2-minute vortex mixing and subsequent bath sonication, the resultant mixture underwent filtration using a 0.2 μm PTFE filter. The concentration of PTX in the filtrate was determined utilizing an HPLC system (Agilent Technologies 1200 series, USA) outfitted with a reversed-phase column (XBridge Shield RP 18, 250 × 4.60 mm, 3.5 μm).

The mobile phase, consisting of 40% H2O and 60% ACN, was utilized with a flow rate set at 0.8 mL/min. Detection of analytes occurred at a wavelength of 227 nm. For HPLC analysis, a 10 μL sample volume was injected onto the column. The calibration curve for PTX was established as y = 25377x with a correlation coefficient of 1.0.

6.3.3 X-ray powder diffraction, XRD

The settings for the X-ray powder diffraction (XRD) instrument align with those detailed in the methodology outlined in Section 3.3.3 of ***Chapter 3***. In short, the Ac-HSA-PLA blank nanoparticle powder, PTX-loaded Ac-HSA-PLA nanoparticle powder, paclitaxel standard powder, PTX + Ac-HSA-PLA NPs powder mixtures, and Abraxane® powder were meticulously ground and positioned onto respective sample holders. Subsequently, these samples underwent scanning using an X-ray diffractometer (MiniFlex 600, Rigaku®).

6.3.4 Dynamic light scattering, DLS

The hydrodynamic diameter, zeta potential, and polydispersity index of Abraxane® nanoparticles, HSA-PLA (PTX) nanoparticles, and Ac-HSA-PLA (PTX) nanoparticles were assessed using the dynamic light scattering (DLS) technique with a Malvern Nano-ZS instrument. Two milligrams of each lyophilized sample were dispersed in 2 mL of distilled water, resulting in nanosuspensions with a pH value of 7. These nanosuspensions were then subjected to measurement in triplicate, and this procedure was performed using three distinct batches of samples.

6.3.5 Transmission electron microscopy, TEM

The sample preparation procedure is consistent with the previous sections. In summary, a droplet of 5 mg/mL Abraxane®, HSA-PLA (PTX), and Ac-HSA-PLA (PTX) nanoparticle colloidal dispersions was deposited onto separate TEM grids. Subsequently, the attached nanoparticles were treated with a 1% (w/v) solution of neutral phosphotungstic acid for staining. The TEM samples thus prepared were stored in a dark environment until imaging.

6.3.6 Storage stability

The lyophilized Ac-HSA-PLA (PTX) nanoparticle powder was stored at room temperature. The storage stability parameters, including drug loading capacity (DLC%), hydrodynamic diameter (D_H), zeta potential, and polydispersity index (PDI) of the Ac-HSA-PLA nanoparticles, were assessed on days 1, 7, 15, and 30, respectively.

6.3.7 Cell culture

The human breast cancer cells MCF-7 and MDA-MB-231, and a mouse mammary carcinoma cell line 4T1 were used for the following *in vitro* studies.

MCF7 cells were cultured in a filter capped tissue culture flask with the Eagle

Minimum Essential Medium, supplemented with 10% (v/v) heat inactivated FBS, 1% (v/v) Glutamax, 1% (v/v) sodium pyruvate, 1%(v/v) penicillin/streptomycin and 1‰ (v/v) human recombinant insulin. Cells were incubated in a humidified incubator with 5% CO_2 at 37°C.

MDA-MB-231 cells were maintained in a non-filter capped tissue culture flask filled with the Leibovitz's L-15 Medium, supplemented with 10% (v/v) heat inactivated FBS and 1% (v/v) penicillin/streptomycin, incubated at 37°C with 5% CO_2 and 95% humidity in an incubator.

4T1 cells were cultured in a vent cap tissue culture flask with the complete medium consisting of the Advanced RPMI 1640 Medium supplemented with 10% (v/v) heat inactivated FBS, 1% (v/v) Glutamax, and 1% (v/v) penicillin/streptomycin, at 37°C in a humidified incubator with 5% CO_2.

6.3.8 In vitro cytotoxicity

The WST-1 reagent (Roche, Sigma Aldrich, UK) was employed to quantify viable cells following treatment with Taxol®, HSA-PLA (PTX) nanoparticles, or Ac-HSA-PLA (PTX) nanoparticles. Approximately 5000 MCF-7 cells, 5000 MDA-MB-231 cells, or 3000 4T1 cells were seeded in each well of VWR® 96-well plates using 0.2 mL of complete medium. The cells were then incubated overnight at 37°C in a humidified incubator with a CO2 concentration of 5%. Each paclitaxel

formulation was diluted with PBS saline (pH 7.4) to achieve a series of pre-determined concentrations. Following the renewal of the complete medium, the serially diluted samples were introduced into the corresponding cell wells and incubated with the cells for 48 hours. Subsequently, the cells were subjected to a 24-hour incubation in fresh complete medium for recovery.

To eliminate dead cells, a cold PBS wash (0.2 mL, pH 7.4) was conducted twice, and fresh complete medium was then added for subsequent incubation with the WST-1 reagent. A volume of 10 µL of WST-1 reagent was introduced into each well and incubated for 4 hours (for MCF-7 and MDA-MB-231 cell lines) or 1 hour (for 4T1 cells) at 37°C in a 5% CO2 incubator. Subsequently, the peak absorbance and background absorbance of the formazan dye were measured at wavelengths of 440 nm and 650 nm, respectively, using a plate reader (SPECTROstar Omega, BMG LABTECH, UK). Each experiment was conducted in triplicate, and data were analyzed using Prism software.

6.3.9 In vivo anticancer study

The NOD-*SCID* female mice (6-8 weeks) were subcutaneously injected with MDA-MB-231 cells (1 x 10^7/100 µL DPBS) in the right flank. Once the tumour volumes reached approximately 100 mm3, the mice were randomly partitioned into four groups (with 5 mice in each group, n = 5). These groups were designated

as follows: the non-treated group, the Abraxane® group, the HSA-PLA (PTX) group, and the Ac-HSA-PLA (PTX) group. The non-treated group consisted of five mice that were utilized as controls and did not undergo any injections. Mice in the Abraxane®, HSA-PLA (PTX), and Ac-HSA-PLA (PTX) groups were intravenously administered with 0.1 mL of the corresponding PTX nanosuspension, each at a dosage of 20 mg/kg PTX. The injections were performed every three days, amounting to a total of five injections for each mouse.

Tumour diameters (both length and width) were measured every three days using a vernier calliper. The formula, tumour volume = 0.5 × length × width^2, was used to calculate the tumour volume. Upon reaching a tumour volume of approximately 600 mm3, or in cases where the loss of body weight exceeded 15%, or if tumour ulceration persisted for more than 3 days, the mice were promptly euthanized.

6.3.10 Statistics

Data are presented as the means ± SD (standard deviation). The student's t-test, one-way ANOVA and two-way ANOVA were used for relative statistical analysis by the Prism software. $p < 0.05$, was considered to be a significant difference.

6.4 Results and discussion

6.4.1 Characterization of the paclitaxel loaded Ac-HSA-PLA nanoparticles

The same drug loading method introduced in section 3.1.2 was utilized to encapsulate paclitaxel in the Ac-HSA-PLA nanoparticles, creating a novel PTX nano-formulation known as Ac-HSA-PLA (PTX) nanoparticles. The essential parameters of the PTX-loaded nanoparticles, encompassing hydrodynamic diameter, PDI, zeta potential, drug loading efficiency, and drug loading capacity of Abraxane®, HSA-PLA (PTX) nanoparticles, and Ac-HSA-PLA (PTX) nanoparticles, were determined and are listed in ***Table 16***. The drug loading capacity of the Abraxane® (10% w/w) was found in the specification of the Abraxane®. The DLC of the HSA-PLA (PTX) and the Ac-HSA-PLA (PTX) nanoparticles is 15.2 ± 0.3 % (w/w) and 16.2 ± 0.2% (w/w), respectively. These two novel PTX-loaded nanoparticles have a higher payload of PTX when compared to the Abraxane®. The hydrodynamic diameter of the Ac-HSA-PLA (PTX) nanoparticles was 200 ± 20 nm.

As shown in the TEM image in ***Fig 66***, there is a thin film surrounding the Ac-HSA-PLA nanoparticle. In this TEM image, excessive salts were employed to coat the TEM copper grid, absorbing most of the electrons during imaging.

Consequently, the background of the TEM image in ***Fig 66*** appears black, as electrons cannot pass through the salt-covered area. However, electrons can penetrate protein-based nanoparticles. This leads to enhanced signal contrast of the interfacial layer between the nanoparticles and the salt, allowing visualization of the thin film around the Ac-HSA-PLA nanoparticle. It is hypothesized that this thin film around the Ac-HSA-PLA nanoparticle is linked to the acetylation level of HSA as well as its binding affinity with cellular receptors such as CD44 and folate receptors.

Table 16. Characterization data of the paclitaxel nano-formulations. The data include the hydrodynamic diameter (D_H), PDI and zeta potential of three PTX-loaded nanoparticles in distilled water, and drug loading efficiency, drug loading capacity of these PTX nano-formulations. Data are presented as mean ± SD, n = 3. ****, p < 0.0001 vs. Abraxane®.

Nanoparticles	Abraxane®	HSA-PLA (PTX)	Ac-HSA-PLA (PTX)
D_H (nm)	157 ± 2	174 ± 7	200 ± 20
PDI	0.09 ± 0.01	0.07 ± 0.01	0.06 ± 0.03
Zeta-potential (mV)	-13.43 ± 3.73	-34.38 ± 1.01****	-34.79 ± 1.38****
DLE (%)	100	91.2 ± 1.6	97.0 ± 1.3
DLC (%)	10	15.2 ± 0.3	16.2 ± 0.2

6.4.2 X ray diffraction, XRD

X-ray Powder Diffraction (XRD) is an analytical technique used to determine the crystallographic structure of the solid materials. Here, the XRD technique was applied to assess the crystalline state of PTX in the Ac-HSA-PLA nanoparticles. According to the XRD patterns (***Fig 84***), the PTX in the nanoparticles of the Ac-HSA-PLA (PTX) and Abraxane® exhibits amorphous characteristics. On the contrary, the paclitaxel powder shows its crystalline nature with three characteristic peaks at 5.6°, 8.9° and 12.5°. Meanwhile, if PTX was not encapsulated in the Ac-HSA-PLA nanoparticles, the characteristic signals of the PTX should be detected, akin to the spectrum of the PTX + Ac-HSA-PLA physical mixtures.

In addition, when compared to the Abraxane® XRD spectrum and the HSA-PLA XRD spectrum (see ***Fig 40***), two additional peaks may be observed between 30°-35° in the spectra of the Ac-HSA-PLA blank nanoparticles. This phenomenon, possibly linked to the acetylation on the nanoparticle surfaces, results in the transformation of the Ac-HSA-PLA nanoparticles into a semi-crystalline material.

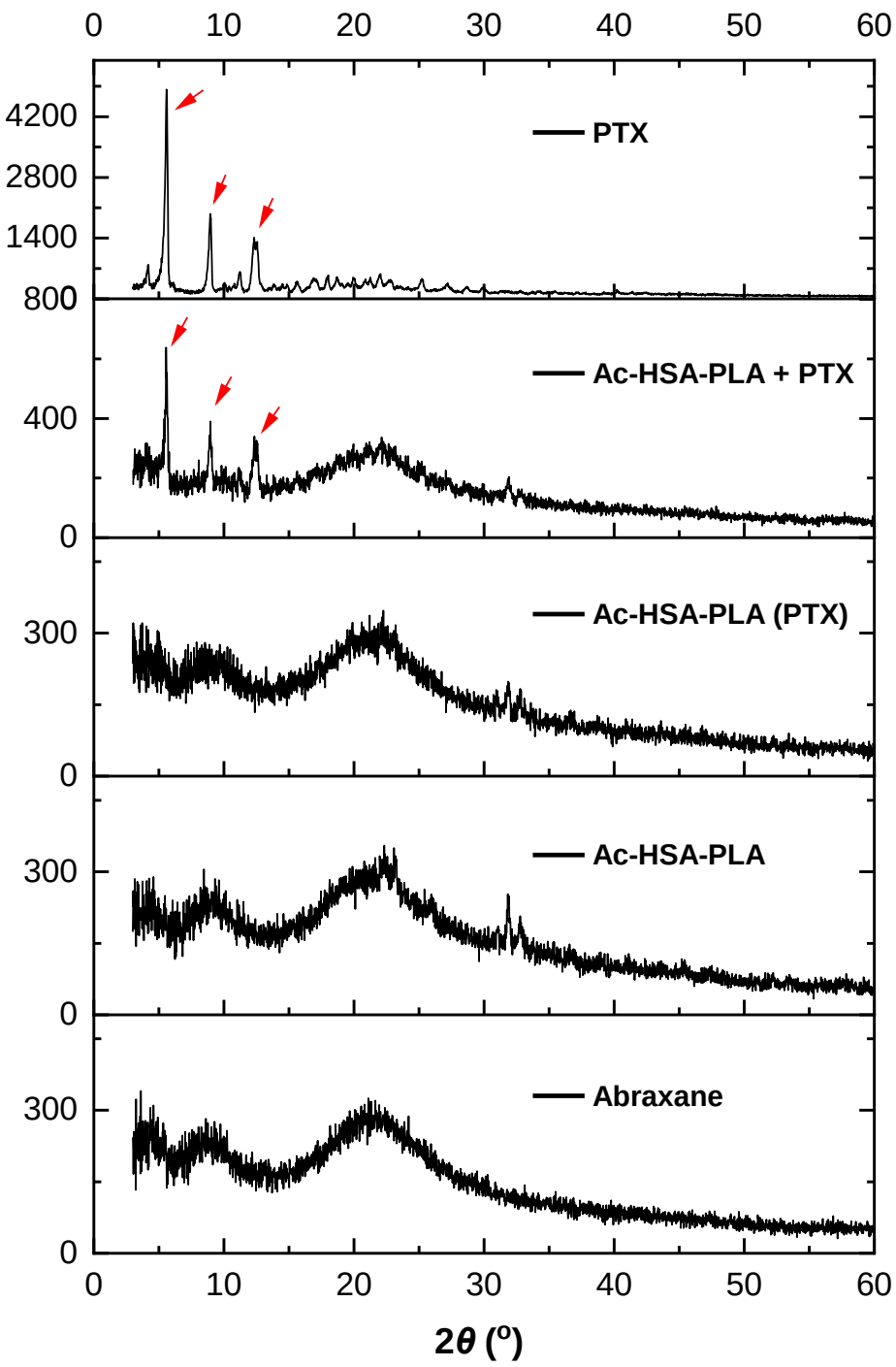

Fig 84. XRD patterns of the various samples. From top to bottom, the XRD patterns of the PTX standard, PTX + Ac-HSA-PLA nanoparticle mixture (1:9 w/w), PTX loaded Ac-HSA-PLA nanoparticles, Ac-HSA-PLA blank nanoparticles and the Abraxane® nanoparticles. Red arrows indicate the characteristic peaks of the crystalline paclitaxel.

6.4.3 Morphology of the paclitaxel loaded nanoparticles

The morphologies of the Abraxane®, the HSA-PLA (PTX) nanoparticles and the Ac-HSA-PLA (PTX) nanoparticles were observed through the technique of transmission electron microscopy (TEM). The TEM images of these nanoparticles are shown in ***Fig 85***. From a wide view of the nanoparticles in TEM images, the size and agglomeration of the Abraxane® nanoparticles are apparently different with those of the HSA-PLA (PTX) nanoparticles and the Ac-HSA-PLA (PTX) nanoparticles, although all of them are spherical nanoparticles.

As shown in the TEM image of the Abraxane® (***Fig 85. A***), the Abraxane® nanoparticles heavily agglomerate into several irregularly shaped clusters with a diameter around 130 nm, and the particle clusters are well separated from each other. In contrast, the TEM image of the Ac-HSA-PLA (PTX) nanoparticles (***Fig 85. C***) reveals significantly reduced nanoparticle aggregation, with individual particles well-separated from each other. Nanoparticles in the TEM image of the HSA-PLA (PTX) nanoparticles (***Fig 85. B***) are also less agglomerated than that of the Abraxane® nanoparticles due to the lower surface-to-volume ratio and lower surface energy of each individual nanoparticle. The phenomenon of nanoparticle agglomeration has been elucidated previously in ***Chapter 3***, with reference to the DLVO theory. Additionally, based on the theory of the thermodynamics [190], the most favorable state for the colloidal system is one

that minimizes free energy. Consequently, the spontaneous process of nanoparticle agglomeration in unstable colloidal systems aims to reduce surface free energy, aligning with the second law of thermodynamics. Therefore, it is reasonable to expect that the colloidal stability of the Ac-HSA-PLA (PTX) nanoparticles is superior to that of Abraxane® nanoparticles.

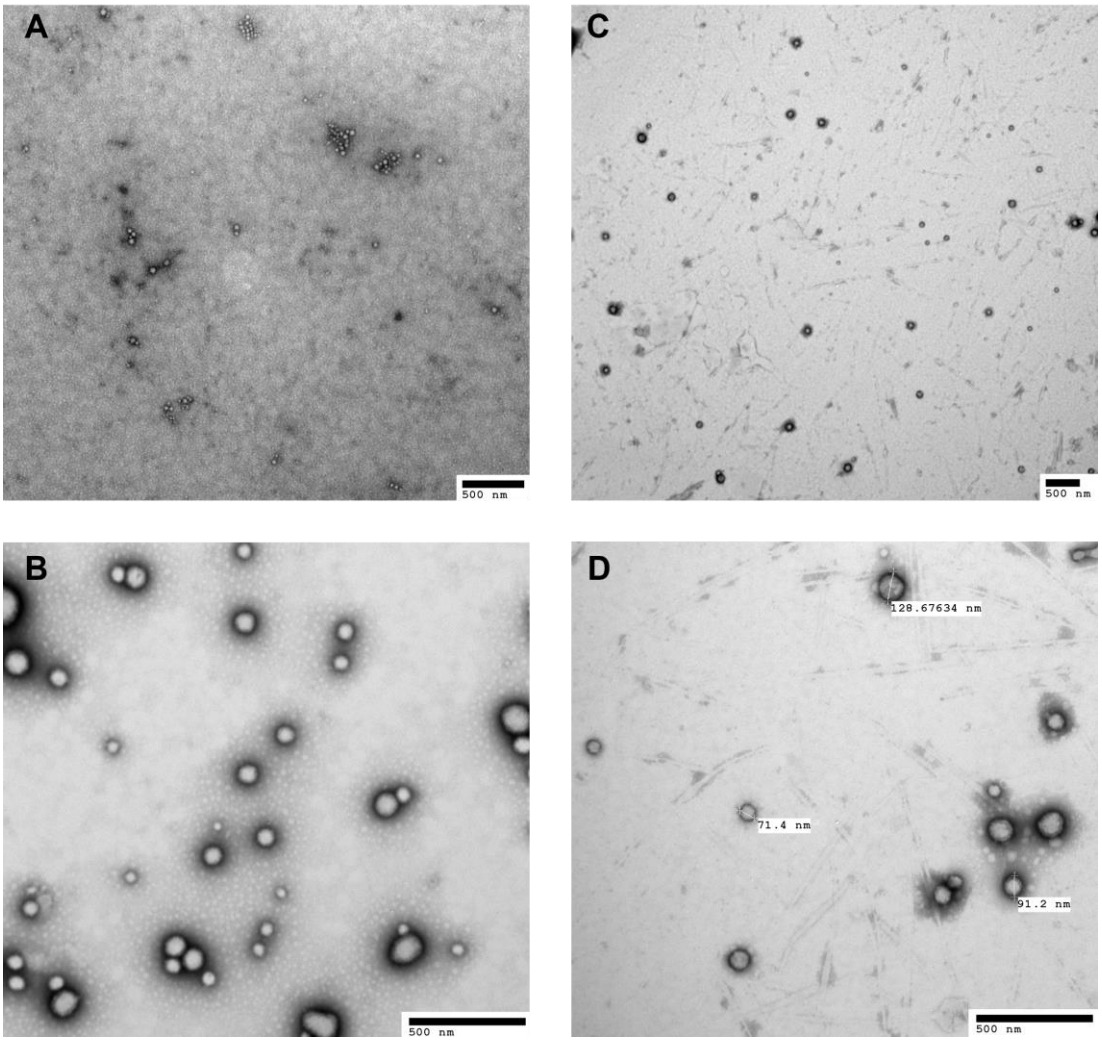

Fig 85. TEM images of A) Abraxane®, B) HSA-PLA (PTX) nanoparticles, C) and D) Ac-HSA-PLA (PTX) nanoparticles. The dark background noise is associated to the residue salt solution.

6.4.4 Storage stability

The one-month storage stability for the lyophilized powder of the Ac-HSA-PLA (PTX) nanoparticle at room temperature has been evaluated in terms of the hydrodynamic diameter, PDI and zeta potential of the Ac-HSA-PLA (PTX) nanoparticles in distilled water as well as the drug contents in the Ac-HSA-PLA (PTX) nanoparticles. As shown in ***Table 17***, following a one-way analysis of variance (ANOVA) for the stability indicators over the one-month storage period, it was observed that there were no significant alterations in the hydrodynamic diameter, PDI, zeta potential, and drug content of the Ac-HSA-PLA (PTX) nanoparticles. This suggests that these indicators remained relatively stable during the entire one-month storage duration.

Table 17. Storage stability indicators for the Ac-HSA-PLA (PTX) nanoparticles during one month storage period at room temperature. Data are presented as mean ± SD, n = 3.

Indicators		D_H (nm)	*PDI*	Zeta-potential (mV)	DLC% (w/w)
Ac-HSA-PLA (PTX)	Day 1	166.4 ± 4.8	0.08 ± 0.04	-33.7 ± 1.0	16.3 ± 0.2
	Day 7	169.8 ± 4.5	0.11 ± 0.04	-33.0 ± 2.5	16.0 ± 0.2
	Day 15	162.9 ± 2.2	0.10 ± 0.02	-33.3 ± 0.9	16.4 ± 0.1
	Day 30	161.5 ± 3.8	0.11 ± 0.07	-32.3 ± 1.1	16.4 ± 0.2

After the one-way ANOVA statistical analysis, no significant changes were observed in these indicators.

6.4.5 In vitro cytotoxicity assays

In vitro cytotoxicity assays were conducted to assess and compare the anticancer activity of each PTX formulation upon direct exposure to cancer cells. Cells were treated with the various PTX formulations at different PTX concentrations respectively. Subsequently, the WST-1 cell proliferation reagent was employed to quantify the viable cells following treatment. Briefly, the added tetrazolium salt (WST-1) was reduced into a water-soluble formazan dye by the mitochondrial dehydrogenases of the live cells, as shown in ***Fig 86***. Consequently, the spectrophotometric measurements taken at a wavelength of 440 nm, corresponding to the intensity of the formazan dye, were proportionate to the quantities of living cells.

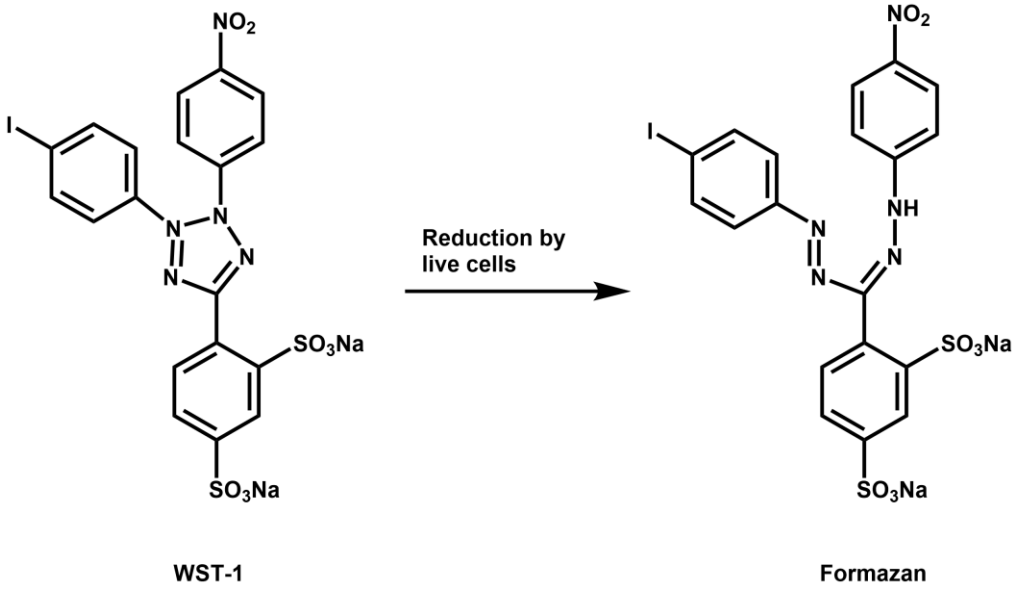

Fig 86. Chemical reaction between the WST-1 reagent and live cells. The stable WST-1 reagent is reduced into a water-soluble formazan dye by the surviving cells. The intensity reading of the resulting formazan dye at a wavelength of 440 nm is proportional to the numbers of living cells.

Subsequently, cytotoxicity curves depicting cell viability (%) against PTX concentrations for Taxol®, HSA-PLA (PTX) nanoparticles, and Ac-HSA-PLA (PTX) nanoparticles were plotted for the breast cancer cell lines MCF-7, 4T1, and MDA-MB-231, as illustrated in ***Fig 87***. The cytotoxicity values (IC_{50}) of the Taxol®, the HSA-PLA (PTX) nanoparticles and the Ac-HSA-PLA (PTX) nanoparticles were calculated and listed in ***Table 18***.

The IC_{50} values for Taxol® in MCF-7, 4T1, and MDA-MB-231 cells were determined to be 0.46 ± 0.19 μg/mL, 0.15 ± 0.03 μg/mL, and 0.40 ± 0.36 μg/mL, respectively. The relatively low IC_{50} of Taxol® in cells can be attributed to the cytotoxic excipient Cremophor EL utilized in the Taxol® formulation. The IC_{50} values of the Ac-HSA-PLA (PTX) nanoparticles in the MCF7 cells and the MDA-MB-231 cells are 7.83 ± 1.78 μg/mL and 1.60 ± 1.29 μg/mL respectively, which are significantly lower those of the HSA-PLA (PTX) nanoparticles (MCF7, 10.79 ± 0.63 μg/mL, $p < 0.05$; MDA-MB-231, 19.56 ± 2.00 μg/mL, $p < 0.0001$).

The significantly lower IC_{50} of the Ac-HSA-PLA (PTX) nanoparticles in the MDA-MB-231 cells indicates that the active targeting of the Ac-HSA-PLA nanocarriers to the MDA-MB-231 cells can be used to enhance the delivery of the PTX *in vitro*.

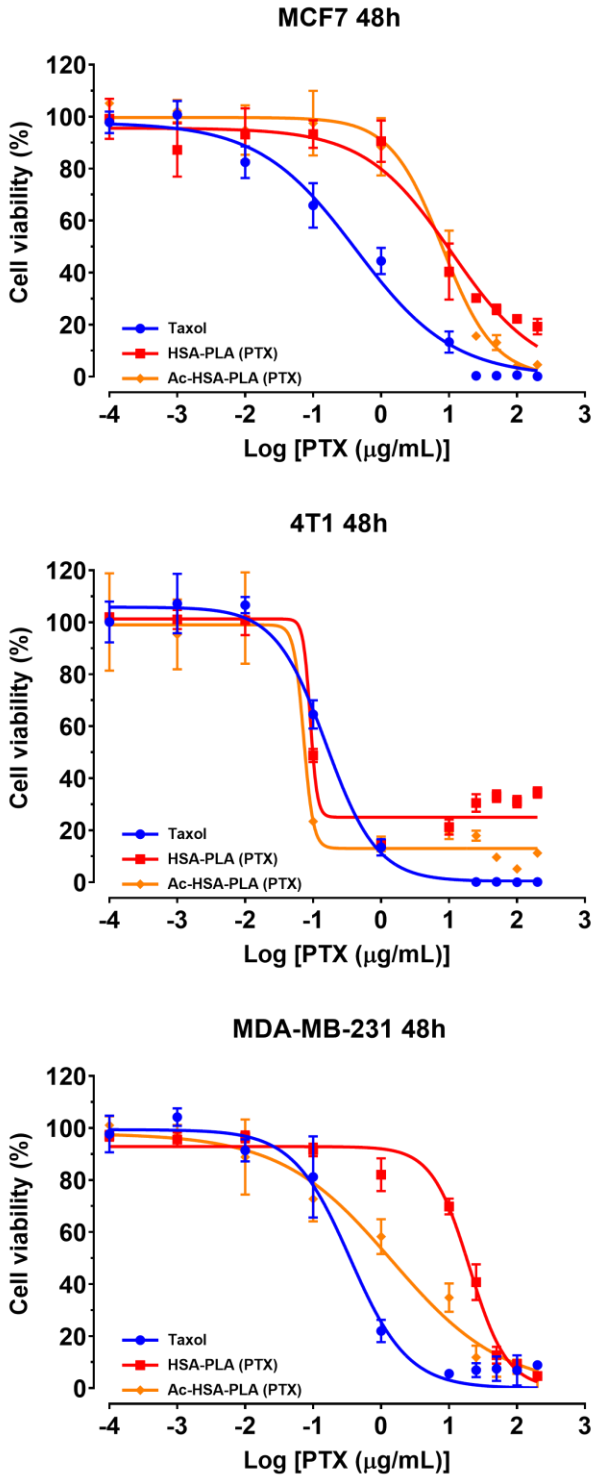

Fig 87. Cytotoxicity of the PTX formulations in breast cancer cell lines: MCF7, 4T1, and MDA-MB-231 cells. The Wst-1 cell viability assays were performed after 48 hours drug treatment. Data are presented as mean ± SD (n = 3).

Table 18. IC_{50} (μg/mL) of the PTX formulations in breast cancer cell lines. Data are presented as mean ± SD (n = 3). *, $p < 0.05$. ****, $p < 0.0001$ vs. HSA-PLA (PTX).

Sample \ Cell line	MCF7	4T1	MDA-MB-231
Taxol®	0.46 ± 0.19	0.15 ± 0.03	0.40 ± 0.36
HSA-PLA (PTX)	10.79 ± 0.63	0.08 ± 0.02	19.56 ± 2.00
Ac-HSA-PLA (PTX)	7.83 ± 1.78 *	0.07 ± 0.02	1.60 ± 1.29 ****

6.4.6 In vivo anticancer study

Based on the biodistribution study of the Ac-HSA-PLA nanoparticles and the HSA-PLA nanoparticles in the MDA-MB-231 tumour bearing mice (see ***Fig 82***), the tumour deposition of the Ac-HSA-PLA nanoparticles was approximately 3-fold higher than that of the HSA-PLA nanoparticles after two hours of intravenous injection. The IC_{50} of the Ac-HSA-PLA (PTX) nanoparticles in the MDA-MB-231 cells is significantly lower than that of the PTX loaded HSA-PLA nanoparticles, 1.60 ± 1.29 μg/mL vs. 19.56 ± 2.00 μg/mL, $p < 0.0001$. These findings suggest that active targeting of the Ac-HSA-PLA nanoparticles to MDA-MB-231 cells could potentially be exploited to enhance the therapeutic efficacy of PTX in triple-negative breast cancer patients by formulating PTX into the nano-formulation Ac-HSA-PLA (PTX) nanomedicine. Therefore, an anticancer study was conducted to

evaluate and compare the *in vivo* tumoricidal activity of Ac-HSA-PLA (PTX) nanoparticles, Abraxane®, and HSA-PLA (PTX) nanoparticles in MDA-MB-231 tumor-bearing NOD-SCID mice.

Briefly, as demonstrated in ***Fig 88***, twenty tumour bearing mice were equally allocated to the non-treated group, Abraxane® group, HSA-PLA (PTX) group and Ac-HSA-PLA (PTX) group, n = 5. Mice allocated in the treatment group were intravenously injected with 0.1 mL of the respective PTX nanosuspension at a dose of PTX 20 mg/kg. Injections to mice were carried out every three days for a total of five injections.

As shown in ***Fig 89. A***, the MDA-MB-231 tumours were eliminated after 4 injections of the Ac-HSA-PLA (PTX) nanosuspension, whereas the injected Abraxane® nanoparticles only suppressed the tumour growth compared to the non-treated group. The tumour volume was decreased after the treatment of the HSA-PLA (PTX) nanoparticles, but tumours began to regrow after treatment ended. Multiple injections of these PTX nanosuspensions did not induce adverse effects such as anaphylactic shock in the immunodeficient mice (NOD-SCID mice). Meanwhile, as shown in ***Fig 89. B***, all mice steadily gained weight, indicating low and acceptable systemic toxicity from these PTX injections. The survival difference between the different group was analyzed by a logrank test (Mantel-Cox test) in the software Prism, the survival of the mice treated with the Abraxane® was significantly improved compared to the non-treated group, p =

0034. The mice in the HSA-PLA (PTX) group gained more survival benefits when compared to the mice in the Abraxane® group, p = 0.0017. The active targeting of the Ac-HSA-PLA nanoparticles provided the best survival benefits to the tumour bearing mice when compared to the mice in the Abraxane® and the HSA-PLA (PTX) groups, p < 0.0001. The cumulative survival curve of the tumour bearing mice is shown in ***Fig 89. C***.

In summary, it is confirmed that the Ac-HSA-PLA (PTX) nano-formulation can significantly inhibit tumor growth and even lead to the cure of cancer-transfected mice.

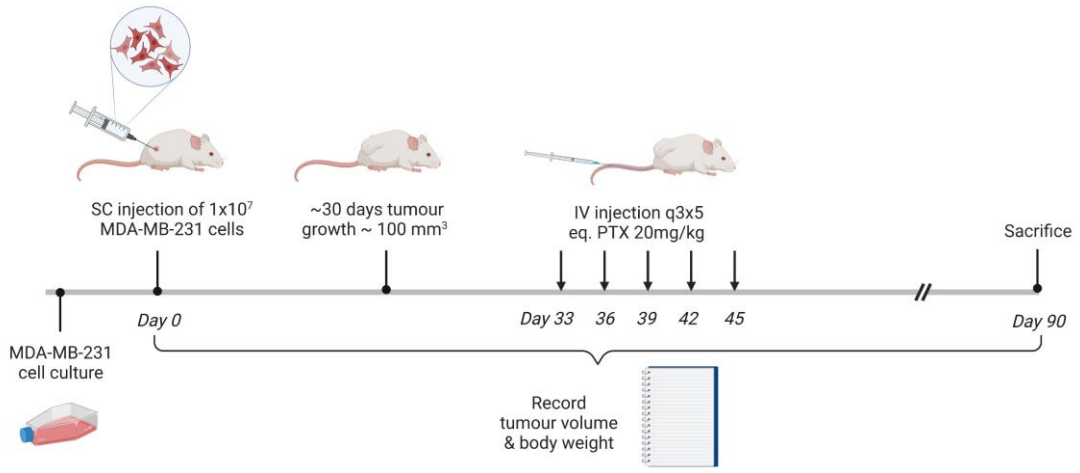

Fig 88. Schematic representation for the methodological flow of the in vivo anti-cancer study. The harvested MDA-MB-231 cells were subcutaneously injected in the right flank of NOD-SCID female mice. When the tumour volume was approximately 100 mm^3, mice were randomly divided into 4 groups (5 mice per group, n = 5) and the groups were named as non-treated group, Abraxane® group, HSA-PLA (PTX) group and Ac-HSA-PLA (PTX) group, respectively. For the non-treated group, there were five mice that served as controls and did not receive any injections. Mice in the Abraxane®, the HSA-PLA (PTX) and the Ac-HSA-PLA (PTX) groups were intravenously injected with 0.1 mL of the respective PTX nanosuspension at a dose of PTX 20 mg/kg. Injections to mice were carried out every three days for a total of five injections.

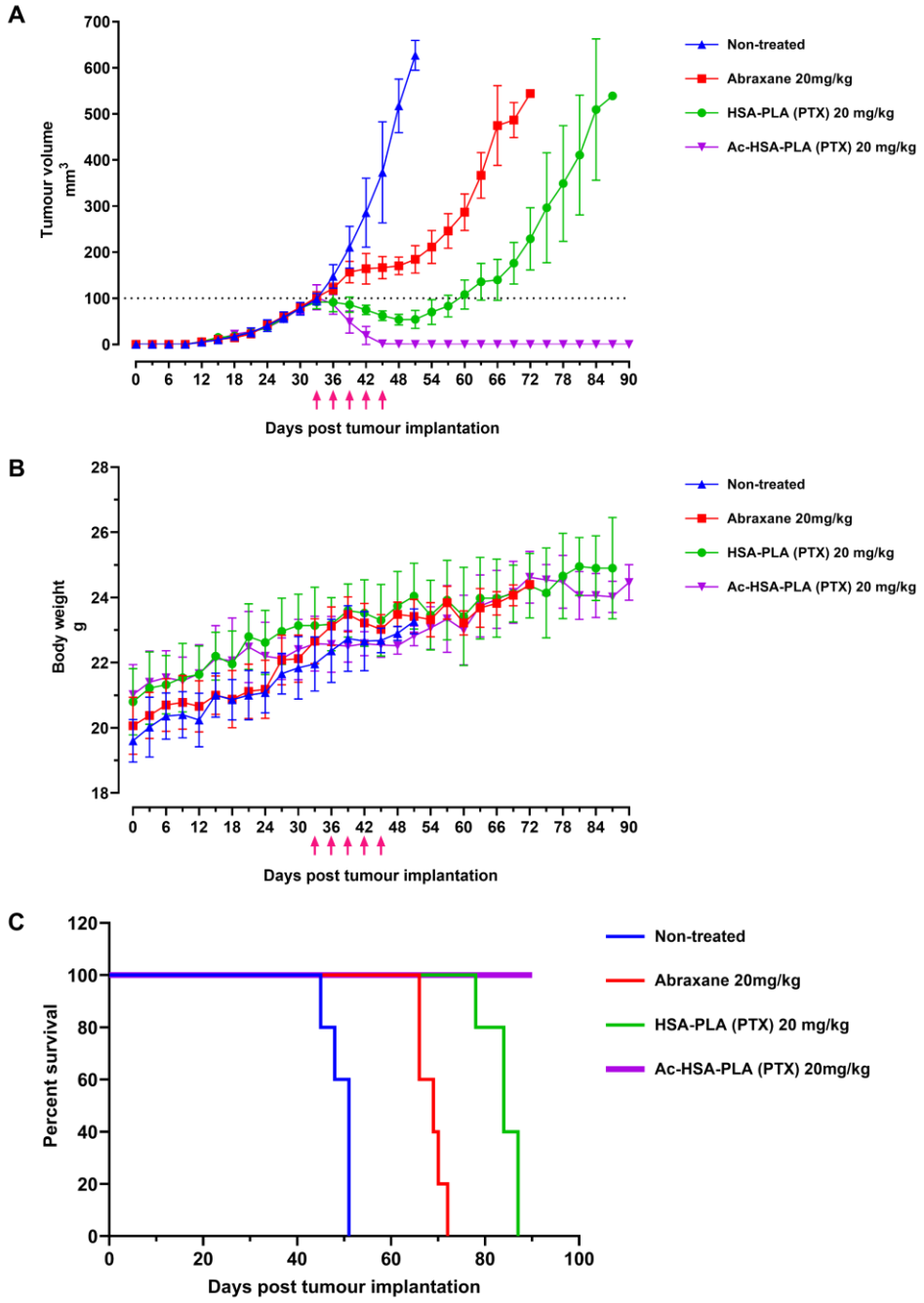

Fig 89. Anticancer activity of Ac-HSA-PLA (PTX) formulation in MDA-MB-231 tumour model. The 1 × 10^7 MDA-MB-231 cells in 100 µL pH 7.4 PBS were implanted in the right flank of each NOD-SCID mouse on Day 0, the Matrigel was not used in this study. **(A)** Tumour growth curves of the MDA-MB-231 tumour bearing mice after different treatments. **(B)** Mice body weight records. **(C)** Cumulative survival of the tumour bearing mice (Kaplan Meier). Data are presented as mean ± SD (n = 5).

6.5 Conclusion

In this section, a novel tumour-targeted nanoparticle loaded with paclitaxel at approximately 16% w/w drug content, referred to as Ac-HSA-PLA (PTX), was developed. These Ac-HSA-PLA (PTX) nanoparticles exhibited an average hydrodynamic diameter of approximately 200 nm and a zeta potential of -34.8 mV. Leveraging the specific binding affinity of the Ac-HSA-PLA nanoparticles to cancer cell CD44 and folate receptors, the PTX-loaded Ac-HSA-PLA nanoparticles demonstrated remarkable anticancer activity against MDA-MB-231 cells in both *in vitro* and *in vivo* studies.

The dissection on the mice treated with the Ac-HSA-PLA (PTX) nanoparticles was conducted on day 90, no signs of the metastasis were found in the five mice and their organs appeared normal in size and appearance. In their right flank sites, only tumour-related stromal tissues were left and the tumour related angiogenic blood vessels were eliminated as well. This observation, coupled with the anticancer study data presented in this chapter, strongly suggests that the treatment with the Ac-HSA-PLA (PTX) nanoparticles led to the successful eradication of tumours in the treated mice. Consequently, the innovative actively targeted nanomedicine presented here holds promise for further in-depth investigation and exploration.

Chapter 7. Conclusion and Future work

7.1 Overall conclusion

Nowadays, an effective treatment for TNBC patients is still an unmet medical need. The nab-paclitaxel (Abraxane®) based combination therapy is recommended by the National Comprehensive Cancer Network® (NCCN®) as the first-line treatment for mTNBC [224]. In numerous phase III clinical trials [225,226], the longest median overall survival of the mTNBC patients was approximately 26 months, and these patients were treated with nab-paclitaxel-based combination therapies. However, the advanced cancer patients benefit limitedly from the nab-paclitaxel monotherapy, the median overall survival of the metastatic breast cancer patients was around 14.9 months in a phase III clinical trial of the nab-paclitaxel monotherapy [66].

In response to the limited efficacy of the Abraxane® in patients, in this work, two feasible solutions have been proposed to improve the *in vivo* chemotherapeutic effectiveness of PTX to address some of the acknowledged limitations of Abraxane®. The Abraxane® nanoparticles are composed of 90% human serum albumin (HSA) and 10% paclitaxel. However, these nanoparticles become unstable at concentrations below 0.3 mg/mL. To improve the deposition of PTX within tumours, it is hypothesized that enhancing the colloidal stability and

payload of the nanocarriers could be beneficial. The eligible nanocarrier (HSA-PLA nanoparticle) was created by the covalent binding of the hydrophobic polymer poly(L-lactide) to the HSA cysteine residue. The resulting PTX loaded HSA-PLA nanoparticles are made up of 85% HSA-PLA polymer and 15% PTX. Notably, the stability of HSA-PLA (PTX) nanoparticles is maintained even at a concentration of 0.01 mg/Ml. The HSA-PLA (PTX) nanomedicine has thereby produced a superior tumoricidal activity when compared to the Abraxane® in the 4T1 tumour bearing mice at the same PTX dose. The final 4T1 tumour weight of the mice treated with the HSA-PLA (PTX) was 239.8 ± 43.0 mg (n = 5) and was statistically smaller than the group (n = 5) treated with the Abraxane®, where the tumour weight was 340.6 ± 62.8 mg ($p < 0.5$).

In the latter part of this dissertation, on the basis of the HSA-PLA nanoparticles, HSA was further modified by the acetylation on the amine groups of the HSA. The resultant Ac-HSA-PLA nanocarriers exhibited specific binding with CD44 and folate receptors on TNBC cells, as demonstrated in *in vitro* studies. Upon encapsulating PTX within the Ac-HSA-PLA nanoparticles, the drug content in the Ac-HSA-PLA (PTX) nanoparticles was 16% w/w. The Ac-HSA-PLA (PTX) nanoparticles have shown a superior cytotoxicity in the TNBC cells (MDA-MB-231 cell line) when compared to that of the HSA-PLA (PTX) nanoparticles, IC_{50}: 1.60 ± 1.29 μg/mL vs. 19.56 ± 2.00 μg/mL, $p < 0.0001$. Additionally, in MDA-MB-231 tumour bearing mice, the TNBC tumours (n = 5) were completely eliminated

after the treatment with the Ac-HSA-PLA (PTX), whereas the injected Abraxane® and HSA-PLA (PTX) at the same PTX dose did not achieve the same outcome. These promising *in vivo* results suggest that the two proposed solutions have the potential to be translated into clinical applications.

7.2 Limitations of this work

The presented work, while promising and innovative, does have certain limitations that should be acknowledged:

1. **Long-Term Stability:** The long-term stability of the developed nanocarriers, both in terms of physical and chemical properties, needs to be examined to ensure consistent therapeutic outcomes.
2. **Binding Site Specificity:** It is hypothesized that only the Cys-34 residue of HSA is reactive to MAL-PLA, this assumption might not be sufficiently definitive. Experimentation or additional characterization is needed to confirm the exact binding site(s) on HSA in the future.
3. **Potential Unforeseen Effects:** Novel materials and modifications, especially in biological contexts, can have unforeseen effects that may become apparent only after extensive testing and real-world applications.
4. **Animal Model:** The *in vivo* experiments are performed in animal models (NOD-SCID and BALB/c female mice). The extrapolation of results to

humans can be challenging due to species differences in metabolism, immune response, and tumour microenvironment.

5. **Specificity of Targeting:** The Ac-HSA-PLA nanoparticles demonstrated enhanced targeting to CD44 and folate receptors, the specificity of this targeting mechanism might not be exclusive to cancer cells. Further investigation is needed to ascertain the selectivity of the nanoparticles for tumour cells over healthy cells.
6. **Mechanism of Action:** Both HSA-PLA (PTX) nanoparticles and Ac-HSA-PLA (PTX) nanoparticles demonstrated effective anticancer activity, the underlying mechanisms of their action were not fully explored. Understanding how these nanoparticles induce tumour regression in animals could facilitate the development of appropriate combination therapies.
7. **Limited Sample Size:** The sample size of mice used for *in vivo* experiments might limit the generalizability of the results. Larger sample sizes are generally more representative and robust.
8. **Biocompatibility and Toxicity:** The study doesn't extensively address potential biocompatibility and long-term toxicity of the developed nanocarriers in animal models or potential human applications. Ensuring the safety of the proposed solutions is critical before clinical translation.
9. **Clinical Translation:** Transitioning from preclinical models to clinical applications introduces additional challenges such as scalability, safety,

patient heterogeneity and regulatory approval. The success observed in animal models does not guarantee the same outcomes in humans.

10. **Ethical Implications:** The ethical implications of using nanoparticles for cancer treatment, especially their long-term effects on human health, need to be addressed and communicated transparently.

In conclusion, this study offers promising results regarding the anticancer potential of the Ac-HSA-PLA (PTX) nanoparticles. Furthermore, addressing these limitations through further research and validation will be essential to ensure the clinical feasibility and safety of this novel approach.

7.3 Future work

In the first part of this dissertation, a comparison of hydrodynamic diameter changes between the HSA-PLA (PTX) nanoparticles and the Abraxane® nanoparticles at low concentrations, along with the assessment of zeta potentials for both nanoparticle types in pH = 7 aqueous medium, and the examination of morphologies through TEM images of the HSA-PLA (PTX) nanoparticles and the Abraxane® nanoparticles, leads to the conclusion that the colloidal stability of the HSA-PLA (PTX) nanoparticles surpasses that of the Abraxane® nanoparticles. Nevertheless, there exists a straightforward method to determine nanoparticle colloidal stability, involving the measurement of contact angle between

nanoparticle solids and water [227]. A smaller contact angle signifies lower surface free energy of the nanoparticles. This, in turn, indicates a more stable colloidal system within aqueous media. The distinction in colloidal stability among the Abraxane® nanoparticles, the HSA-PLA (PTX) nanoparticles, and the Ac-HSA-PLA (PTX) nanoparticles can be visualized through this approach. Additionally, a comprehensive assessment of long-term storage stability for the HSA-PLA (PTX) nanoparticles and the Ac-HSA-PLA (PTX) nanoparticles should be undertaken.

As the active targeting of the Ac-HSA-PLA nanoparticles towards the TNBC cells is a novel proposition within this thesis, a range of mechanistic cellular experiments can be pursued to enhance understanding. For example, as shown in the ***Fig 80. A***, the cellular association between the Ac-HSA-PLA nanoparticles and the MDA-MB-231 cells was decreased after 3 hours incubation. It seems that the Ac-HSA-PLA nanoparticles may escape from the cells after the cellular uptake and this hypothesis may be validated through an endothelial permeability assay in the future experiments. Based on the data of the competitive assays, the CD44 and folate receptors of the MDA-MB-231 cells are the potential receptors for specific binding with the Ac-HSA-PLA nanoparticles. It is advisable to use specific antibodies to further confirm these findings. Further investigations employing anti-CD44 and anti-folate receptor antibodies, combined with techniques like confocal laser scanning microscopy or western blotting, would solidify these conclusions.

From the *ex-vivo* image ***Fig 82***, the fluorescence labelled Ac-HSA-PLA nanoparticles were found in the mice bones. This prompts the need for a murine hematopathology experiment [228] to ascertain whether the injected Ac-HSA-PLA (PTX) nanoparticles potentially impact bone marrow function and consequently induce related side effects. According to the ***Fig 82***, the biodistribution of the Ac-HSA-PLA nanoparticles is highly overlapped with the metastatic sites of the advanced breast cancer. This highlights the significance of conducting an anticancer study involving Ac-HSA-PLA (PTX) nanoparticles in a breast cancer metastatic mouse model. In addition, the Ac-HSA-PLA (PTX) nanomedicine may work on the ovarian cancer cell line (SKOV3) as well. As the SKOV3 cell is also the aggressive cancer cell and enriched with the CD44 and folate receptors.

Finally, the superior tumoricidal activity displayed by both HSA-PLA (PTX) nanoparticles and Ac-HSA-PLA (PTX) nanoparticles in comparison to the Abraxane® nanoparticles in *in vivo* studies signifies their potential. Consequently, considering clinical trials involving these PTX injections in future plans is advisable.

References

[1] F. Bray, M. Laversanne, E. Weiderpass, I. Soerjomataram, The ever-increasing importance of cancer as a leading cause of premature death worldwide, Cancer. 127 (2021) 3029–3030. https://doi.org/10.1002/cncr.33587.

[2] H. Sung, J. Ferlay, R.L. Siegel, M. Laversanne, I. Soerjomataram, A. Jemal, F. Bray, Global Cancer Statistics 2020: GLOBOCAN Estimates of Incidence and Mortality Worldwide for 36 Cancers in 185 Countries, CA A Cancer J Clin. 71 (2021) 209–249. https://doi.org/10.3322/caac.21660.

[3] E.Y.H.P. Lee, W.J. Muller, Oncogenes and Tumor Suppressor Genes, Cold Spring Harbor Perspectives in Biology. 2 (2010) a003236–a003236. https://doi.org/10.1101/cshperspect.a003236.

[4] D.A. Howell, D. McCaughan, A.G. Smith, R. Patmore, E. Roman, Incurable but treatable: Understanding, uncertainty and impact in chronic blood cancers—A qualitative study from the UK's Haematological Malignancy Research Network, PLoS ONE. 17 (2022) e0263672. https://doi.org/10.1371/journal.pone.0263672.

[5] L. Yang, S. Yang, C. Ren, S. Liu, X. Zhang, A. Sui, Deciphering the roles of miR-16-5p in malignant solid tumors, Biomedicine & Pharmacotherapy. 148 (2022) 112703. https://doi.org/10.1016/j.biopha.2022.112703.

[6] R. Lugano, M. Ramachandran, A. Dimberg, Tumor angiogenesis: causes, consequences, challenges and opportunities, Cell. Mol. Life Sci. 77 (2020) 1745–1770. https://doi.org/10.1007/s00018-019-03351-7.

[7] X. Zhang, J.F. Wang, B. Chandran, K. Persaud, B. Pytowski, J. Fingeroth, J.E. Groopman, Kaposi's Sarcoma-associated Herpesvirus Activation of Vascular Endothelial Growth Factor Receptor 3 Alters Endothelial Function and Enhances Infection, Journal of Biological Chemistry. 280 (2005) 26216–26224. https://doi.org/10.1074/jbc.M411392200.

[8] M. Potente, T. Mäkinen, Vascular heterogeneity and specialization in development and disease, Nat Rev Mol Cell Biol. 18 (2017) 477–494. https://doi.org/10.1038/nrm.2017.36.

[9] K. Alitalo, The lymphatic vasculature in disease, Nat Med. 17 (2011) 1371–1380. https://doi.org/10.1038/nm.2545.

[10] R. Paduch, The role of lymphangiogenesis and angiogenesis in tumor metastasis, Cell Oncol. 39 (2016) 397–410. https://doi.org/10.1007/s13402-016-0281-9.

[11] S. Clara-Trujillo, G. Gallego Ferrer, J.L. Gómez Ribelles, In Vitro Modeling of Non-Solid Tumors: How Far Can Tissue Engineering Go?, IJMS. 21 (2020) 5747. https://doi.org/10.3390/ijms21165747.

[12] M. Jagannathan-Bogdan, L.I. Zon, Hematopoiesis, Development. 140 (2013) 2463–2467. https://doi.org/10.1242/dev.083147.

[13] B.J. Bain, Structure and function of red and white blood cells and platelets, Medicine. 49 (2021) 183–188. https://doi.org/10.1016/j.mpmed.2021.01.001.

[14] O.L. Lanier, E. Pérez-Herrero, A.P.D.' Andrea, K. Bahrami, E. Lee, D.M. Ward, N. Ayala-Suárez, S.M. Rodríguez-Méndez, N.A. Peppas, Immunotherapy approaches for hematological cancers, IScience. 25 (2022) 105326. https://doi.org/10.1016/j.isci.2022.105326.

[15] T. Terwilliger, M. Abdul-Hay, Acute lymphoblastic leukemia: a comprehensive review and 2017 update, Blood Cancer J. 7 (2017) e577–e577. https://doi.org/10.1038/bcj.2017.53.

[16] F.R. Appelbaum, Acute Leukemias in Adults, in: Abeloff's Clinical Oncology, Elsevier, 2020: pp. 1783-1797.e1. https://doi.org/10.1016/B978-0-323-47674-4.00095-5.

[17] M. Lin, M. Haas, Paraprotein-associated thrombotic microangiopathy: expanding the spectrum of renal disease related to plasma cell dyscrasias, Kidney International. 91 (2017) 532–534. https://doi.org/10.1016/j.kint.2016.10.043.

[18] Y. Lazebnik, What are the hallmarks of cancer?, Nat Rev Cancer. 10 (2010) 232–233. https://doi.org/10.1038/nrc2827.

[19] Benign Tumors, in: High-Yield Imaging: Gastrointestinal, Elsevier, 2010: pp. 325–328. https://doi.org/10.1016/B978-1-4160-5544-0.00127-6.

[20] K.M. Newkirk, E.M. Brannick, D.F. Kusewitt, Neoplasia and Tumor Biology, in:

Pathologic Basis of Veterinary Disease, Elsevier, 2017: pp. 286-321.e1. https://doi.org/10.1016/B978-0-323-35775-3.00006-0.

[21] X. Wang, X. Huang, Y. Zhang, Involvement of Human Papillomaviruses in Cervical Cancer, Front. Microbiol. 9 (2018) 2896. https://doi.org/10.3389/fmicb.2018.02896.

[22] S. Jain, K. Raza, A.K. Agrawal, A. Vaidya, Solid tumor: Addressing the problems associated, in: Nanotechnology Applications for Cancer Chemotherapy, Elsevier, 2021: pp. 393–419. https://doi.org/10.1016/B978-0-12-817846-1.00020-5.

[23] R.L. Siegel, K.D. Miller, H.E. Fuchs, A. Jemal, Cancer Statistics, 2021, CA A Cancer J. Clin. 71 (2021) 7–33. https://doi.org/10.3322/caac.21654.

[24] T.C. King, Neoplasia, in: Elsevier's Integrated Pathology, Elsevier, 2007: pp. 111–143. https://doi.org/10.1016/B978-0-323-04328-1.50011-5.

[25] M. Moballegh Nasery, M. Varzandeh, S. Pahlavanneshan, N. Mohamadi, S. Sarhadi, H. Samareh Fekri, R. Mohammadinejad, K.S. Ahn, Curcumin: A potential therapeutic natural product for adenocarcinomas, Phytochemistry Letters. 49 (2022) 45–55. https://doi.org/10.1016/j.phytol.2022.02.013.

[26] H. Kurn, D.T. Daly, Histology, Epithelial Cell, in: StatPearls, StatPearls Publishing, Treasure Island (FL), 2022. http://www.ncbi.nlm.nih.gov/books/NBK559063/ (accessed December 19, 2022).

[27] W. Yan, I.I. Wistuba, M.R. Emmert-Buck, H.S. Erickson, Squamous Cell Carcinoma - Similarities and Differences among Anatomical Sites, Am J Cancer Res. 1 (2011) 275–300.

[28] P.T.C. So, E. Yew, C. Rowlands, Applications of Multiphoton Microscopy in Dermatology, in: Imaging in Dermatology, Elsevier, 2016: pp. 241–268. https://doi.org/10.1016/B978-0-12-802838-4.00019-4.

[29] A.C. Krakowski, F. Hafeez, A. Westheim, E.Y. Pan, M. Wilson, Advanced basal cell carcinoma: What dermatologists need to know about diagnosis, Journal of the American Academy of Dermatology. 86 (2022) S1–S13. https://doi.org/10.1016/j.jaad.2022.03.023.

[30] P.B. Tchounwou, U.K. Udensi, R.D. Isokpehi, C.G. Yedjou, S. Kumar, Arsenic and Cancer, in: Handbook of Arsenic Toxicology, Elsevier, 2015: pp. 533–555. https://doi.org/10.1016/B978-0-12-418688-0.00023-X.

[31] H.K. Birdi, A. Jirovec, S. Cortés-Kaplan, J. Werier, C. Nessim, J.-S. Diallo, M. Ardolino, Immunotherapy for sarcomas: new frontiers and unveiled opportunities, J Immunother Cancer. 9 (2021) e001580. https://doi.org/10.1136/jitc-2020-001580.

[32] F. Trautmann, M. Schuler, J. Schmitt, Burden of soft-tissue and bone sarcoma in routine care, Cancer Epidemiology. 39 (2015) 440–446. https://doi.org/10.1016/j.canep.2015.03.002.

[33] I.-M. Schaefer, A. Gronchi, WHO Pathology, Surgical Oncology Clinics of

North America. 31 (2022) 321–340. https://doi.org/10.1016/j.soc.2022.03.001.

[34] K.M. Skubitz, D.R. D'Adamo, Sarcoma, Mayo Clinic Proceedings. 82 (2007) 1409–1432. https://doi.org/10.4065/82.11.1409.

[35] A.C. Gamboa, A. Gronchi, K. Cardona, Soft-tissue sarcoma in adults: An update on the current state of histiotype-specific management in an era of personalized medicine, CA A Cancer J Clin. 70 (2020) 200–229. https://doi.org/10.3322/caac.21605.

[36] T. Fujiwara, Y. Fujita, Y. Nezu, A. Kawai, T. Ozaki, T. Ochiya, MicroRNAs in Bone and Soft Tissue Sarcomas and Their Value as Biomarkers, in: Epigenetic Biomarkers and Diagnostics, Elsevier, 2016: pp. 613–642. https://doi.org/10.1016/B978-0-12-801899-6.00030-9.

[37] B. Gerber, M. Freund, T. Reimer, Recurrent Breast Cancer, Deutsches Ärzteblatt International. (2010). https://doi.org/10.3238/arztebl.2010.0085.

[38] D. Barba, A. León-Sosa, P. Lugo, D. Suquillo, F. Torres, F. Surre, L. Trojman, A. Caicedo, Breast cancer, screening and diagnostic tools: All you need to know, Critical Reviews in Oncology/Hematology. 157 (2021) 103174. https://doi.org/10.1016/j.critrevonc.2020.103174.

[39] Y. Feng, M. Spezia, S. Huang, C. Yuan, Z. Zeng, L. Zhang, X. Ji, W. Liu, B. Huang, W. Luo, B. Liu, Y. Lei, S. Du, A. Vuppalapati, H.H. Luu, R.C. Haydon, T.-C. He, G. Ren, Breast cancer development and progression: Risk factors, cancer stem cells, signaling pathways, genomics, and molecular

pathogenesis, Genes & Diseases. 5 (2018) 77–106. https://doi.org/10.1016/j.gendis.2018.05.001.

[40] H.K. Chew, Adjuvant therapy for breast cancer: who should get what?, Western Journal of Medicine. 174 (2001) 284–287. https://doi.org/10.1136/ewjm.174.4.284.

[41] K.J. Huber-Keener, Cancer genetics and breast cancer, Best Practice & Research Clinical Obstetrics & Gynaecology. 82 (2022) 3–11. https://doi.org/10.1016/j.bpobgyn.2022.01.007.

[42] C.M. Perou, T. Sørlie, M.B. Eisen, M. van de Rijn, S.S. Jeffrey, C.A. Rees, J.R. Pollack, D.T. Ross, H. Johnsen, L.A. Akslen, Ø. Fluge, A. Pergamenschikov, C. Williams, S.X. Zhu, P.E. Lønning, A.-L. Børresen-Dale, P.O. Brown, D. Botstein, Molecular portraits of human breast tumours, Nature. 406 (2000) 747–752. https://doi.org/10.1038/35021093.

[43] X. Dai, T. Li, Z. Bai, Y. Yang, X. Liu, J. Zhan, B. Shi, Breast cancer intrinsic subtype classification, clinical use and future trends, Am J Cancer Res. 5 (2015) 2929–2943.

[44] A.S. Nahed, M.Y. Shaimaa, Ki-67 as a prognostic marker according to breast cancer molecular subtype, Cancer Biology & Medicine. 13 (2016) 496. https://doi.org/10.20892/j.issn.2095-3941.2016.0066.

[45] N. Ribelles, L. Perez-Villa, J.M. Jerez, B. Pajares, L. Vicioso, B. Jimenez, V. de Luque, L. Franco, E. Gallego, A. Marquez, M. Alvarez, A. Sanchez-Muñoz,

L. Perez-Rivas, E. Alba, Pattern of recurrence of early breast cancer is different according to intrinsic subtype and proliferation index, Breast Cancer Res. 15 (2013) R98. https://doi.org/10.1186/bcr3559.

[46] V. Masoud, G. Pagès, Targeted therapies in breast cancer: New challenges to fight against resistance, WJCO. 8 (2017) 120. https://doi.org/10.5306/wjco.v8.i2.120.

[47] X. Dai, T. Li, Z. Bai, Y. Yang, X. Liu, J. Zhan, B. Shi, Breast cancer intrinsic subtype classification, clinical use and future trends, Am J Cancer Res. 5 (2015) 2929–2943.

[48] J.-Q. Chen, J. Russo, ERα-negative and triple negative breast cancer: Molecular features and potential therapeutic approaches, Biochimica et Biophysica Acta (BBA) - Reviews on Cancer. 1796 (2009) 162–175. https://doi.org/10.1016/j.bbcan.2009.06.003.

[49] Y. Chen, K. Wang, F. Xie, Z. Zhuo, C. Liu, Y. Yang, S. Wang, X. Zhao, Novel biomarkers identified in triple-negative breast cancer through RNA-sequencing, Clinica Chimica Acta. 531 (2022) 302–308. https://doi.org/10.1016/j.cca.2022.04.990.

[50] C.A. Hudis, L. Gianni, Triple-Negative Breast Cancer: An Unmet Medical Need, The Oncologist. 16 (2011) 1–11. https://doi.org/10.1634/theoncologist.2011-S1-01.

[51] R. Dent, M. Trudeau, K.I. Pritchard, W.M. Hanna, H.K. Kahn, C.A. Sawka,

L.A. Lickley, E. Rawlinson, P. Sun, S.A. Narod, Triple-Negative Breast Cancer: Clinical Features and Patterns of Recurrence, Clinical Cancer Research. 13 (2007) 4429–4434. https://doi.org/10.1158/1078-0432.CCR-06-3045.

[52] H.A. Wahba, H.A. El-Hadaad, Current approaches in treatment of triple-negative breast cancer, Cancer Biol Med. 12 (2015) 106–116. https://doi.org/10.7497/j.issn.2095-3941.2015.0030.

[53] G. Bianchini, J.M. Balko, I.A. Mayer, M.E. Sanders, L. Gianni, Triple-negative breast cancer: challenges and opportunities of a heterogeneous disease, Nat Rev Clin Oncol. 13 (2016) 674–690. https://doi.org/10.1038/nrclinonc.2016.66.

[54] K.E. Skinner, A. Haiderali, M. Huang, L.S. Schwartzberg, Real-world effectiveness outcomes in patients diagnosed with metastatic triple-negative breast cancer, Future Oncology. 17 (2021) 931–941. https://doi.org/10.2217/fon-2020-1021.

[55] L.D. Volk-Draper, S. Rajput, K.L. Hall, A. Wilber, S. Rana, Novel Model for Basaloid Triple-negative Breast Cancer: Behavior In Vivo and Response to Therapy, Neoplasia. 14 (2012) 926-IN13. https://doi.org/10.1593/neo.12956.

[56] M. Robson, S.-A. Im, E. Senkus, B. Xu, S.M. Domchek, N. Masuda, S. Delaloge, W. Li, N. Tung, A. Armstrong, W. Wu, C. Goessl, S. Runswick, P. Conte, Olaparib for Metastatic Breast Cancer in Patients with a Germline *BRCA* Mutation, N Engl J Med. 377 (2017) 523–533.

https://doi.org/10.1056/NEJMoa1706450.

[57] E.P. Winer, O. Lipatov, S.-A. Im, A. Goncalves, E. Muñoz-Couselo, K.S. Lee, P. Schmid, K. Tamura, L. Testa, I. Witzel, S. Ohtani, N. Turner, S. Zambelli, N. Harbeck, F. Andre, R. Dent, X. Zhou, V. Karantza, J. Mejia, J. Cortes, Pembrolizumab versus investigator-choice chemotherapy for metastatic triple-negative breast cancer (KEYNOTE-119): a randomised, open-label, phase 3 trial, The Lancet Oncology. 22 (2021) 499–511. https://doi.org/10.1016/S1470-2045(20)30754-3.

[58] H.H. Blume, B.S. Schug, The biopharmaceutics classification system (BCS): Class III drugs — better candidates for BA/BE waiver?, European Journal of Pharmaceutical Sciences. 9 (1999) 117–121. https://doi.org/10.1016/S0928-0987(99)00076-7.

[59] E. Blanco, H. Shen, M. Ferrari, Principles of nanoparticle design for overcoming biological barriers to drug delivery, Nat Biotechnol. 33 (2015) 941–951. https://doi.org/10.1038/nbt.3330.

[60] L. Yu, Z. Hua, X. Luo, T. Zhao, Y. Liu, Systematic interaction of plasma albumin with the efficacy of chemotherapeutic drugs, Biochimica et Biophysica Acta (BBA) - Reviews on Cancer. 1877 (2022) 188655. https://doi.org/10.1016/j.bbcan.2021.188655.

[61] M.A. Swartz, N. Iida, E.W. Roberts, S. Sangaletti, M.H. Wong, F.E. Yull, L.M. Coussens, Y.A. DeClerck, Tumor Microenvironment Complexity: Emerging

Roles in Cancer Therapy, Cancer Research. 72 (2012) 2473–2480. https://doi.org/10.1158/0008-5472.CAN-12-0122.

[62] S. Jiang, Y. Qin, S. Wu, S. Xu, K. Li, P. Yang, K. Zhao, L. Lin, J. Gong, Solubility Correlation and Thermodynamic Analysis of Sorafenib Free Base and Sorafenib Tosylate in Monosolvents and Binary Solvent Mixtures, J. Chem. Eng. Data. 62 (2017) 259–267. https://doi.org/10.1021/acs.jced.6b00630.

[63] W.J. Gradishar, Albumin-bound paclitaxel: a next-generation taxane, Expert Opinion on Pharmacotherapy. 7 (2006) 1041–1053. https://doi.org/10.1517/14656566.7.8.1041.

[64] C. Fornaguera, M. García-Celma, Personalized Nanomedicine: A Revolution at the Nanoscale, JPM. 7 (2017) 12. https://doi.org/10.3390/jpm7040012.

[65] A.C. Anselmo, S. Mitragotri, Nanoparticles in the clinic: An update, Bioeng Transl Med. 4 (2019). https://doi.org/10.1002/btm2.10143.

[66] W.J. Gradishar, S. Tjulandin, N. Davidson, H. Shaw, N. Desai, P. Bhar, M. Hawkins, J. O'Shaughnessy, Phase III Trial of Nanoparticle Albumin-Bound Paclitaxel Compared With Polyethylated Castor Oil–Based Paclitaxel in Women With Breast Cancer, JCO. 23 (2005) 7794–7803. https://doi.org/10.1200/JCO.2005.04.937.

[67] U.H. Gala, D.A. Miller, R.O. Williams, Harnessing the therapeutic potential of anticancer drugs through amorphous solid dispersions, Biochimica et

Biophysica Acta (BBA) - Reviews on Cancer. 1873 (2020) 188319. https://doi.org/10.1016/j.bbcan.2019.188319.

[68] T.M. Allen, P.R. Cullis, Drug Delivery Systems: Entering the Mainstream, Science. 303 (2004) 1818–1822. https://doi.org/10.1126/science.1095833.

[69] D. Needham, Development of clinically effective formulations for anticancer applications: why it is so difficult?, in: Biomaterials for Cancer Therapeutics, Elsevier, 2020: pp. 599–723. https://doi.org/10.1016/B978-0-08-102983-1.00022-3.

[70] A.M. Sofias, M. Dunne, G. Storm, C. Allen, The battle of “nano” paclitaxel, Advanced Drug Delivery Reviews. 122 (2017) 20–30. https://doi.org/10.1016/j.addr.2017.02.003.

[71] B. Wilson, K.M. Geetha, Lipid nanoparticles in the development of mRNA vaccines for COVID-19, Journal of Drug Delivery Science and Technology. 74 (2022) 103553. https://doi.org/10.1016/j.jddst.2022.103553.

[72] Y. Matsumura, H. Maeda, A new concept for macromolecular therapeutics in cancer chemotherapy: mechanism of tumoritropic accumulation of proteins and the antitumor agent smancs, Cancer Res. 46 (1986) 6387–6392.

[73] U. Prabhakar, H. Maeda, R.K. Jain, E.M. Sevick-Muraca, W. Zamboni, O.C. Farokhzad, S.T. Barry, A. Gabizon, P. Grodzinski, D.C. Blakey, Challenges and Key Considerations of the Enhanced Permeability and Retention Effect for Nanomedicine Drug Delivery in Oncology, Cancer Research. 73 (2013)

2412–2417. https://doi.org/10.1158/0008-5472.CAN-12-4561.

[74] H. Lee, A.F. Shields, B.A. Siegel, K.D. Miller, I. Krop, C.X. Ma, P.M. LoRusso, P.N. Munster, K. Campbell, D.F. Gaddy, S.C. Leonard, E. Geretti, S.J. Blocker, D.B. Kirpotin, V. Moyo, T.J. Wickham, B.S. Hendriks, 64Cu-MM-302 Positron Emission Tomography Quantifies Variability of Enhanced Permeability and Retention of Nanoparticles in Relation to Treatment Response in Patients with Metastatic Breast Cancer, Clinical Cancer Research. 23 (2017) 4190–4202. https://doi.org/10.1158/1078-0432.CCR-16-3193.

[75] L.-P. Wu, D. Wang, Z. Li, Grand challenges in nanomedicine, Materials Science and Engineering: C. 106 (2020) 110302. https://doi.org/10.1016/j.msec.2019.110302.

[76] S.N. Bhatia, X. Chen, M.A. Dobrovolskaia, T. Lammers, Cancer nanomedicine, Nat Rev Cancer. 22 (2022) 550–556. https://doi.org/10.1038/s41568-022-00496-9.

[77] S. Wilhelm, A.J. Tavares, Q. Dai, S. Ohta, J. Audet, H.F. Dvorak, W.C.W. Chan, Analysis of nanoparticle delivery to tumours, Nat Rev Mater. 1 (2016) 16014. https://doi.org/10.1038/natrevmats.2016.14.

[78] T. Shukla, N. Upmanyu, S.P. Pandey, M.S. Sudheesh, Site-specific drug delivery, targeting, and gene therapy, in: Nanoarchitectonics in Biomedicine, Elsevier, 2019: pp. 473–505. https://doi.org/10.1016/B978-0-12-816200-2.00013-X.

[79] W. Yu, R. Liu, Y. Zhou, H. Gao, Size-Tunable Strategies for a Tumor Targeted Drug Delivery System, ACS Cent. Sci. 6 (2020) 100–116. https://doi.org/10.1021/acscentsci.9b01139.

[80] S. Kotopoulis, G. Dimcevski, O. Helge Gilja, D. Hoem, M. Postema, Treatment of human pancreatic cancer using combined ultrasound, microbubbles, and gemcitabine: A clinical case study: Clinical sonoporation setup for human pancreatic cancer, Med. Phys. 40 (2013) 072902. https://doi.org/10.1118/1.4808149.

[81] G. Dimcevski, S. Kotopoulis, T. Bjånes, D. Hoem, J. Schjøtt, B.T. Gjertsen, M. Biermann, A. Molven, H. Sorbye, E. McCormack, M. Postema, O.H. Gilja, A human clinical trial using ultrasound and microbubbles to enhance gemcitabine treatment of inoperable pancreatic cancer, Journal of Controlled Release. 243 (2016) 172–181. https://doi.org/10.1016/j.jconrel.2016.10.007.

[82] B. Theek, M. Baues, T. Ojha, D. Möckel, S.K. Veettil, J. Steitz, L. van Bloois, G. Storm, F. Kiessling, T. Lammers, Sonoporation enhances liposome accumulation and penetration in tumors with low EPR, Journal of Controlled Release. 231 (2016) 77–85. https://doi.org/10.1016/j.jconrel.2016.02.021.

[83] P. Tharkar, R. Varanasi, W.S.F. Wong, C.T. Jin, W. Chrzanowski, Nano-Enhanced Drug Delivery and Therapeutic Ultrasound for Cancer Treatment and Beyond, Front. Bioeng. Biotechnol. 7 (2019) 324. https://doi.org/10.3389/fbioe.2019.00324.

[84] J.W. Nichols, Y.H. Bae, Odyssey of a cancer nanoparticle: From injection site to site of action, Nano Today. 7 (2012) 606–618. https://doi.org/10.1016/j.nantod.2012.10.010.

[85] S.K. Golombek, J.-N. May, B. Theek, L. Appold, N. Drude, F. Kiessling, T. Lammers, Tumor targeting via EPR: Strategies to enhance patient responses, Advanced Drug Delivery Reviews. 130 (2018) 17–38. https://doi.org/10.1016/j.addr.2018.07.007.

[86] A. Nagamitsu, K. Greish, H. Maeda, Elevating Blood Pressure as a Strategy to Increase Tumor-targeted Delivery of Macromolecular Drug SMANCS: Cases of Advanced Solid Tumors, Japanese Journal of Clinical Oncology. 39 (2009) 756–766. https://doi.org/10.1093/jjco/hyp074.

[87] T. Lammers, P. Peschke, R. Kühnlein, V. Subr, K. Ulbrich, J. Debus, P. Huber, W. Hennink, G. Storm, Effect of radiotherapy and hyperthermia on the tumor accumulation of HPMA copolymer-based drug delivery systems, Journal of Controlled Release. 117 (2007) 333–341. https://doi.org/10.1016/j.jconrel.2006.10.032.

[88] Y.-H. Cheng, C. He, J.E. Riviere, N.A. Monteiro-Riviere, Z. Lin, Meta-Analysis of Nanoparticle Delivery to Tumors Using a Physiologically Based Pharmacokinetic Modeling and Simulation Approach, ACS Nano. 14 (2020) 3075–3095. https://doi.org/10.1021/acsnano.9b08142.

[89] K.M. Tsoi, S.A. MacParland, X.-Z. Ma, V.N. Spetzler, J. Echeverri, B. Ouyang,

S.M. Fadel, E.A. Sykes, N. Goldaracena, J.M. Kaths, J.B. Conneely, B.A. Alman, M. Selzner, M.A. Ostrowski, O.A. Adeyi, A. Zilman, I.D. McGilvray, W.C.W. Chan, Mechanism of hard-nanomaterial clearance by the liver, Nature Mater. 15 (2016) 1212–1221. https://doi.org/10.1038/nmat4718.

[90] A. Chow, B.D. Brown, M. Merad, Studying the mononuclear phagocyte system in the molecular age, Nat Rev Immunol. 11 (2011) 788–798. https://doi.org/10.1038/nri3087.

[91] J.V. Jokerst, T. Lobovkina, R.N. Zare, S.S. Gambhir, Nanoparticle PEGylation for imaging and therapy, Nanomedicine. 6 (2011) 715–728. https://doi.org/10.2217/nnm.11.19.

[92] E. Beltrán-Gracia, A. López-Camacho, I. Higuera-Ciapara, J.B. Velázquez-Fernández, A.A. Vallejo-Cardona, Nanomedicine review: clinical developments in liposomal applications, Cancer Nano. 10 (2019) 11. https://doi.org/10.1186/s12645-019-0055-y.

[93] D. Pozzi, V. Colapicchioni, G. Caracciolo, S. Piovesana, A.L. Capriotti, S. Palchetti, S. De Grossi, A. Riccioli, H. Amenitsch, A. Laganà, Effect of polyethyleneglycol (PEG) chain length on the bio–nano-interactions between PEGylated lipid nanoparticles and biological fluids: from nanostructure to uptake in cancer cells, Nanoscale. 6 (2014) 2782. https://doi.org/10.1039/c3nr05559k.

[94] Y. Li, R. Liu, J. Yang, Y. Shi, G. Ma, Z. Zhang, X. Zhang, Enhanced retention

and anti-tumor efficacy of liposomes by changing their cellular uptake and pharmacokinetics behavior, Biomaterials. 41 (2015) 1–14. https://doi.org/10.1016/j.biomaterials.2014.11.010.

[95] T. Ishida, M. Ichihara, X. Wang, H. Kiwada, Spleen plays an important role in the induction of accelerated blood clearance of PEGylated liposomes, Journal of Controlled Release. 115 (2006) 243–250. https://doi.org/10.1016/j.jconrel.2006.08.001.

[96] A. Li, H.P. Luehmann, G. Sun, S. Samarajeewa, J. Zou, S. Zhang, F. Zhang, M.J. Welch, Y. Liu, K.L. Wooley, Synthesis and *In Vivo* Pharmacokinetic Evaluation of Degradable Shell Cross-Linked Polymer Nanoparticles with Poly(carboxybetaine) *versus* Poly(ethylene glycol) Surface-Grafted Coatings, ACS Nano. 6 (2012) 8970–8982. https://doi.org/10.1021/nn303030t.

[97] J.K. Armstrong, G. Hempel, S. Koling, L.S. Chan, T. Fisher, H.J. Meiselman, G. Garratty, Antibody against poly(ethylene glycol) adversely affects PEG-asparaginase therapy in acute lymphoblastic leukemia patients, Cancer. 110 (2007) 103–111. https://doi.org/10.1002/cncr.22739.

[98] D. Rosenblum, N. Joshi, W. Tao, J.M. Karp, D. Peer, Progress and challenges towards targeted delivery of cancer therapeutics, Nat Commun. 9 (2018) 1410. https://doi.org/10.1038/s41467-018-03705-y.

[99] J.D. Friedl, V. Nele, G. De Rosa, A. Bernkop-Schnürch, Bioinert, Stealth or Interactive: How Surface Chemistry of Nanocarriers Determines Their Fate In

Vivo, Adv Funct Materials. 31 (2021) 2103347. https://doi.org/10.1002/adfm.202103347.

[100] X. Han, Y. Lu, J. Xie, E. Zhang, H. Zhu, H. Du, K. Wang, B. Song, C. Yang, Y. Shi, Z. Cao, Zwitterionic micelles efficiently deliver oral insulin without opening tight junctions, Nat. Nanotechnol. 15 (2020) 605–614. https://doi.org/10.1038/s41565-020-0693-6.

[101] A.C. Anselmo, M. Zhang, S. Kumar, D.R. Vogus, S. Menegatti, M.E. Helgeson, S. Mitragotri, Elasticity of Nanoparticles Influences Their Blood Circulation, Phagocytosis, Endocytosis, and Targeting, ACS Nano. 9 (2015) 3169–3177. https://doi.org/10.1021/acsnano.5b00147.

[102] P. Valent, B. Groner, U. Schumacher, G. Superti-Furga, M. Busslinger, R. Kralovics, C. Zielinski, J.M. Penninger, D. Kerjaschki, G. Stingl, J.S. Smolen, R. Valenta, H. Lassmann, H. Kovar, U. Jäger, G. Kornek, M. Müller, F. Sörgel, Paul Ehrlich (1854-1915) and His Contributions to the Foundation and Birth of Translational Medicine, J Innate Immun. 8 (2016) 111–120. https://doi.org/10.1159/000443526.

[103] P.L. Bedard, A.R. Hansen, M.J. Ratain, L.L. Siu, Tumour heterogeneity in the clinic, Nature. 501 (2013) 355–364. https://doi.org/10.1038/nature12627.

[104] A.C. Anselmo, S. Mitragotri, Nanoparticles in the clinic: An update, Bioeng Transl Med. 4 (2019). https://doi.org/10.1002/btm2.10143.

[105] P. Decuzzi, D. Peer, D.D. Mascolo, A.L. Palange, P.N. Manghnani, S.M.

Moghimi, Z.S. Farhangrazi, K.A. Howard, D. Rosenblum, T. Liang, Z. Chen, Z. Wang, J.-J. Zhu, Z. Gu, N. Korin, D. Letourneur, C. Chauvierre, R. van der Meel, F. Kiessling, T. Lammers, Roadmap on nanomedicine, Nanotechnology. 32 (2021) 012001. https://doi.org/10.1088/1361-6528/abaadb.

[106] B.M. Necela, J.A. Crozier, C.A. Andorfer, L. Lewis-Tuffin, J.M. Kachergus, X.J. Geiger, K.R. Kalari, D.J. Serie, Z. Sun, A. Moreno-Aspitia, A.M. Aspita, D.J. O'Shannessy, J.D. Maltzman, A.E. McCullough, B.A. Pockaj, H.E. Cunliffe, K.V. Ballman, E.A. Thompson, E.A. Perez, Folate receptor-α (FOLR1) expression and function in triple negative tumors, PLoS One. 10 (2015) e0122209. https://doi.org/10.1371/journal.pone.0122209.

[107] M. Scaranti, E. Cojocaru, S. Banerjee, U. Banerji, Exploiting the folate receptor α in oncology, Nat Rev Clin Oncol. 17 (2020) 349–359. https://doi.org/10.1038/s41571-020-0339-5.

[108] K.N. Moore, A.M. Oza, N. Colombo, A. Oaknin, G. Scambia, D. Lorusso, G.E. Konecny, S. Banerjee, C.G. Murphy, J.L. Tanyi, H. Hirte, J.A. Konner, P.C. Lim, M. Prasad-Hayes, B.J. Monk, P. Pautier, J. Wang, A. Berkenblit, I. Vergote, M.J. Birrer, Phase III, randomized trial of mirvetuximab soravtansine versus chemotherapy in patients with platinum-resistant ovarian cancer: primary analysis of FORWARD I, Annals of Oncology. 32 (2021) 757–765. https://doi.org/10.1016/j.annonc.2021.02.017.

[109] Y. Matsumura, 35 years of discussions with Prof. Maeda on the EPR

effect and future directions, Journal of Controlled Release. 348 (2022) 966–969. https://doi.org/10.1016/j.jconrel.2022.06.035.

[110] Y. Matsumura, M. Gotoh, K. Muro, Y. Yamada, K. Shirao, Y. Shimada, M. Okuwa, S. Matsumoto, Y. Miyata, H. Ohkura, K. Chin, S. Baba, T. Yamao, A. Kannami, Y. Takamatsu, K. Ito, K. Takahashi, Phase I and pharmacokinetic study of MCC-465, a doxorubicin (DXR) encapsulated in PEG immunoliposome, in patients with metastatic stomach cancer, Annals of Oncology. 15 (2004) 517–525. https://doi.org/10.1093/annonc/mdh092.

[111] H. Fuchigami, S. Manabe, M. Yasunaga, Y. Matsumura, Chemotherapy payload of anti-insoluble fibrin antibody-drug conjugate is released specifically upon binding to fibrin, Sci Rep. 8 (2018) 14211. https://doi.org/10.1038/s41598-018-32601-0.

[112] E. Boedtkjer, S.F. Pedersen, The Acidic Tumor Microenvironment as a Driver of Cancer, Annu. Rev. Physiol. 82 (2020) 103–126. https://doi.org/10.1146/annurev-physiol-021119-034627.

[113] V. Petrova, M. Annicchiarico-Petruzzelli, G. Melino, I. Amelio, The hypoxic tumour microenvironment, Oncogenesis. 7 (2018) 10. https://doi.org/10.1038/s41389-017-0011-9.

[114] B.T. Finicle, V. Jayashankar, A.L. Edinger, Nutrient scavenging in cancer, Nat Rev Cancer. 18 (2018) 619–633. https://doi.org/10.1038/s41568-018-0048-x.

[115] D.C. Sullivan, L. Huminiecki, J.W. Moore, J.J. Boyle, R. Poulsom, D. Creamer, J. Barker, R. Bicknell, EndoPDI, a Novel Protein-disulfide Isomerase-like Protein That Is Preferentially Expressed in Endothelial Cells Acts as a Stress Survival Factor, Journal of Biological Chemistry. 278 (2003) 47079–47088. https://doi.org/10.1074/jbc.M308124200.

[116] D. Neri, R. Bicknell, Tumour vascular targeting, Nat Rev Cancer. 5 (2005) 436–446. https://doi.org/10.1038/nrc1627.

[117] F. Chen, H. Hong, Y. Zhang, H.F. Valdovinos, S. Shi, G.S. Kwon, C.P. Theuer, T.E. Barnhart, W. Cai, *In Vivo* Tumor Targeting and Image-Guided Drug Delivery with Antibody-Conjugated, Radiolabeled Mesoporous Silica Nanoparticles, ACS Nano. 7 (2013) 9027–9039. https://doi.org/10.1021/nn403617j.

[118] E. Fonsatti, A.P. Jekunen, K.J.A. Kairemo, S. Coral, M. Snellman, M.R. Nicotra, P.G. Natali, M. Altomonte, M. Maio, Endoglin Is a Suitable Target for Efficient Imaging of Solid Tumors: In Vivo Evidence in a Canine Mammary Carcinoma Model, (n.d.) 7.

[119] M.J. Mitchell, M.M. Billingsley, R.M. Haley, M.E. Wechsler, N.A. Peppas, R. Langer, Engineering precision nanoparticles for drug delivery, Nat Rev Drug Discov. 20 (2021) 101–124. https://doi.org/10.1038/s41573-020-0090-8.

[120] ANTIGEN PRESENTATION, in: Immunology Guidebook, Elsevier, 2004: pp. 267–276. https://doi.org/10.1016/B978-012198382-6/50031-5.

[121] M.A. Morse, D. Niedzwiecki, J.L. Marshall, C. Garrett, D.Z. Chang, M. Aklilu, T.S. Crocenzi, D.J. Cole, S. Dessureault, A.C. Hobeika, T. Osada, M. Onaitis, B.M. Clary, D. Hsu, G.R. Devi, A. Bulusu, R.P. Annechiarico, V. Chadaram, T.M. Clay, H.K. Lyerly, A Randomized Phase II Study of Immunization With Dendritic Cells Modified With Poxvectors Encoding CEA and MUC1 Compared With the Same Poxvectors Plus GM-CSF for Resected Metastatic Colorectal Cancer, Annals of Surgery. 258 (2013) 879–886. https://doi.org/10.1097/SLA.0b013e318292919e.

[122] N.K. Ibrahim, J.L. Murray, D. Zhou, E.A. Mittendorf, D. Sample, M. Tautchin, D. Miles, Survival Advantage in Patients with Metastatic Breast Cancer Receiving Endocrine Therapy plus Sialyl Tn-KLH Vaccine: Post Hoc Analysis of a Large Randomized Trial, J. Cancer. 4 (2013) 577–584. https://doi.org/10.7150/jca.7028.

[123] S.H. van der Burg, R. Arens, F. Ossendorp, T. van Hall, C.J.M. Melief, Vaccines for established cancer: overcoming the challenges posed by immune evasion, Nat Rev Cancer. 16 (2016) 219–233. https://doi.org/10.1038/nrc.2016.16.

[124] T.M. Fahmy, P.M. Fong, A. Goyal, W.M. Saltzman, Targeted for drug delivery, Materials Today. 8 (2005) 18–26. https://doi.org/10.1016/S1369-7021(05)71033-6.

[125] R. Xu, G. Zhang, J. Mai, X. Deng, V. Segura-Ibarra, S. Wu, J. Shen, H.

Liu, Z. Hu, L. Chen, Y. Huang, E. Koay, Y. Huang, J. Liu, J.E. Ensor, E. Blanco, X. Liu, M. Ferrari, H. Shen, An injectable nanoparticle generator enhances delivery of cancer therapeutics, Nat Biotechnol. 34 (2016) 414–418. https://doi.org/10.1038/nbt.3506.

[126] L. Palanikumar, S. Al-Hosani, M. Kalmouni, V.P. Nguyen, L. Ali, R. Pasricha, F.N. Barrera, M. Magzoub, pH-responsive high stability polymeric nanoparticles for targeted delivery of anticancer therapeutics, Commun Biol. 3 (2020) 95. https://doi.org/10.1038/s42003-020-0817-4.

[127] Y. Zhou, H. Ye, Y. Chen, R. Zhu, L. Yin, Photoresponsive Drug/Gene Delivery Systems, Biomacromolecules. 19 (2018) 1840–1857. https://doi.org/10.1021/acs.biomac.8b00422.

[128] P.M. Price, W.E. Mahmoud, A.A. Al-Ghamdi, L.M. Bronstein, Magnetic Drug Delivery: Where the Field Is Going, Front. Chem. 6 (2018) 619. https://doi.org/10.3389/fchem.2018.00619.

[129] G.C. Terstappen, A.H. Meyer, R.D. Bell, W. Zhang, Strategies for delivering therapeutics across the blood–brain barrier, Nat Rev Drug Discov. 20 (2021) 362–383. https://doi.org/10.1038/s41573-021-00139-y.

[130] N.I. Millagaha Gedara, X. Xu, R. DeLong, S. Aryal, M. Jaberi-Douraki, Global Trends in Cancer Nanotechnology: A Qualitative Scientific Mapping Using Content-Based and Bibliometric Features for Machine Learning Text Classification, Cancers. 13 (2021) 4417.

https://doi.org/10.3390/cancers13174417.

[131] H. He, L. Liu, E.E. Morin, M. Liu, A. Schwendeman, Survey of Clinical Translation of Cancer Nanomedicines—Lessons Learned from Successes and Failures, Acc. Chem. Res. 52 (2019) 2445–2461. https://doi.org/10.1021/acs.accounts.9b00228.

[132] M.R. Green, G.M. Manikhas, S. Orlov, B. Afanasyev, A.M. Makhson, P. Bhar, M.J. Hawkins, Abraxane®, a novel Cremophor®-free, albumin-bound particle form of paclitaxel for the treatment of advanced non-small-cell lung cancer, Annals of Oncology. 17 (2006) 1263–1268. https://doi.org/10.1093/annonc/mdl104.

[133] N.K. Ibrahim, N. Desai, S. Legha, P. Soon-Shiong, R.L. Theriault, E. Rivera, B. Esmaeli, S.E. Ring, A. Bedikian, G.N. Hortobagyi, J.A. Ellerhorst, Phase I and pharmacokinetic study of ABI-007, a Cremophor-free, protein-stabilized, nanoparticle formulation of paclitaxel, Clin Cancer Res. 8 (2002) 1038–1044.

[134] W.J. Gradishar, S. Tjulandin, N. Davidson, H. Shaw, N. Desai, P. Bhar, M. Hawkins, J. O'Shaughnessy, Phase III Trial of Nanoparticle Albumin-Bound Paclitaxel Compared With Polyethylated Castor Oil–Based Paclitaxel in Women With Breast Cancer, JCO. 23 (2005) 7794–7803. https://doi.org/10.1200/JCO.2005.04.937.

[135] J. Gallego-Jara, G. Lozano-Terol, R.A. Sola-Martínez, M. Cánovas-Díaz,

T. de Diego Puente, A Compressive Review about Taxol®: History and Future Challenges, Molecules. 25 (2020) 5986. https://doi.org/10.3390/molecules25245986.

[136] H. Yuan, H. Guo, X. Luan, M. He, F. Li, J. Burnett, N. Truchan, D. Sun, Albumin Nanoparticle of Paclitaxel (Abraxane) Decreases while Taxol Increases Breast Cancer Stem Cells in Treatment of Triple Negative Breast Cancer, Mol. Pharmaceutics. 17 (2020) 2275–2286. https://doi.org/10.1021/acs.molpharmaceut.9b01221.

[137] D.W. Nyman, K.J. Campbell, E. Hersh, K. Long, K. Richardson, V. Trieu, N. Desai, M.J. Hawkins, D.D. Von Hoff, Phase I and Pharmacokinetics Trial of ABI-007, a Novel Nanoparticle Formulation of Paclitaxel in Patients With Advanced Nonhematologic Malignancies, JCO. 23 (2005) 7785–7793. https://doi.org/10.1200/JCO.2004.00.6148.

[138] J. Huang, B. Wu, Z. Zhou, S. Hu, H. Xu, Y. Piao, H. Zheng, J. Tang, X. Liu, Y. Shen, Drug-binding albumins forming stabilized nanoparticles for efficient anticancer therapy, Nanomedicine: Nanotechnology, Biology and Medicine. 21 (2019) 102058. https://doi.org/10.1016/j.nano.2019.102058.

[139] V. Hornok, Serum Albumin Nanoparticles: Problems and Prospects, Polymers. 13 (2021) 3759. https://doi.org/10.3390/polym13213759.

[140] A. Jahanban-Esfahlan, S. Dastmalchi, S. Davaran, A simple improved desolvation method for the rapid preparation of albumin nanoparticles,

International Journal of Biological Macromolecules. 91 (2016) 703–709. https://doi.org/10.1016/j.ijbiomac.2016.05.032.

[141] C. Weber, C. Coester, J. Kreuter, K. Langer, Desolvation process and surface characterisation of protein nanoparticles, International Journal of Pharmaceutics. 194 (2000) 91–102. https://doi.org/10.1016/S0378-5173(99)00370-1.

[142] S. Li, Y. Cao, F. Geng, Genome-Wide Identification and Comparative Analysis of Albumin Family in Vertebrates, Evol Bioinform Online. 13 (2017) 117693431771608. https://doi.org/10.1177/1176934317716089.

[143] T. Pappa, S. Refetoff, Thyroid Hormone Transport Proteins: Thyroxine-Binding Globulin, Transthyretin, and Albumin ☆, in: Reference Module in Neuroscience and Biobehavioral Psychology, Elsevier, 2017: p. B9780128093245034000. https://doi.org/10.1016/B978-0-12-809324-5.03494-5.

[144] A.O. Elzoghby, W.M. Samy, N.A. Elgindy, Albumin-based nanoparticles as potential controlled release drug delivery systems, Journal of Controlled Release. 157 (2012) 168–182. https://doi.org/10.1016/j.jconrel.2011.07.031.

[145] Z. Ahmad, A. Shah, M. Siddiq, H.-B. Kraatz, Polymeric micelles as drug delivery vehicles, RSC Adv. 4 (2014) 17028–17038. https://doi.org/10.1039/C3RA47370H.

[146] A. Hashidzume, A. Harada, Micelles and Vesicles, in: S. Kobayashi, K.

Müllen (Eds.), Encyclopedia of Polymeric Nanomaterials, Springer Berlin Heidelberg, Berlin, Heidelberg, 2015: pp. 1238–1241. https://doi.org/10.1007/978-3-642-29648-2_56.

[147] L. Zhang, A. Eisenberg, Multiple Morphologies of “Crew-Cut” Aggregates of Polystyrene-b-poly(acrylic acid) Block Copolymers, Science. 268 (1995) 1728–1731. https://doi.org/10.1126/science.268.5218.1728.

[148] Y. Lu, E. Zhang, J. Yang, Z. Cao, Strategies to improve micelle stability for drug delivery, Nano Res. 11 (2018) 4985–4998. https://doi.org/10.1007/s12274-018-2152-3.

[149] K. Kataoka, A. Harada, Y. Nagasaki, Block copolymer micelles for drug delivery: design, characterization and biological significance, Advanced Drug Delivery Reviews. 47 (2001) 113–131. https://doi.org/10.1016/S0169-409X(00)00124-1.

[150] J. Bergfreund, P. Bertsch, P. Fischer, Effect of the hydrophobic phase on interfacial phenomena of surfactants, proteins, and particles at fluid interfaces, Current Opinion in Colloid & Interface Science. 56 (2021) 101509. https://doi.org/10.1016/j.cocis.2021.101509.

[151] J.L. Benesch, B.T. Ruotolo, Mass spectrometry: come of age for structural and dynamical biology, Current Opinion in Structural Biology. 21 (2011) 641–649. https://doi.org/10.1016/j.sbi.2011.08.002.

[152] S.S. Rubakhin, J.V. Sweedler, A mass spectrometry primer for mass

spectrometry imaging, Methods Mol Biol. 656 (2010) 21–49. https://doi.org/10.1007/978-1-60761-746-4_2.

[153] Z. Takáts, J.M. Wiseman, B. Gologan, R.G. Cooks, Mass Spectrometry Sampling Under Ambient Conditions with Desorption Electrospray Ionization, Science. 306 (2004) 471–473. https://doi.org/10.1126/science.1104404.

[154] G. Kaklamanos, E. Aprea, G. Theodoridis, Mass Spectrometry: Principles and Instrumentation, in: Encyclopedia of Food and Health, Elsevier, 2016: pp. 661–668. https://doi.org/10.1016/B978-0-12-384947-2.00447-5.

[155] K. Chen, D. Baluya, M. Tosun, F. Li, M. Maletic-Savatic, Imaging Mass Spectrometry: A New Tool to Assess Molecular Underpinnings of Neurodegeneration, Metabolites. 9 (2019) 135. https://doi.org/10.3390/metabo9070135.

[156] A. Dutta, Fourier Transform Infrared Spectroscopy, in: Spectroscopic Methods for Nanomaterials Characterization, Elsevier, 2017: pp. 73–93. https://doi.org/10.1016/B978-0-323-46140-5.00004-2.

[157] G.G. Emch, QUANTUM STATISTICAL PHYSICS, in: Philosophy of Physics, Elsevier, 2007: pp. 1075–1182. https://doi.org/10.1016/B978-044451560-5/50013-0.

[158] K.Y. Bliokh, D. Smirnova, F. Nori, Quantum spin Hall effect of light, (n.d.) 5.

[159] P.R. Griffiths, Fourier Transform Infrared Spectrometry, Science. 222

(1983) 297–302. https://doi.org/10.1126/science.6623077.

[160] N.J. Greenfield, Using circular dichroism spectra to estimate protein secondary structure, Nat Protoc. 1 (2006) 2876–2890. https://doi.org/10.1038/nprot.2006.202.

[161] A. Kumar, C.K. Dixit, Methods for characterization of nanoparticles, in: Advances in Nanomedicine for the Delivery of Therapeutic Nucleic Acids, Elsevier, 2017: pp. 43–58. https://doi.org/10.1016/B978-0-08-100557-6.00003-1.

[162] J. Stetefeld, S.A. McKenna, T.R. Patel, Dynamic light scattering: a practical guide and applications in biomedical sciences, Biophys Rev. 8 (2016) 409–427. https://doi.org/10.1007/s12551-016-0218-6.

[163] A.S. Parmar, M. Muschol, Hydration and Hydrodynamic Interactions of Lysozyme: Effects of Chaotropic versus Kosmotropic Ions, Biophysical Journal. 97 (2009) 590–598. https://doi.org/10.1016/j.bpj.2009.04.045.

[164] M. Malatesta, Transmission Electron Microscopy as a Powerful Tool to Investigate the Interaction of Nanoparticles with Subcellular Structures, IJMS. 22 (2021) 12789. https://doi.org/10.3390/ijms222312789.

[165] L. Graham, J.M. Orenstein, Processing tissue and cells for transmission electron microscopy in diagnostic pathology and research, Nat Protoc. 2 (2007) 2439–2450. https://doi.org/10.1038/nprot.2007.304.

[166] G. Fanali, A. di Masi, V. Trezza, M. Marino, M. Fasano, P. Ascenzi, Human

serum albumin: From bench to bedside, Molecular Aspects of Medicine. 33 (2012) 209–290. https://doi.org/10.1016/j.mam.2011.12.002.

[167] M. Taverna, A.-L. Marie, J.-P. Mira, B. Guidet, Specific antioxidant properties of human serum albumin, Ann Intensive Care. 3 (2013) 4. https://doi.org/10.1186/2110-5820-3-4.

[168] M. Henkel, N. Röckendorf, A. Frey, Selective and Efficient Cysteine Conjugation by Maleimides in the Presence of Phosphine Reductants, Bioconjugate Chem. 27 (2016) 2260–2265. https://doi.org/10.1021/acs.bioconjchem.6b00371.

[169] N. Vanparijs, S. Maji, B. Louage, L. Voorhaar, D. Laplace, Q. Zhang, Y. Shi, W.E. Hennink, R. Hoogenboom, B.G. De Geest, Polymer-protein conjugation *via* a ‘grafting to’ approach – a comparative study of the performance of protein-reactive RAFT chain transfer agents, Polym. Chem. 6 (2015) 5602–5614. https://doi.org/10.1039/C4PY01224K.

[170] P.C. Nauka, J. Lee, H.D. Maynard, Enhancing the conjugation yield of brush polymer–protein conjugates by increasing the linker length at the polymer end-group, Polym. Chem. 7 (2016) 2352–2357. https://doi.org/10.1039/C6PY00080K.

[171] Y. Zhao, B. Jin, R. Tang, Biomineralization, in: Reference Module in Chemistry, Molecular Sciences and Chemical Engineering, Elsevier, 2021: p. B9780128231449000000. https://doi.org/10.1016/B978-0-12-823144-

9.00052-2.

[172] W.F. Wolkers, H. Oldenhof, eds., Cryopreservation and Freeze-Drying Protocols, Springer US, New York, NY, 2021. https://doi.org/10.1007/978-1-0716-0783-1.

[173] D. Usoltsev, V. Sitnikova, A. Kajava, M. Uspenskaya, FTIR Spectroscopy Study of the Secondary Structure Changes in Human Serum Albumin and Trypsin under Neutral Salts, Biomolecules. 10 (2020) 606. https://doi.org/10.3390/biom10040606.

[174] Sigma Aldrich, Product information of Albumin, Human, (n.d.). https://www.sigmaaldrich.com/deepweb/assets/sigmaaldrich/product/documents/318/740/a1653pis.pdf.

[175] M.L.E. Lundahl, S. Fogli, P.E. Colavita, E.M. Scanlan, Aggregation of protein therapeutics enhances their immunogenicity: causes and mitigation strategies, RSC Chem. Biol. 2 (2021) 1004–1020. https://doi.org/10.1039/D1CB00067E.

[176] D.R. Perinelli, M. Cespi, N. Lorusso, G.F. Palmieri, G. Bonacucina, P. Blasi, Surfactant Self-Assembling and Critical Micelle Concentration: One Approach Fits All?, Langmuir. 36 (2020) 5745–5753. https://doi.org/10.1021/acs.langmuir.0c00420.

[177] L. Piñeiro, M. Novo, W. Al-Soufi, Fluorescence emission of pyrene in surfactant solutions, Advances in Colloid and Interface Science. 215 (2015)

1–12. https://doi.org/10.1016/j.cis.2014.10.010.

[178] C. Wu, Y. Gao, Y. Liu, X. Xu, Pure paclitaxel nanoparticles: preparation, characterization, and antitumor effect for human liver cancer SMMC-7721 cells, IJN. Volume 13 (2018) 6189–6198. https://doi.org/10.2147/IJN.S169209.

[179] F.Y. Alqahtani, F.S. Aleanizy, E. El Tahir, H.M. Alkahtani, B.T. AlQuadeib, Paclitaxel, in: Profiles of Drug Substances, Excipients and Related Methodology, Elsevier, 2019: pp. 205–238. https://doi.org/10.1016/bs.podrm.2018.11.001.

[180] S. Kotta, H.M. Aldawsari, S.M. Badr-Eldin, A.B. Nair, K. Yt, Progress in Polymeric Micelles for Drug Delivery Applications, Pharmaceutics. 14 (2022) 1636. https://doi.org/10.3390/pharmaceutics14081636.

[181] B. Nikolin, B. Imamović, S. Medanhodžić-Vuk, M. Sober, High performance liquid chromatography in pharmaceutical analyses, Bosn J of Basic Med Sci. 4 (2004) 5–9. https://doi.org/10.17305/bjbms.2004.3405.

[182] W. Lei, V.N. Mochalin, D. Liu, S. Qin, Y. Gogotsi, Y. Chen, Boron nitride colloidal solutions, ultralight aerogels and freestanding membranes through one-step exfoliation and functionalization, Nat Commun. 6 (2015) 8849. https://doi.org/10.1038/ncomms9849.

[183] M. Gumustas, C.T. Sengel-Turk, A. Gumustas, S.A. Ozkan, B. Uslu, Effect of Polymer-Based Nanoparticles on the Assay of Antimicrobial Drug

Delivery Systems, in: Multifunctional Systems for Combined Delivery, Biosensing and Diagnostics, Elsevier, 2017: pp. 67–108. https://doi.org/10.1016/B978-0-323-52725-5.00005-8.

[184] V. Gupta, P. Trivedi, In vitro and in vivo characterization of pharmaceutical topical nanocarriers containing anticancer drugs for skin cancer treatment, in: Lipid Nanocarriers for Drug Targeting, Elsevier, 2018: pp. 563–627. https://doi.org/10.1016/B978-0-12-813687-4.00015-3.

[185] V.S. Kulkarni, Handbook of non-invasive drug delivery systems: non-invasive and minimally-invasive drug delivery systems for pharmaceutical, and personal care products, 1st ed, Elsevier, Oxford, 2010.

[186] S. Samimi, N. Maghsoudnia, R.B. Eftekhari, F. Dorkoosh, Lipid-Based Nanoparticles for Drug Delivery Systems, in: Characterization and Biology of Nanomaterials for Drug Delivery, Elsevier, 2019: pp. 47–76. https://doi.org/10.1016/B978-0-12-814031-4.00003-9.

[187] D.J. Pochapski, C. Carvalho dos Santos, G.W. Leite, S.H. Pulcinelli, C.V. Santilli, Zeta Potential and Colloidal Stability Predictions for Inorganic Nanoparticle Dispersions: Effects of Experimental Conditions and Electrokinetic Models on the Interpretation of Results, Langmuir. 37 (2021) 13379–13389. https://doi.org/10.1021/acs.langmuir.1c02056.

[188] J. Bhattacharyya, J.J. Bellucci, I. Weitzhandler, J.R. McDaniel, I. Spasojevic, X. Li, C.-C. Lin, J.-T.A. Chi, A. Chilkoti, A paclitaxel-loaded

recombinant polypeptide nanoparticle outperforms Abraxane in multiple murine cancer models, Nat Commun. 6 (2015) 7939. https://doi.org/10.1038/ncomms8939.

[189] C.E. Callmann, C.L.M. LeGuyader, S.T. Burton, M.P. Thompson, R. Hennis, C. Barback, N.M. Henriksen, W.C. Chan, M.J. Jaremko, J. Yang, A. Garcia, M.D. Burkart, M.K. Gilson, J.D. Momper, P.A. Bertin, N.C. Gianneschi, Antitumor Activity of 1,18-Octadecanedioic Acid-Paclitaxel Complexed with Human Serum Albumin, J. Am. Chem. Soc. 141 (2019) 11765–11769. https://doi.org/10.1021/jacs.9b04272.

[190] A. Tsuda, N.V. Konduru, The role of natural processes and surface energy of inhaled engineered nanoparticles on aggregation and corona formation, NanoImpact. 2 (2016) 38–44. https://doi.org/10.1016/j.impact.2016.06.002.

[191] M. Zhao, C. Lei, Y. Yang, X. Bu, H. Ma, H. Gong, J. Liu, X. Fang, Z. Hu, Q. Fang, Abraxane, the Nanoparticle Formulation of Paclitaxel Can Induce Drug Resistance by Up-Regulation of P-gp, PLoS ONE. 10 (2015) e0131429. https://doi.org/10.1371/journal.pone.0131429.

[192] B.A. Weaver, How Taxol/paclitaxel kills cancer cells, MBoC. 25 (2014) 2677–2681. https://doi.org/10.1091/mbc.e14-04-0916.

[193] M.C. Wani, H.L. Taylor, M.E. Wall, P. Coggon, A.T. McPhail, Plant antitumor agents. VI. Isolation and structure of taxol, a novel antileukemic and antitumor agent from Taxus brevifolia, J. Am. Chem. Soc. 93 (1971) 2325–

2327. https://doi.org/10.1021/ja00738a045.

[194] P.B. Schiff, J. Fant, S.B. Horwitz, Promotion of microtubule assembly in vitro by taxol, Nature. 277 (1979) 665–667. https://doi.org/10.1038/277665a0.

[195] B. Yameen, W.I. Choi, C. Vilos, A. Swami, J. Shi, O.C. Farokhzad, Insight into nanoparticle cellular uptake and intracellular targeting, Journal of Controlled Release. 190 (2014) 485–499. https://doi.org/10.1016/j.jconrel.2014.06.038.

[196] R. Firdessa, T.A. Oelschlaeger, H. Moll, Identification of multiple cellular uptake pathways of polystyrene nanoparticles and factors affecting the uptake: Relevance for drug delivery systems, European Journal of Cell Biology. 93 (2014) 323–337. https://doi.org/10.1016/j.ejcb.2014.08.001.

[197] J.J. Rennick, A.P.R. Johnston, R.G. Parton, Key principles and methods for studying the endocytosis of biological and nanoparticle therapeutics, Nat. Nanotechnol. 16 (2021) 266–276. https://doi.org/10.1038/s41565-021-00858-8.

[198] T.-G. Iversen, T. Skotland, K. Sandvig, Endocytosis and intracellular transport of nanoparticles: Present knowledge and need for future studies, Nano Today. 6 (2011) 176–185. https://doi.org/10.1016/j.nantod.2011.02.003.

[199] R. Lakshminarayan, C. Wunder, U. Becken, M.T. Howes, C. Benzing, S. Arumugam, S. Sales, N. Ariotti, V. Chambon, C. Lamaze, D. Loew, A. Shevchenko, K. Gaus, R.G. Parton, L. Johannes, Galectin-3 drives

glycosphingolipid-dependent biogenesis of clathrin-independent carriers, Nat Cell Biol. 16 (2014) 592–603. https://doi.org/10.1038/ncb2970.

[200] R.G. Parton, M.A. Pozo, S. Vassilopoulos, I.R. Nabi, S. Le Lay, R. Lundmark, A.K. Kenworthy, A. Camus, C.M. Blouin, W.C. Sessa, C. Lamaze, Caveolae: The FAQs, Traffic. 21 (2020) 181–185. https://doi.org/10.1111/tra.12689.

[201] M. Kirkham, A. Fujita, R. Chadda, S.J. Nixon, T.V. Kurzchalia, D.K. Sharma, R.E. Pagano, J.F. Hancock, S. Mayor, R.G. Parton, Ultrastructural identification of uncoated caveolin-independent early endocytic vehicles, Journal of Cell Biology. 168 (2005) 465–476. https://doi.org/10.1083/jcb.200407078.

[202] B.L. Wolfe, J. Trejo, Clathrin-Dependent Mechanisms of G Protein-coupled Receptor Endocytosis, Traffic. 8 (2007) 462–470. https://doi.org/10.1111/j.1600-0854.2007.00551.x.

[203] J.E. Heuser, R.G. Anderson, Hypertonic media inhibit receptor-mediated endocytosis by blocking clathrin-coated pit formation., Journal of Cell Biology. 108 (1989) 389–400. https://doi.org/10.1083/jcb.108.2.389.

[204] M. Mettlen, P.-H. Chen, S. Srinivasan, G. Danuser, S.L. Schmid, Regulation of Clathrin-Mediated Endocytosis, Annu. Rev. Biochem. 87 (2018) 871–896. https://doi.org/10.1146/annurev-biochem-062917-012644.

[205] M. Kaksonen, A. Roux, Mechanisms of clathrin-mediated endocytosis,

Nat Rev Mol Cell Biol. 19 (2018) 313–326. https://doi.org/10.1038/nrm.2017.132.

[206] A. Casamento, E. Boucrot, Molecular mechanism of Fast Endophilin-Mediated Endocytosis, Biochemical Journal. 477 (2020) 2327–2345. https://doi.org/10.1042/BCJ20190342.

[207] S. Sabharanjak, Folate receptor endocytosis and trafficking, Advanced Drug Delivery Reviews. 56 (2004) 1099–1109. https://doi.org/10.1016/j.addr.2004.01.010.

[208] Y. Hui, X. Yi, D. Wibowo, G. Yang, A.P.J. Middelberg, H. Gao, C.-X. Zhao, Nanoparticle elasticity regulates phagocytosis and cancer cell uptake, Sci. Adv. 6 (2020) eaaz4316. https://doi.org/10.1126/sciadv.aaz4316.

[209] J.A. Swanson, C. Watts, Macropinocytosis, Trends in Cell Biology. 5 (1995) 424–428. https://doi.org/10.1016/S0962-8924(00)89101-1.

[210] F. Niedergang, S. Grinstein, How to build a phagosome: new concepts for an old process, Current Opinion in Cell Biology. 50 (2018) 57–63. https://doi.org/10.1016/j.ceb.2018.01.009.

[211] C. Commisso, R.J. Flinn, D. Bar-Sagi, Determining the macropinocytic index of cells through a quantitative image-based assay, Nat Protoc. 9 (2014) 182–192. https://doi.org/10.1038/nprot.2014.004.

[212] S.G. Arbuck, H. Strauss, E. Rowinsky, M. Christian, M. Suffness, J. Adams, M. Oakes, W. McGuire, E. Reed, H. Gibbs, A reassessment of cardiac

toxicity associated with Taxol, J Natl Cancer Inst Monogr. (1993) 117–130.

[213] A. Sparreboom, C.D. Scripture, V. Trieu, P.J. Williams, T. De, A. Yang, B. Beals, W.D. Figg, M. Hawkins, N. Desai, Comparative Preclinical and Clinical Pharmacokinetics of a Cremophor-Free, Nanoparticle Albumin-Bound Paclitaxel (ABI-007) and Paclitaxel Formulated in Cremophor (Taxol), Clin Cancer Res. 11 (2005) 4136–4143. https://doi.org/10.1158/1078-0432.CCR-04-2291.

[214] K.-H. Diehl, R. Hull, D. Morton, R. Pfister, Y. Rabemampianina, D. Smith, J.-M. Vidal, C.V.D. Vorstenbosch, A good practice guide to the administration of substances and removal of blood, including routes and volumes, J. Appl. Toxicol. 21 (2001) 15–23. https://doi.org/10.1002/jat.727.

[215] S. Wilhelm, A.J. Tavares, Q. Dai, S. Ohta, J. Audet, H.F. Dvorak, W.C.W. Chan, Analysis of nanoparticle delivery to tumours, Nat Rev Mater. 1 (2016) 16014. https://doi.org/10.1038/natrevmats.2016.14.

[216] K. Ray, Clearance of nanomaterials in the liver, Nat Rev Gastroenterol Hepatol. 13 (2016) 560–560. https://doi.org/10.1038/nrgastro.2016.136.

[217] D. Sun, S. Zhou, W. Gao, What Went Wrong with Anticancer Nanomedicine Design and How to Make It Right, ACS Nano. 14 (2020) 12281–12290. https://doi.org/10.1021/acsnano.9b09713.

[218] G.M. Rothe, ELECTROPHORESIS | Porosity Gradient Gels, in: Encyclopedia of Separation Science, Elsevier, 2000: pp. 1315–1342.

https://doi.org/10.1016/B0-12-226770-2/03621-8.

[219] S. Zhang, X. Liu, T. Bawa-Khalfe, L.-S. Lu, Y.L. Lyu, L.F. Liu, E.T.H. Yeh, Identification of the molecular basis of doxorubicin-induced cardiotoxicity, Nat Med. 18 (2012) 1639–1642. https://doi.org/10.1038/nm.2919.

[220] W.J. Gradishar, S. Tjulandin, N. Davidson, H. Shaw, N. Desai, P. Bhar, M. Hawkins, J. O'Shaughnessy, Phase III Trial of Nanoparticle Albumin-Bound Paclitaxel Compared With Polyethylated Castor Oil–Based Paclitaxel in Women With Breast Cancer, JCO. 23 (2005) 7794–7803. https://doi.org/10.1200/JCO.2005.04.937.

[221] D.B. Kirpotin, D.C. Drummond, Y. Shao, M.R. Shalaby, K. Hong, U.B. Nielsen, J.D. Marks, C.C. Benz, J.W. Park, Antibody Targeting of Long-Circulating Lipidic Nanoparticles Does Not Increase Tumor Localization but Does Increase Internalization in Animal Models, Cancer Research. 66 (2006) 6732–6740. https://doi.org/10.1158/0008-5472.CAN-05-4199.

[222] A.K. Barui, J.Y. Oh, B. Jana, C. Kim, J. Ryu, Cancer-Targeted Nanomedicine: Overcoming the Barrier of the Protein Corona, Adv. Therap. 3 (2020) 1900124. https://doi.org/10.1002/adtp.201900124.

[223] J.J. Calvin, A.S. Brewer, A.P. Alivisatos, The role of organic ligand shell structures in colloidal nanocrystal synthesis, Nat Synth. 1 (2022) 127–137. https://doi.org/10.1038/s44160-022-00025-4.

[224] National Comprehensive Cancer Network, NCCN Clinical Practice

Guidelines in Oncology (NCCN Guidelines®) for Breast Cancer Version 2.2023, (2023). https://www.nccn.org/professionals/physician_gls/pdf/breast.pdf.

[225] B. Wang, T. Sun, Y. Zhao, S. Wang, J. Zhang, Z. Wang, Y.-E. Teng, L. Cai, M. Yan, X. Wang, Z. Jiang, Y. Pan, J. Luo, Z. Shao, J. Wu, X. Guo, X. Hu, A randomized phase 3 trial of Gemcitabine or Nab-paclitaxel combined with cisPlatin as first-line treatment in patients with metastatic triple-negative breast cancer, Nat Commun. 13 (2022) 4025. https://doi.org/10.1038/s41467-022-31704-7.

[226] P. Schmid, H.S. Rugo, S. Adams, A. Schneeweiss, C.H. Barrios, H. Iwata, V. Diéras, V. Henschel, L. Molinero, S.Y. Chui, V. Maiya, A. Husain, E.P. Winer, S. Loi, L.A. Emens, Atezolizumab plus nab-paclitaxel as first-line treatment for unresectable, locally advanced or metastatic triple-negative breast cancer (IMpassion130): updated efficacy results from a randomised, double-blind, placebo-controlled, phase 3 trial, The Lancet Oncology. 21 (2020) 44–59. https://doi.org/10.1016/S1470-2045(19)30689-8.

[227] C.G. Jothi Prakash, R. Prasanth, Approaches to design a surface with tunable wettability: a review on surface properties, J Mater Sci. 56 (2021) 108–135. https://doi.org/10.1007/s10853-020-05116-1.

[228] K.E. O'Connell, A.M. Mikkola, A.M. Stepanek, A. Vernet, C.D. Hall, C.C. Sun, E. Yildirim, J.F. Staropoli, J.T. Lee, D.E. Brown, Practical murine

hematopathology: a comparative review and implications for research, Comp Med. 65 (2015) 96–113.